X-ray Fluorescence Analysis of Complex Materials

**Author:**
Ganly, Brianna

**Publication Date:**
2018

**DOI:**
https://doi.org/10.26190/unsworks/2078

**License:**
https://creativecommons.org/licenses/by-nc-nd/3.0/au/
Link to license to see what you are allowed to do with this resource.

Downloaded from http://hdl.handle.net/1959.4/60116 in https://unsworks.unsw.edu.au on 2024-03-29

# X-ray Fluorescence Analysis of Complex Materials

*A thesis in fulfilment of the requirements for the degree of*

**Doctor of Philosophy**

*from the*

**University of New South Wales**

*by*

**Brianna Ganly**

School of Materials Science and Engineering

Faculty of Science

April, 2018

PLEASE TYPE

**THE UNIVERSITY OF NEW SOUTH WALES**
**Thesis/Dissertation Sheet**

Surname or Family name: Ganly

First name: Brianna Other name/s:

Abbreviation for degree as given in the University calendar: PhD

School: Materials Science and Engineering Faculty: Science

Title: X-ray fluorescence analysis of complex material


**Abstract 350 words maximum: (PLEASE TYPE)**

**Portable, in-situ and on-stream X-ray fluorescence (XRF) is widely used in minerals industry applications to analyse materials with little or no sample preparation. These XRF techniques have been found particularly useful for measuring the concentrations of precious and base metals such as gold, platinum, nickel and copper in mineral slurries. The consequence of measuring mineral samples in slurry form is that physical sample effects can limit the accuracy of XRF analysis. This thesis describes two different approaches for improving the XRF analysis of in-situ slurries: thorough characterisation of heavy element L-shell spectra for improved spectral fitting, and the development of a particle size effect correction technique.**

**L-shell X-ray spectra have been measured for 8 elements with atomic numbers between 68 and 79, and the measured line intensity ratios and total subshell intensity ratios are compared to existing theoretical and experimental values. The spectra were carefully fitted to determine line energies and intensities, accounting for Lorentzian line broadening, Compton scattering, incomplete charge collection and the silicon escape effect. A Monte Carlo approach was used to calculate geometry, attenuation and detector efficiency corrections. Up to 15 line intensity ratios and total L1/L3 and L2/L3 subshell intensity ratios are reported for each element. Substantial disagreement is found in both magnitude and trend with atomic number when compared to theory. The measured results are used to predict the errors introduced during elemental composition determination using theoretical basis-function fitting when measured XRF spectra are analysed with incorrect theoretical X-ray emission intensities.**

**The intensity of characteristic fluorescent radiation from mineral phases in particulate materials such as slurries decreases as the particle size of the ore being measured increases. The particle size effect can lead to significant analysis errors, but is usually ignored in on-stream applications where there is limited control over the particle size. This thesis describes measurements of the particle size effect for copper and iron powders in a weakly absorbing matrix. The measured results are compared to a theoretical model and Monte Carlo simulations. A preliminary correction method involving measurements using dual exciting radiation energies is discussed and evaluated using measured and simulated data.**


**Declaration relating to disposition of project thesis/dissertation**

I hereby grant to the University of New South Wales or its agents the right to archive and to make available my thesis or dissertation in whole or in part in the University libraries in all forms of media, now or here after known, subject to the provisions of the Copyright Act 1968. I retain all property rights, such as patent rights. I also retain the right to use in future works (such as articles or books) all or part of this thesis or dissertation.

I also authorise University Microfilms to use the 350 word abstract of my thesis in Dissertation Abstracts International (this is applicable to doctoral theses only).

12/10/17

Signature Witness Signature Date

The University recognises that there may be exceptional circumstances requiring restrictions on copying or conditions on use. Requests for restriction for a period of up to 2 years must be made in writing. Requests for a longer period of restriction may be considered in exceptional circumstances and require the approval of the Dean of Graduate Research.

**FOR OFFICE USE ONLY** Date of completion of requirements for Award:

**COPYRIGHT STATEMENT**

'I hereby grant the University of New South Wales or its agents the right to archive and to make available my thesis or dissertation in whole or part in the University libraries in all forms of media, now or here after known, subject to the provisions of the Copyright Act 1968. I retain all proprietary rights, such as patent rights. I also retain the right to use in future works (such as articles or books) all or part of this thesis or dissertation.
I also authorise University Microfilms to use the 350 word abstract of my thesis in Dissertation Abstract International (this is applicable to doctoral theses only).
I have either used no substantial portions of copyright material in my thesis or I have obtained permission to use copyright material; where permission has not been granted I have applied/will apply for a partial restriction of the digital copy of my thesis or dissertation.'

Signed

Date 3/4/2018

**AUTHENTICITY STATEMENT**

'I certify that the Library deposit digital copy is a direct equivalent of the final officially approved version of my thesis. No emendation of content has occurred and if there are any minor variations in formatting, they are the result of the conversion to digital format.'

Signed

Date 3/4/2018

**ORIGINALITY STATEMENT**

'I hereby declare that this submission is my own work and to the best of my knowledge it contains no materials previously published or written by another person, or substantial proportions of material which have been accepted for the award of any other degree or diploma at UNSW or any other educational institution, except where due acknowledgement is made in the thesis. Any contribution made to the research by others, with whom I have worked at UNSW or elsewhere, is explicitly acknowledged in the thesis. I also declare that the intellectual content of this thesis is the product of my own work, except to the extent that assistance from others in the project's design and conception or in style, presentation and linguistic expression is acknowledged.'

Signed

Date 3/4/2018

**ABSTRACT**

Portable, in-situ and on-stream X-ray fluorescence (XRF) is widely used in minerals industry applications to analyse materials with little or no sample preparation. These XRF techniques have been found particularly useful for measuring the concentrations of precious and base metal such as gold, platinum, nickel and copper in mineral slurries. The consequence of measuring mineral samples in slurry form is that physical sample effects can limit the accuracy of XRF analysis. This thesis describes two different approaches for improving the XRF analysis of in-situ slurries: thorough characterisation of heavy element L-shell spectra for improved spectral fitting, and the development of a particle size effect correction technique.

L-shell X-ray spectra have been measured for 8 elements with atomic numbers between 68 and 79, and the measured line intensity ratios and total subshell intensity ratios are compared to existing theoretical and experimental values. The spectra were carefully fitted to determine line energies and intensities, accounting for Lorentzian line broadening, Compton scattering, incomplete charge collection and the silicon escape effect. A Monte Carlo approach was used to calculate geometry, attenuation and detector efficiency corrections. Up to 15 line intensity ratios and total L1/L3 and L2/L3 subshell intensity ratios are reported for each element. Substantial disagreement is found in both magnitude and trend with atomic number when compared to theory. The measured results are used to predict the errors introduced during elemental composition determination using theoretical basis-function fitting when measured XRF spectra are analysed with incorrect theoretical X-ray emission intensities.

The intensity of characteristic fluorescent radiation from mineral phases in particulate materials such as slurries decreases as the particle size of the ore being measured increases. The particle size effect can lead to significant analysis errors, but is usually ignored in on-stream applications where there is limited control over the particle size. This thesis describes measurements of the particle size effect for copper and iron powders in a weakly absorbing matrix. The measured results are compared to a theoretical model and Monte Carlo simulations. A preliminary correction method involving measurements using dual exciting radiation energies is discussed and evaluated using measured and simulated data.

**ACKNOWLEDGEMENTS**

I would like to sincerely thank my CSIRO supervisor, Dr James Tickner, for his guidance and inspiration over the past three years. I am very grateful for all the time that he has invested into this project and his constant support and encouragement of me to explore various research opportunities. Much of my success is owed to his knowledge and passion for research.

I am appreciative of everyone in the Sensing and Sorting CSRIO group at Lucas Heights, with whom this project was conducted. The many cakes and biscuits at morning tea always eased the pain of any long day. In particular, I would like to thank Dr Nick Cutmore and Mike Millen, for their helpful advice and encouragement. I would also like to thank Dr Yves Van Haarlem, for his patience teaching me how to code fitting scripts as well as David Abernethy and Dr Joel O'Dwyer for providing advice and assistance with XRF experiments.

I would like to acknowledge Professor J L (Iain) Campbell, for welcoming me to the University of Guelph for 4 months of this PhD and sharing his vast knowledge of fitting XRF spectra. His passion for research is inspirational and I am very grateful for the opportunity to work with him.

Without the support of my UNSW supervisor, Professor Veena Sahajwalla, I would of not of been able to undertake this thesis. I am grateful that she has always believed in me throughout my eight years at UNSW, and that she has always supported my research endeavours.

Finally I would like thank my friends and family. I am indebted to my parents, for their unwavering love and support and to my partner Lachlan for always being there for me. I would like to thank my friends for providing many laughs throughout the years spent working on this thesis.

I would like to dedicate this thesis to my dear friend Gavin Chan. Gavin believed in me before I believed in myself and I will always appreciate his support of me applying for this PhD. Gavin passed away in 2014 just before I began my PhD, but knowing that he had confidence in me always made it easier to get through any long days.

**PUBLICATION LIST**

J. L. Campbell, B. Ganly, C. M. Heirwegh, and J. A. Maxwell, “Separation of detector non-linearity issues and multiple ionization satellites in alpha-particle PIXE,” *Nucl. Instruments Methods Phys. Res. Sect. B Beam Interact. with Mater. Atoms*, vol. 414, pp. 38–44, Jan. 2018.

B. Ganly, Y. Van Haarlem, and J. Tickner, “Relative total L-subshell X-ray emission intensities and their impact on the fitting of complex X-ray fluorescence spectra,” *X-Ray Spectrom.*, 2017.

J. Tickner, R. Rajarao, B. Lovric, B. Ganly, and V. Sahajwalla, “Measurement of Gold and Other Metals in Electronic and Automotive Waste Using Gamma Activation Analysis,” *J. Sustain. Metall.*, vol. 2, no. 4, pp. 296–303, Dec. 2016.

J. L. Campbell, C. M. Heirwegh, and B. Ganly, “Non-linearity issues and multiple ionization satellites in the PIXE portion of spectra from the Mars alpha particle X-ray spectrometer,” *Nucl. Instruments Methods Phys. Res. Sect. B Beam Interact. with Mater. Atoms*, vol. 383, pp. 143–151, 2016.

B. Ganly, Y. Van Haarlem, and J. Tickner, “Measurement of relative line intensities for L-shell X-rays from selected elements between Z = 68 (Er) and Z = 79 (Au),” *X-Ray Spectrom.*, vol. 45, no. 4, pp. 233–243, Jul. 2016.

## TABLE OF CONTENTS

**ABSTRACT** ..... i
**ACKNOWLEDGEMENTS** ..... ii
**PUBLICATION LIST** ..... iii
**TABLE OF CONTENTS** ..... iv
**LIST OF FIGURES** ..... vii
**PART 1: INTRODUCTION AND LITERATURE REVIEW** ..... 1
1 Introduction ..... 1
1.1 Thesis Aim ..... 3
1.2 Overview ..... 5
2 Review of the Fundamental Parameters Method and Parameter Databases ..... 6
2.1 History of Density Functional Theory ..... 7
2.2 Calculation of X-ray Emission Rates from Basic Data ..... 9
2.3 Evaluation of Fundamental Parameters Databases ..... 10
2.3.1 Fluorescence Yields and Coster-Kronig Transition Probabilities ..... 11
2.3.2 Line Widths ..... 12
2.3.3 Photoionisation Cross-sections ..... 13
2.3.4 Mass attenuation Coefficients ..... 14
2.3.5 X-ray Line Energies ..... 16
2.3.6 Relative L-subshell Line Intensities ..... 19
3 Particle Size Effect ..... 21
3.1 Physical Interpretation of the Particle Size Effects ..... 21
3.2 Theoretical Models ..... 24
3.2.1 Claisse and Samson ..... 25
3.2.2 Lubecki ..... 25
3.2.3 Berry, Furuta and Rhodes ..... 27
3.3 Particle Size Effect Correction Methods ..... 28
3.3.1 Exciting Radiation Energy ..... 28
3.3.2 Exciting Radiation Angle ..... 31
3.4 Summary ..... 32
**PART 2: IMPROVING FUNDAMENTAL PARAMETERS CORRECTIONS FOR XRF APPLICATIONS** 34
4 Developing Fitting Methods for Complicated XRF Spectra ..... 34
4.1 Fit Details ..... 34
4.1.1 Line Shape ..... 34

4.1.2 Background Function ..... 40
4.1.3 Universal Fit Parameters ..... 41
4.2 Fitting Method ..... 42
4.3 Peak Error Determination ..... 44
4.4 Peak Area Determination ..... 45
5 Total L-subshell and Individual Line Relative Measurements ..... 46
5.1 Theoretical Treatment ..... 46
5.2 Experimental Measurements ..... 47
5.3 Fitted Spectra ..... 52
5.4 Correction for X-ray Absorption and Detection Efficiency ..... 58
5.4.1 Fundamental Parameters Calculation ..... 58
5.4.2 Monte Carlo Simulation ..... 59
5.4.3 Fundamental Parameters Error Component ..... 59
5.5 Relative Line Intensity Ratio Measurements ..... 60
5.6 Relative Line Intensity Discussion ..... 71
5.6.1 Systematic Errors ..... 71
5.6.2 Comparison with DHS and DF data ..... 73
5.6.3 Comparison Between Metals and Metallic Oxides ..... 75
5.6.4 Tantalum Line Energy Positions ..... 76
5.7 Relative Total L-subshell Emission Intensities ..... 80
5.7.1 Measured Total L-subshell Emission Intensities ..... 80
5.7.2 Results ..... 81
5.7.3 Discussion ..... 85
5.8 Impact of Fitting Measured XRF Spectra with Incorrect L-shell Emission Intensities. 85
5.8.1 Modelling Approach for Estimating Errors ..... 86
5.8.2 Results and Discussion ..... 87
5.8.3 Error Propagation ..... 89
5.8.4 Impact of Relative Total L-shell Emission Intensity vs Individual Line Intensities 91
**PART 3: THE PARTICLE SIZE EFFECT** ..... 92
6 Experimental Method for Measuring the Particle Size Effect ..... 94
6.1 Sample Preparation ..... 94
6.1.1 Powder Sizing ..... 94
6.1.2 Particle Dispersion ..... 102
6.1.3 Samples with Zero Particle Size ..... 111
6.2 Monte Carlo Simulations ..... 113

6.3 Exciting Energy ..... 114
6.3.1 Selecting the Experimental Exciting Radiation Spectra ..... 119
6.4 Experimental Set Up ..... 124
6.5 Particle Size Results ..... 126
6.5.1 Spectra Fitting Details ..... 127
6.5.2 Particle Size Measurements ..... 130
7 Developing a Particle Size Effect Correction Method ..... 133
7.1 Comparison between Experiment, Analytical and Monte Carlo Simulation Results 133
7.2 Discussion of Discrepancies between Experiment, Analytical and Monte Carlo Simulation Particle Size Results ..... 138
7.2.1 The Perlin Noise Function Results ..... 138
7.2.2 The Particulate Model Results ..... 143
7.2.3 Effect of Uncertainty in Filter Thickness ..... 145
7.2.4 Analytical Results ..... 147
7.3 Dual Energy Correction ..... 147
7.3.1 Particle Size Effect Correction using Multiple Exciting Radiation Energies ..... 147
7.4 Future work: Improvements to the Quantitative Comparison of Simulation and Experimental Results ..... 152
7.4.1 Standards Method ..... 154
7.4.2 Particle Shape Effects ..... 155
7.5 Future Work: Particle Size Correction of Unknown Materials ..... 159
7.6 Conclusion ..... 162
**PART 4: CONCLUSIONS AND RECOMMENDATIONS** ..... 164
8 Conclusion ..... 164
8.1 L-shell Emission Intensity Measurements and their Impact on X-ray Fluorescence 164
8.2 Measurement and Modelling of Particle Size Effects ..... 166
8.3 Recommendations for Future Work ..... 167

## LIST OF FIGURES

**Figure 2-1**: A recreated figure from the Jitschin et al study showing a scan of the X-ray absorption spectrum for tungsten taken at room temperature [67]. ..... 16

**Figure 3-1**: The change in fluorescence radiation intensity with particle size. Line 1 represents a sample with a weakly absorbing matrix and line 2 represents a sample with a strongly absorbing matrix [16]. ..... 22

**Figure 3-2**: (A) Shielding of fluorescent X-rays from large particles compared to (B) a homogenous flat sample with no particulate effects [16]. ..... 24

**Figure 3-3**: Theoretical curves of relative intensity of the characteristic K lines of iron versus particle size recreated from Lubecki et al.'s study [87]. Curve (a) is iron in a calcium matrix excited by 9.2 keV radiation. Curve (b) is the same material excited by 22.6 keV radiation. Curves (c) and (d) show the intensity of fluorescence from iron in a silicon matrix excited by 9.2 and 22.6 keV radiation respectively. ..... 29

**Figure 3-4**: (A) the particle size effect for copper particles in a silica matrix, calculated using Lubecki et al.'s theoretical model at various exciting radiation energies. (B) The ratios of the 11-17 keV fluorescence response to the 9.6 keV fluorescence response versus particle size... 30

**Figure 4-1**: Compton scattering of a photon. ..... 36

**Figure 4-2**: Components of the line-shape model used to fit L-shell X-ray spectra. A simple Gaussian peak shape is shown for comparison. See text for details. ..... 39

**Figure 5-1**: Illustration of the steel frame and the experimental set-up used to collect the XRF spectra. ..... 48

**Figure 5-2**: the Ebel model prediction of the exciting radiation spectrum from a molybdenum target tube with a zirconium filter. ..... 49

**Figure 5-3**: Measured XRF spectrum taken with no sample in place measured over 30 min. .. 50

**Figure 5-4**: the fitted erbium L-shell spectrum, reduced $\chi^2 = 1.44$. ..... 53

**Figure 5-5**: The fitted thulium L-shell spectrum, reduced $\chi^2 = 1.60$. ..... 53

**Figure 5-6**: The fitted ytterbium L-shell spectrum, reduced $\chi^2 = 1.24$. ..... 54

**Figure 5-7**: The fitted hafnium L-shell spectrum, reduced $\chi^2 = 1.30$. ..... 54

**Figure 5-8**: The fitted tantalum L-shell spectrum, reduced $\chi^2 = 1.46$. ..... 55

**Figure 5-9**: The fitted tantalum oxide L-shell spectrum, reduced $\chi^2 = 1.33$. ..... 55

**Figure 5-10**: The fitted tungsten L-shell spectrum, reduced $\chi^2 = 1.19$. ..... 56

**Figure 5-11**: The fitted tungsten oxide L-shell spectrum, reduced $\chi^2 = 1.66$. ..... 56

**Figure 5-12**: The fitted platinum L-shell spectrum, reduced $\chi^2 = 1.63$. ..... 57

**Figure 5-13**: The fitted gold L-shell spectrum, reduced $\chi^2 = 1.47$. ..... 57

**Figure 5-14**: Line intensity ratios plotted against atomic number for 8 different selected line pairs. Measured ratios are shown as points; error bars denote the total calculated error. Results from DF [73], DHS [11] and Elam [75] are shown for comparison. ..... 74
**Figure 5-15**: the measured tantalum and tantalum oxide spectra, both normalised to the highest count in each spectra. ..... 76
**Figure 5-16**: the tantalum spectra fitted with the NIST theoretical line energy positions, $\chi^2$ = 39.9. ..... 77
**Figure 5-17:** measured $I_{L2}/I_{L3}$ ratios (at 17.44 keV) compared to calculated values using fundamental parameters from the EADL database and Campbell's recommended Coster-Kronig and L-shell fluorescence yields. ..... 83
**Figure 5-18:** measured $I_{L1}/I_{L3}$ ratios (at 17.44 keV) compared to calculated values using fundamental parameters from the EADL database and Campbell's recommended Coster-Kronig and L-shell fluorescence yields. ..... 84
**Figure 5-19:** The modelled 'experimental' spectrum with a composition of 33% W, 33% Au and 33% Ta, shown with blue data points. The individual element contributions, fitted with the DHS values, are shown as solid coloured lines. The total fit is shown as a black solid line. ..... 90
**Figure 5-20:** The modelled 'experimental' spectrum with a composition of 25% W, 25% Yb, 25% Tm and 25% Hf, shown with blue data points. The individual element contributions, fitted with the DHS values, are shown as solid coloured lines. The total fit is shown as a black solid line..... 91
**Figure 6-1:** The cyclosizer used to sort the smaller-sized particles into 5 different size fractions. ..... 96
**Figure 6-2:** a schematic diagram of the cyclosizer reproduced from the manual [117], with the labels of the main control valve and apex valves, shown in blue, added in..... 97
**Figure 6-3**: The 5 different powder fractions for iron and copper settling after being released from each cyclone. The smallest particle size fraction CS5 settles significantly slower than the larger particle size fractions. ..... 98
**Figure 6-4**: Discrete (blue) and cumulative (red) volume fraction size distribution for material retained in a 45 µm sieve but passing a 53 µm sieve. ..... 100
**Figure 6-5**: Copper particles from the sieved 90-106 um fraction. ..... 102
**Figure 6-6:** The design of the miniature slurry tank with a U-shaped bottom, slot for an X-ray window, and slot for a stirrer to enter through the tank lid and stir the slurry. ..... 104

**Figure 6-7**: The tumbling slurry tank set-up: (a) the rotating sample jar with an open end (b) The sample jar is inserted to a plastic holder that locks the sample in place. (c) The 24 V motor used to rotate the sample jar and holder. ..... 105
**Figure 6-8**: The XRF response versus time for a 1% copper sample suspended in (a) peanut oil and (b) a mixture of 90% glucose syrup and 10% water. Each sample is being rotated at a speed of 60 rpm to help keep the particles suspended. ..... 109
**Figure 6-9:** Randomly distributed Perlin function particles calculated with (a) the smooth and (b) the fractal noise functions. ..... 113
**Figure 6-10**: The ratio of the fluorescence mass attenuation coefficient to the exciting radiation mass attenuation coefficient for various elements, predicted for samples containing 3% of each element in a dough matrix. ..... 115
**Figure 6-11**: The ratio of the fluorescence mass attenuation coefficient to the exciting radiation mass attenuation coefficient for various samples with varying copper concentrations and matrixes. ..... 116
**Figure 6-12**: Monte Carlo simulations of the particle size effect, shown as fluorescence intensity vs particle size, for a 3% copper sample in a dough, simulated with various exciting radiation energies. ..... 117
**Figure 6-13**: Monte Carlo simulations of the particle size effect, shown as fluorescence intensity vs particle size, for a 5% iron sample in a dough, simulated with various exciting radiation energies. ..... 117
**Figure 6-14**: The change in fluorescence intensity resulting from Monte Carlo simulations using exciting radiation energies varying from 9 to 30 keV, all simulated with equal source strength. The change in fluorescence is shown for 3% copper in dough samples, simulated with 4 different particle sizes. ..... 119
**Figure 6-15**: The filtered X-ray tube spectrum predicted by the Ebel model for a molybdenum target X-ray tube with a zinc filter (0.1 g/cm$^2$) operated at a tube voltage of 20 kV. The energy positions of the copper Kα and Kβ peaks are shown over the spectrum to show the overlap. 122
**Figure 6-16:** The filtered X-ray tube spectrum predicted by the Ebel model for a molybdenum target X-ray tube with a silver filter (0.4 g/cm$^2$) operated at a tube voltage of 40 kV. ..... 123
**Figure 6-17**: The filtered X-ray tube spectrum predicted by the Ebel model for a molybdenum target X-ray tube with a zirconium filter (0.305 g/cm$^2$) operated at a tube voltage of 40 kV.. 124
**Figure 6-18**: The placement of (a) the detector, (b) the X-ray tube, (c) the X-ray tube filter and (d) the slurry tank wall and X-ray the detector and (e), the XRF block. The left panel shows the

view from above the set-up, with the XRF block not shown to simplify the view of the set-up. The right panel shows the view looking directly at the XRF block screwed into positon..... 125
**Figure 6-19**: (a) shows the front of an X-ray tube with no filter applied to the X-ray window, (b) and (c) show how the filter switch can be adjusted to interpose either the Zr (light blue square) or the Zn filter (light green square) into the X-ray beam. ..... 126
**Figure 6-20**: the fitted spectrum of a sample excited with the zinc filtered exciting radiation. The sample contains 3% copper. A small iron foil introduced additional peaks used for calibration and stability monitoring..... 128
**Figure 6-21**: fitted spectrum of a sample excited with the zirconium filtered exciting radiation. The sample contains 3% copper plus a small iron foil. The background is fitted with a third-degree polynomial function; however the background counts are of too low intensity to appear on the selected scale. ..... 129
**Figure 6-22**: The change in copper fluorescence intensity with varying particle size, measured for samples with a 3% copper concentration in dough, prepared with different sized copper particles..... 131
**Figure 6-23**: the change in iron fluorescence intensity with varying particle size, measured for samples with a 5% iron concentration in dough, prepared with different sized iron particles. ..... 132
**Figure 7-1**: The measured particle size effect for samples containing 3% copper in dough compared with Monte Carlo simulations of the experimental set-up using the particulate and Perlin noise function modelling approaches. ..... 136
**Figure 7-2**: The measured particle size effect for samples containing 5% iron in dough compared with Monte Carlo simulations of the experimental set-up using the particulate and Perlin noise function modelling approaches. ..... 136
**Figure 7-3**: The measured relative particle size effect for samples containing 3% copper in dough compared with Monte Carlo simulations of the relative particle size effect using the particulate and perlin functions, as well as a theoretical prediction of the particle size effect using Lubecki et al.'s formula [87]. ..... 137
**Figure 7-4**: The measured relative particle size effect for samples containing 5% iron in dough compared with Monte Carlo simulations of the relative particle size effect using the particulate and perlin functions, as well as a theoretical prediction of the particle size effect using Lubecki et al.'s formula [87]..... 137

**Figure 7-5**: The distribution of copper particles from a 1 $cm^2$ region on the surface of a dough sample containing 3% copper particles generated using (a) the smooth Perlin noise function and (b) the fractal Perlin noise function ..... 139
**Figure 7-6**: The particle equivalent sphere diameter distribution of copper particles calculated using the fractal Perlin noise function with a scale parameter set to give an average equivalent sphere diameter of 100 µm. Note the logarithmic scale on the X-axis. ..... 140
**Figure 7-7**: The particle equivalent sphere diameter distribution of copper particles calculated using the smooth Perlin noise function with a scale parameter set to give an average equivalent sphere diameter of 100 µm. Note the logarithmic scale on the X-axis. ..... 140
**Figure 7-8**: The left panel shows copper particles from the sieved 90-106 um fraction and the right panel shows the cyclosized iron powders in the 20-40 µm fraction. ..... 144
**Figure 7-9**: Close up image of the zinc foil used showing tears and holes in the foil. ..... 145
**Figure 7-10**: The measured particle size effect for samples containing 3% copper in dough compared with Monte Carlo simulations of the relative particle size effect using the particulate function with varying zinc filter thickness. 0.065 $g/cm^2$ is the measured thickness of the zinc filter used in the experimental measurements, and 0.0715 and 0.0585 $g/cm^2$ are the measured thickness plus or minus 10%, respectively. The left panel shows the absolute c/s measurements, and the right panel shows the normalised relative values. ..... 146
**Figure 7-11**: I1/I2 vs I1/I1(0) for a measured 3% copper in dough sample compared to Monte Carlo simulated data using the particulate function, MC Particulate, and the corrected equivalent smooth sphere diameter values, MC Particulate ESD, and theoretically predicted data using Lubecki et al.'s theoretical model. ..... 150
**Figure 7-12**: I1/I2 vs I1/I1(0) for a measured 5% iron in dough sample compared to Monte Carlo simulated data using the particulate function, MC Particulate, and the corrected equivalent smooth sphere diameter values, MC Particulate ESD, and theoretically predicted data using Lubecki et al.'s theoretical model. ..... 151
**Figure 7-13**: The relationship between the measured particle size and the equivalent smooth sphere diameter, defined as the particle size modelled using the particulate function that gives the same drop in intensity measured experimentally. The equivalent smooth sphere diameter is plotted for iron powder measurements, measured with both the zinc and zirconium filtered exciting radiation. For each case a trend line is also included to show the linearity of the relationship between the measured particle size and the particulate function calculated equivalent smooth sphere diameter. ..... 156

**Figure 7-14**: The measured particle size effect for samples containing 5% iron in dough compared with Monte Carlo simulations of the particle size effect using the particulate function and the equivalent smooth sphere diameter particle size. The top two panels, (A) and (B), show the zinc filtered exciting radiation case and the bottom two panels, (C) and (D), show the zirconium filtered exciting radiation case. (A) and (C) show the fluorescence response in counts/second while (B) and (D) show the fluorescence response normalised to the sample with no particle size effects. ..... 158
**Figure 7-15**: I1(s)/I2(s) vs I1(s)/I1(0) for Monte Carlo particulate function simulated silica and copper slurries containing 1%, 3% and 5% copper concentrations. An example measurement of I1(s)/I2(s) of 1.04 and the corresponding I1(s)/I1(0) range over the different concentration curves is shown. ..... 161

## LIST OF TABLES

**Table 5-1**: Thickness of foils used for XRF measurements and the corresponding number of mean free paths for both incident and typical fluorescent X-rays. The L3-M5 X-ray is the brightest L-shell line and is used in this table as an example of a typical L-shell X-ray transition. ..... 51

**Table 5-2**: Erbium..... 63

**Table 5-3**: Thulium ..... 64

**Table 5-4**: Ytterbium ..... 65

**Table 5-5**: Hafnium ..... 66

**Table 5-6**: Tantalum ..... 67

**Table 5-7**: Tungsten ..... 68

**Table 5-8**: Platinum..... 69

**Table 5-9**: Gold..... 70

**Table 5-10**: Energy separation of the L1-M3 line and nearby L3-N5 and L3-N1 lines, and the corresponding error on the fitted area of the L1-M3 peak. ..... 72

**Table 5-11**: Energy separation of the L2-M4 line and the nearby L3-N1 line, and the corresponding error on the fitted area of the L2-M4 peak. ..... 73

**Table 5-12**: A comparisons of the Tantalum line positions from the NIST Theoretical data, NIST experimental data and experimentally measured in this study. ..... 78

**Table 5-13:** shows the difference in eV between the NIST theoretical values and the NIST experimental values; the NIST theoretical values and the measured values; and the NIST experimental values and the measured values of the tantalum line energy positions..... 79

**Table 5-14**: The root mean square errors on the determined elemental compositions for 500 randomly generated compositions of Ta, W and Au. The randomly generated XRF spectra, created from the measured data, were fitted with DHS data and the Campbell recommended data. ..... 88

**Table 5-15**: The root mean square errors on the determined elemental compositions for 500 randomly generated compositions of Yb, Tm, Hf and W. The randomly generated XRF spectra, created from our measured data, were fitted with DHS data and the Campbell recommended data. ..... 88

**Table 6-1**: List of powders and their details used in this chapter..... 94

**Table 6-2**: The effective particle size separation lower cut off of each cyclone in the cyclosizer. ..... 99

**Table 6-3**: A comparison of the sieve diameter range and the volume equivalent sphere diameter range as determined using laser diffraction analysis. The particle size range returned from the laser diffraction reports is expressed as d(0.1), d(0.5) and d(0.9) which are respectively the particle diameters larger than 10%, 50% and 90% of the particles by volume. D[4,3] and D[3,2] are the volume weighted and surface area weighted mean diameters respectively. ..... 101
**Table 6-4**: A comparison of the velocity different sized particles will settle in various liquids.106
**Table 6-5**: the copper fluorescence response from 3 different dough samples all made to have a concentration of 3% copper CS1 particles. ..... 110
**Table 6-6**: The measured weights of the raw materials used to create the glass fusion sample with 5% iron and 1% copper. ..... 112
**Table 6-7**: The measured weights of the raw materials used to create the glass fusion sample with 1% iron and 3% copper. ..... 112
**Table 6-8**: The K-edge of elements above copper in the periodic table. ..... 120
**Table 7-1**: Particles are generated using a fractal Perlin function to create a 3% copper sample, where the median particle diameter is 100 µm. The number of particles and their area are examined and sorted into fractions depending on how many pixels are in each particle, reported as the 'Area'. The equivalent sphere diameter for each area fraction is given for comparison. The percentage of each area fraction to the total area is reported. ..... 143
**Table 7-2**: The coefficients a and b are listed for the four different ESSD correction trend lines shown in Figure 7-13, as well as the $R^2$ values to indicate the goodness of the fit of the trend line to the data. ..... 157

**PART 1: INTRODUCTION AND LITERATURE REVIEW**

# 1 Introduction

First explained more than a century ago in Einstein's 1905 paper [1], the photoelectric effect occurs when photons eject bound electrons from atoms. If suitably energetic electromagnetic radiation is used – typically in the X-ray region – then inner-shell electrons can be ejected. Transitions of higher-shell electrons into these vacancies leads to the emission of fluorescent X-rays whose energy is equal to the difference in energy of the electron in the initial and final shells ($E_\gamma = E_j - E_i$). As the energies of the electron shells and subshells for each element are unique, the energies of the emitted X-rays are characteristic of that element and the exact transition that occurred [2]. Therefore, fluorescent X-ray emission provides a useful signature that can be used to deduce qualitative and quantitative information about material composition. The term X-ray fluorescence (XRF) is used to describe the analysis of material composition using X-ray induced fluorescent X-ray emission.

Two main technological advances have allowed XRF to successfully become a useful technique for portable and in-situ measurement: the development of miniature X-ray tube sources, and the development of non-cryogenic Energy Dispersive Spectroscopy (EDS) detectors [3]. With these developments, a complete XRF system can be provided in a small and portable package. A portable XRF tube source, typically running at voltages up to 50 kV, allows light elements with atomic number $Z < 40$-$50$ to be measured using their innermost or K-shell X-ray emission lines, and heavier elements with $Z > 40$-$60$ to be measured using their second innermost or L-shell X-rays.

Portable, in-situ and on-stream XRF has become widespread in the minerals industry, where it is used to provide rapid information about the composition of ore deposits during exploration, mining and mineral processing [4]–[6].

There are two widely-used methods for accurately analysing X-ray emission spectra to determine the material's elemental composition: the standards method and a standard-less physics-based approach [7].

The standards approach compares X-ray emission of unknown samples to emission from well-characterised materials. It can provide meaningful concentration results if the calibration standards are close to the composition of the sample and are measured under similar conditions.

The physics-based fundamental parameters method instead uses tabulated values of parameters such as photoelectric cross-section and X-ray emission probabilities to transform measured X-ray peak intensities into elemental concentration [8]. The fundamental parameters approach is limited by uncertainties in the values of the parameters being used, and by simplifications made in the calculations.

When conducting XRF in a laboratory environment, various sample preparation techniques are commonly used to improve the analysis accuracy. For example, when measuring geological mineral samples, materials are ground into fine powders and then either pressed into pellets or mixed with flux materials and melted into fusion glass bead samples [9]. Sample preparation techniques are used to make the samples as homogeneous as possible; however they require bulky and sometimes expensive equipment and can be time-consuming. The introduction of XRF equipment for field work means that more often than not, no sample preparation is possible and the samples being measured are heterogeneous.

Both the standards method and the fundamental parameters methods have their flaws, and most portable and in-situ XRF applications used in the minerals industry will rely on a combination of both methods to achieve the most accurate results. Field samples may not accurately emulate the composition of available standards and can have different physical properties such as particle size. The fundamental parameters approach assumes that the sample is homogenous, which is often not the case for unprepared field samples. Many samples being measured in the field are particulate materials, such as soil or crushed ore. As a result, portable and in-situ XRF techniques can often return misleading elemental concentrations.

In theory each time an XRF instrument is used to measure a new type of sample, it should be recalibrated with a standard with similar properties. However, in practice, the physical properties and compositions of samples can change dramatically between

sites and different ore deposits. It is unlikely that the user will recalibrate the XRF analyser as often as required, as this is a time-consuming process. For this reason, this thesis will instead focus on ways to improve the fundamental parameters approach and to minimise the need for the regular measurement of standards for portable and in-situ XRF applications. In particular this thesis will focus on the in-situ measurements on slurries – mixtures of ground ore and water commonly encountered in mineral applications - and the problems associated with slurry measurements using XRF.

### 1.1 Thesis Aim

The CSIRO X-ray team develops industrial XRF instruments designed to measure the concentrations of precious and base metal such as gold, platinum, nickel and copper in mineral slurries. While XRF is a well-developed technique, there are still many challenges when measuring in situ non-homogeneous samples, for example slurries in a mineral processing plant. Many of these challenges can be associated with limitations in the physics based approach of transforming XRF spectra peak measurements into elemental concentrations using the fundamental parameters method. The aim of this thesis is to improve the analysis of slurries using two different approaches.

The first approach will involve an in-depth analysis of the fundamental parameters used to calculate the XRF response from heavy elements often found in precious metal ores. Gold and platinum mineral samples are often accompanied by low-value, heavy metals such as lead, tungsten and uranium present at significantly higher concentrations. Errors in the XRF responses of these heavy elements predicted using the fundamental parameters method can lead to significant inaccuracies in the determined elemental composition of the sample.

Currently, the parameters used to calculate L-shell X-ray emission intensities of heavy elements mainly come from theoretical calculations performed in the 1970s by Scofield (see literature review in the next chapter) [10]–[12]. These calculations underpin the X-ray emission intensity tabulations almost universally used by practicing spectroscopists. Despite the widespread use of Scofield's values, there have only been a handful of small-scale studies comparing experimentally measured L-shell line

intensity ratios to Scofield's results, and no consistent demonstration of the validity of the theoretical models used [13]–[15]. These observations prompted the first aim of this thesis: to conduct a detailed study measuring the L-shell intensities of various heavy elements, and to compare the results with Scofield's theoretical values and any other comprehensive database tabulations available.

The second approach focuses on improvements that can be made when measuring particulate slurry samples. The intensity of characteristic fluorescent radiation from mineral phases in a slurry is affected by the particle size of the ore being measured [16]. This particle size effect can lead to substantial analysis errors, but is usually ignored in on-stream applications where no control of particle size is possible. If the particle size effect can be accounted for, then a fundamental parameters based approach can be used to analyse the slurry without the need for regular calibration with known slurry samples.

Theoretical models predicting the relationship between the intensity of characteristic fluorescent radiation and particle size in powdered samples date back to the 1960s [17], [18]. While there is reasonable agreement between these theoretical models and experimental data, a detailed comparison is limited by the quality of available experimental results. For example, particle size measurements often have large errors due to the difficulties of using sieves to separate out different size fractions. To be mathematically tractable, simple theoretical models also have to make significant assumptions and approximations.

The second aim of this thesis is to measure the particle size effect more accurately than has been achieved in previous studies, and to compare the results to both theoretical models and Monte Carlo simulations. A method for correcting for the particle size effect is proposed, and the feasibility of using this method to correct for particle size effects in XRF measurements of slurries is discussed.

## 1.2 Overview

This thesis is divided into three parts.

Part 1 contains this introduction and a detailed review of existing literature. Chapter 2 introduces the fundamental parameters concept and Chapter 3 discusses current theoretical models for predicting the particle size effect.

Part 2 describes the measurement of the relative L-subshell intensities of 8 different heavy elements with Z = 68-79. Chapter 4 gives a detailed description of the fitting scripts created to measure the individual L-subshell line areas and energy positions. Chapter 5 details the total L-subshell and individual line relative intensity measurements and discusses the impact of fitting XRF spectra with incorrect relative line intensities.

Part 3 describes the measurement of the particle size effect and discusses the potential for correcting for this when performing XRF measurements. Chapter 6 details the experimental methods used to produce powdered materials with different particle size fractions, and to obtain accurate, quantitative XRF measurements of these samples. In chapter 7, these results are used to develop a method for correcting for the particle size effect. Future work that could improve the correction method is also outlined.

## 2 Review of the Fundamental Parameters Method and Parameter Databases

In portable X-ray fluorescence (XRF) applications, due to limits on the maximum energy of conveniently available X-ray tubes, elements with atomic numbers greater than about 50 are generally analysed using their L-shell emission lines, rather than the more energetic K-shell lines that used to analyse lighter elements. Each element emits a large number of L-shell X-rays with different energies and a wide range of relative intensities, making the spectra of materials containing several elements of similar atomic number particularly complex.

In principle, the X-ray emission spectrum can be predicted from first principles from a knowledge of the ionisation and atomic relaxation processes. The so-called Fundamental Parameters method calculates the X-ray emission signatures of different elements and hence can be used to perform standard-less XRF analysis. It is important when fitting complicated L-shell X-ray spectra that the relative line intensities of the individual L-shell lines are accurately calculated. A brief history of the calculations for fundamental parameters using density functional theory is given in section 2.1.

The most important physical parameters required include the photoionisation cross-sections, Coster-Kronig transition probabilities, fluorescence yields, which are used to predict the X-ray emission spectra of an element. Other parameters such as the natural line widths, transition energies and the mass attenuation coefficients are also required at different stages of the analysis process.

Many of these parameters can be predicted theoretically using models such as the independent particle model. Various tabulations of the different physical parameters are available; more comprehensive tabulations such as the EADL [19] and EPDL [20] databases try to provide internally consistent sets of values for end users .

Each of these parameters has an associated uncertainty, which can contribute to poorly predicted X-ray emission spectra. The Coster-Kronig transition probabilities and the subshell fluorescence yields have notably large uncertainties that can lead to inaccurately determined line intensities.

There are many difficulties associated with measuring the parameters discussed so far, and there is currently an initiatives underway to improve the quality of available

experimental data [21]. This thesis does not aim to attempt to measure any individual fundamental physical parameters; instead, it aims to compare theoretically calculated X-ray emission spectra derived from these parameters with measured data. This will involve measuring high statistics L-shell spectra from various heavy elements and using in-house developed fitting procedures to extract as much detail as possible from these spectra.

In many cases, it is easier to compare the experimentally measured X-ray line intensities as ratios to another line within the same L-subshell. This allows many of the parameter values in the theoretical calculations to cancel out, and provides for a simpler comparison framework.

This chapter describes the theoretical calculations used for predicting the L-subshell X-ray emission spectra and the data on which these are based. A brief introduction is given to the nomenclature used to describe the two most prominent independent particle models. The underlying physical parameters are briefly introduced and the most recent publications for the theoretical calculations and experimental measurements of their values are discussed.

## 2.1 History of Density Functional Theory

The fundamental parameters method uses parameters calculated with density functional theory (DFT). The electronic structure calculations that lead to the development of density functional theory trace back to the late 1920s when Hartree introduced the Hartree function, used to calculate approximate wave functions for atoms and ions [22] and Dirac introduced approximations for the self-consistent field individual electrons move through [23], [24]. In 1930 Fock proposed a self-consistent function which adhered to the Pauli principles [25]. The Hartree-Fock method was so complicated that it was not regularly used until the 1950's when Slater developed the Hartree-Fock-Slater approximation [26] which simplified the previous methods by substituting the Hartree-Fock exchange operator with Dirac's exchange formula for the free electron density. The Slater approximation can be considered the ancestor of modern DFT methods [27].

In 1964, Hohenberg and Kohn published a paper that is considered to be the foundation of the modern DFT method [28]. Hohenberg and Kohn suggested that a many-electron wavefunction, containing 3N variables where N is the number of electrons, can be solved with the functional of electron density, containing only three variables. A year later a paper by Khom and Sham [29] was published, further developing on the theory suggested by Hohenberg and Kohn (HK). Kohn and Sham (KS) simplified the multi-electron problem by considering the non-interaction electrons in an effective potential, allowing them to include external potential and Coulomb interactions.

The previous studies were limited to light elements so that relativistic effects did not have to be included. The development of relativistic DFT (RDFT) has been slower than the non-relativistic DFT. Extensions to the HK and KS theories to include relativistic effects have been applied in studies by Rajagopal and Callaway [30], Rajagopal [31], and MacDonald and Vosko [32].

The capability to investigate many electron systems using RDFT is limited by the available computer programs and their capability to solve difficult coupled differential equations. Desclaux [33] published the first significant technical development in 1975 with his computer program for multi-configuration self-consistent field (SCF) code. Desclaux continuously extended his code over the next four decades [34]. In 1980 Grant et al [35] published their multi-configuration SCF code, which is also known as the GRASP package [36]. Charlotte Froese-Fischer led the developments of sophisticated RDFT calculations that were able to run using algorithms written in FORTRAN for computers available in the 1970s [37], [38]. In 1977 Froese-Fischer published a book describing her numerical approaches to using the Hartree-Fock method to compute the structures of atoms with relativistic corrections for a large range of elements [39].

More recent work in the RDFT space involves predications of K-shell line intensities and energy positions using multi-configuration Dirac-Hartree-Fock theory. Deutsch [40] used the GRASP code [36] to calculate the relativistic Dirac-Fock calculations for the transition and satellite lines of copper, showing that the 3d electron hole satellites

were responsible for asymmetry of the copper Kα and Kβ peaks. Chantler et al [41]–[43] built upon the work of Deutsch by modifying the relativistic Dirac-Fock calculations to account for correlation and ex-change corrections. Chantler et al. found excellent agreement between their theoretical predictions for the copper characteristic X-ray spectrum and wavelength-dispersive XRF experimental measurements of copper. As RDFT calculations are complicated and require lengthy computations, there are no comprehensives databases of calculated X-ray emission line intensities including satellite peaks available for XRF analysis.

In the L-shell case there are even less modern RDFT calculations. The most recent databases containing comprehensive calculations for the L-shell transmissions have been published by Scofield in the 1970's. Scofield published two different databases using the Dirac-Hartree-Slater (DHS) approach [11] and a partially relativistic Dirac-Hartree-Fock (DF[1]) approach [10].

### 2.2 Calculation of X-ray Emission Rates from Basic Data

The following relationships are used to calculate the theoretical intensity of the total X-ray emission arising from the L1, L2 or L3 subshells with vacancies generated via photoexcitation:

Equation 2.1

$$I_{L1} = \sigma_{L1}(E)\omega_{L1}$$

$$I_{L2} = (\sigma_{L2}(E) + \sigma_{L2}(E)f_{L1-L2})\omega_{L2}$$

$$I_{L3} = (\sigma_{L1}(E)f_{L1-L3} + \sigma_{L1}(E)f_{L1-L2}f_{L2-L3} + \sigma_{L2}(E)f_{L2-L3} + \sigma_{L3})\omega_{L3}$$

where $I_{L1}$, $I_{L2}$ and $I_{L3}$ are the intensity of X-ray emission from each subshell per unit incident photon flux, given by the product of the subshell photoionisation cross-sections $\sigma_{L1}$, $\sigma_{L2}$ and $\sigma_{L3}$ of the chosen element at a particular incident X-ray energy $E$ multiplied by the fluorescent yields $\omega_{L1}$, $\omega_{L2}$ and $\omega_{L3}$. Finally, $f_{L1\text{-}L2}$, $f_{L1\text{-}L3}$, $f_{L2\text{-}L3}$ are the Coster-Kronig transition probabilities between respective L-subshells.

[1] Many authors use the acronym 'DF' to describe the Dirac-Hartree-Fock model, as they assume the Dirac-Hartree method is implied. To remain consistent, the acronym 'DF' will be used in this thesis to describe the Dirac-Hartree-Fock model.

The X-ray emission rate is equal to the total rate of decay of a vacancy state of an atom multiplied by the fluorescence yield. This accounts for the probability of a vacancy forming in an atom, and then the probability of that atom undergoing a radiative transition to fill the vacancy and release a characteristic photon. The individual line intensities are the emission rate associated with the corresponding transition between a vacancy from a specific subshell being filled by an electron from a specific subshell.

To calculate the X-ray emission of a particular individual transition, equation 2.1 is expressed as:

Equation 2.2

$$I_{L1-i} = \sigma_{L1}(E)\omega_{L1}P_{L1-i}$$

$$I_{L2-i} = (\sigma_{L2}(E) + \sigma_{L2}(E)f_{L1-L2})\omega_{L2}P_{L2-i}$$

$$I_{L3-i} = (\sigma_{L1}(E)f_{L1-L3} + \sigma_{L1}(E)f_{L1-L2}f_{L2-L3} + \sigma_{L2}(E)f_{L2-L3} + \sigma_{L3})\omega_{L3}P_{L3-i}$$

Where $P_{L1\text{-}i}$, $P_{L2\text{-}i}$ and $P_{L3\text{-}i}$ are the fraction of the $i^{th}$ emission from the L1, L2 or L3 subshell produced by electron transitions from shell i. $I_{L1\text{-}i}$, $I_{L2\text{-}i}$ and $I_{L3\text{-}i}$ are all individual line transitions, which produce unique characteristic photons depending on which shell, i, the electron is decaying from. Each of these transitions has different probabilities of occurring, and together with their unique energy positions and intensities they form the total L-shell emission spectrum of a given element.

The definition, available data sources and uncertainties associated with each parameter used in equation 2.2 are discussed in the following sections. For some of the Coster-Kronig transition probabilities and the $\omega_{L1}$ fluorescence yield in particular, the uncertainties can be large [44]. These uncertainties significantly complicate a direct comparison of experimentally measured X-ray line intensities and the transition probabilities *p*.

## 2.3 Evaluation of Fundamental Parameters Databases

This section summarises the existing literature discussing the following basic physics: fluorescence yields, Coster-Kronig transition probabilities, line widths, photoionisation cross-sections, mass attenuation coefficients, line energies and the individual L-

subshell X-ray emission rates. These fundamental parameters are discussed because they are all required in the calculation of L-subshell X-ray emission rates. For instance, the fluorescence yields, Coster-Kronig transition probabilities and photoionisation cross-sections all appear in equation 2.1. The natural line widths and line energies are both needed when performing detailed fits to experimental spectra, and the mass attenuation coefficients are used as part of the fundamental parameters method for correcting the measured X-ray emission rates for sample absorption and detector efficiency. Finally, the individual L-subshell X-ray emission rates values are used to compare with experimental measurements of relative line intensities within the same L-subshell.

For majority of these parameters, this thesis adopts values from the EADL database family [20],[19] which contains photon and electron interaction data. The databases in this family are the Evaluated Atomic Data Library (EADL), Evaluated Photon Data Library (EPDL), and the Evaluated Electron Data Library (EEDL). For this work, values are taken from the EPDL and EADL database to obtain photon interaction and atomic relaxation data.

### 2.3.1 Fluorescence Yields and Coster-Kronig Transition Probabilities

The fluorescence yield is the probability that an inner-shell atomic vacancy will be filled by an electron from a higher shell via a radiative transition. Non-radiative or Auger transitions can also occur, where the excess energy is used to eject an additional atomic electron. The Coster-Kronig transition probabilities are a special case of non-radiative transitions where an electron from a higher subshell within the same shell as the vacancy fills the vacancy. Values for these parameters are needed to calculate the X-ray emission intensity of the L-subshells for heavy elements.

An important theoretical database of fluorescence yields and Coster-Kronig probabilities was developed by Chen et al. in 1981 [45]. For the L-shell case, Chen et al. [45] calculated $\omega_i$ and $f_{i-j}$ for 22 elements, using a DHS version of the particle model. In 1993 Puri et al. [46] used logarithmic interpolation from Chen's values to determine the $\omega_i$ and $f_{i-j}$ values for all elements in the range Z = 25-96.

The EADL database contains all the L-shell radiative transition probabilities based upon the DHS work of Scofield [47] and the non-radiative transition probabilities based upon Chen's work [48]. Perkins et al. [19] discusses how the non-radiative transition probabilities, particularly the Coster-Kronig transitions, were modified so that the derived fluorescence yields would agree better with the values given by Hubbell et al.[49], [50]. Cullen et al. explain that for the Coster-Kronig transitions, 'the widths can be too large by up to a factor of 2. These uncertainties directly affect the competition between radiative and non-radiative yields, e.g., the fluorescence yield' [20].

In 2003, Campbell conducted an extensive review of the current theoretical predictions and experimental measurements of the L-subshell $\omega_i$ and $f_{ij}$ values [44]. Campbell recommended a set of values based on his critical analysis of available data for elements in the range of Z = 25-96. Campbell's 2003 review also discusses the large uncertainties associated with L-shell Coster-Kronig probabilities and fluorescence yields, which are estimated to be up to 30% for $\omega_{L1}$, 5% for $\omega_{L2}$ and $\omega_{L3}$, 50% for $f_{L1\text{-}L2}$, 30% for $f_{L1\text{-}L3}$ and 25% for $f_{L2\text{-}L3}$. The $\omega_{L1}$ value is thought to have higher errors due to large scatter in the available experimental data and because theory cannot accurately predict the L1 level widths [51].

In 2009 Campbell published a second review [52], reassessing the problematic $\omega_{L1}$ fluorescence yield and $f_{L1\text{-}L3}$ and $f_{L1\text{-}L2}$ Coster-Kronig probabilities using new experimental data, and recommended a new set of values in the range Z = 64-92. Campbell offers more specific ranges of uncertainties depending on the Z number, which can be up to 35% for $\omega_{L1}$, 20% for $f_{L1\text{-}L2}$ and up to 100% for $f_{L1\text{-}L3}$ in the case where Z > 84. For some Z values in the range 64-92 Campbell declined to recommend any values. Campbell also declined to recommend any values for Z < 60 due to the low availability of experimental data in this region.

### 2.3.2 Line Widths

The natural line width, Γ, of an atomic level can be expressed as the sum of the radiative width, $\Gamma_R$, the Auger width, $\Gamma_A$ and the Coster-Kronig width, $\Gamma_{CK}$ [53]:

$$\Gamma = \Gamma_R + \Gamma_A + \Gamma_{CK} \qquad 2.3$$

These widths are determined from the corresponding transition rates that are calculated using the independent particle model. The EADL database draws upon Scofield's DHS calculated radiative widths [47] and Chen et al.'s DHS calculated non-radiative widths [48].

The most recent review of the natural line widths was done by Campbell and Pap in 2001 [51]. Campbell and Pap formed an extensive database that combines the theoretical values in the EADL database with experimental values obtained using a variety of spectroscopic methods for the K, L, M and N shell natural widths. Campbell and Pap provide K-shell width values for all elements in the range Z = 10-92, while the various L, M and N shell natural line widths are provided for subsets of these elements. Campbell and Pap provide estimates of the uncertainties in their recommended values for the natural linewidths that vary over different ranges of elements and for the different natural line widths. In the worst cases these uncertainties can be as large as 30%, but they are generally less than 10%.

The natural linewidth is only a minor contributing factor to the total line shape of each XRF peak being fit in the L-shell spectra. For this reason, Campbell and Papp's 2001 values should be satisfactory for use in the fitting methods used during this thesis.

### 2.3.3 Photoionisation Cross-sections

The photoionisation cross-section is the probability of a particle being ejected from an atomic orbital after an interaction with a photon. The photoionisation cross-section values are not only needed to calculate the total fluorescence emission rate, but also form a major component of the total mass attenuation coefficient. The photoionisation cross-section is included in the two most well-known mass attenuation databases, XCOM [54] and FFAST [55], as the photoelectric cross-section. For XRF processes where only electrons can be ejected to ionise the atom, the photoionisation cross-section and the photoelectric cross-section are equivalent cross-sections and the terms are used interchangeably by different authors.

The XCOM database references Scofield's 1973 study for photoelectric cross-sections for elements in the range Z = 1-101 at various energy values between 1 and 1500 keV [12]. This dataset was the most comprehensive database compiled at that time and

are still the most commonly used [50]. Scofield's study uses DHS calculations, a Dirac-Hartree approach with a Slater approximation.

The FFAST database references Chantler et al.'s 1995 and 2000 studies [56][57]. Chantler references the DHS theoretical calculations introduced by Cromer, Mann and Liberman in the 1960s [58]–[61]. Cromer et al.'s DHS calculations differed from Scofield's with a modification to the Slater approximation and the use of experimental binding energies [62] for calculating wave functions. Cromer et al. only calculated the photoionisation cross-sections for 5 elements. Chantler et al. applied the approach described by Cromer et al. to all elements in the range of Z = 1-92, for energies in the range of 1-10 eV to 400-1000 keV [55].

The EPDL database cites Scofield's DHS photoionisation cross-section calculations [12] in the energy range up to 1 MeV. The EPDL documentation estimates the uncertainties in these values to be approximately 5% in the energy range from 1-5 keV and 2% in the energy range from 5-10 keV. The EPDL database includes the photoionisation coefficients for all the subshells from their ionization edge energies up to 1 MeV, as well as the total photoionisation cross-section given as the sum of the individual subshell cross-sections.

### 2.3.4 Mass attenuation Coefficients

In the relevant energy range for X-ray fluorescence processes, the mass attenuation coefficient is equal to the sum of the incoherent scattering or Compton cross-section, the coherent scattering or Rayleigh cross-section and the photoionization cross-section. The previous section introduced the two most popular mass attenuation databases: XCOM and FFAST, and described the different sources each database uses to determine the photoionisation cross-section. In both the XCOM and the FFAST databases, the sources for the coherent [63] and incoherent [64] scattering cross-sections are identical.

A study by Heirwegh [62], published in 2014 as their PhD dissertation compared a large range of recent experimental measurements against both the XCOM and FFAST databases. Heirwegh came to the conclusions that neither database is universally

superior to the other, but one or the other of the two databases agrees better with experimental data over selected energy regions.

Mass attenuation coefficients are used in this thesis to calculate the attenuation of emitted X-ray, in the sample material itself, in any intervening material, and in the detector. Whilst there are known differences in the absolute cross-section values in the XCOM and FFAST databases, the expected impact on the line intensity ratios is expected to be small, as the ratio of two values at similar energies should be comparable from either database. This point is returned to in latter chapters.

Neither database accounts for fine-structure in the mass attenuation coefficients near absorption edges. In the regions just above an edge, the mass attenuation coefficient does not follow a smooth trend and can exhibit fine-structure effects that show oscillatory behaviour [65][66]. The magnitude of these oscillations is expected to amount to at most a few percent [65], but could possibly be higher. The fine-structure shows in experimental measurements of the mass attenuation coefficients, but is generally not included in the theoretical databases as it is dependent on experimental factors such as the sample temperature.

A study by Jitschin et al. shows X-ray absorption spectra of Hf, W, Pt, Au and Pb in the L-edge energy region measured at room temperature [67]. Figure 2-1 shows the X-ray absorption spectrum measured by Jitschin et al. for tungsten. The large jump in X-ray absorption occurs at each L-edge and is followed by oscillations in the regions just after each L-edge.

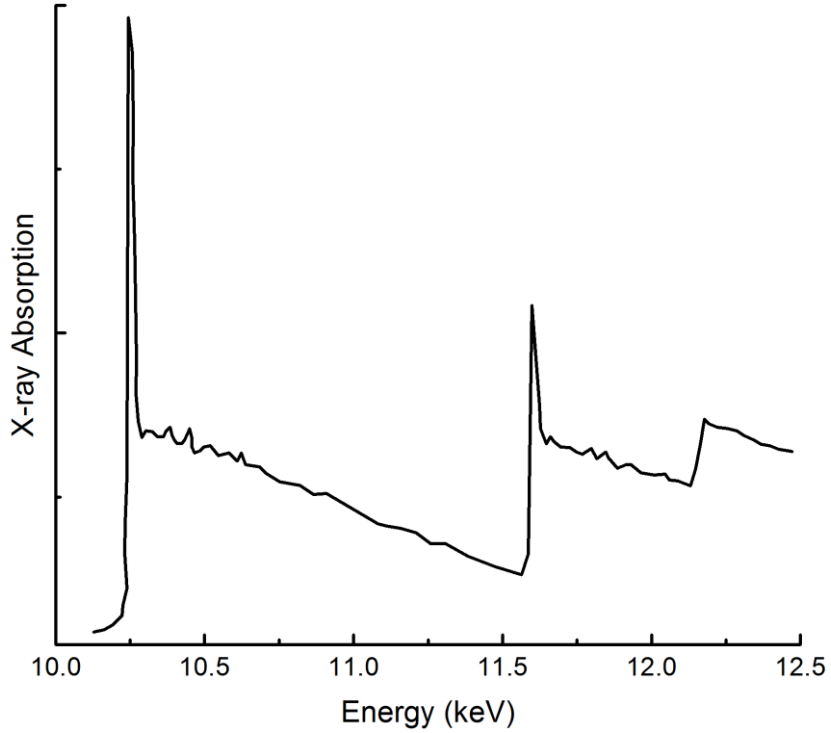


Figure 2-1: A recreated figure from the Jitschin et al study showing a scan of the X-ray absorption spectrum for tungsten taken at room temperature [67].

The L-shell measurements made in this thesis should not be greatly affected by the choice of mass attenuation database used, as long as the same database is used consistently. To account for the oscillating fine structure near the L-edges, both databases increase the uncertainties of their values just after any edge. The FFAST database quotes uncertainties of 1% for values well above the L-edges but for values near the L-edges the uncertainties can be as high as 40% [55]. The XCOM database does not provide uncertainty estimates, but these are assumed to be of similar magnitude to those reported for the FFAST database.

### 2.3.5 X-ray Line Energies

Energies of individual X-ray transitions can be calculated theoretically as the difference in the final and initial electronic states of the electron involved in the X-ray fluorescence process. Absolute X-ray energies of diagram lines can also be measured experimentally, traditionally using X-ray diffraction techniques. If the geometry of the set-up and crystal lattice spacing are well known, then the X-ray wavelength can be determined absolutely from the angles of the intense diffraction features. Limitations

in the resolution of the wavelength-dispersive measurements limit the accuracy of the measurements.

#### 2.3.5.1 NIST Database

The work of Bearden et al. in 1967 [68] provided a comprehensive database of all the recommended X-ray wavelength values from lithium (Z = 3) up to americium (Z = 95) by interpolating between existing experimental data. Many of the measurements included in Bearden's review were made before standard reference materials were available with wavelengths traceable to the definition of the meter. The conversion from early units and as well as other experimental factors can introduce systematic errors.

Deslattes et al. [69] undertook a comprehensive review of X-ray energies in 2003 and found that the interpolations of Bearden were not always correct. Deslattes et al. created their own database by relying on selected experimental measurements of photon emissions and interpolating those using theoretical DF edge energies. This work formed the NIST database of X-ray energies. The NIST database provides the K, L1, L2 and L3 absorption edge energies as well as both the K-shell and L-shell X-ray energies for transitions having final states out to N7. The NIST database does not include the L-shell transitions to the O-shells, or any of the M-shell X-ray transitions. Deslattes et al. published another review of X-ray wavelengths in the 2004 International Tables of Crystallography C, section 4.2.2 [70], where they give a detailed description of how they have combined experimental and theoretical values to provide the most up to date X-ray line transition database for the K-shell lines. They used line positions that have been directly measured on an optically based scale to test the quality of theoretical predictions. As there are only a limited number of L-shell emission lines that have been directly measured experimentally, only a limited number of L-shell lines are included in the study.

#### 2.3.5.2 EADL Database

The EADL database calculates the X-ray energies from Scofield's 1975 DHS data and a more comprehensive set of X-ray line energies can be calculated from the EADL database than the NIST database. In the latest (1997) release of the EADL database

[19], the authors recognise some uncertainty in the EPDL97 atomic orbital energies, stating that 'Comparisons with more recent values shows difference of less than 1%'. The authors discuss that a 1% difference between measured values and their calculated values is small when compared to the differences expected from elements combining into compounds. Exact elemental binding energy values are less important in the EPDL database than the consistency between the photon and electron data [20]. For these reasons, the energy transition values derived from the EADL database family are not expected to be as accurate as the values in the NIST database. An uncertainty of even 1% on the values can lead to errors of 100s of eV for the higher energy transition values.

#### 2.3.5.3 Comparing the NIST and EADL Databases

Roach et al. [71] conducted a comparison of the NIST and EPDL X-ray energy values and found discrepancies of up to several hundred eV. Roach et al. compared experimentally measured XRF spectra with fits using both the NIST and EPDL calculated transition energies, and found that the fits using the NIST energies agreed significantly better than the fits using the EPDL values.

While the NIST database is found to be superior to the EADL database for X-ray transition energy positions, accuracy is limited by the possible systematic errors in Bearden's original review data; the database is also not complete as it does not include all possible X-ray transitions. NIST has recognised that while the NIST database has 'published the best available value for each transition … there remain numerous opportunities for modern measurements to offer meaningful improvements in such tabulations' [72]. A 2017 study by Fowler et al. [72] describes how NIST is currently using very high-energy microcalorimeters to measure the L-shell X-ray emission lines of various lanthanide-series elements. They are able to measure the absolute line energies with a level of accuracy not seen in any other studies, with an uncertainty in the absolute line energies being less than 0.4 eV in the energy range of 4.5 keV to 7.5 keV. This work is ongoing, with more measurements planned to resolve differences between the NIST recommended values and experimental values currently in the database.

For this thesis, the NIST X-ray energy values will be used in preference to those from the EADL database for fitting XRF spectra. In the cases where the NIST database does not include a certain transition's energy value, the energy will be taken from the EADL database. If the transition originates from a K or L-shell, the energy will be corrected by the difference between the energies of the corresponding shell in the two databases.

### 2.3.6 Relative L-subshell Line Intensities

Scofield [11] first calculated theoretical predictions for L and K X-ray transition emission rates using the Dirac-Hartree-Slater (DHS) version of the independent particle model. In 1974, Scofield also developed a new set of theoretical values based off the more complicated Dirac-Fock (DF) independent particle model; however the DF values were only calculated for 21 elements with single atom vacancies in the L-shell [10]. In 1989 Campbell and Wang [73] interpolated the existing DF data to create values for a much wider range of elements.

In 1974, Salem [74] conducted a review of available experimental data of L-shell X-ray relative intensities and compared the experimental measurement of K and L line ratios to the DF theoretical values and found good agreement. Salem's experimental database [74] contained up to 11 relative line intensity ratios for every second element from iron (Z = 26) up to curium (Z = 96).

In 2002, Elam et al. developed their own database of fundamental parameters, using calculations and values from a wide range of sources available at the time. Elam et al. [75] extended Salem's experimental database to the range Z = 1-96 by fitting the given values to the lowest order polynomial that gave an acceptable fit by eye[2]. However, as this thesis concentrated on relative X-ray emission from L-shell spectra, Elam's database should still provide a useful comparison.

[2] Elam's 2002 database of fundamental parameters is no longer recommended for use as the K-shell fluorescence yields used by Elam were the 1994 values recommended by Hubbell et al [129]. In 2004, after Elam's database was created, Hubbell et al. issued an Erratum to recommend that their proposed recommendations be set aside in favour of other more accurate values, due to systematic errors in the values they recommended [130].

Experiments calculating the K-shell X-ray relative line intensities have been conducted by many teams providing evidence that the DF theoretical model agreed well with experiment [76]–[78]. The L-shell case is more complicated, due to the presence many overlapping lines in the L-shell spectra. The majority of studies do not attempt to measure the individual L-shell line transitions, but instead measure groups of lines in the spectrum. There are many studies comparing the relative intensities of the L-beta, L-gamma and L-L groups to the L-alpha group of peaks [79]–[85]. This method involves comparing the sums of multiple transitions from within different L-subshells, which complicates the theoretical calculations and the uncertainties involved in the calculated values.

There have been few studies that measure the L-shell X-ray line intensity ratios from within the same L-subshell, allowing a direct comparison with theory. Simsek [13] analysed only the L3-subshell spectra for Re, Au, Tl and Pb and reported the intensity ratios of up to four lines per element. Vlaicu et al. [14], [86] analysed the L-shell spectrum of tungsten and reported the intensity ratios for eight different lines. Papp et al. [15] measured the L-subshell intensity ratios of gadolinium and uranium for up to thirteen lines. Simsek [13] and Papp et al. [15] both compared their experimental results to Scofield's DHS and DF calculated values, and both studies found better agreement with the DF values.

# 3 Particle Size Effect

The particle size effect in X-ray fluorescence refers to the dependence of the intensity of fluorescence radiation emitted from a sample on the size of the individual grains containing the element in question. The fundamental parameters correction method used to adjust for the matrix absorption in a sample generally ignores particles size effects and assumes that the material is homogeneous. In general, heterogeneous samples containing particles with size comparable to or larger than the X-ray interaction length will exhibit particle size effects.

For laboratory X-ray fluorescence (XRF) applications, the particle size effects are minimised using appropriate sample preparation techniques. Powders can be milled to sub-micron sizes, homogenised using the glass fusion method, or dissolved to form a solution. These techniques can be time consuming and costly, and are not available when measuring samples using in-situ or portable XRF.

The particle size effect for X-ray fluorescence is well-established in literature. Papers cover experimental studies of the particle size effect and the development of theoretical models to predict the size of the particle size effect. Early theoretical models show that the particle size effect is dependent on the exciting radiation energy and that there is potential to correct for the particle size effect using multiple exciting radiation energies [87].

This chapter will discuss the physical reasons behind the particle size effect, the theoretical models available and options for correcting for the particle size effect.

## 3.1 Physical Interpretation of the Particle Size Effects

Particle size effects are dependent on the matrix of the sample and the mineralogy of the particles that contain the element of interest. For a very absorbing matrix, the intensity of fluorescence will increase with particle size. For a weakly absorbing matrix, the intensity of fluorescence will decrease with increasing particle size. Figure 3-1 shows an example of the particle size effect in two different samples. In the applications of interest in this thesis, the elements being measured (over valuable metals such as copper or gold) will have a higher Z than the average matrix element

(typically oxygen, silicon or aluminium), so the fluorescence intensity of the measured elements will almost always decrease with increasing particle size.

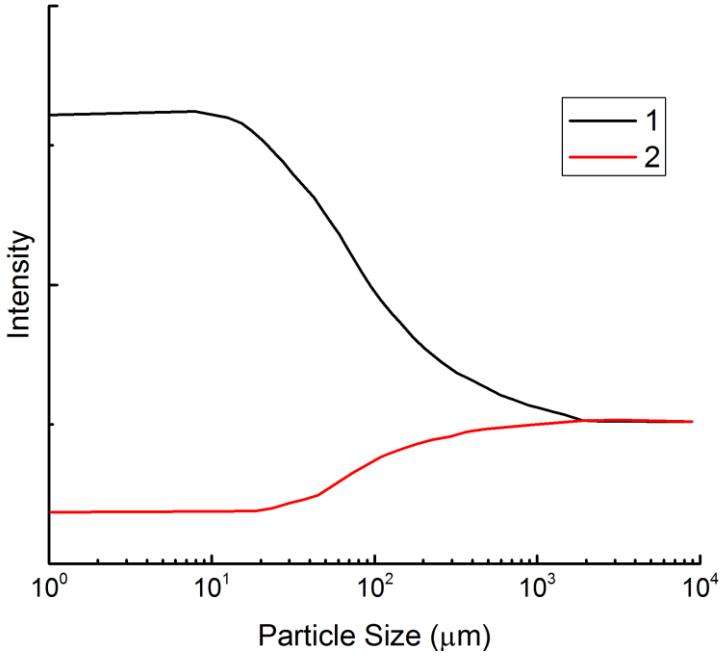


Figure 3-1: The change in fluorescence radiation intensity with particle size. Line 1 represents a sample with a weakly absorbing matrix and line 2 represents a sample with a strongly absorbing matrix [16].

There is a transition zone for every material where fluorescence intensity varies most strongly with particle size. On either side of this transition zone, the fluorescence intensity depends only relatively weakly on the particle size. The particle size of the transition zone varies with material. In practice, it is often possible to approach the region where particle size effects are minimal, but for most samples it occurs at very small particle sizes that cannot be achieved using conventional grinding [88].

In its simplest form, the particle size effect is due to the relationship between the mean free path of the incident and fluorescence X-rays within the material of the particle, and within the bulk matrix. The mean free path of a photon, ι, is the average distance that an X-ray will travel through a particular material before it interacts and is calculated as:

$$\iota = \frac{1}{\mu_{mass}\,\rho} \qquad (3.1)$$

where $\mu_{mass}$ is the mass attenuation coefficient of the material at a particular X-ray energy and ρ is the density of the material.

A sample is considered to be 'infinitely thick' when its thickness is many mean free paths, so that any further increase in thickness would produce only a negligible increase in fluorescence intensity. An estimate of a significant reduction in intensity would be that the radiation is reduced to 1% of its original value [16]. The depth that can be considered 'infinitely thick' is also called the penetration range.

Figure 3-2 illustrates how particle size effects arise in the specific case of strongly absorbing particles suspended in a weakly absorbing matrix. A conventional equal-angle XRF setup is assumed, with source radiation incident from the top-right and the detector positioned top-left.

In the particulate case (A), incident X-rays can only penetrate a certain distance into the strongly absorbing particles before being absorbed. Similarly, emitted fluorescent X-rays are only likely to be detected if produced on the side of the particle nearest to the detector (3) and not if emitted on the other side (4). Effectively, a large volume of each particle is 'invisible', shielded from either the source or the detector.

When a homogeneous sample (B) is excited under the same conditions, the fluorescence radiation only has to travel through the weakly absorbing matrix to reach the detector, irrespective of the position inside the particles where the interaction occurs, and the fluorescent intensity will be higher.

The effective fluorescent volume of a given sample is the volume of material within the sample that produces fluorescent radiation capable of reaching the detector. For particulate sample cases, when the penetration range is smaller than the particle diameter, the effective fluorescence volume of the sample will be less than that of an equivalent homogeneous sample. As the particle size increases, the effective fluorescence volume will decrease. As the effective fluorescence volume decreases, the intensity of the fluorescence radiation also decreases.

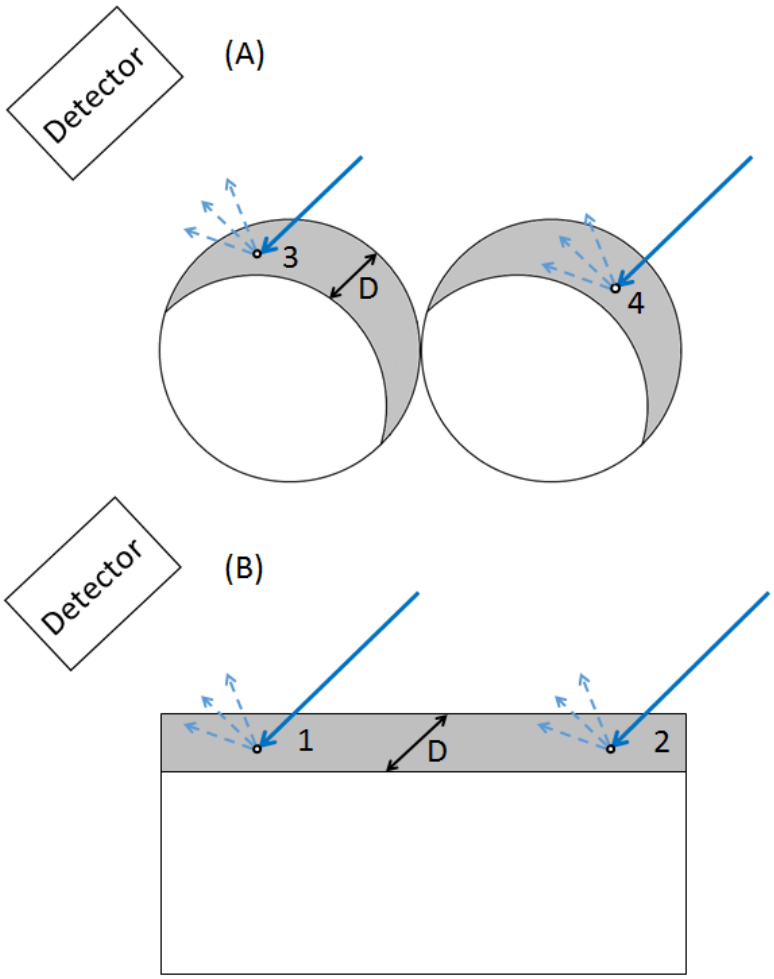


Figure 3-2: (A) Shielding of fluorescent X-rays from large particles compared to (B) a homogenous flat sample with no particulate effects [16].

## 3.2 Theoretical Models

The above discussion only describes the simplest of cases. The particle size effect is directly related to the absorption and self-absorption of X-rays entering and leaving a particulate sample. In simple cases the absorption of X-rays entering and leaving the sample can easily be traced using fundamental parameters methods and mass attenuation coefficients if the geometry of the experiment and the sample composition are well known [89]. Realistically, the material analysed will contain multiple different phases with varied shape and particle size distributions. In these cases, various mathematical models have been developed to predict the particle size effects based on the effective values of the absorption coefficients for the primary and

fluorescence radiation in heterogeneous particulate samples. The most prominent mathematical models are discussed in the following sections.

### 3.2.1 Claisse and Samson

In 1962, Claisse and Samson [90] presented the first mathematical model for the theoretical treatment of the particle size effect. Their model involved describing a sample as a number of vertical columns filled with cubical particles, where a defined fraction of the cubes contain the fluorescent phase and the rest the matrix phase. They derive a complicated formula that gives the fluorescent intensity from a given element as a function of the weight fraction of that element, the size of the particles, the composition of the matrix and the associated mass absorption coefficients of the fluorescent and exciting radiation in both the fluorescent and the matrix particles.

The Claisse and Samson model was the first to predict the existence of the transition zone, and while it is significant as the first model presented in literature, it also has some significant flaws. The model is only applicable to binary samples. If the fluorescent phase is present at a high concentration, the model will predict a particle size effect that is too small when compared with experimental measurements [16]. The theory is limited by the treatment of all particles as cubes, and does not account for the solid packing fraction of the sample.

### 3.2.2 Lubecki

Lubecki, Holynska and Wasilewska developed a new theory that describes the sample as horizontal layers of spherical particles, spaced according to the concentration of the fluorescent phase and the solid packing fraction [87]. Lubecki et al.'s model assumes that the exciting radiation is mono-energetic and that only first order fluorescence interactions occur. The intensity of the fluorescent radiation is calculated to be:

$$I = \frac{I_0 \cdot p \cdot k_1}{\mu} \cdot \frac{1 - e^{-\mu \cdot p_z \cdot d}}{1 - \exp[-\left(\mu + \frac{1-w}{w} \cdot \mu^M\right) p \cdot p_z \cdot d]} \tag{3.2}$$

where $I_0$ is the intensity of the primary exciting radiation at the grain surface, $w$ is the weight concentration of the fluorescent element in the sample, $d$ is the average linear dimension of a grain where $d$ is equal to two thirds of the diameter of a spherical grain, $\mu$ is the sum of the mass absorption coefficients of the fluorescent element for the

primary and the fluorescent radiation, $\mu^M$ is the sum of the mass absorption coefficients of the non-fluorescent, matrix material, for the primary and the fluorescent radiation, $p_z$ is the density of the fluorescent grains, $k_1$ is a constant that depends on some atomic parameters, and $p$ is a constant that depends on the density of the sample as described below. The parameter $k_1$ is given by equation 3.3:

$$k_1 = \frac{\omega}{4\pi R^2}\frac{S-1}{S}F \cdot \tau \cdot p\frac{\lambda_0}{\lambda_f}\, w_0 \qquad (3.3)$$

where $\omega$ is the fluorescence yield, $R$ is the distance between the sample and detector, $S$ is jump in the absorption coefficient, $F$ is the area of the layer of particles being analysed, $\tau$ is the total mass absorption coefficient of the determined element for primary radiation, $\lambda_0$ is the wavelength of the exciting radiation and $\lambda_f$ is the wavelength of the fluorescent radiation and $w_0$ is the weight concentration of the fluorescent element within the fluorescent grains. When working with pure element particles, $w_0$ is equal to 1.

The constant $p$ is determined by equation 3.4:

$$p = \frac{\eta}{1+\frac{1-w}{w}\cdot\frac{p_Z}{p_M}} \qquad (3.4)$$

where η is the packing degree and $p_M$ is the density of the non-fluorescent grains.

Lubecki et al.'s theoretical equation is designed to calculate the fluorescence intensity of a particular element coming from a particulate sample. A large number of factors are involved, which is problematic if they are not all accurately known.

Lubecki et al. measured samples consisting of limestone powder of various particle sizes containing elements such as iron, silicon and zirconium. They compared their measured data with their theoretical calculations as well as those based on the model of Claisse and Samson [90], and found better agreement with their own mathematical model. However, the experimental details given in Lubecki et al.'s paper on the sample preparation are minimal and it is difficult to determine the quality of the measured data due to the lack of information.

### 3.2.3 Berry, Furuta and Rhodes

Berry, Rhodes and Furuta [18] developed a simplified model for the influence of particle size in 1969 based on three simplifying assumptions. First, the model only considers the case where radiation interacts with the sample perpendicular to the sample surface. Incident radiation enters the sample perpendicular to the sample's surface and fluorescence radiation leaves the sample perpendicular to the sample's surface. The second assumption is that all particles are of the same size and that a value, *d*, represents the average linear dimension of the particles. For spherical particles, *d* is 2/3 of the particle diameter, and for cubical particles, *d* is approximately 0.7 of the of the cube side [16]. Third, it is assumed that the distribution of particles throughout a sample is completely random, but when a layer of thickness *d* is being considered, the average volume distribution of the layer is assumed to be the same as the average volume distribution of the whole sample. Based on these three assumptions Berry et al. came up with the following model:

$$I = \frac{I_0 \omega \tau_0 \rho_f W_0}{\mu_0 + \mu_f}\left(1 - e^{-(\mu_0+\mu_f)d}\right) \tag{3.5}$$

where $I_0$ is the intensity of primary radiation at the sample surface, ω is the fluorescence yield for the X-ray transition excited, $\tau_0$ is the photoelectric cross-section for that transition at the source energy, $\rho_f$ is the density of the fluorescent particles, $W_0$ is the weight concentration of the fluorescent element in the fluorescent particles, $\mu_0$ is the linear attenuation for the primary photons and $\mu_f$ is the linear attenuation for the fluorescent photons.

Equation 3.5 can be simplified to a particle size heterogeneity correction factor:

$$F = \frac{1 - e^{-(\mu_0+\mu_f)d}}{(\mu_0+\mu_f)d} \tag{3.6}$$

The Berry and Rhodes model, like the other two models described, only accounts for particles of a well-defined shape and of a given size. In practice, most particulate samples being measured will have continuous particle size distribution. Rhodes and Hunter [91] extended the model so that it could account for a particle size distribution:

$$F = \int_{d_{min}}^{d_{max}} \frac{f(d)\left(1-e^{-(\mu_0+\mu_f)d}\right)dd}{(\mu_0+\mu_f)d} \quad (3.7)$$

the particle size correction factor, *K*, is equal to 1/*F*.

Rhodes and Hunter found that the particle size effect is less pronounced for samples with a continuous particle size distribution compared to samples with monosized particles.

Holynska and Markowicz [92], [93] found that application of Berry and Rhodes' approach is limited due to the fact that the particle size distribution is rarely known comprehensively. To overcome this issue, they instead use an average particle size diameter to represent the particle size distribution. They calculated the particle size correction factor, *K*, with their average diameter and the particle distribution (equation 3.7) and found that they obtained very similar results for $Fe_3O_4$ particles.

Finkelshtein [94] found that the volume fraction of voids in a sample should be taken into account when calculating the concentration of the sample. Finkelstein used the Berry-Furuta-Rhodes formula (equation 3.5) to obtain good agreement with their experimental measurements. However the experimental measurements were taken for large particle size ranges which results in large x-axis error bars on each point, limiting the accuracy of the comparison between experimental and theoretical results.

## 3.3 Particle Size Effect Correction Methods

The following sections describe studies that have collected experimental data on the particle size effects and compared them to a mathematical model for the purposes of deducing a particle size correction.

### 3.3.1 Exciting Radiation Energy

Lubecki et al. [87] investigated the effects of the primary radiation energy on the particle size effect. The intensity of fluorescence from a sample with constant chemical composition and grain size should only depend on the primary energy through its effect on the mass coefficient $\mu_0$. Figure 3-3 shows the grain size effect for K-shell radiation emitted by iron for two primary radiation energy values, 9.2 and 22.6 keV, and for two different matrix materials.

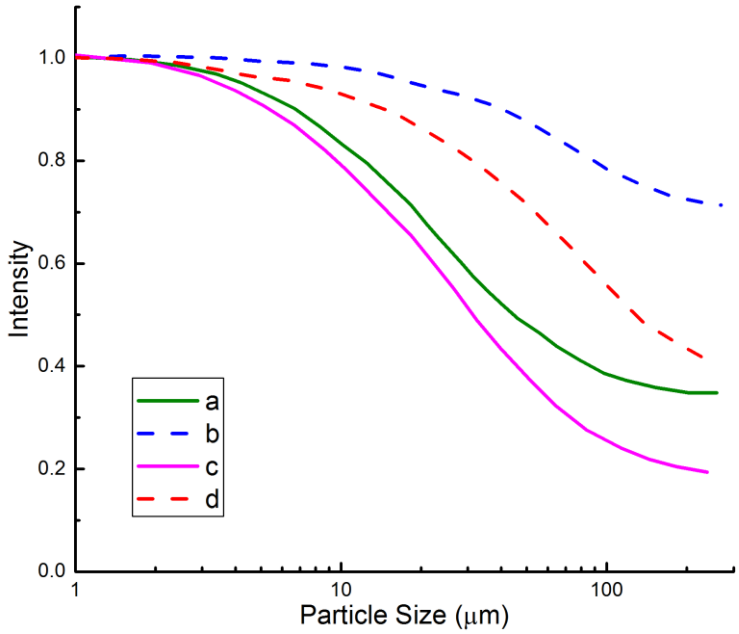


Figure 3-3: Theoretical curves of relative intensity of the characteristic K lines of iron versus particle size recreated from Lubecki et al.'s study [87]. Curve (a) is iron in a calcium matrix excited by 9.2 keV radiation. Curve (b) is the same material excited by 22.6 keV radiation. Curves (c) and (d) show the intensity of fluorescence from iron in a silicon matrix excited by 9.2 and 22.6 keV radiation respectively.

In the case of a weakly absorbing matrix, the particle size effect will decrease with increasing primary radiation energy. Increasing the primary radiation will therefore minimise the particle size effect. However, there are disadvantages to using higher excitation energy, such as decreasing the overall fluorescence intensity of lower energy X-ray lines. However, as particle size is a function of the incident energy, then the effect of particle size could possibly be estimated and corrected for by measuring the same sample at two different energies.

For the best particle size correction results, the two exciting radiation energies should be chosen so that one results in a small particle size effect and the other a large particle size effect.

Figure 3-4 (A) shows the particle size effect calculated using Lubecki et al.'s model for a sample consisting of copper powder in a silica matrix, calculated at multiple exciting radiation energies. The predicted particle size effect is greatest for the lowest exciting radiation energy (just above the copper K-edge); as the exciting radiation energy

increases, the particle size effect reduces. Figure 3-4 (B) shows the intensity ratio between the lowest possible exciting radiation energy for conveniently measuring copper, 9.6 keV, and various exciting radiation energies greater than 9.6 keV. As the denominator exciting radiation energy increases, the ratio of the fluorescent response from the two measurements changes more strongly with particle size. This shows that larger differences between the exciting radiation energies lead to a greater difference in the relative particle size effect, and hence a better probability of being able use to a measurement of intensity at two different exciting energies to determine a particle size correction.

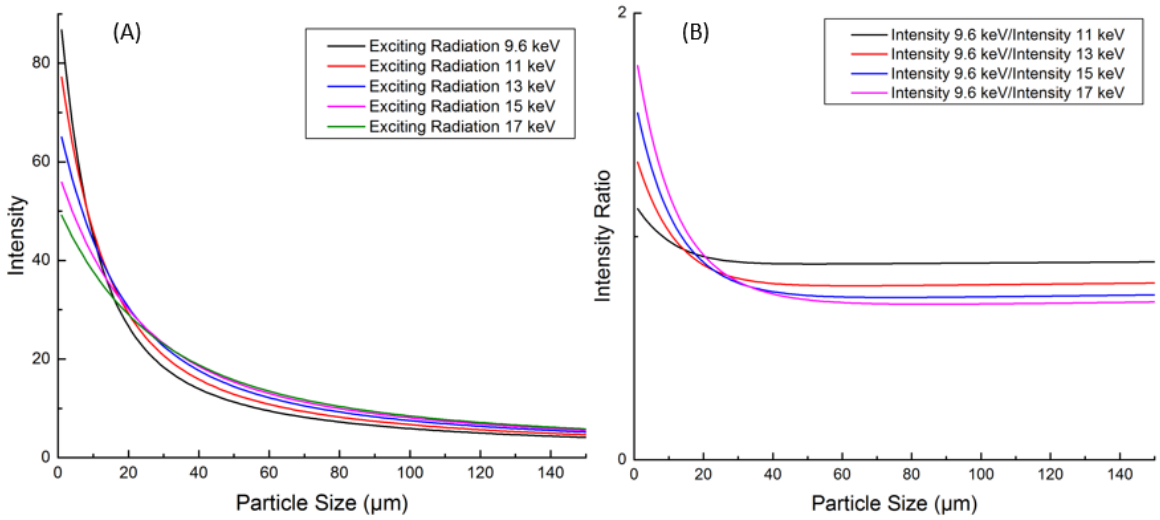


Figure 3-4: (A) the particle size effect for copper particles in a silica matrix, calculated using Lubecki et al.'s theoretical model at various exciting radiation energies. (B) The ratios of the 11-17 keV fluorescence response to the 9.6 keV fluorescence response versus particle size.

Holynska [95] first suggested a method using XRF to analyse ore slurries using X-rays from two different radioisotope sources yielding different X-ray energies. Synthetic slurry samples with known concentrations and particle size were created and separately excited by each primary radiation source. The fluorescence intensity from iron was measured using an argon filled proportional counter. Holynska uses Lubecki et al.'s theoretical model [87] to calculate the relative intensity of the fluorescent radiation as a function of the particle size, concentration of the sample and the exciting radiation energy being used.

Holynska employs nomographs to determine the concentration of the iron in a sample corrected for particle size effects. He calculates relative intensities of the count rates of a certain element including particle sizes effect for two exciting energies, $I_{rel}$(En1) and $I_{rel}$(En2), and plot the data on a theoretical nomograph with $I_{rel}$(En1) and $I_{rel}$(En2) as the x and y coordinates. They plot multiple curves of $I_{rel}$(En1) vs $I_{rel}$(En2) at different concentrations of the fluorescent element of interest. Holynska found that the nomograph approach gave clearer results when it was created with $I_{rel}$(En1)/ $I_{rel}$(En2) vs $I_{rel}$(En2) as the x and y coordinates.

Holynska took experimental data on the particle size effect using $^{3}$H/Zr, $^{238}$Pu and $^{241}$Am radioisotope sources and compared the results to those predicted by using Lubecki et al.'s theoretical calculations of particle size effect. He found that the particle size effect observed for the $^{241}$Am and $^{3}$H/Zr sources is considerably smaller than that predicted by theory. While the experimental results qualitatively resembled the theoretical results, there was no quantitative agreement. He suggested the discrepancy is due to Lubecki et al.'s model being developed for mono-energetic exciting radiation sources, but the sources used by Holynska, especially the $^{3}$H/Zr Bremsstrahlung source, emit a continuous energy spectrum.

Lankosz [96] further develops theoretical equations to determine the particle size effect for XRF analysis of ore slurries. Lankosz's method utilises a concept of expressing particle size as a weight fraction of particles smaller than 75 µm. Lankosz compares his theoretical equations to experimental measurements and finds good agreement. However the method Lankosz develops relies on always knowing the weight fraction of particles smaller than 75 µm for each slurry tested; in other words the particle size of the slurry must be known through independent testing. There is no easy solution to test for the particle size of a slurry, so this method is not very practical compared to the method proposed later in this thesis that requires no prior knowledge of the particle size distribution.

### 3.3.2 Exciting Radiation Angle

Maruyama et al. [97] crushed standard rocks and sieved the results into various particle size fractions to measure the particle size effect of silicon at various angles.

They found that the particle size effect increases with increasing source to surface to detector angles.

Dyck et al [98] use their equations to determine whether the best method to correct for particle size effect is to use two different exciting energies or two different geometries. They calculate the particle size effects for both cases and find there is a more significant difference in the PSE between two different exciting energies than using two different geometry set-ups. For this reason they conclude using two different exciting energies is the preferable method. They do not conduct any experimental measurements to compare with their theoretical calculations.

## 3.4 Summary

There are multiple existing mathematical models for predicting the particle size effect. All of them make assumptions about the experimental conditions that are unrealistic. One assumption is that the exciting radiation is mono-energetic, which is not often true, particularly when X-ray tube sources are used in place of radioisotopes. Another problematic assumption is that all the particles are spherical, which is usually not the case for the slurry, mineral and environmental samples.

The two most prominent of these models are those by Lubecki et al. [87] and by Berry et al. [18]. The Lubecki et al. model assumes all the particles are of a given size, but the Berry et al. model can account for a particle distribution range. The Berry et al. model assumes that both the exciting radiation and fluorescent radiation are perpendicular to the sample surface, where the Lubecki et al. model accounts for all possible exciting radiation and fluorescent radiation angles. Depending on the details of the experimental set-up, either model could be superior.

There is very limited high-quality experimental data on the particle size effect in the literature. This is due to the limitations of sieves to accurately size non-spherical powders, as well as the difficulties in measuring binary samples and ensuring that the two phases are evenly mixed. Of the few studies making experimental measurements of the particle size effect, even fewer compare their results to a mathematical model of the particle size effect.

The only study that comprehensively attempts to correct for the particle size effect is that by Holynska [95]. This study is limited by the accuracy of the Lubecki et al. mathematical model to predict the particle size effects, especially for non mono-energetic sources.

This study aims to accurately measure the particle size effect experimentally, and compare the experimental measurements to both theoretical models and Monte Carlo simulations. The possibility of correcting for the particle size effect will be discussed, using new methods to improve the agreement between experiment and theoretically predictions.

**PART 2: IMPROVING FUNDAMENTAL PARAMETERS CORRECTIONS FOR XRF APPLICATIONS**

# 4 Developing Fitting Methods for Complicated XRF Spectra

The core goal of this thesis is to develop methods to improve the accuracy of X-ray fluorescence techniques, particularly in difficult cases such as measuring coarse, unprepared samples or trying to quantify and resolve spectral overlaps for heavy elements such as gold present at very low concentrations. Whilst the quality of the experimental data is limited by current detector and X-ray tube technology, the information that can extracted from XRF spectra is limited by the fitting program.

Commonly used fitting packages [99], [100] typically focus on either non-linear fitting of individual lines or small groups of lines, or linear fitting of more complex spectra where line positions, shapes and relative intensities can be considered fixed. To extract as much information as possible from complex spectra with large numbers of potentially overlapping peaks, custom fitting methods are required where the user has total control over the line-shape, total spectrum description and fitting methods.

This chapter describes in depth the spectral fitting methods used, which were developed as fitting scripts running in the Matlab data processing environment [101]. The methods described in this chapter are used to fit all the spectra analysed throughout this thesis. In particular, the L-shell fitting work described in Part 2 requires particularly careful fitting techniques. For this reason, this chapter will be illustrated with examples drawn from the fitting of L-shell X-ray spectra.

## 4.1 Fit Details

### 4.1.1 Line Shape

It is common for X-ray fitting programs to make assumptions about line shape to simply the fitting process. Fitting peaks with simple Gaussian functions can be acceptable for low quality spectra with poor detector resolution. However, as the resolution and statistical precision improves other effects such as Lorentz broadening and Compton scattering become more apparent and need to be accounted for in the fitting process. This section describes the construction of a suitable function to accurately describe the measured line shape. The line-shape function is constructed

from individual components that ignore detector resolution; the sum of these components is then convoluted with a Gaussian function to account for the detector resolution broadening. This approach is used to simplify the mathematical treatment, as analytical convolution of the different peak shape components a Gaussian detector broadening function is either complex or not possible at all.

The incoming photons are measured in the detector in by an analog to digital converter that records the 'energy' of the photon in channels. The channels of the measured spectrum are assumed to be linearly related to X-ray energy, *E*, as follows:

$$E = a + bx \qquad 5.1$$

where a and b are fit parameters to be determined. The spectrum is fed into the fitting regime in channels so that parameters a and b can be adjusted alongside all the other parameters in the non-linear least squares fit.

#### 4.1.1.1 Lorentzian natural line shape

Each peak has a natural line shape broadening due to the uncertainty of the energy of the atomic orbital involved in the X-ray emission, which is in turn inversely related to the orbital lifetime. The Lorenztian function can be expressed as:

$$L(x) = \frac{1}{\pi} \frac{\frac{1}{2}\Gamma}{(x-x_0)^2+(\frac{1}{2}\Gamma)^2} \qquad 5.2$$

where $x_0$ refers to the centre of the peak is the mean peak energy (expressed in ADC channels), and Γ is a parameter specifying the full width at half maximum (FWHM), again expressed in ADC channels.

The Lorentzian function is the main component of the peak description. The natural Lorentz line widths, typically of order eV, are small compared to the detector resolution of around 130-150 eV in the 7-14 keV energy range. In the vicinity of the peak centroid, the variation in peak shape introduced by including the natural line width is negligible. However, the Lorenztian profile's contribution can become significant in the wings of the larger peaks. Hildner et al. [102] report a reduction in $\chi^2$ of up to 9% when including the Lorentz contribution to a description of Kα peaks of various elements. Campbell and Wang [103] compared the fit of the Thorium Lα peak

with and without a Lorentzian contribution and found the reduced $\chi^2$ value decreased from 7.2 to 1.02. As this study is interested in accurately determining the areas of small peaks that may be situated on the extreme tails of much more intense lines, inclusion of the Lorentz broadening is important.

#### 4.1.1.2 Compton scattering profile

The next function included in the line-shape description accounts for Compton scattering. Compton scattering refers to the inelastic scattering of photons with matter, resulting in a transfer of part of the photon's energy to an atomic electron. Fluorescent X-rays generated in a sample can undergo Compton scattering, causing them to lose a fraction of their energy.

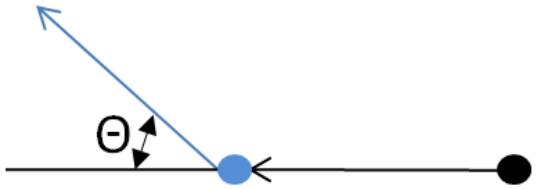


Figure 4-1: Compton scattering of a photon.

Figure 4-1 shows a fluorescent photon being released and interacting with an electron of another atom in the sample. The photon scatters at an angle, Θ, and transfers energy in the process. The amount of energy transferred depends on the angle that the photon is scattered at, as can be determined by equation 5.3:

$$E' = \frac{E}{1+\frac{E}{m_e c^2}(1-\cos(\theta))} \qquad 5.3$$

Where *E'* is the wavelength after scattering, *E* is the initial wavelength, $m_e$ is the electron rest mass and *c* is the speed of light. As the scattering angle approaches 180˚, the energy of the Compton shift will increase. The probability of a photon scattering is not equal for angles, with low-energy X-rays more likely to scatter at angles close to 0˚ or 180˚ (forward or backwards directions) than they are to scatter at angles close to 90˚. Considering the variability in the energy shift and the probability of scattering at different angles, the exact shape of the Compton scattered photons measured in the detector of a particular set-up geometry is difficult to predict. The Compton scattering

also depends on the electron momentum distributions in the material, so it is also dependent on the composition of the material being measured.

As these fitting scripts are being designed to measure the L-shell lines from pure, heavy element foils, Compton scattering will be minimal. For example, at 12 keV in gold, Compton scattering accounts for only 0.03% of the total cross-section. A simplified treatment is therefore used, with the Compton scattering component modelled as an exponential function, as described by the 'hypermet' functions of Phillips and Marlow [104].

An exponentially decreasing tail function, *D(x)*, was introduced by Phillips and Marlow to account for various mechanism of partial energy loss, including Compton scattering of fluorescence X-rays between the sample and detector, and incomplete charge collection in the detector volume. Inclusion of low-energy tailing was found to improve agreement with experimental data [105]. Here, the normalisation of the original hypermet equation has being adjusted to express the intensity of the exponential tail function in terms of its total area rather than its amplitude:

$$D(x) = \frac{f_D}{\beta} e^{\left(\frac{x-x_0}{\beta}\right)} H(x_0 - x), \qquad \beta < x_0 \qquad 5.4$$

where *H(x)* is the Heaviside step function (*H(x)*=0 for x<0 and 1 otherwise), $f_D$ is the fraction of the total counts in a given line present in the decreasing tail component and β is a parameter describing the slope of the exponential tail.

#### 4.1.1.3 Other line shape additions

X-rays reaching the silicon detector interact mainly via the photoelectric effect. If the interaction occurs near the surface of the detector, then there is a non-zero probability that the fluorescent X-ray may escape the active detector volume. In this situation the detector will record 1.74 keV of energy less than the full incident X-ray energy, which causes a small peak to occur 1.74 keV below the main line; this is referred to as the silicon escape peak. The magnitude of this peak will depend on the energy of the original X-ray interacting with the silicon detector, and the detector geometry.

The escape peak is modelled as a delta-function at an energy 1.74 keV below the central peak energy. The low intensity of the escape peak justifies this simplified

treatment. The intensity of the silicon escape peak relative to the full-energy peak was determined using a Monte Carlo simulation of X-ray transport in a model of the SDD detector being used for the L-shell measurements (J. Tickner, private communication). Results from this model were fitted as a function of incident X-ray energy using the simple empirical form:

$$K(E) = 0.0452e^{-0.4256E} + 0.0004149e^{0.01327E} \qquad 5.5$$

The final line-shape component is the so-called flat-shelf function S(x), which was also introduced by Phillips and Marlow [104]. The origin of these incomplete energy deposition events is not completely clear, but is believed to be caused by incomplete charge collection when an X-ray interacts far away from the anode in the detector and the electric field only manages to sweep a certain fraction of the produced charge to the anode. Experience of the Lucas Heights CSIRO group with the Amptek silicon drift detectors used in this work indicates that the flat-shelf can account for 1-1.3% of the total detected counts, and that these X-rays are recorded uniformly at all energies below the peak energy. The equation for the flat-shelf line-shape component is given by:

$$S(x) = \frac{f_S}{x_0} H(x_0 - x) \qquad 5.6$$

where $f_S$ is the fraction of the total counts in a given line present in the flat shelf component.

The normalised full-energy peak function, *L(x)*, is given by:

$$L(x) = A(1 - f_D - f_S - f_K)\frac{1}{\pi}\frac{\frac{1}{2}\Gamma}{(x-x_0)^2+(\frac{1}{2}\Gamma)^2} \qquad 5.7$$

where *A* is the total area of the peak, and $f_D$, $f_S$ , and $f_K$ are the fractions of total peak counts reporting to the decreasing exponential tail, flat-shelf and escape peak components respectively.

Figure 4-2 shows the individual line-shape components for a hypothetical line at 10 keV after convolution with a Gaussian function to account for the detector response. The convolution of a Gaussian and Lorentz profiles results in a Voigt profile. A pure

Gaussian line shape is also shown for comparison to highlight how the low intensity wings of the Lorentzian profile contribute to the Voigt profile.

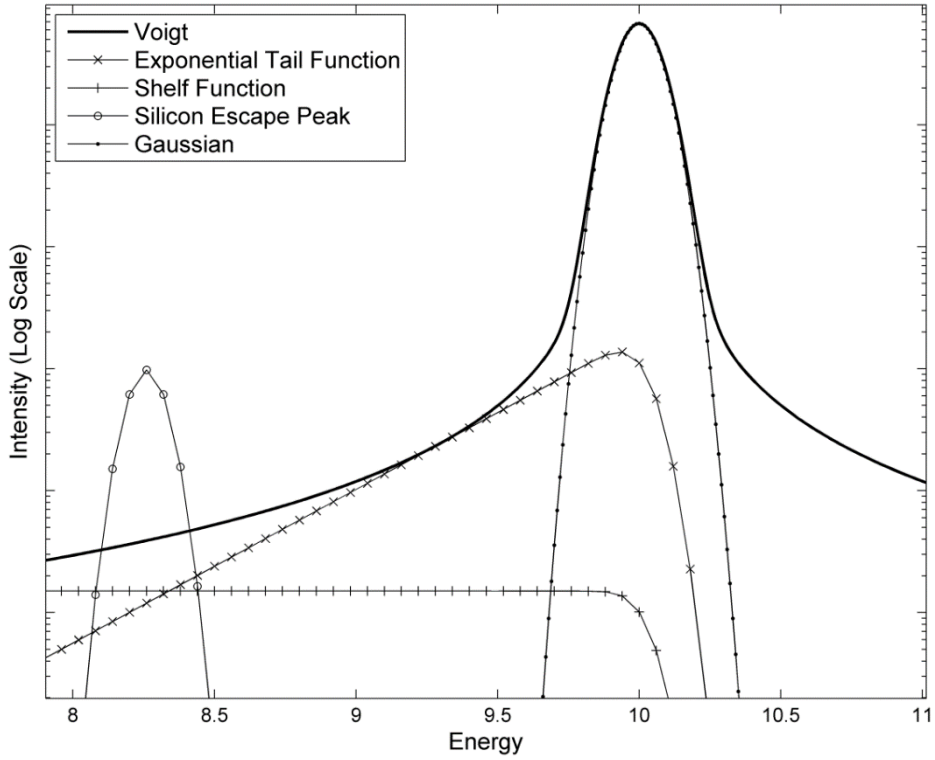


Figure 4-2: Components of the line-shape model used to fit L-shell X-ray spectra. A simple Gaussian peak shape is shown for comparison. See text for details.

#### 4.1.1.4 Convolution

All of these line-shape components are summed together to give the total line-shape function. The line-shape is then finally convoluted with a Gaussian function to include the detector resolution broadening. The line shape function used to describe each individual line, *F(x)*, is now written as:

$$F(x) = [L(x) + D(x) + S(x) + K(x)] * G(x) \qquad 5.8$$

where *L, D, S* and K are full-energy, decreasing exponential tail, flat-shelf and silicon K-shell escape peak components respectively, and *G* is a Gaussian resolution function. The symbol * denotes convolution.

The Gaussian function, *G(x)*, has form:

$$G(x) = \frac{1}{\sqrt{2\pi}\sigma} e^{\frac{-(x-x_0)^2}{2\sigma^2}} \quad 5.9$$

where $\sigma$ is the peak resolution (one standard deviation). The peak FWHM is related to $\sigma$ by *FWHM* = 2.355$\sigma$.

The variation in resolution with energy of an SDD detector can be rather accurately described using the following simple form:

$$\sigma = \sqrt{c^2 + d^2 E} \quad 5.10$$

with empirically fitted parameters *c* and *d*.

The convolution of Lorentzian and Gaussian profiles results in a so-called Voigt profile whose shape cannot be written analytically. Whilst analytical approximations exist [19], to simplify the mathematical treatment of the fitting process the convolution is performed numerically. The computational time is increased by the numerical convolution method.

### 4.1.2 Background Function

With the line-shape function established, the next step is to fit the entire energy region of interest as a whole, rather than just fitting individual lines. One additional component is required at this stage to account for background counts that do not arise from fluorescent peaks.

The background continuum is caused by Compton and Rayleigh scattering of source X-rays and Bremsstrahlung radiation emitted by excited electrons. Compton scattering and incomplete charge collection from each individual fluorescence peak is accounted for with the tail and shelf functions, D(x) and S(x). However Compton and Rayleigh scattering of the continuum exciting radiation are not included in the model so far. Similarly, recoiling electrons produced during photoelectric and Compton scattering interactions can give rise to Bremsstrahlung photons that can reach the detector.

For the L-shell X-ray emission fitting case, none of the elements measured overlap significantly with the exciting radiation scatter profiles, and the background is in general very low in intensity. A simple quadratic form suffices to describe the background component:

$$B(x) = g + hx + jx^2 \quad 5.11$$

### 4.1.3 Universal Fit Parameters

The overall fit is finally written as:

$$S(x) = \sum_{i=1}^{N} F_i(x) + B(x) \quad 5.12$$

where the sum extends over all *N* peaks contributing to the X-ray fluorescence spectrum of the element(s) being measured, and *B(x)* is the background contribution.

There are 6 universal parameters associated with the energy calibration function (*a* and *b*), Gaussian resolution function (*c* and *d*) and the background function (*g*, *h* and *j*). These parameters are separate from the individual peak line shapes and remain constant across the whole fit. In addition to the universal parameters, the individual peak values *A, $x_o$, $f_S$, $f_D$, $f_K$,* $\beta$ and $\Gamma$. With the L-shell X-ray spectrum of a typical heavy element comprising 30 or more individual lines, this would entail determining the values of 200 or more parameters per spectrum being fit.

In practice, fitting 200 parameters in a non-linear least squares fit would be unreasonable. Especially considering the complicated nature of fitting L-shell spectra, where there are many overlapping lines that span several orders of magnitude in intensity range. The separation of many of the overlapping lines is significantly less than the resolution of the energy-dispersive detector, so that the experimental data is not sufficient to independently determine all of these parameters.

Fortunately, several simplifying assumptions can be made when fitting the heavy element L-shell spectra.

According to Phillip and Marlow's hypermet equations, the peak-shape parameters $f_S$, $f_D$, $f_K$, and $\beta$ can be treated as constant over a limited energy-range. Of the L-shell spectra measured, the energy of the L-shell peaks span across an energy range only 3 to 6 keV wide. For example erbium has peaks in the range of 6.1 to 9.7 keV, spanning across a range of 3.6 keV. As pure, high-Z element foils are being measured, the Compton scattering component for each peak will be relatively low and the shelf function and silicon escape peaks are also low intensity features in general. This justifies the simplified hypermet approach of using constant parameters across the

energy range of each fit. The values of these parameters can be determined rather accurately from the most intense L-shell lines in each measured X-ray spectrum and then applied to all of the L-shell lines being fit within a spectrum.

For fitting the intensities of the L-shell X-ray lines, existing values for peak positions and natural line widths can be used. As discussed in section 2.3.5, the NIST [14] database contains more accurate line energy values, but is less comprehensive than EPDL. Consequently, line energies are taken from the NIST database where available, or from the EPDL database if not. The peak position values are used to initialise the fitting process, and to place constraints on allowed peak positions. Natural line width values $\Gamma$ are taken from Campbell's 2001 review [77].

The fitting procedure then reduces to determining the values of 13 universal parameters and the area and constrained position for each L-shell X-ray line.

## 4.2 Fitting Method

As the fitting scripts are being designed for complicated L-shell spectra, there is a need to carry out the fitting process in two stages: a non-linear fitting stage to determine the global parameter values, and a linear least squares fitting stage to refine individual peak parameters and determine their errors.

A least squares fitting model is linear when it can be written as a sum of individual functions multiplied by coefficients. The functions themselves may be non-linear functions of energy, but the dependence on fit coefficients is linear.

A non-linear least squares fit is used in cases where the parameters that need to be determined do not have a linear relationship with the peak functions. If multiple unknown parameters need to be determined, such as the energy calibration parameters, resolution parameters and the peak amplitudes, then a numerical multi-parameter optimisation needs to be performed.

Each measured X-ray spectrum is first fitted to determine the values of the 13 universal parameters, which can only be found from a non-linear least squares fit. A numerical optimisation routine called MINUIT [106] is used to determine the values of these parameters. The MINUIT package is available within the MATLAB [101] data

analysis framework using the FMINUIT extension [107]. Least-squares optimisation of the parameter values is performed by numerical minimisation of the $\chi^2$ function

$$\chi^2 = \sum_k \frac{(y_k - S(x_k))^2}{y_k} \qquad 5.13$$

where *y* is the number of experimentally measured counts in the *k*th bin and $S(x_k)$ is the value of the fitted spectral function, evaluated at the centre of that bin. The number of experimentally measured counts in each bin is assumed to be sufficiently large that the error on this number can be assumed to be $\sqrt{y_k}$.

Each L-shell fit requires up to 70 parameters values to be determined. Fitting the parameters takes approximately 10-15 minutes to complete on a desktop PC, in part due to the numerical convolution approach used to model detector resolution broadening.

Whilst the MINUIT fit returns both parameter values and their errors, the estimated errors returned by MINUIT have the potential to be unreliable for three reasons. First, the large difference in the magnitudes of the returned parameters introduces numerical stability problems, an issue discussed in the MINUIT documentation [106]. Second, certain pairs or groups of peaks have energies sufficiently close that they cannot be resolved by the fitting process, which returns spurious and large error values for fitted areas. This introduces additional numerical instability into the fitting process. Third, as the values of the Lorentzian line widths are held constant, the estimated parameter errors do not include a potential contribution arising from uncertainties in these widths.

MINUIT is used to perform a non-linear least squares fit to best fit the universal parameter values. A second-stage linear fit is performed to more accurately estimate peak areas and their errors.

Once the values of the universal fit parameters and peak centroids have been determined, the spectral function *S* given by equation 5.12 becomes a linear function of the peak areas $A_i$ and the parameters *g, h* and *j* appearing in the background term *B*. Straightforward linear regression can then be used to determine the values of these parameters and the component of their error that arises from finite counting statistics

of the measured spectrum. This avoids the difficulty in obtaining reliable errors from the MINUIT fitting routine due to the numerical instability issues.

To solve the second problem involving overlapping peaks, unresolvable pairs or triplets of peaks originating from the same L-shell were combined, and only a single parameter corresponding to their total summed area was determined using the fit. The relative intensities of the peaks in these clusters were fixed equal to the values predicted from the EPDL database.

The linear fit only returns the statistical error values for the peak areas. However a bootstrap method can be applied to calculate to solve the third problem and calculate a systematic error value on each peak area that includes all sources of fit uncertainty.

### 4.3 Peak Error Determination

For each peak or group of peaks a statistical error and a systematic error were calculated. The linear model provides a statistical uncertainty for each area. A Bootstrap Monte Carlo model was used to calculate the systematic errors by performing 6000 repetitions of each fit, where the universal parameters are randomly varied between each fit. The universal parameters $a, b, c$ and $d$, the peak shape parameters $f_S, f_D, f_K,$ and $\beta$, and the peak centroids $x_0$ and widths $\Gamma$, were varied by adding to their value the product of their error multiplied by a variable sampled from a Gaussian distributed random noise function. The errors of the universal parameters were determined by varying their values until the overall fit $\chi^2$ value increased by 1 unit. For the Lorentzian line widths, the errors are taken from the same Campbell and Pap study [51] that the line width values are sourced from. The systematic error on each line is then calculated as the standard deviation on the area of each peak or peak group calculated over the 6000 fits.

A similar check was done on the statistical error by carrying out multiple fits on the measured spectrum with added normally distributed statistical noise and then calculating the standard deviation of the fits. Excellent agreement was found with the statistical error calculated over multiple fits and the statistical error given by the linear model.

## 4.4 Peak Area Determination

For each L-shell spectrum, an energy region of width 3-6 keV is typically fitted. It would be inconsistent to sum peak areas only over this region. For example, a peak at the lower energy end of the region would have its silicon escape peak sit outside the fitted region and those counts would not be included in the total peak area determination, which would not be the case for a peak with a higher energy. To avoid this problem, counts under each peak are summed across the whole energy range of the measured spectrum to obtain the total line area. After the areas of the peaks are determined using the linear fit, those parameters are then used to extend each line over the whole spectrum range, approximately 2-20 keV, and the counts summed.

# 5 Total L-subshell and Individual Line Relative Measurements

The fundamental parameters method is introduced in chapter 2, where it is shown that the L-shell X-ray emission rates of different elements can be predicted using theoretical fundamental parameter values (equation 2.1). It is also discussed in chapter 2 that many of these fundamental parameters have large errors associated with them, especially the L-subshell fluorescence yields and Coster-Kronig transition probabilities. Despite this there are limited experimental studies comparing measurements of the L-shell emission spectra to theoretically predicted values.

L-shell X-ray emission spectra from eight heavy elements are measured and analysed using the fitting scripts developed in chapter 4. These elements are erbium, thulium, ytterbium, hafnium, tantalum, tungsten, platinum and gold. L-shell line intensity ratios from within each subshell and the ratios of the L1 and L2 subshells to the L3-subshells are measured and compared to theoretically calculated values.

The individual line intensity ratios from within the same L-subshell allows are directly compared with Scofield's DHS and DF predicted X-ray transition emission rates, as well as Elam's database. The ratios of the L1 and L2 subshells to the L3-subshells are compared to calculated values using equation 2.1, using the fluorescence yield and Coster-Kronig values sourced from Chen's DHS predictions [45] and the recommended values published by Campbell in his 2003 and 2009 reviews [44], [52]. The photoionisation cross-sections are taken from the EPDL database [20].

## 5.1 Theoretical Treatment

To simply the comparison between theoretically calculated values and measured values, the individual line intensities are calculated as ratios between X-ray lines originating from the same subshell, so that factors involving the Coster-Kronig probabilities, total fluorescence yield and photoionisation cross-sections cancel:

Equation 5.1

$$\frac{I_{L2-X}}{I_{L2-Y}} = \frac{p_{L2-X}}{p_{L2-Y}}$$

$$\frac{I_{L2-X}}{I_{L2-Y}} = \frac{p_{L2-X}}{p_{L2-Y}}$$

$$\frac{I_{L3-X}}{I_{L3-Y}} = \frac{p_{L3-X}}{p_{L3-Y}}$$

For this reason, the measurements of the individual X-ray line intensities will be reported as ratios to the brightest line in each L-subshell.

The errors for each individual line intensity measurement are calculated as a sum-in-quadrature combination of the statistical and systematic error contributions. These errors are used to calculate the experimental uncertainty on the total X-ray emission from each shell; these total emission rates are, to within an undetermined constant of proportionality, equal to the total X-ray emission rates $I_{L1}$, $I_{L2}$ and $I_{L3}$. For comparison with theoretical results, the total X-ray emission rates are presented as the ratios $I_{L1}/I_{L3}$ and $I_{L2}/I_{L3}$.

## 5.2 Experimental Measurements

The data was collected by Dr. Yves Van Haarlem. The details of the X-ray fluorescence set-up are given in a paper by Ganly et al. co-authored by Dr. Van Haarlem [108]. The data was measured with an in-house-designed X-ray Fluorescence instrument that consisted of an X-ray tube, X-ray filter, silicon drift detector and two collimators, supported in place by a steel frame.

Both the detector and X-ray tube are collimated with lead free PVC hollowed cones to prevent lead from fluorescing and interfering lead L-shell lines being recorded in the spectrum. The cone collimator on the X-ray tube was used to minimise the spot size of the exciting radiation on the sample and prevent X-rays exciting the set-up materials. The cone collimator on the detector was so that only the fluorescent X-rays emitted from the sample at small range of angles could be collected in the detector.

Figure 5-1 shows the design of the steel frame, including the angle between the X-ray tube and the sample, and the angle between the X-ray tube and the detector. The detector was mounted 10 cm from the sample, while the X-ray tube was mounted 14

cm from the sample. The collimators in front of the detector and X-ray tube had openings at their most narrow ends of 1.5 mm and 2.4 mm, respectively.

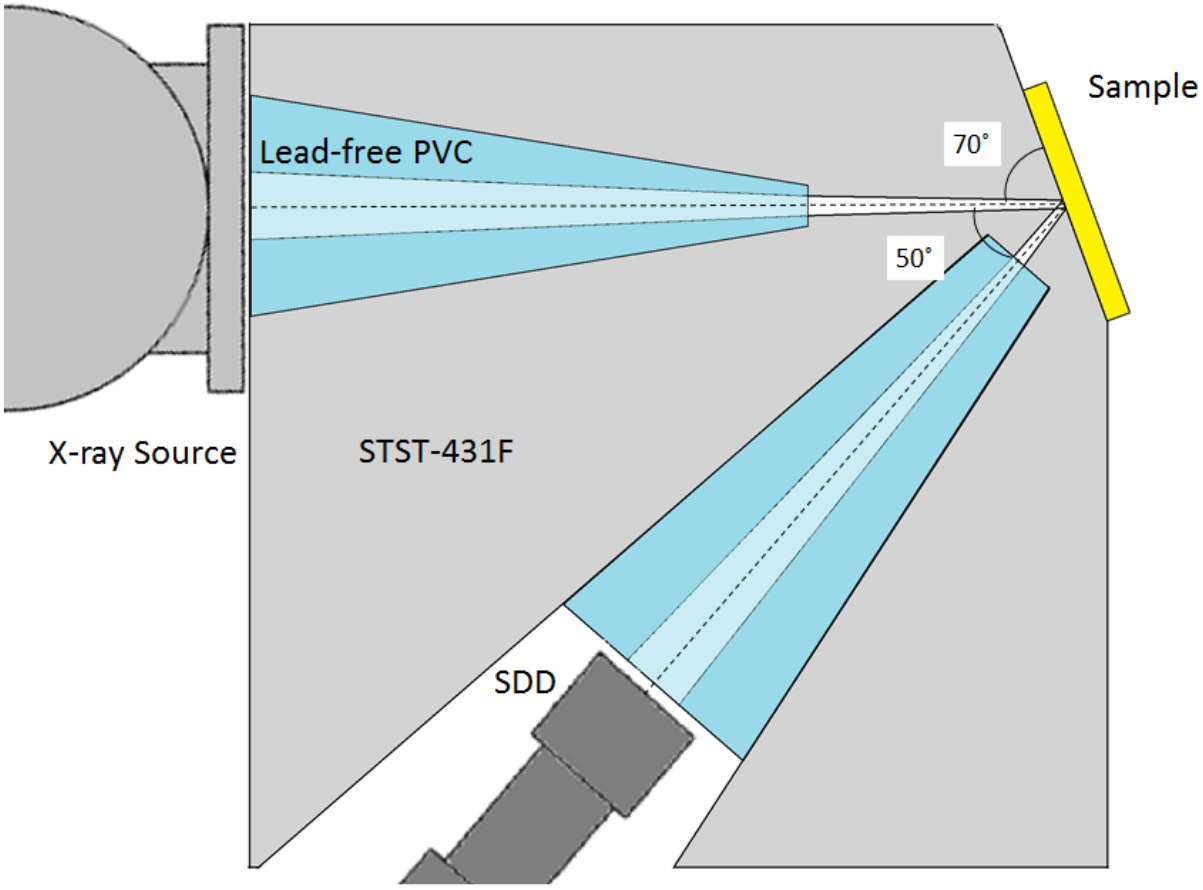


Figure 5-1: Illustration of the steel frame and the experimental set-up used to collect the XRF spectra.

The X-ray tube used was an Oxford-instruments[3] Apogee packaged X-ray tube with a molybdenum target. A pure zirconium filter was used, 0.163 g/cm$^2$ thick. The zirconium filter reduced the low-energy bremsstrahlung X-rays emitted by the tube. Figure 5-2 shows the exciting radiation spectrum from the X-ray tube, predicted by the Ebel model [109]–[111] an analytical model for predicting the output spectrum of an X-ray tube. The exciting radiation spectrum consists mostly of the molybdenum K-alpha characteristic line, which is simulated to have a finite width however in practice this width is much narrower.

[3] Oxford Instruments, Tubney Woods, Abington, Oxfordshire, OX13 5QX, UK, http://www.ofxord-instruments.com/

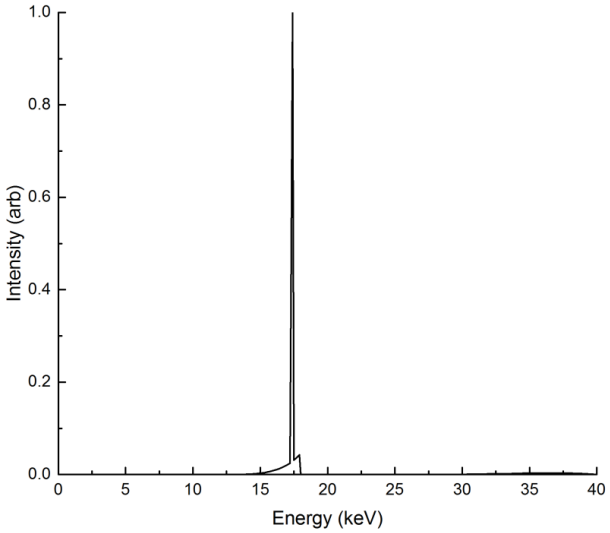


Figure 5-2: the Ebel model prediction of the exciting radiation spectrum from a molybdenum target tube with a zirconium filter.

An Amptek[4] silicon drift detector (X-123SDD) was used with the settings optimised to achieve the best possible energy resolution. At an incident X-ray energy of 6.9 keV, the FWHM resolution was measured to be 139 eV. The typical count rate of each measurement was around 50 c/s and was measured with negligible dead time.

Individual spectra were measured in half hour intervals, with each element measured for a total of at least 24 hours. Figure 5-3 shows a spectrum taken with no sample present to demonstrate the low intensity background results from fluorescent lines being excited from elements in the steel frame. Iron, manganese, nickel and copper peaks can be seen, originating from the stainless steel. The iron peaks are the most intense, followed by the chromium peaks, whereas the copper and nickel peaks are of such a low intensity they should not interfere with the measured heavy element spectra but will still be considered in the element fits if needed. The chromium peaks sit outside the energy region of the L-shell peaks being measured, but the iron peaks will show some overlap with the low-energy erbium L-shell peaks and need to be included in the erbium fit.

Both the Rayleigh and Compton scattered peaks can be observed. The Compton peak sits at approximately 16.5 keV, which is outside the energy region of the L-shell peaks being measured in this study.

[4] Amptek Inc., 14 DeAngelo Drive, Bedford, MA 01730, USA, http://www.amptek.com

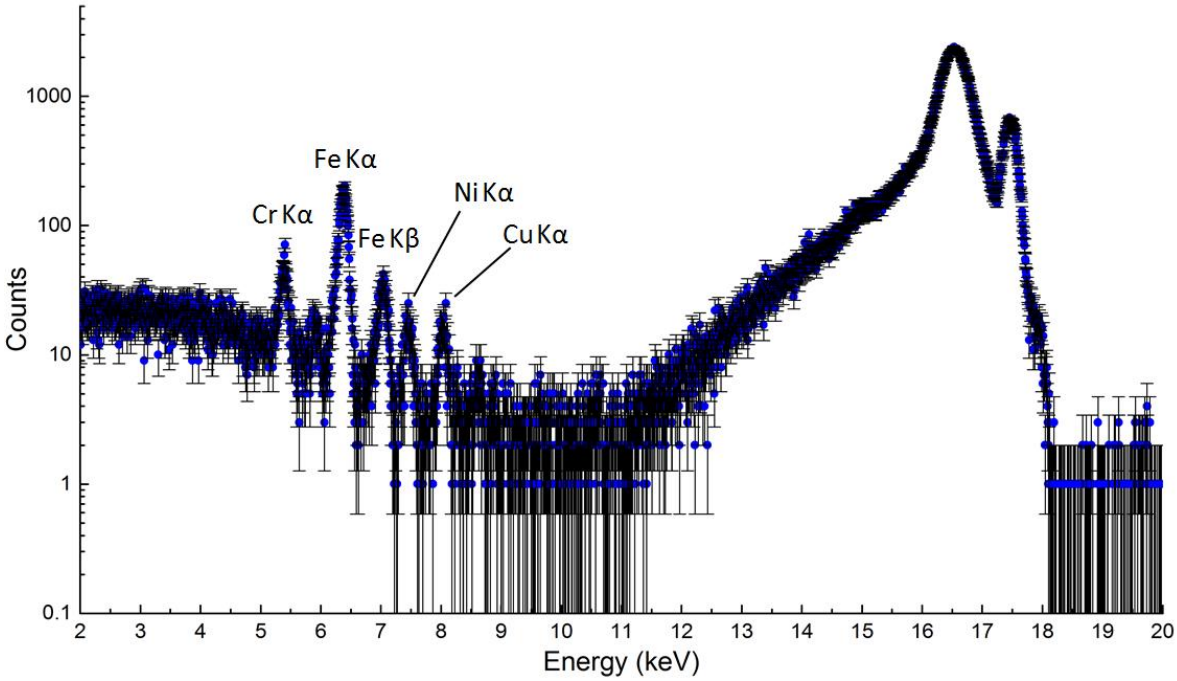


Figure 5-3: Measured XRF spectrum taken with no sample in place measured over 30 min.

Eight heavy elements were measured covering the range Z = 68 – 79; they were erbium, thulium, ytterbium, hafnium, tantalum, tungsten, platinum and gold. High purity metallic foils were used throughout, except for the tungsten foil which contained iron and nickel impurities that were accounted for in the fitting process.

To investigate if the L-subshell line intensities are affected by the chemical state of the atoms in oxide or pure form, oxides of tungsten and tantalum, $WO_3$ and $Ta_2O_5$, were also measured. The oxide powders were combined with 10 % paraffin wax and pressed into pellets with a diameter of 4 cm and a depth of 4 mm.

Each foil or pressed pellet was thick enough to be considered as an infinitely thick sample. A useful check to confirm a sample is a 'thick' sample is to ensure it is unlikely an exciting radiation photon will transmit through the sample without interacting with an atom. The mean free path of a 17.4 keV exciting X-ray travelling through each foil was calculated using equation 3.1 and the number of mean free paths that X-ray can travel through each foil is presented in Table 5-1.

Table 5-1: Thickness of foils used for XRF measurements and the corresponding number of mean free paths for both incident and typical fluorescent X-rays. The L3-M5 X-ray is the brightest L-shell line and is used in this table as an example of a typical L-shell X-ray transition.

| | Sample Thickness (mm) | No. of MFP exciting radiation (17.4 keV) | No. of MFP L1-M3 line |
|---|---|---|---|
| Er | 0.5 | 35 | 88 |
| Tm | 0.2 | 15 | 35 |
| Yb | 0.3 | 17 | 37 |
| Hf | 0.2 | 24 | 43 |
| Ta | 0.2 | 31 | 52 |
| $Ta_2O_5$ | 4.0 | 454 | 790 |
| W | 3.8 | 710 | 1131 |
| $WO_3$ | 4.0 | 536 | 867 |
| Pt | 0.4 | 95 | 115 |
| Au | 0.3 | 67 | 76 |

## 5.3 Fitted Spectra

Every element was measured for at least 24 hours in 30 minute increments. The 30 minute increment spectra were compared and found to have negligible variations in gain, so the spectra were summed together to create one high-intensity spectrum. The summed spectrum of each element was then fitted carefully using the fitting scripts described in chapter 4. For each spectra, the most 30 intense L-shell lines were included in the fit. Some L-shell lines occur so close together it is impossible to fit each peak individually; for example, the L3-N4 and L3-N5 peaks sit only a few eV to a few 10s of eV apart. In these cases the lines are fitted as a pair of peaks. The intensity of the less-intense is peak fixed to the more-intense peak using the DHS predicted ratio of the two peaks, and the pair of peaks are fitted as a unit with only one area parameter.

Figure 5-4 to Figure 5-13 show the fitted spectra and fit residuals for each element. In each spectrum, the measured data is shown with blue dot points, the fitted total spectrum with a black solid line, the background contribution with a dashed black line, and the contributions from individual L-shell lines are and plotted by colour according to L-subshell group. The bottom panel of each figure shows the residuals and overall reduced chi-squared value as a representation of the goodness of fit.

Iron, nickel and lead lines originating from the XRF set-up were added in to each spectrum if needed. In the Erbium case, there were obvious missing peaks that matched the L-shell signature of holmium. Erbium and Holmium sit next to each other on the periodic table, and while it is unlikely for erbium to have holmium impurities, the foils are stored in order of Z-number and it is possible oxidised holmium could have contaminated the erbium foil.

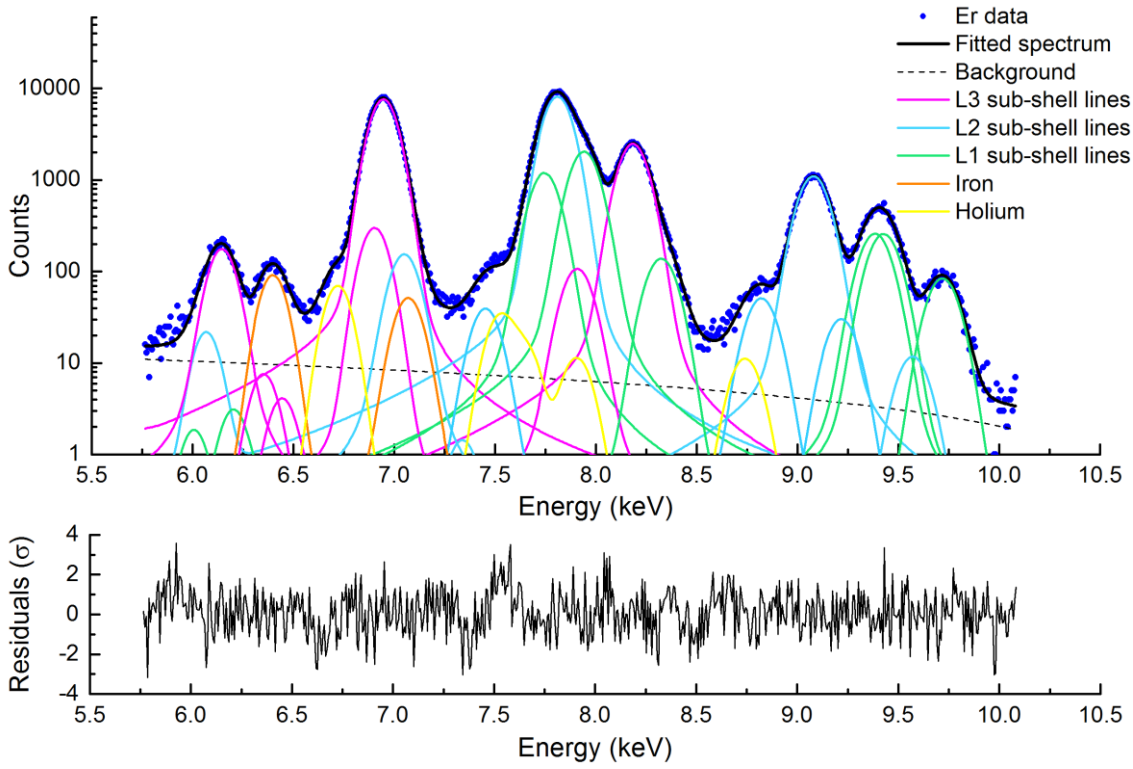


Figure 5-4: the fitted erbium L-shell spectrum, reduced $\chi^2$ = 1.44.

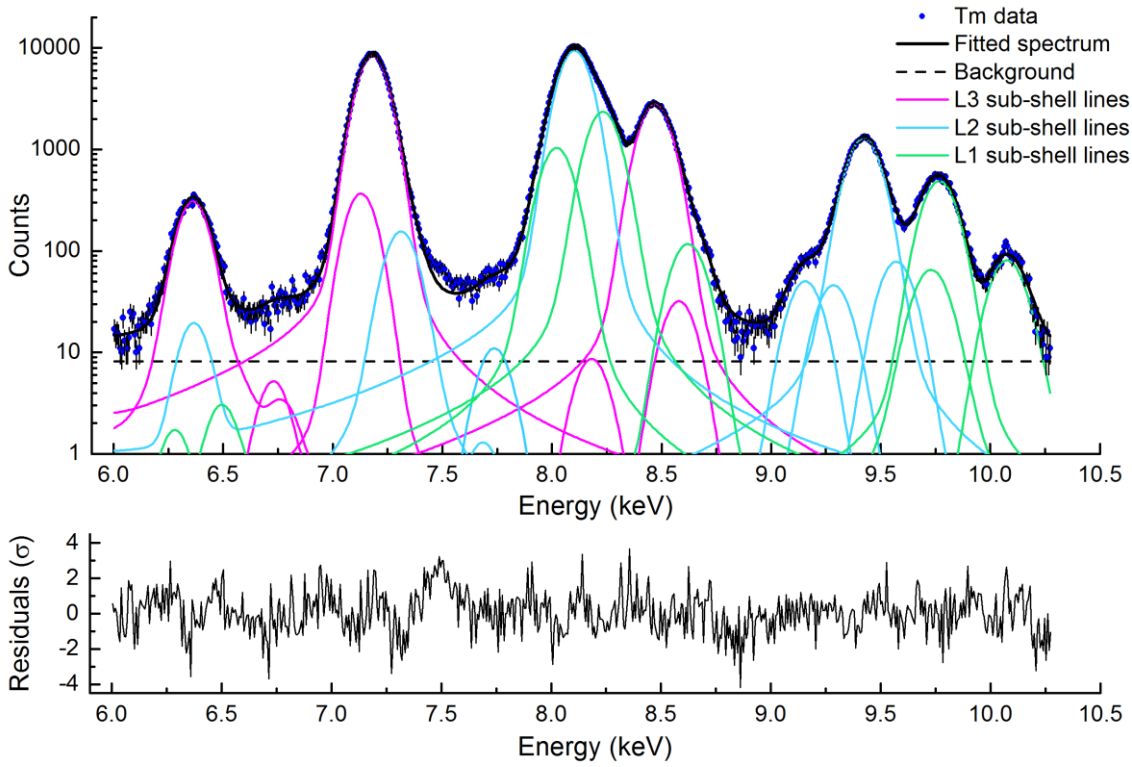


Figure 5-5: The fitted thulium L-shell spectrum, reduced $\chi^2$ = 1.60.

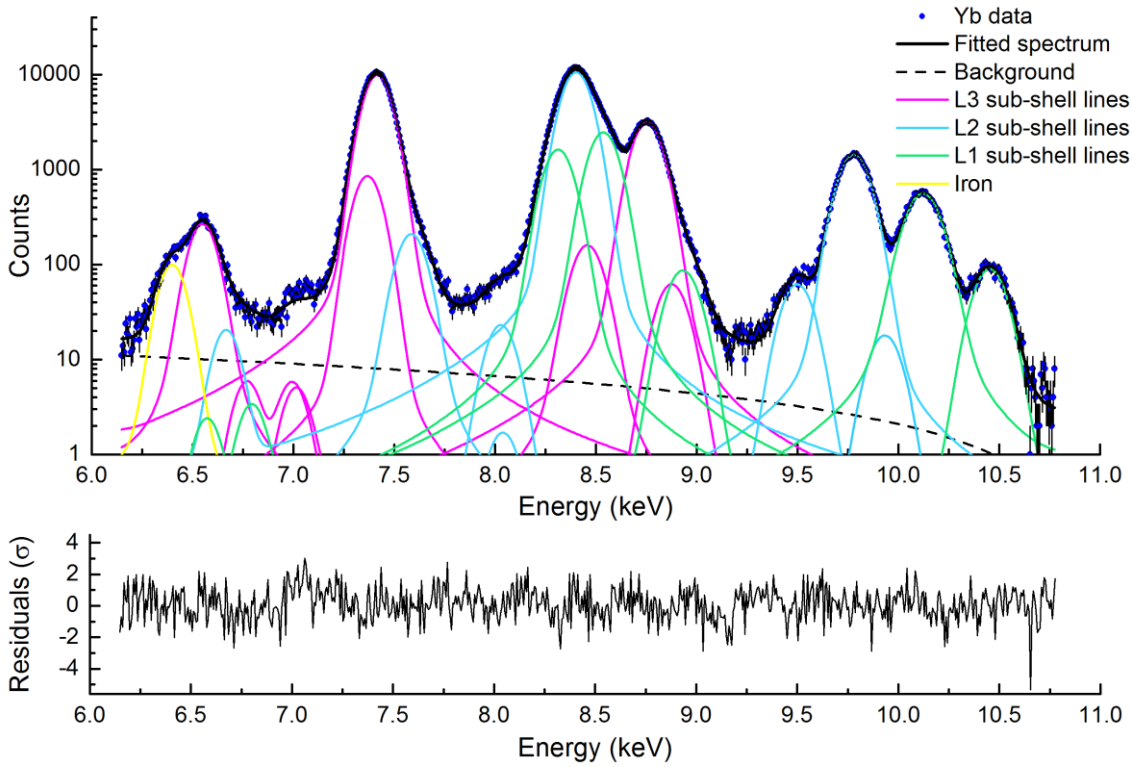


Figure 5-6: The fitted ytterbium L-shell spectrum, reduced $\chi^2 = 1.24$.

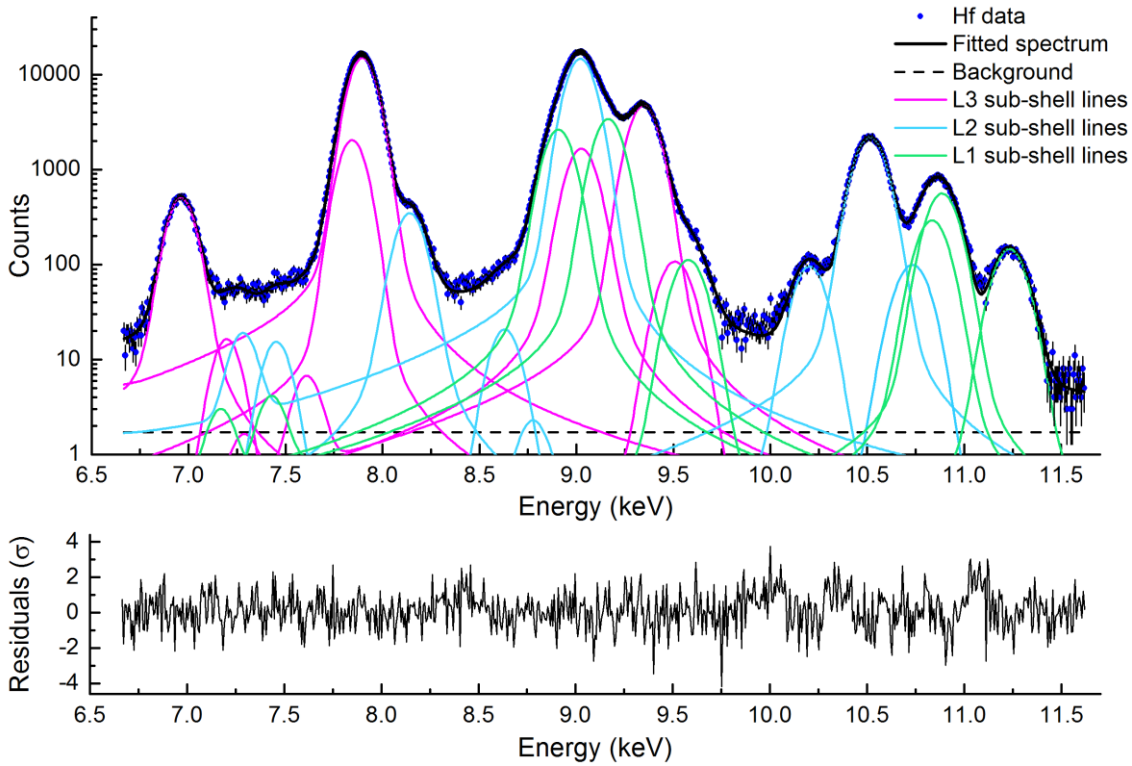


Figure 5-7: The fitted hafnium L-shell spectrum, reduced $\chi^2 = 1.30$.

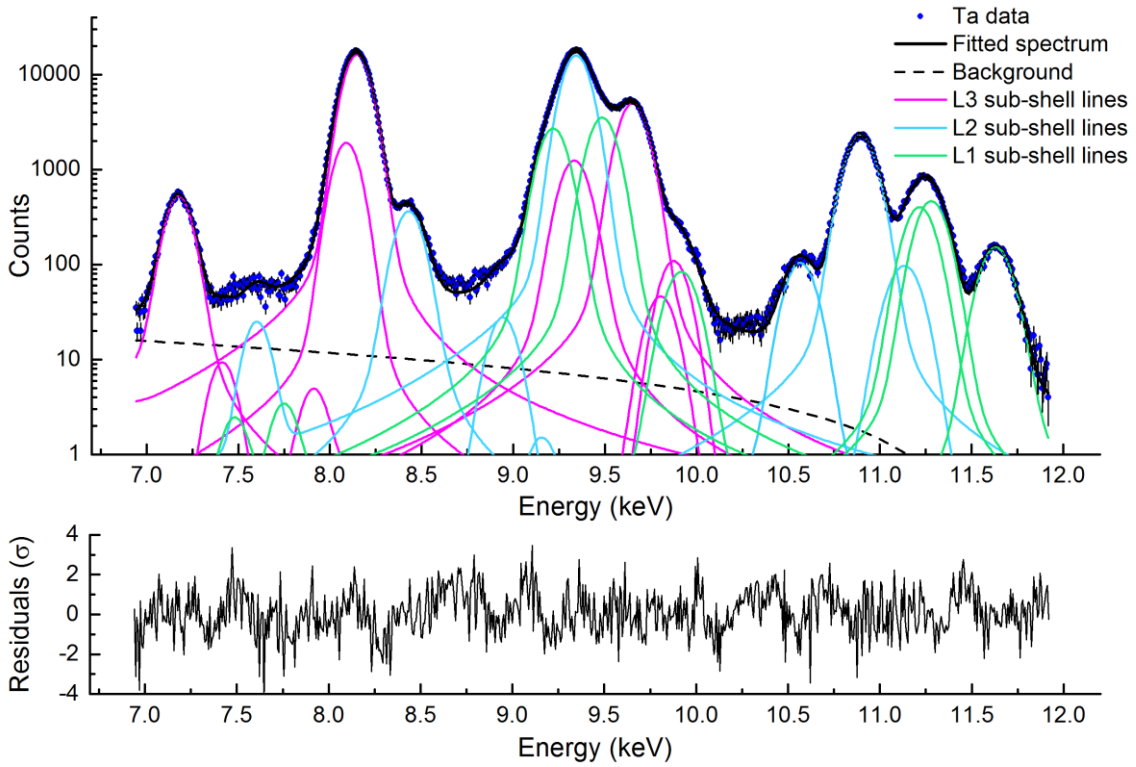


Figure 5-8: The fitted tantalum L-shell spectrum, reduced $\chi^2 = 1.46$.

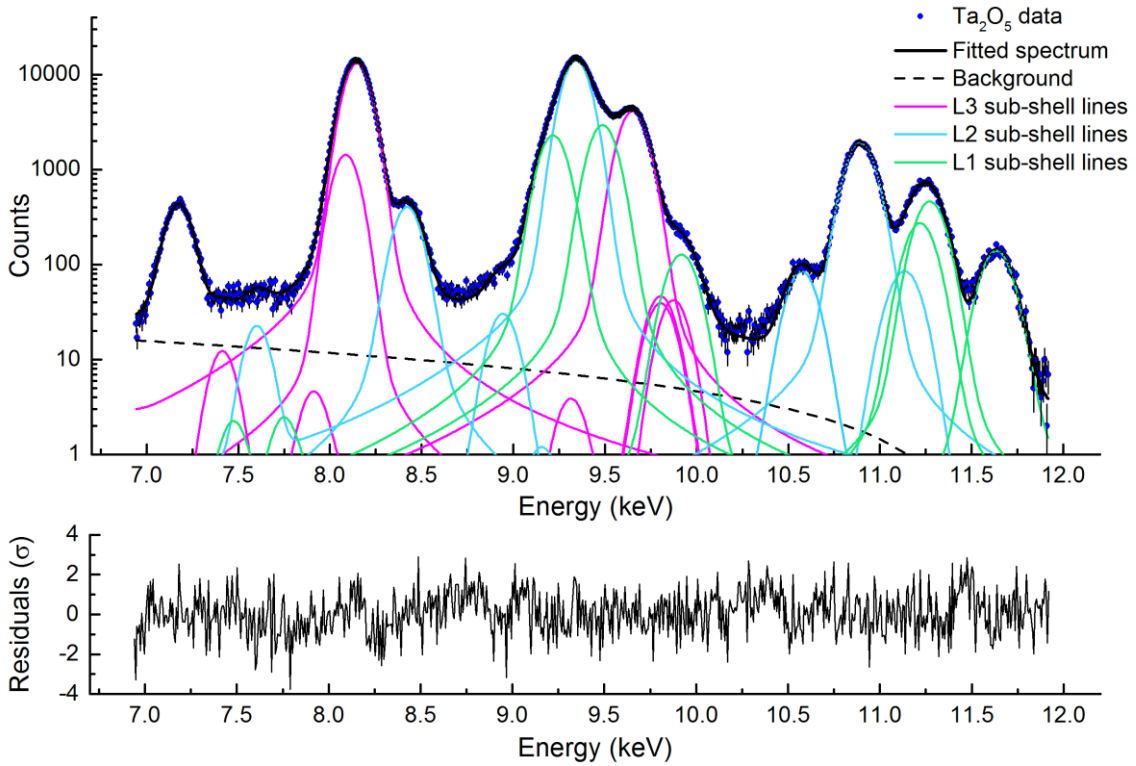


Figure 5-9: The fitted tantalum oxide L-shell spectrum, reduced $\chi^2 = 1.33$.

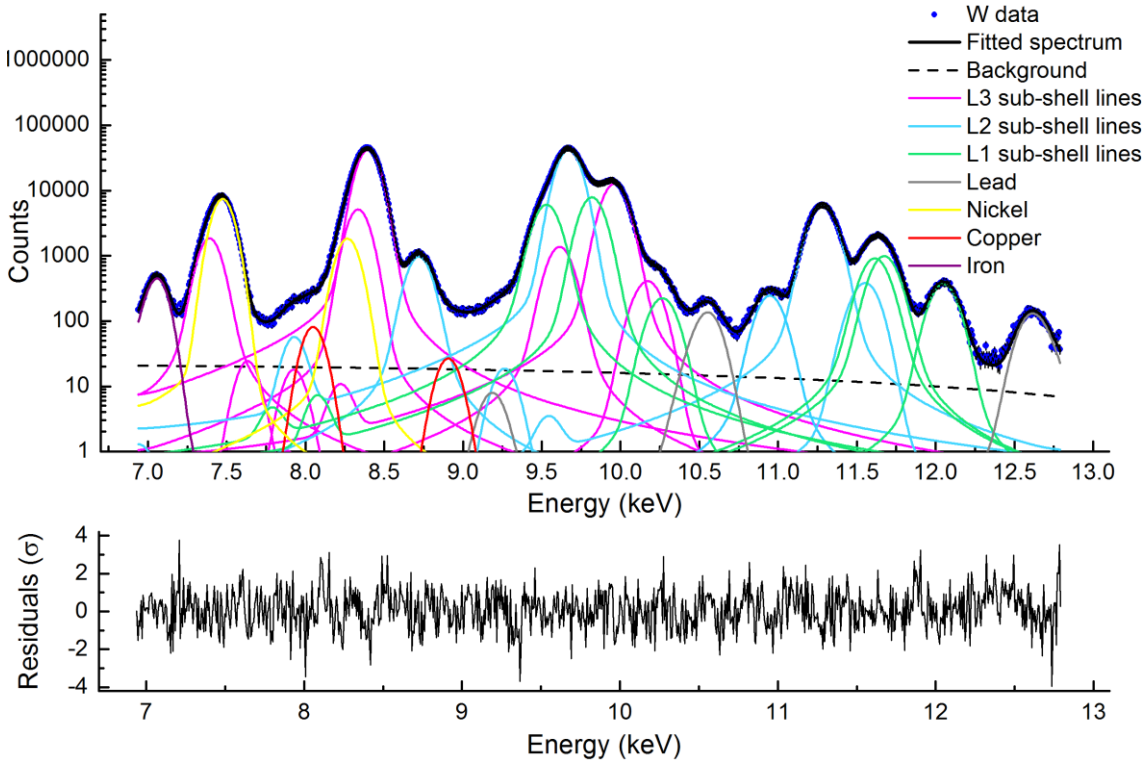


Figure 5-10: The fitted tungsten L-shell spectrum, reduced $\chi^2$ = 1.19.

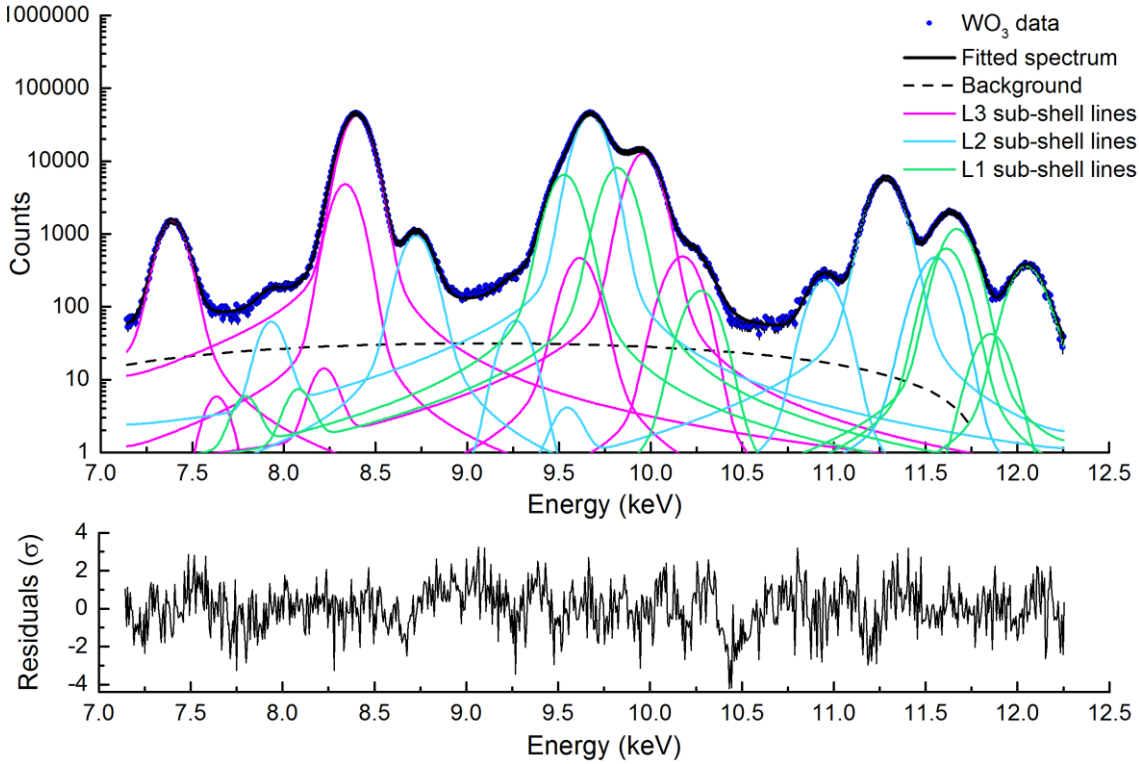


Figure 5-11: The fitted tungsten oxide L-shell spectrum, reduced $\chi^2$ = 1.66.

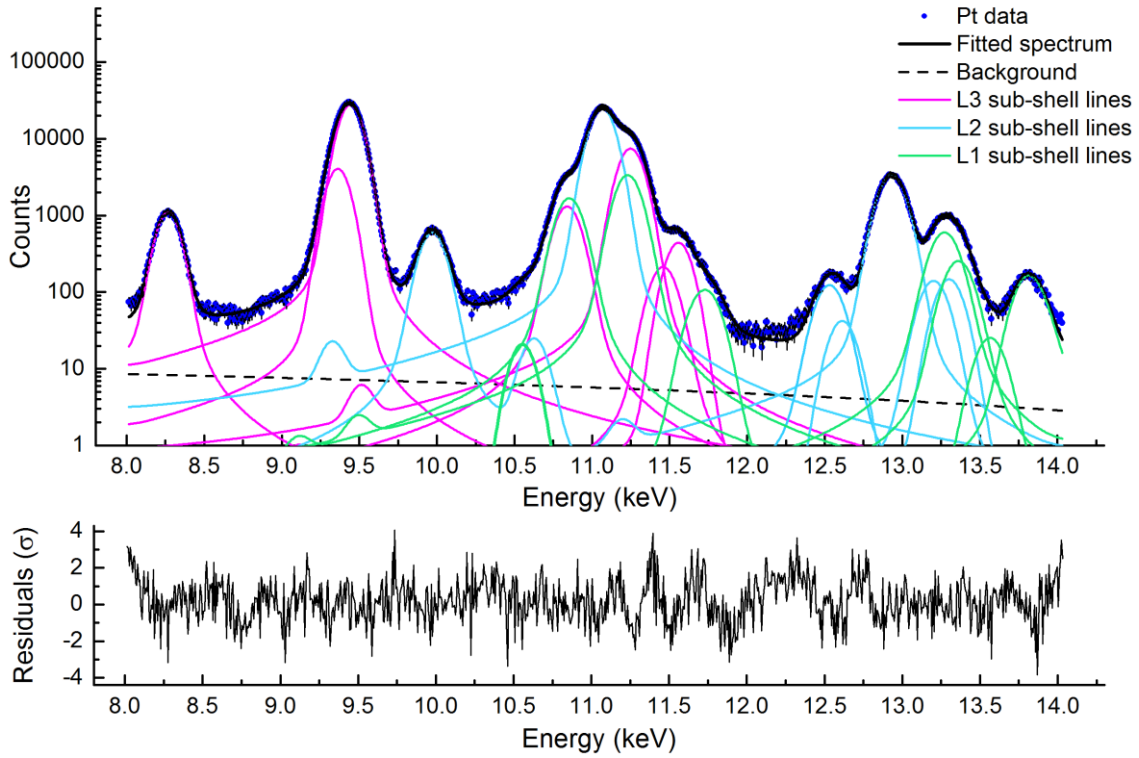


Figure 5-12: The fitted platinum L-shell spectrum, reduced $\chi^2 = 1.63$.

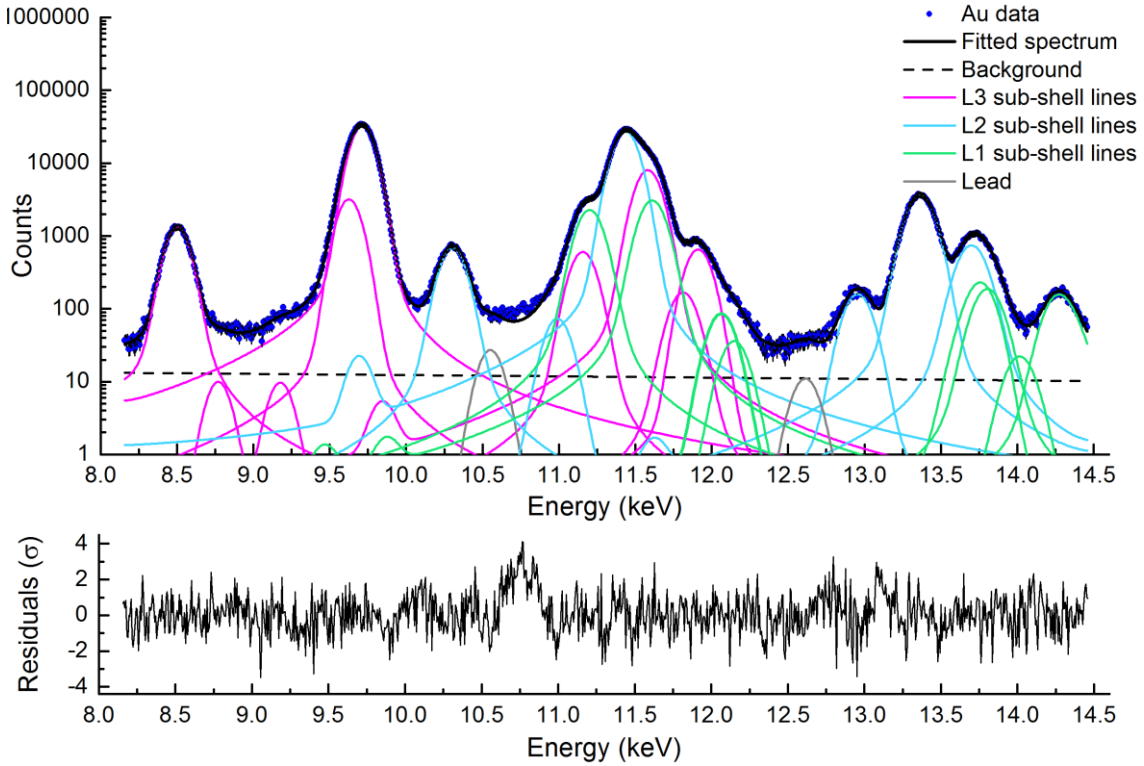


Figure 5-13: The fitted gold L-shell spectrum, reduced $\chi^2 = 1.47$.

## 5.4 Correction for X-ray Absorption and Detection Efficiency

### 5.4.1 Fundamental Parameters Calculation

The measured counts in each line need to be corrected for experimental factors to give the true X-ray emission intensity. These experimental factors include: the X-ray source intensity, the source position relative to the sample, the photoelectric cross-section, the detector area and position relative to the sample, X-ray absorption effects, and detection efficiencies.

When the intensities of each line are presented as a ratio to the brightest line from the same L-subshell, the majority of these factors cancel out. A fundamental parameters method can be used to correct for the absorption of X-rays as they travel through the sample, the air between the sample and the detector. An additional factor is included to account for the detection efficiency of X-rays of different energies in the silicon detector. The relationship between the emitted line intensity, $I_0$, and the detected line intensities for each line, $I$, can be approximated by:

$$\frac{I}{I_0} = \frac{1}{(\mu_{FOIL,out}+\mu_{FOIL,in})} \cdot \frac{\mu_{Si,PE}}{\mu_{Si,tot}} (1 - e^{-\mu_{Si,tot} x_{Si} \rho_{Si}}) \cdot e^{-\mu_{air} x_{air} \rho_{air}} \qquad 5.2$$

where $\mu_{FOIL,out}$ and $\mu_{FOIL,in}$ are the total mass attenuation coefficients for X-rays in the target foil at the emitted line energy and incident exciting radiation energy respectively, $\mu_{Si,PE}$ and $\mu_{Si,tot}$ are the photoelectric and total mass attenuation coefficients at the emitted line energy for silicon respectively, $x_{Si}$ is the thickness of the silicon detector and $\rho_{Si}$ is the density of silicon, $x_{air}$ is the distance between the sample and detector, $\rho_{air}$ is the density of air and $\mu_{air}$ is the total mass attenuation coefficient of air at the emitted line energy.

This method is a first order approximation and makes many simplifying assumptions. The two most significant assumptions are that the exciting radiation is monoenergetic and monodirectional and that only first-order fluorescence interactions in the sample and detector are considered. The first assumption should not affect the correction of the experimental measurements significantly, as the exciting radiation was filtered to give an almost monoenergetic spectrum. However, the second assumption needs to be considered, as the L-shell lines vary greatly in energy; adding to that, lines from the L1-

subshell can be above the L3 and L2-edges, causing secondary or tertiary fluorescence of these lines. An alternative to method to using equation 5.2 is to use a Monte Carlo simulation method.

### 5.4.2 Monte Carlo Simulation

A Monte Carlo simulation true to the experimental set-up was performed using the EGSnrc photon transport code [112], [113]. The simulation modelled the exact experimental set-up including the positioning of the X-ray tube, detector, collimators and sample. The radiation source was modelled as a polychromatic filtered X-ray spectrum from a molybdenum target X-ray tube with a zirconium filter, using the Ebel model [109], [110], [114], [111]. Secondary and higher interactions of the fluorescent photons are automatically modelled in the simulation. The simulation gave the expected X-ray emission intensities of each line based on the experimental set-up. A second simulation was performed to simulate a perfect case scenario with no X-rays absorption or multiple interactions and a perfectly efficient detector. This was achieved by modelling a perfect detector, making the sample infinitely dilute and replacing the air in the set-up with vacuum. The intensity of each line was compared between the 'perfect case' and the real case and the ratio of these intensities used as a correction. The accuracy of this approach is limited by uncertainties used in the fundamental parameters sourced by the EGSnrc photon transport code [112], [113], however as shown in equation 5.1, when the measurements are reported as ratios to the brightest line from within the same subshell, these uncertainties will cancel out.

### 5.4.3 Fundamental Parameters Error Component

A further component was added to the systematic error to compensate for errors in the mass attenuation values used in the fundamental parameters correction approach detailed in the previous section. A Monte Carlo simulation was set up to imitate the correction described in equation 5.2, using a monoenergetic and monodirectional source. Equation 5.2 was evaluated using mass attenuation values from the XCOM database [54] while the Monte Carlo simulation used slightly differing mass attenuation values built into the EGS software. The root mean square difference of the line intensity ratios calculated from each method varied from 1.2-2.5% for different elements and was used to estimate the contribution to the systematic error from the

uncertainty in the mass attenuation coefficient values. The uncertainty in the mass attenuation coefficient values was added in quadrature to the systematic error.

As previously discussed in section 2.3.4, tabulated mass attenuation databases do not account for the fine structure in the mass attenuation values near the L-edges. This fine structure appears as large oscillating fluctuations that reduce with increasing energy above the L-edge position. The fine structure is temperature dependent and therefore it varies from experiment to experiment in a way that makes it hard to include in universal mass attenuation databases.

Of all the lines measured across the eight elements L-shell spectra, only two lines are found in a region just after an L-edge that could be affected by fine structure. They are the Ta and W L1-N2 lines which both sit roughly 70 eV above the respective Ta and W L2-edge energies. While fine structure could exist in these regions, there is no way to determine whether these peaks at their energy positions will be affected by the fine structure. Del Grande [115]observed that the largest, most problematic oscillations occur within 50 eV of an edge [66], and so it is assumed that L1-N2 peaks 70 eV from the L2-edge will not incur large errors in the mass attenuation values.

## 5.5 Relative Line Intensity Ratio Measurements

The relative line-intensities ratios are the measured as the total counts under a given peak divided by the total counts under the brightest peak from the same L-subshell as the given peak. The counts under each peak were summed used the method presented in section 4.4 to determine the total line intensity of each peak. The methods for calculating the statistical and systematic error on each measurement are detailed in sections 4.3 and 5.4.3. The absorption and detector efficiency correction was determined by both methods described in section 5.4; Monte Carlo simulation and the approximate fundamental parameters calculation using equation 5.2. It was found the two different analytical approaches differed by up to 2.5%, which is assumed to be due to the simulation of the polychromatic source and the secondary and tertiary interactions, as well as differences in the mass attenuation values used in each method. The Monte Carlo simulated values are used to correct the results as they are

assumed to be more accurate as they account for the polychromatic source and the secondary and tertiary interactions.

Tables 5.2-5.9 present the measured results for each element analysed, along with a comparison with existing literature values where available. The tables first present the raw measured line intensity in terms of X-ray counts, along with the statistical and systematic uncertainty components. The total error for each measured line intensity is not presented, but can be calculated by adding the statistical and systematic error components in quadrature:

$$error_{tot}(Line\ A) = \sqrt{error_{stat}(Line\ A)^2 + error_{sys}(Line\ A)^2} \quad 5.3$$

The total error in counts for each line intensity can be transformed to the relative error on each line intensity by dividing it by the number of counts in that line.

Calculated from the measured line intensities, the tables also present the X-ray intensity ratio of each line to the brightest line from the same L-subshell, and its associated total error. The relative error on the ratio of two different lines, A and B, is given by:

$$error_{rel}(\frac{Line\ A}{Line\ B}) = \sqrt{error_{rel}(Line\ A)^2 + error_{rel}(Line\ B)^2} \quad 5.4$$

The relative error on the ratio is transformed to the total error on the ratio by multiplying the relative error by the ratio. The intensity ratio of the brightest line in each L-subshell to the brightest line in the same L-subshell is consequently equal to one and is not reported. Where available, the intensity ratios calculated from the DHS [11], DF [10] and Elam databases [75], are included.

Tables 5.2-5.9 also present the measured energy position for each line along with the associated total error as well the NIST database theoretical line energies, [69], where available. Known energy positions of L-shell lines from the NIST and EADL database are used to initialize the fitting process and to place constraints on the allowed line energy positions. Line energies are preferably taken from the NIST database where available, or otherwise from the EADL database. The energy-channel calibration parameters are established separately for each spectrum, and then the peak positions

and energy calibration parameters are allowed to be free parameters in the non-linear fitting stage, to best fit the experimental data. A single slope and offset correction is added to the measured energy values, and then the values of these correction parameters is chosen to minimize the root-mean squared discrepancy between the measured energy values and those reported in the NIST database for all lines for the given element. For all elements except tantalum, the theoretical NIST values are used. For tantalum the NIST experimental values are used for reasons discussed in section 5.6.4. The measurements are sensitive to deviations from the NIST values for individual lines, but will not reveal any systematic biases.

Table 5-2: Erbium

| Transition | Energy (this work, keV) | Energy (NIST, keV) | Line intensity (counts) | Absorption correction | Intensity ratio (this work) | Intensity ratio (DHS) | Intensity ratio (DF) | Intensity ratio (Elam) |
|---|---|---|---|---|---|---|---|---|
| L3-M5 | 6.94628(16) | 6.9479(11) | 176714±833±4535 | 0.720 | Line intensities relative to L3-M5 transition | | | |
| L3-N4,5 | 8.18398(12) | 8.18452(55) | 62582±279±1582 | 0.516 | 0.2493(91) | 0.1889 | 0.2005 | 0.2005 |
| L3-M4 | 6.9032(26) | 6.9058(12) | 6951±645±1260 | 0.732 | 0.0399(82) | 0.1131 | 0.1133 | 0.1115 |
| L3-M1 | 6.14430(20) | 6.1414(16) | 4212±76±123 | 1 | 0.0331(14) | 0.0481 | 0.0483 | 0.0439 |
| L2-M4 | 7.811569(20) | 7.8115(13) | 198697±1061±5853 | 0.566 | Line intensities relative to L2-M4 transition | | | |
| L2-N4 | 9.07962(47) | 9.0781(16) | 28953±190±733 | 0.851 | 0.2203(88) | 0.1768 | 0.1875 | 0.1773 |
| L2-M1 | 7.0493(42) | 7.0471(21) | 3884±212±436 | 0.711 | 0.0249(32) | 0.0269 | 0.0273 | 0.0222 |
| L2-N1 | 8.8227(28) | 8.8145(34) | 1342±52±52 | 0.901 | 0.01104(69) | 0.0065 | 0.0066 | |
| L1-M3 | 7.9422(11) | 7.9395(26) | 52188±1260±63645 | 0.534 | Line intensities relative to L1-M3 transition | | | |
| L1-M2 | 7.74565(59) | 7.7455(25) | 30037±571±1211 | 0.566 | 0.60(50) | 0.7352 | 0.7315 | 0.6348 |
| L1-N3 | 9.4286(63) | 9.4303(18) | 6906±309±1578 | 0.990 | 0.25(22) | 0.2499 | 0.2574 | 0.2884 |
| L1-N2 | 9.3866(65) | 9.3866(44) | 6994±313±1679 | 1.018 | 0.25(22) | 0.1755 | 0.1788 | 0.1983 |
| L1-O2,3 | 9.7215(20) | | 2232±58±63 | 0.935 | 0.075(63) | 0.0553 | 0.0593 | |

Table 5-3: Thulium

| Transition | Energy (this work, keV) | Energy (NIST, keV) | Line intensity (counts) | Absorption correction | Intensity ratio (this work) | Intensity ratio (DHS) | Intensity ratio (DF) | Intensity ratio (Elam) |
|---|---|---|---|---|---|---|---|---|
| L3-M5 | 7.18018(16) | 7.1801(11) | 198395±719±2681 | 0.737 | Line intensities relative to L3-M5 transition | | | |
| L3-N4,5 | 8.46961(15) | 8.46765(55) | 70588±342±1008 | 0.524 | 0.2507(52) | 0.1894 | 0.2011 | 0.1973 |
| L3-M4 | 7.1267(15) | 7.1354(12) | 8676±524±646 | 0.741 | 0.0439(44) | 0.1133 | 0.1136 | 0.1115 |
| L3-M1 | 6.35981(66) | 6.3435(16) | 7630±97±124 | 1 | 0.0523(13) | 0.0487 | 0.0488 | 0.0445 |
| L2-M4 | 8.103081(80) | 8.1038(13) | 232920±1162±3892 | 0.573 | Line intensities relative to L2-M4 transition | | | |
| L2-N4 | 9.42390(51) | 9.4239(13) | 34756±208±475 | 0.843 | 0.2222(46) | 0.1763 | 0.1885 | 0.1794 |
| L2-M1 | 7.30996(38) | 7.3118(22) | 3994±162±294 | 0.709 | 0.0216(18) | 0.0269 | 0.0273 | 0.0221 |
| L2-N1 | 9.1556(33) | 9.1496(33) | 1339±41±40 | 0.908 | 0.00927(42) | 0.0065 | 0.0067 | 0.0067 |
| L2-O1 | 9.5725(54) | | 1982±138±195 | 0.835 | 0.0125(13) | 0.0012 | 0.0011 | |
| L1-M3 | 8.23229(22) | 8.2343(26) | 60440±932±9327 | 0.539 | Line intensities relative to L1-M3 transition | | | |
| L1-M2 | 8.02108(50) | 8.0261(26) | 26427±465±780 | 0.578 | 0.468(74) | 0.7447 | 0.7404 | 0.6440 |
| L1-O2,3 | 10.0778(18) | | 2193±54±45 | 0.947 | 0.064(10) | 0.0551 | 0.0590 | |

Table 5-4: Ytterbium

| Transition | Energy (this work, keV) | Energy (NIST, keV) | Line intensity (counts) | Absorption correction | Intensity ratio (this work) | Intensity ratio (DHS) | Intensity ratio (DF) | Intensity ratio (Elam) |
|---|---|---|---|---|---|---|---|---|
| L3-M5 | 7.41644(17) | 7.4163(12) | 233030±818±4552 | 0.741 | Line intensities relative to L3-M5 transition | | | |
| L3-N4,5 | 8.75569(45) | 8.75569(55) | 80637±353±1597 | 0.529 | 0.2472(70) | 0.1896 | 0.2014 | 0.1945 |
| L3-M4 | 7.36818(78) | 7.3691(13) | 20165±652±1351 | 0.753 | 0.0880(68) | 0.1131 | 0.1134 | 0.1115 |
| L3-M1 | 6.5497(12) | 6.5484(17) | 6466±95±136 | 1 | 0.0375(12) | 0.0494 | 0.0495 | 0.0451 |
| L2-M4 | 8.40305(22) | 8.4036(14) | 263566±1566±24028 | 0.577 | Line intensities relative to L2-M4 transition | | | |
| L2-N4 | 9.77836(35) | 9.7782(10) | 38684±213±741 | 0.854 | 0.217(20) | 0.1782 | 0.1892 | 0.1815 |
| L2-M1 | 7.5843(28) | 7.5828(23) | 5362±131±245 | 1.033 | 0.0364(38) | 0.0268 | 0.0273 | 0.0220 |
| L2-N1 | 9.4980(34) | 9.4927(31) | 1679±52±50 | 0.912 | 0.0101(10) | 0.0065 | 0.0067 | |
| L1-M3 | 8.53619(63) | 8.5368(28) | 64086±719±8952 | 0.550 | Line intensities relative to L1-M3 transition | | | |
| L1-M2 | 8.3137(16) | 8.3136(27) | 41830±495±2048 | 0.581 | 0.69(10) | 0.7545 | 0.7502 | 0.6540 |
| L1-O2,O3 | 10.4509(21) | | 2498±55±57 | 0.961 | 0.0681(97) | 0.0550 | 0.0588 | |

Table 5-5: Hafnium

| Transition | Energy (this work, keV) | Energy (NIST, keV) | Line intensity (counts) | Absorption correction | Intensity ratio (this work) | Intensity ratio (DHS) | Intensity ratio (DF) | Intensity ratio (Elam) |
|---|---|---|---|---|---|---|---|---|
| L3-M5 | 7.898390(60) | 7.8991(12) | 363216±966±4735 | 0.752 | Line intensities relative to L3-M5 transition | | | |
| L3-N4,5 | 9.34866(38) | 9.34854(55) | 123066±419±1617 | 0.559 | 0.2517(48) | 0.1931 | 0.2053 | 0.2129 |
| L3-M4 | 7.84458(74) | 7.8447(12) | 49327±778±2459 | 0.766 | 0.1383(75) | 0.1133 | 0.1135 | 0.1115 |
| L3-M1 | 6.96317(69) | 6.9631(17) | 12422±118±283 | 1 | 0.0455(13) | 0.0507 | 0.0508 | 0.0465 |
| L2-M4 | 9.020618(60) | 9.0224(13) | 372989±11341±50599 | 0.591 | Line intensities relative to L2-M4 transition | | | |
| L2-N4 | 10.51431(25) | 10.5129(16) | 60753±259±798 | 0.877 | 0.242(34) | 0.1819 | 0.1934 | 0.1857 |
| L2-M1 | 8.1420(13) | 8.1408(24) | 9139±126±350 | 0.726 | 0.0301(43) | 0.0268 | 0.0273 | 0.0218 |
| L2-N1 | 10.2040(25) | 10.2036(32) | 2646±62±93 | 0.910 | 0.0109(16) | 0.0066 | 0.0067 | |
| L1-M3 | 9.166069(80) | 9.1624(28) | 90073±727±2397 | 0.565 | Line intensities relative to L1-M3 transition | | | |
| L1-M2 | 8.90913(42) | 8.9060(27) | 69772±490±1527 | 0.594 | 0.814(29) | 0.7756 | 0.7709 | 0.6766 |
| L1-N3 | 10.8869(10) | 10.8905(19) | 15812±354±938 | 1.035 | 0.322(22) | 0.2557 | 0.2638 | 0.3077 |
| L1-N2 | 10.8350(40) | 10.8325(42) | 8300±458±1675 | 1.045 | 0.17 0(36) | 0.1884 | 0.1921 | 0.2106 |
| L1-O2,3 | 11.2342(25) | | 4173±69±64 | 0.969 | 0.0795(29) | 0.0622 | 0.0660 | |

Table 5-6: Tantalum

| Transition | Ta Energy (this work, keV) | $Ta_2O_5$ Energy (this work, keV) | Energy (NIST, keV) | Ta Line intensity (counts) | Ta2O5 Line intensity (counts) | Ta Absorption correction | $Ta_2O_5$ Absorption correction | Ta Intensity ratio (this work) | $Ta_2O_5$ Intensity ratio (this work) | Intensity ratio (DHS) | Intensity ratio (DF) | Intensity ratio (Elam) |
|---|---|---|---|---|---|---|---|---|---|---|---|---|
| L3-M5 | 8.146170(50) | 8.146307(30) | 8.1465(12) | 399059±956±9856 | 324485±829±10202 | 0.759 | 0.761 | Line intensities relative to L3-M5 transition | | | | |
| L3-N4,5 | 9.65011(24) | 9.65101(14) | 9.66878(56) | 134555±482±3369 | 111372±439±3508 | 0.561 | 0.55 | 0.2492(88) | 0.251(12) | 0.1951 | 0.2075 | 0.2199 |
| L3-M4 | 8.08707(83) | 8.08369(81) | 8.0882(12) | 47230±744±1742 | 35150±624±1126 | 0.781 | 0.779 | 0.1218(57) | 0.1113(70) | 0.1133 | 0.1135 | 0.1116 |
| L3-M1 | 7.17085(68) | 7.17129(78) | 7.1744(17) | 13090±123±346 | 10451±110±328 | 1 | 1 | 0.0432(16) | 0.0428(24) | 0.0514 | 0.0515 | 0.0472 |
| L2-M4 | 9.34353(22) | 9.34246(54) | 9.3434(13) | 412492±8422±67382 | 363147±3033±11964 | 0.609 | 0.599 | Line intensities relative to L2-M4 transition | | | | |
| L2-N4 | 10.89519(32) | 10.89368(34) | 10.9634(17) | 65275±267±1627 | 53925±243±1699 | 0.881 | 0.828 | 0.229(38) | 0.208(12) | 0.1839 | 0.1957 | 0.1878 |
| L2-M1 | 8.4286(11) | 8.4191(11) | 8.4296(24) | 9760±123±327 | 10835±127±342 | 0.728 | 0.724 | 0.0283(47) | 0.0357(22) | 0.0268 | 0.0273 | 0.0218 |
| L2-N1 | 10.5678(25) | 10.5745(28) | 10.5880(32) | 2974±65±88 | 2399±59±76 | 0.913 | 0.861 | 0.0108(18) | 0.00964(69) | 0.0066 | 0.0068 | |
| L1-M3 | 9.48586(39) | 9.48681(94) | 9.4871(28) | 95578±566±3529 | 79874±535±2561 | 0.572 | 0.556 | Line intensities relative to L1-M3 transition | | | | |
| L1-M2 | 9.2175(12) | 9.21589(25) | 9.2126(27) | 73348±813±3582 | 62267±674±2079 | 0.609 | 0.596 | 0.817(51) | 0.829(49) | 0.7862 | 0.7815 | 0.6893 |
| L1-N3 | 11.2826(26) | 11.2731(43) | 11.2942(19) | 13614±313±2008 | 13425±352±559 | 1.045 | 0.942 | 0.260(40) | 0.292(23) | 0.2577 | 0.2659 | 0.3128 |
| L1-N2 | 11.2184(52) | 11.2200(80) | 11.2317(42) | 11579±486±4294 | 7976±498±586 | 1.046 | 0.949 | 0.221(83) | 0.175(25) | 0.1920 | 0.1958 | 0.2150 |
| L1-O2,3 | 11.6349(14) | 11.6369(27) | | 4508±71±116 | 4149±68±130 | 0.985 | 0.928 | 0.0812(39) | 0.0854(53) | 0.0657 | 0.0694 | |

Table 5-7: Tungsten

| Transition | W Energy (this work, keV) | $WO_3$ Energy (this work, keV) | Energy (NIST, keV) | W Line intensity (counts) | $WO_3$ Line intensity (counts) | W Absorption correction | $WO_3$ Absorption correction | W Intensity ratio (this work) | $WO_3$ Intensity ratio (this work) | Intensity ratio (DHS) | Intensity ratio (DF) | Intensity ratio (Elam) |
|---|---|---|---|---|---|---|---|---|---|---|---|---|
| L3-M5 | 8.39731(90) | 8.39762(16) | 8.3976(12) | 1034170±1744±23766 | 1037056±1455±18487 | 0.810 | 0.756 | Line intensities relative to L3-M5 transition | | | | |
| L3-N4,5 | 9.96329(90) | 9.96182(13) | 9.96299(56) | 340158±740±6386 | 345425±751±5967 | 0.598 | 0.557 | 0.2428(72) | 0.2496(62) | 0.1972 | 0.2098 | 0.2257 |
| L3-M4 | 8.33489(80) | 8.33364(75) | 8.3352(12) | 125241±1990±6765 | 118745±1104±2257 | 0.789 | 0.767 | 0.1179(72) | 0.116 0(32) | 0.1134 | 0.1137 | 0.1116 |
| L3-M1 | 7.39062(93) | 7.39073(63) | 7.3881(17) | 46282±398±976 | 37048±202±633 | 1 | 1 | 0.0553(18) | 0.0474(12) | 0.0521 | 0.0523 | 0.0480 |
| L2-M4 | 9.672099(70) | 9.67094(11) | 9.6721(13) | 1026135±2414±33724 | 1130982±2621±20175 | 0.633 | 0.854 | Line intensities relative to L2-M4 transition | | | | |
| L2-N4 | 11.28325(13) | 11.28073(12) | 11.2854(21) | 173911±433±3644 | 166727±423±2850 | 0.869 | 0.713 | 0.2326(91) | 0.216 0(54) | 0.1861 | 0.1983 | 0.1900 |
| L2-M1 | 8.72040(68) | 8.72047(68) | 8.7250(24) | 26199±194±591 | 25612±189±443 | 0.764 | 0.882 | 0.0308(13) | 0.0270(70) | 0.0269 | 0.0273 | 0.0218 |
| L2-N1 | 10.9501(16) | 10.9494(16) | 10.9501(33) | 7526±104±167 | 6719±101±117 | 0.887 | 0.593 | 0.01028(43) | 0.00889(26) | 0.0066 | 0.0068 | |
| L1-M3 | 9.81993(20) | 9.81842(22) | 9.8195(29) | 217920±957±10205 | 221851±982±4001 | 0.606 | 0.560 | Line intensities relative to L1-M3 transition | | | | |
| L1-M2 | 9.53067(83) | 9.5288(82) | 9.5260(28) | 175111±1089±5743 | 177852±1096±3621 | 0.644 | 0.598 | 0.853(49) | 0.852(24) | 0.7988 | 0.7941 | 0.7029 |
| L1-N3 | 11.6760(14) | 11.6707(14) | 11.6761(19) | 34180±563±1946 | 34396±665±688 | 0.998 | 0.975 | 0.258(19) | 0.2728(91) | 0.2602 | 0.2683 | 0.3179 |
| L1-N2 | 11.6165(50) | 11.6133(66) | 11.6094(44) | 18236±979±2027 | 18521±1109±547 | 1.018 | 1.006 | 0.140(18) | 0.152(11) | 0.1961 | 0.2000 | 0.2200 |
| L1-O2,3 | 12.0521(17) | 12.0484(18) | | 11510±115±204 | 10822±115±185 | 0.962 | 0.984 | 0.0838(69) | 0.0846(23) | 0.0694 | 0.0729 | |

Table 5-8: Platinum

| Transition | Energy (this work, keV) | Energy (NIST, keV) | Line intensity (counts) | Absorption correction | Intensity ratio (this work) | Intensity ratio (DHS) | Intensity ratio (DF) | Intensity ratio (Elam) |
|---|---|---|---|---|---|---|---|---|
| L3-M5 | 9.442300(90) | 9.4423(13) | 721623±1126±9404 | 0.775 | Line intensities relative to L3-M5 transition | | | |
| L3-N4,5 | 11.25108(13) | 11.2334(24) | 214790±4386±9146 | 0.625 | 0.240(12) | 0.2054 | 0.0218 | 0.2407 |
| L3-M4 | 9.36238(54) | 9.3620(13) | 105955±803±1757 | 0.800 | 0.1515(34) | 0.1134 | 0.1137 | 0.1116 |
| L3-M1 | 8.26739(44) | 8.2683(18) | 29160±179±385 | 1 | 0.0521(10) | 0.0552 | 0.0553 | 0.0515 |
| L3-O4,5 | 11.55781(33) | | 12524±232±197 | 0.772 | 0.01727(48) | 0.0156 | 0.0189 | |
| L2-M4 | 11.06446(13) | 11.0705(14) | 707908±1122±9157 | 0.645 | Line intensities relative to L2-M4 transition | | | |
| L2-N4 | 12.93185(25) | 12.9420(25) | 103216±335±1443 | 0.958 | 0.2166(42) | 0.1952 | 0.2070 | 0.1993 |
| L2-M1 | 9.97190(76) | 9.9768(24) | 18288±154±298 | 0.728 | 0.0292(11) | 0.0270 | 0.0274 | 0.0222 |
| L2-N1 | 12.53135(63) | 12.5496(34) | 3957±123±82 | 0.974 | 0.00844(46) | 0.0068 | 0.0070 | |
| L1-M3 | 11.2312(11) | 11.2344(30) | 100475±4837±9251 | 0.611 | Line intensities relative to L1-M3 transition | | | |
| L1-O2,3 | 13.8161(32) | | 5475±81±192 | 1.122 | 0.100(11) | 0.0830 | 0.0863 | |

Table 5-9: Gold

| Transition | Energy (this work, keV) | Energy (NIST, keV) | Line intensity (counts) | Absorption correction | Intensity ratio (this work) | Intensity ratio (DHS) | Intensity ratio (DF) | Intensity ratio (Elam) |
|---|---|---|---|---|---|---|---|---|
| L3-M5 | 9.714482(40) | 9.7133(12) | 873098±1169±14965 | 0.795 | Line intensities relative to L3-M5 transition | | | |
| L3-N4,5 | 11.58475(26) | 11.58212(57) | 236400±3277±7590 | 0.668 | 0.2277(89) | 0.2089 | 0.2198 | 0.2430 |
| L3-M4 | 9.62569(78) | 9.6281(13) | 85309±756±2280 | 0.806 | 0.0991(32) | 0.1134 | 0.1138 | 0.1116 |
| L3-M1 | 8.50177(42) | 8.4943(18) | 35784±197±695 | 1 | 0.0516(14) | 0.0560 | 0.0562 | 0.0525 |
| L3-O4,5 | 11.9116(10) | | 18999±303±492 | 0.753 | 0.02063(72) | 0.0185 | 0.0222 | |
| L3-N1 | 11.15640(90) | 11.1564(33) | 17925±836±1658 | 0.681 | 0.0176(19) | 0.0137 | 0.0139 | 0.0146 |
| L2-M4 | 11.43529(12) | 11.4420(14) | 789326±1155±13544 | 0.671 | Line intensities relative to L2-M4 transition | | | |
| L2-N4 | 13.36391(15) | 13.3779(26) | 113823±348±1967 | 1.004 | 0.2159(53) | 0.1974 | 0.2089 | 0.2018 |
| L2-M1 | 10.30396(70) | 10.3082(26) | 20042±156±388 | 0.856 | 0.03241(88) | 0.0270 | 0.0275 | 0.0224 |
| L2-N1 | 12.9560(18) | 12.9703(35) | 5045±84±103 | 1.029 | 0.00980(31) | 0.0069 | 0.0071 | |
| L2-M3 | 10.99 00(10) | 10.9900(21) | 2163±125±369 | 0.695 | 0.00284(51) | 0.0010 | | |
| L1-M3 | 11.6105(16) | 11.6105(32) | 94693±2936±6674 | 0.637 | Line intensities relative to L1-M3 transition | | | |
| L1-M2 | 11.20097(30) | 11.2048(30) | 69755±972±2446 | 0.660 | 0.762(65) | 0.8674 | 0.8631 | 0.7841 |
| L1-O2,3 | 14.27211(40) | | 5436±83±98 | 1.194 | 0.1076(87) | 0.0866 | 0.0901 | |
| L1-M4 | 12.0626(58) | 12.0626(24) | 2610±189±203 | 1.078 | 0.0466(61) | 0.0289 | | |

## 5.6 Relative Line Intensity Discussion

The line intensities reported in tables 5.2-5.9 show varying degrees of errors, which is to be expected due to the complex nature of L-shell spectra shown in figures 5.4-5.13. In each spectrum there are areas with many overlapping lines that can be difficult to separate, directly resulting in large uncertainties on the measured line intensities. The following section discusses which specific factors most contribute to the uncertainties.

### 5.6.1 Systematic Errors

The results show that for most lines the total error is dominated by the systematic component; consequently, it is useful to look at the importance of different components of the systematic error. To explore this, a fitting scenario was set up where the systematic error was recalculated taking into account variations of the different universal parameters one-by-one. It was found that varying the line positions, $x_{0,i}$, made the greatest contribution to the systematic error. This is not unexpected, as the complicated L-shell spectra have many lines that sit at very similar energies; in these cases, if the line positions shift even a fraction of an eV, a significant transfer of counts can occur from one line to the other during the fitting process. Changes in the distribution of counts between the lines result in large systematic errors.

The uncertainty in each peak's position is calculated by determining how much the peak energy can be changed to cause the overall fit $\chi^2$ to increase by one unit. This method calculates each peak position error separately, ignoring any covariance between the variables.

Large systematic errors are particularly problematic when the brightest line in one of the L-subshell groups is affected. As the line intensity ratios are represented as a ratio to the brightest line each L-subshell, a large error on the brightest line will propagate through to all the ratios in that same L-subshell, even if the errors on the other measured lines are small.

Table 5-10 shows the proximity of the L1-M3 lines to L3-N5 and L3-N1 lines and Table 5-11 shows the proximity of the L2-M4 line to the L3-N1 line. The L1-M3 and L2-M4 lines are the brightest lines in the L1 and L2-subshells, respectively.

The most problematic case is the measurement of the erbium L1-M3 line, where the systematic error is as large as the actual measurement, so that no meaningful results can be determined from this measurement. The Erbium L1-M3 line is particularly close to the L3-N1 line, only separated by 33 eV, and the L3-N1 line is also close to the intense L2-M4 line. The high intensity of the L2-M4 line will cause significant uncertainty in the lower intensity L3-N1 line that will propagate to the neighbouring L1-M3 line. The L1-M3 lines for thulium and ytterbium also have large errors due to close proximity to the L3-N1 lines. As atomic number increases, the L1-M3 and L3-N1 lines are positioned further apart, so the overlap of the L3-N1 line with the intense L2-M4 line has less of an effect on the error of the L1-M3 line.

As the L1-M3 and L3-N5 lines draw closer together with increasing atomic number, the errors on the L1-M3 line again increase. Gold and platinum are the two elements most affected, with relative errors on the L1-M3 lines of 10.4% and 7.1%, respectively.

Large errors of 9.1%, 13.9% and 16.5% are reported for the L2-M4 line for ytterbium, hafnium, and tantalum, respectively. These elements have very close L2-M4 and L3-N1 lines, as shown in Table 5-11; the two lines are only 3.5 eV apart in the hafnium spectrum. Such close proximity lines lead to large systematic errors.

Table 5-10: Energy separation of the L1-M3 line and nearby L3-N5 and L3-N1 lines, and the corresponding error on the fitted area of the L1-M3 peak.

| Atomic number | Energy difference E(L1-M3)-E(L3-N5) (eV) | Energy difference E(L1-M3)-E(L3-N1) (eV) | Relative error on L1-M3 line (%) |
|---|---|---|---|
| 68 | -241.8 | 33.5 | 100 |
| 69 | -237.3 | 51.1 | 15 |
| 70 | -219.5 | 78.0 | 14 |
| 72 | -182.6 | 140.2 | 2.8 |
| 73 | -164.2 | 170.9 | 3.7 |
| 74 | -143.4 | 206.7 | 4.7 |
| 78 | -19.9 | 390.1 | 10.4 |
| 79 | 25.8 | 454.1 | 7.1 |

Table 5-11: Energy separation of the L2-M4 line and the nearby L3-N1 line, and the corresponding error on the fitted area of the L2-M4 peak.

| Z | Energy difference E(L2-M4)-E(L3-N1) (eV) | Relative error on L2-M4 line (%) |
|---|---|---|
| 68 | -97.2 | 3.0 |
| 69 | -77.4 | 1.7 |
| 70 | -54.6 | 9.1 |
| 72 | -3.5 | 13.9 |
| 73 | 10.6 | 16.5 |
| 74 | 58.9 | 3.3 |
| 78 | 222.4 | 1.3 |
| 79 | 280.1 | 1.7 |

### 5.6.2 Comparison with DHS and DF data

Figure 5-14 plots the measured variation in intensity ratio for selected lines as a function of atomic number, and compares the measured results with predictions from the DHS and DF theoretical calculations and the Elam database. The measured ratios are shown as points with error bars, the DHS data and DF data as solid and dashed lines respectively, and the Elam data is shown using plus-symbol ('+') markers.

The L2-N1/L2-M4, L2-N4/L2-M4, and L3-N4,5/L3-M5 measured ratios are all significantly higher than the DHS, DF and Elam data for almost all elements. All three ratios also show a trend of decreasing value with atomic number, which in all three cases is opposite to the trend predicted by the DHS, DF and Elam values. In the L2-N1/L2-M4 and L2-N4/L2-M4 cases the trend is not strong and is also complicated by large errors on the hafnium and tantalum measurements. For the L3-N4,5/L3-M5 case, the measured data values have small errors and the trend is very apparent.

The L2-M1/L2-M4 and L1-M2/L1-M3 measured ratios are slightly higher than the predicted DHS and DF ratios, and significantly higher than the Elam data for most elements measured; however no clear trend with atomic number is observed in either case. The L1-O2,O3/L1-M3 measured ratios increase with atomic number, agreeing

with the DHS and DF data trends, but sit at a slightly higher intensity than that predicted.

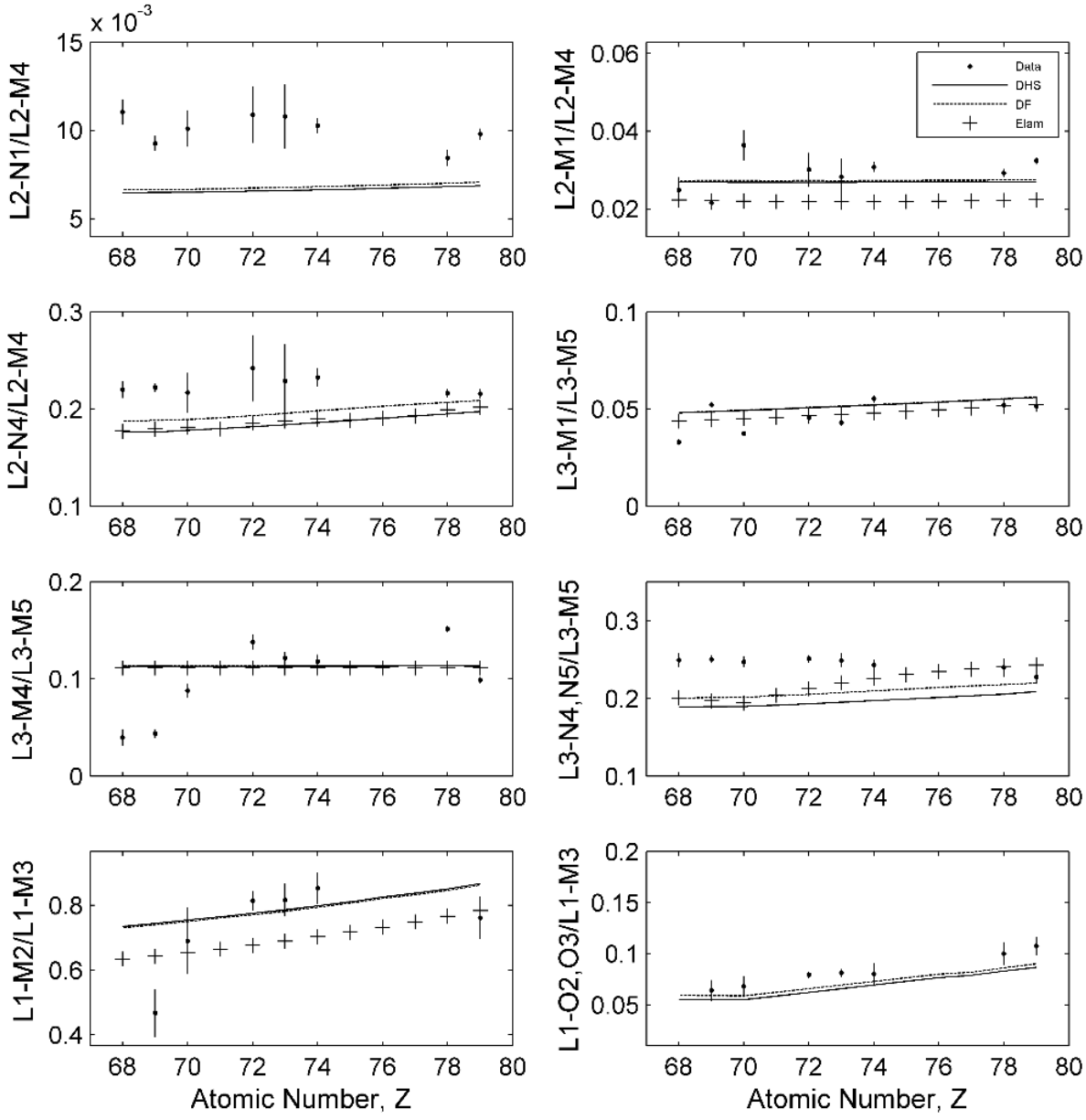


Figure 5-14: Line intensity ratios plotted against atomic number for 8 different selected line pairs. Measured ratios are shown as points; error bars denote the total calculated error. Results from DF [73], DHS [11] and Elam [75] are shown for comparison.

The L3-M1/L3-M5 and L3-M4/L3-M5 ratios can be measured with high accuracy due to an absence of closely neighbouring or overlapping peaks. Both ratios show significant variations with atomic number, which are is significant disagreement with the smooth DHS, DF and Elam data trends.

### 5.6.3 Comparison Between Metals and Metallic Oxides

Both elemental and oxide forms of tantalum and tungsten were measured and analysed to separately determine the X-ray line intensities. Table 5-6 and Table 5-7 include information on the measured intensity ratios for both chemical forms. For the majority of the measured relative line intensities, only a small variation is observed. The variation in intensity ration is generally 10% or less and most ratios are consistent within the calculated errors. However, for both Ta and W, there are a few outliers between the two measured chemical forms.

The $WO_3$ L3-M1/L3-M5 and L1-N2/L1-M3 intensity ratios are smaller than the metal form by 20±5.4% and 24±13% respectively. The L3-M4/L3-M5 line intensity is larger than the metal form by 18 ±7.2%. The tungsten foil spectrum was particularly challenging to fit as the spectrum was measured from impure tungsten metal that showed strong lines from iron, copper, nickel and lead. While every effort was made to fit the impurity fluorescent lines, it is possible that there are further impurities in the spectrum that have not been accounted for, and that these are affecting the line intensity measurements.

The $Ta_2O_5$ L2-M1/L2-M4 and L1-O2,3/L1-M3 intensity ratios are greater by 30±14% and 23±10% respectively compared to the metal form. Figure 5-15 plots the tantalum metal spectrum vs the tantalum oxide spectrum, with each spectrum normalised to the highest count. The two spectra visually agree for all lines except the L2-M1 line at 8.4 keV. The reason why only the L2-M1 line shows a large difference in intensity between the two chemical forms is unknown. Error bars are not included in Figure 5-15 so that the difference in the intensity of the two spectra at 8.4 keV can be more clearly seen.

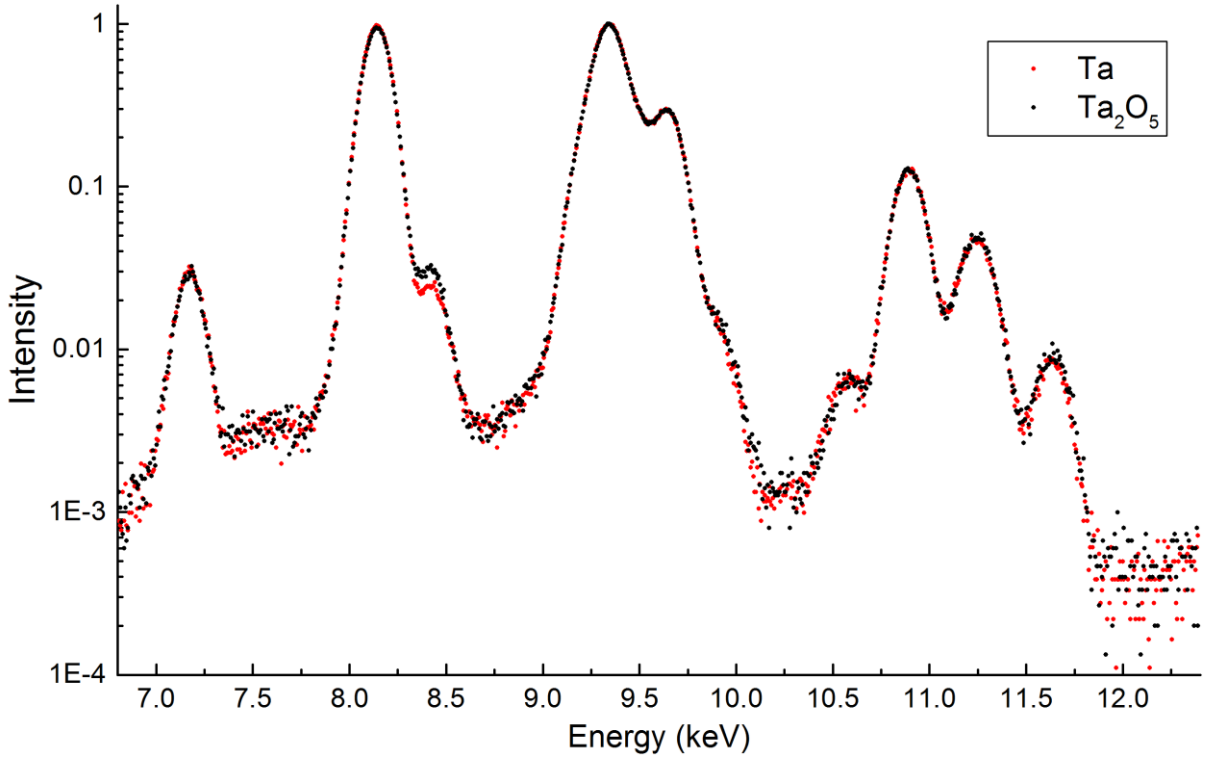


Figure 5-15: the measured tantalum and tantalum oxide spectra, both normalised to the highest count in each spectra.

### 5.6.4 Tantalum Line Energy Positions

The tantalum experimental spectrum showed a large number of lines exhibiting significant disagreement with the tabulated NIST theoretical energies. Figure 5-16 shows the poor fit that is achieved when the tantalum spectrum is fit with the NIST theoretical line energies. Peaks can be seen to sit out of place and the reduced $\chi^2$ increased to 39.9, from 1.46 when being fit with the measured line energies. The tantalum oxide spectrum also fitted poorly with the NIST line energy theoretical values (reduced $\chi^2$ = 31.93) so the experimental values of this study were used and a much better fit was achieved (reduced $\chi^2$ = 1.28). Both the tantalum and tantalum oxide experimental spectra agree well with the NIST experimental data over the NIST theoretical data, suggesting that it is not an issue of faulty measurements but maybe an issue of the calculation of the theoretical values for tantalum.

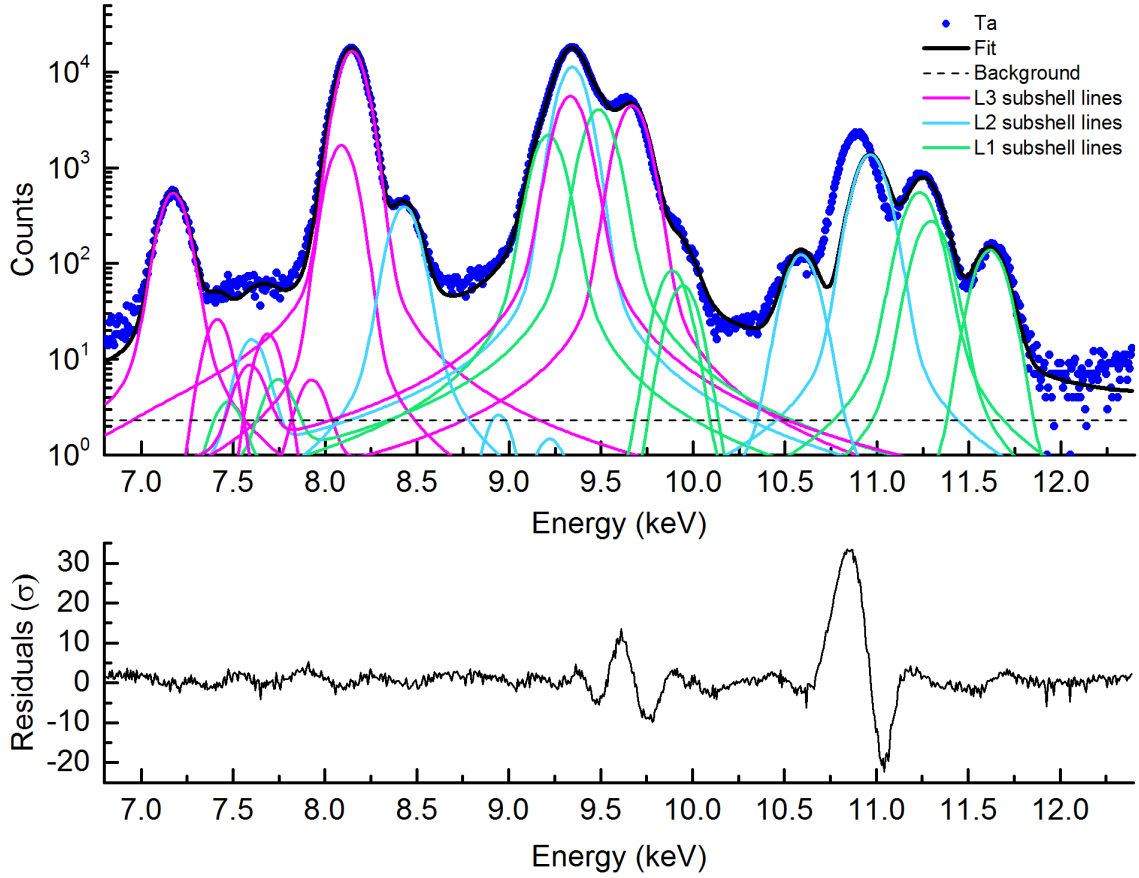


Figure 5-16: the tantalum spectra fitted with the NIST theoretical line energy positions, $\chi^2 = 39.9$.

The worst case was found to be the L2-N4 line, which was measured to be 70 eV lower than the NIST theoretical energy. The NIST database includes a selection of experimental values and in the tantalum case, the NIST experimental and theoretical line energies show similarly large differences.

Table 5-12 compares the experimentally determined line energies to the NIST theoretical and experimental values; much better agreement with the NIST experimental values is found.

Table 5-13 compares the NIST theoretical, NIST experimental and measured line energies in more detail. Large discrepancies between theoretical and experimentally measured values are observed for seven of the L-shell lines: L3N1, L3N5, L3N4, L2N1, L2N4, L1N2 and L1N3. The discrepancies occur from lines of all three L-subshells, but are limited to transitions involving the N-shell.

Table 5-12**:** A comparisons of the Tantalum line positions from the NIST Theoretical data, NIST experimental data and experimentally measured in this study.

| Line | NIST Theoretical Energy (eV) | Error (eV) | NIST Experimental Energy (eV) | Error (eV) | Experimental Measured Energy (eV) | Error (eV) |
|---|---|---|---|---|---|---|
| L3M1 | 7174.4 | 1.7 | 7173.2 | 0.31 | 7174.4 | 0.47 |
| L3M2 | 7413.8 | 1.7 | 7412.13 | 0.35 | 7413.8 | 2.6 |
| L3M4 | 8088.2 | 1.2 | 8087.93 | 0.16 | 8088.2 | 1.69 |
| L3M5 | 8146.5 | 1.2 | 8146.17 | 0.16 | 8148.2 | 0.04 |
| L2M1 | 8429.6 | 2.4 | 8428.09 | 0.42 | 8429.6 | 0.46 |
| L2M3 | 8943.4 | 1.9 | 8941.76 | 0.54 | 8943.4 | 3.05 |
| L1M2 | 9212.6 | 2.7 | 9212.47 | 0.3 | 9216.9 | 0.79 |
| L3N1 | 9332.8 | 3.1 | 9315.4 | 0.83 | 9315 | 17.23 |
| L2M4 | 9343.4 | 1.3 | 9343.19 | 0.31 | 9343.4 | 1.13 |
| L1M3 | 9487.1 | 2.8 | 9487.62 | 0.32 | 9487.1 | 0.3 |
| L3N5 | 9668.78 | 0.56 | 9651.89 | 0.22 | 9650 | 0.09 |
| L3N4 | 9708.2 | 1.6 | 9639.5 | 0.55 | 9655.5 | 0.74 |
| L1M4 | 9887 | 2.3 | 9889.3 | 2.3 | 9884.7 | 13.7 |
| L1M5 | 9945.3 | 2.2 | 9945.6 | 2.4 | 9937.3 | 3.85 |
| L2N1 | 10588 | 3.2 | 10570.6 | 1.3 | 10565 | 4.12 |
| L2N4 | 10963.4 | 1.7 | 10895.33 | 0.43 | 10893 | 0.47 |
| L1N2 | 11231.7 | 4.2 | 11217.1 | 1.5 | 11217 | 2.3 |
| L1N3 | 11294.2 | 1.9 | 11277.68 | 0.61 | 11276 | 1 |

Table 5-13**:** shows the difference in eV between the NIST theoretical values and the NIST experimental values; the NIST theoretical values and the measured values; and the NIST experimental values and the measured values of the tantalum line energy positions.

| Line | (NIST Theoretical Energy) – (NIST Experimental Energy) (eV) | (NIST Theoretical Energy) – (Experimental Measured Energy) (eV) | (NIST experimental Energy) – (Experimental Measured Energy) (eV) |
|---|---|---|---|
| L3M1 | 1.2 | 0 | -1.2 |
| L3M2 | 1.67 | 0 | -1.67 |
| L3M4 | 0.27 | 0 | -0.27 |
| L3M5 | 0.33 | -1.7 | -2.03 |
| L2M1 | 1.51 | 0 | -1.51 |
| L2M3 | 1.64 | 0 | -1.64 |
| L1M2 | 0.13 | -4.3 | -4.43 |
| L3N1 | 17.4 | 17.8 | 0.4 |
| L2M4 | 0.21 | 0 | -0.21 |
| L1M3 | -0.52 | 0 | 0.52 |
| L3N5 | 16.89 | 18.78 | 1.89 |
| L3N4 | 68.7 | 52.7 | -16 |
| L1M4 | -2.3 | 2.3 | 4.6 |
| L1M5 | -0.3 | 8 | 8.3 |
| L2N1 | 17.4 | 23 | 5.6 |
| L2N4 | 68.07 | 70.4 | 2.33 |
| L1N2 | 14.6 | 14.7 | 0.1 |
| L1N3 | 16.52 | 18.2 | 1.68 |

The large deviations between experimental and theoretical values are only found in the tantalum case for the eight elements measured. The discrepancies are unexplained in the NIST database, but they appear to be due to an error in the values used for the N-shell energies.

## 5.7 Relative Total L-subshell Emission Intensities

This section will build on the measurements in section 5.5 and use those measurements to determine the relative total X-ray emission intensity of the L1 and L2-subshells to the L3-subshells for the eight elements measured. The total X-ray emission of the three L-subshells are expressed as the ratios $I_{L1}/I_{L3}$ and $I_{L2}/I_{L3}$ and compared to theoretically calculated values using two different sets of fundamental parameters.

### 5.7.1 Measured Total L-subshell Emission Intensities

For each element, the intensities of up to 15 individual X-ray lines have been determined. These intensities are corrected for absorption, detector efficiency, and for geometry effects using a Monte Carlo method. These measured line intensities can be summed over each L-subshell to determine a value that is closely related to the total X-ray emission intensity for a given L-subshell under the current experimental conditions.

To obtain the total emission of counts from each L-subshell, the area under each individual line needs to be summed across each L-subshell. However, there are up to 43 individual lines in each of the L-subshell spectra measured in this thesis, and not all of these lines can be measured. Fortunately not all the lines in each spectrum need to be measured, as the contribution of many of these lines is so small their area is negligible compared to the high intensity lines. For each L-subshell, the strongest 4-8 lines are responsible for the majority of the L-subshell's X-ray emission intensity. Due to the low intensity of the other lines in each L-subshell it is possible to estimate their intensities using theoretical values and attach large errors to account for the inaccuracies in the theoretical values.

The low intensity lines that could not be fitted using the experimental approach described above had their intensities estimated using their theoretical line intensities. The DHS theoretical values were used as the DHS emission rate data is the most comprehensive dataset and the only one that provides data for all the low intensity lines. However, as the results from the measurements of the relative line intensities within each L-subshell shows cases of significant disagreement with the DHS data, a large arbitrary error of 50% was assigned to the contribution of these weak lines to the

total emission intensity. For each element measured, the sum of these low intensity lines represented less than 1.6%, 0.5% and 3.3% of the total counts for the L3, L2 and L1 subshells, respectively.

The error on the total counts over each L-subshell is calculated as a sum-in-quadrature of the absolute error on each individual lines or line pairs that are added up within each L-subshell. The error on the ratio of the L-subshells is also a sum-in-quadrature of the relative errors on each L-subshell involved in the ratio.

### 5.7.2 Results

The relationships used to calculate the theoretical intensity of the total X-ray emission of each L-subshell arising from vacancies generated via photoexcitation are discussed in detail in section 2.1. To show the dependence of the total X-ray emission of each L-subshell on various fundamental parameters, Equations 2.1 are repeated here:

Equation 2.1

$$I_{L1} = \sigma_{L1}(E)\omega_{L1}$$

$$I_{L2} = (\sigma_{L2}(E) + \sigma_{L2}(E)f_{L1-L2})\omega_{L2}$$

$$I_{L3} = (\sigma_{L1}(E)f_{L1-L3} + \sigma_{L1}(E)f_{L1-L2}f_{L2-L3} + \sigma_{L2}(E)f_{L2-L3} + \sigma_{L3})\omega_{L3}$$

where $I_{L1}$, $I_{L2}$ and $I_{L3}$ are the intensity of X-ray emission from each subshell, given by the total number of vacancies produced in that subshell multiplied by the fluorescence yield. $\sigma_{L1}$, $\sigma_{L2}$ and $\sigma_{L3}$ are the subshell photoionisation cross-sections of the chosen element at incident X-ray energy $E$. $\omega_{L1}$, $\omega_{L2}$ and $\omega_{L3}$ are the total fluorescence yields and $f_{L1\text{-}L2}$, $f_{L1\text{-}L3}$, $f_{L2\text{-}L3}$ are the Coster-Kronig transition probabilities between respective L subshells.

Two different sets of values for the Coster-Kronig probabilities and fluorescence yields are used in the calculations: the Dirac-Hartree-Slater (DHS) values of Chen [45] and the recommended values published by Campbell in his 2003 and 2009 reviews [44], [52].

Campbell's 2003 review discusses the large uncertainties associated with L-shell Coster-Kronig probabilities and fluorescence yields, which for the range of elements studied in this thesis are estimated to be up to 25% for $\omega_{L1}$, 5% for $\omega_{L2}$ and $\omega_{L3}$, 40% for

$f_{L1\text{-}L2}$, 30% for $f_{L1\text{-}L3}$ and 25% for $f_{L2\text{-}L3}$. The 2009 review reassesses the problematic ωL1 fluorescence yield and $f_{L1\text{-}L3}$ and $f_{L1\text{-}L2}$ Coster-Kronig probabilities using new experimental data and recommends a new set of values. The L-subshell total X-ray emission intensity values calculated using the Campbell 2003 review values for $\omega_{L2}$, $\omega_{L3,}$ and $f_{L2\text{-}L3}$ and the Campbell 2006 review values for $\omega_{L1}$, $f_{L1\text{-}L2}$, and $f_{L1\text{-}L3}$ are labelled 'Campbell Rec' in Figure 5-17 and Figure 5-18.

L-subshell photoionisation cross-sections are taken from Scofield [12] and used in the theoretical calculation of both the 'DHS' and 'Campbell rec' sets of L-subshell total X-ray emission intensity values. The uncertainties of these photoionisation cross-sections are estimated to be less than 0.1%.

Figure 5-17 and Figure 5-18 compare the measured results for the total X-ray emission rate ratios $I_{L1}/I_{L3}$ and $I_{L2}/I_{L3}$ to two sets of values calculated using theoretical and semi-theoretical values. The L-subshell total X-ray emission intensity values calculated with the DHS values of Chen are labelled 'DHS' in Figure 5-17 and Figure 5-18.

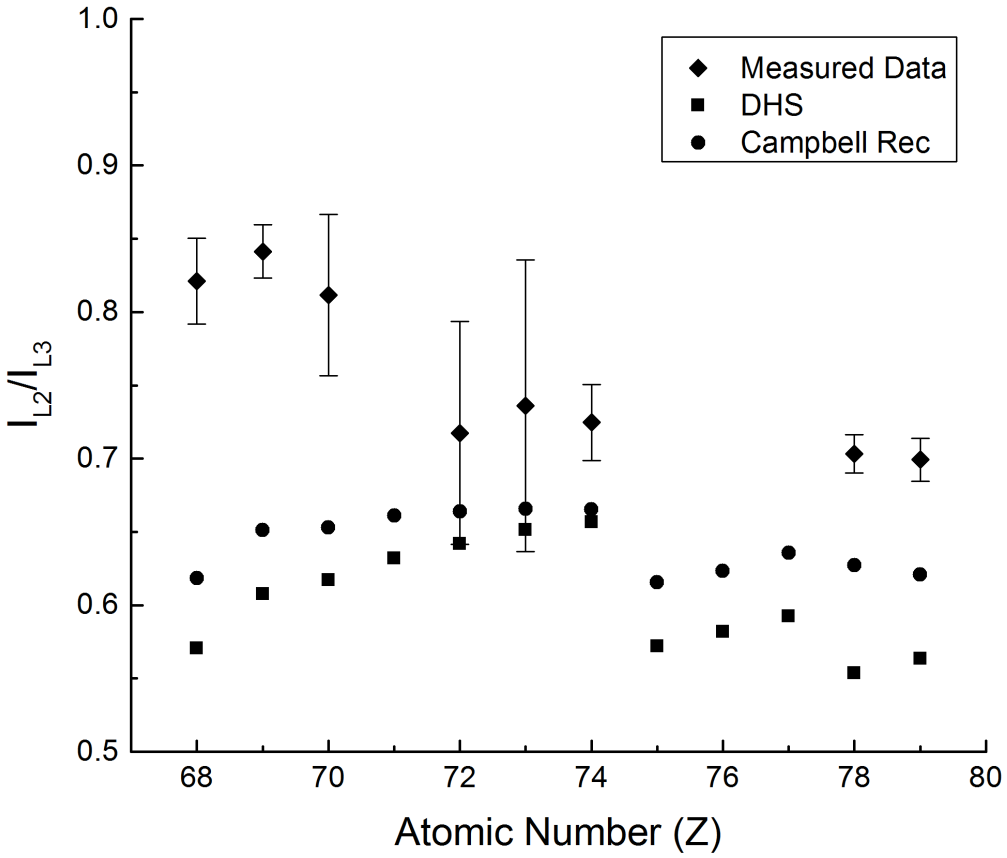


Figure 5-17: measured $I_{L2}/I_{L3}$ ratios (at 17.44 keV) compared to calculated values using fundamental parameters from the EADL database and Campbell's recommended Coster-Kronig and L-shell fluorescence yields.

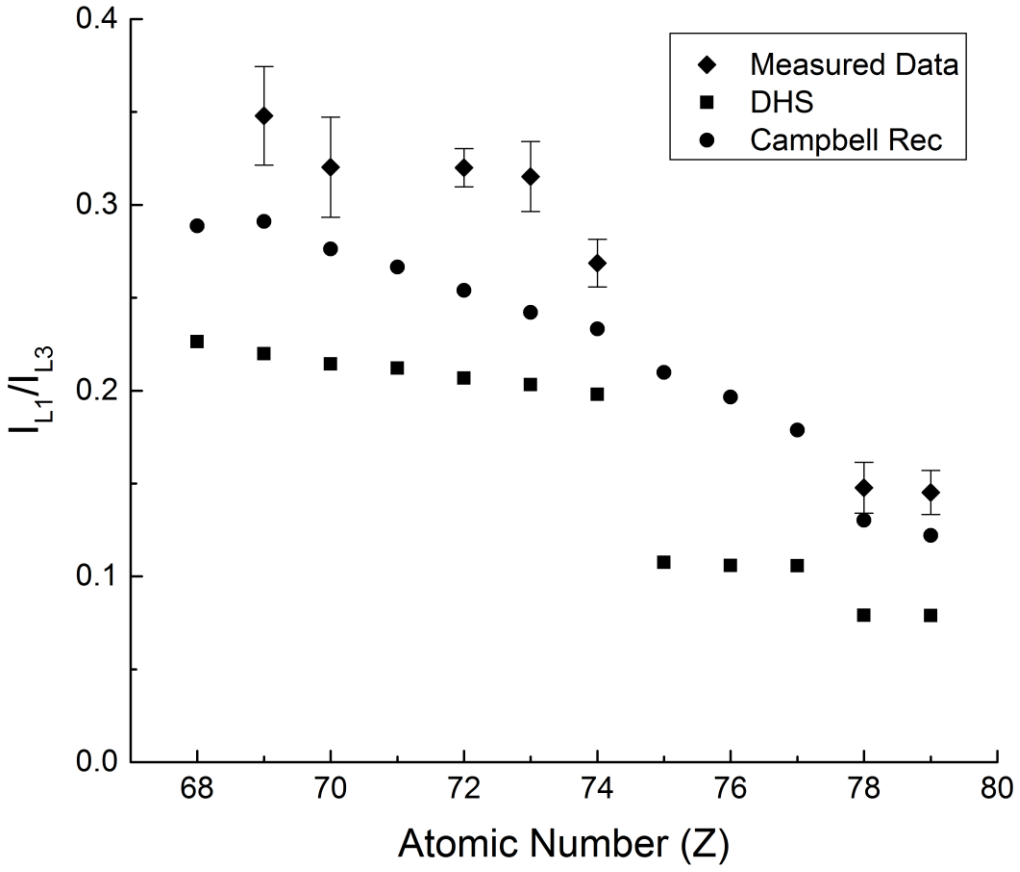


Figure 5-18: measured $I_{L1}/I_{L3}$ ratios (at 17.44 keV) compared to calculated values using fundamental parameters from the EADL database and Campbell's recommended Coster-Kronig and L-shell fluorescence yields.

### 5.7.3 Discussion

The large error on the brightest line in the erbium L1-subshell means that a meaningful value for the $I_{L1}/I_{L3}$ ratio cannot be reported. This error is due to the L1-M3 line, the brightest line in the L1-subshell, being in close proximity to other lines. Both the L1-M3 lines for thulium and ytterbium, and the L2-M4 lines for hafnium and tantalum also have large errors due to close proximity with other lines, further details are provided in section 5.6.1.

The L1-M3 line contributes to around 40 % of the total L1-subshell X-ray emission intensity, therefore the large errors on the L1-M3 line will propagate through to the large errors on the $I_{L1}/I_{L3}$ ratio for thulium and ytterbium. The L2-M4 line contributes around 80 % of the total L2-subshell X-ray emission intensity; consequently the large errors on the L2-M4 lines for hafnium and tantalum contribute to the large errors on the measured the $I_{L2}/I_{L3}$ ratios for those elements.

Figure 5-17 and Figure 5-18 compare our measured values for the $I_{L2}/I_{L3}$ and $I_{L1}/I_{L3}$ ratios to values calculated using the DHS and Campbell recommended values. The measured values agree best with Campbell's recommend values, but there is still a significant discrepancy between measured and the calculated results. The measured values demonstrate a trend where both the $I_{L2}/I_{L3}$ and $I_{L1}/I_{L3}$ ratios decrease with atomic number. The DHS and Campbell recommended calculated values both disagree with this trend for the $I_{L2}/I_{L3}$ ratio, causing significant differences in the $I_{L2}/I_{L3}$ ratio for erbium, thulium and ytterbium. The $I_{L1}/I_{L3}$ measured ratios agree better with the calculated values, and appear to follow a similar trend to the Campbell recommended calculated values.

## 5.8 Impact of Fitting Measured XRF Spectra with Incorrect L-shell Emission Intensities

Fitting experimentally measured XRF spectra with poor theoretical L-shell X-ray emission values can cause poor quality fits. As a direct result, the elemental composition determined from the poorly fitted spectra can include large errors. A novel approach is used to estimate the magnitude of error that is introduced by fitting

experimentally measured XRF spectra with basis functions calculated using poor theoretical values.

In some cases, the measured total L-subshell X-ray emission intensity ratios between L-subshells are almost twice as large as the values calculated using DHS database. The discrepancies in the total X-ray emission ratios between the L-subshells will compound with the discrepancies found for individual L-subshell line intensities (reported in section 5.5), leading to large errors in predicted L-shell X-ray emission spectra for individual elements.

### 5.8.1 Modelling Approach for Estimating Errors

To investigate the influence of fitting complex spectra with poor L-shell X-ray emission values, theoretically calculated L-shell emission spectra, labelled 'basis functions', are used to fit complex experimental XRF spectra. The errors in the determined elemental composition are measured and reported.

The main limitation of this investigation is that only eight different heavy elements were measured and analysed. It would be difficult measure samples that consist only of eight different heavy elements, so instead the impact of fitting with inaccurate line intensities are explored using a simple modelling approach. Simulated 'experimental' spectra were constructed using the measured values of L-subshell total emission intensity ratios and the relative line intensities from within each subshell. The modelled experimental spectra are not intended to represent realistic mineral samples; however it is common for mineral samples to contain multiple heavy elements with overlapping L-shell lines. For example, gold and tungsten can often occur in the same ore. So while the modelled materials are not particularly realistic, the errors reported should provide an indication of the magnitude of errors that can arise from fitting experimental spectra with inaccurate L-shell emission intensity values.

Multi-element spectra are modelled by combining spectra from individual elements in proportion to the desired elemental composition. Suites of 3 and 4 elements were chosen at random from the 8 elements measured. The first suite of elements contained gold, tungsten and tantalum. The second suite contained thulium, tungsten,

tantalum and ytterbium. For each suite of elements, 500 different compositions were randomly generated. Sample absorption and detector efficiency effect corrections are included in each of the 500 spectra, to accurately predict the experimental spectrum that would be measured using incident 17.4 keV X-rays as the exciting source.

The modelled 'experimental' spectra of known concentration were fitted using the basis functions for each element present. Three sets of basis functions were used for each element, differing in the relative total X-ray emission rates of the L1, L2 and L3 subshells. The first set, based on theoretical data, calculated the relative total X-ray emission rate of each L-subshell using fluorescent yields and Coster-Kronig probabilities taken from the DHS values. The second used the recommended values for fluorescent yields and Coster-Kronig probabilities taken from the two Campbell review papers, which are a combination of theoretical and experimental data. Both the first and second set of basis functions calculated the relative total X-ray emission rate of each L-subshell using equations 2.1 and Scofield's [12] photoionisation cross-sections values. The third set of basis used the experimentally measured values for the total relative L-subshell intensities. All three sets of basis functions used relative line intensities within each L-subshell taken from the DHS calculations used in the EADL database.

For each of the 500 sample spectra in the two element suites, three different fits were performed using the three sets of element basis functions. The errors on the fits were calculated as the difference between the known compositions and the fitted compositions for the 500 sample spectra. For each suite of elements, the root mean square average of the relative error on each element across the 500 spectra was calculated. If the error on the concentration of an element from a fitted spectrum is more than two standard deviations from the root mean square error on the concentration of that element across the 500 spectra, then that particular measured error is considered an outlier and excluded from a further calculation of the root mean square error.

### 5.8.2 Results and Discussion

The results are presented in Table 5-14 and Table 5-15.

Table 5-14: The root mean square errors on the determined elemental compositions for 500 randomly generated compositions of Ta, W and Au. The randomly generated XRF spectra, created from the measured data, were fitted with DHS data and the Campbell recommended data.

| | Fit error % (DHS values) | Fit error % (Campbell values) | Fit error % (Exp. Values) |
|---|---|---|---|
| Ta | 3.3 | 2.5 | 0.64 |
| W | 12 | 8.3 | 2.8 |
| Au | 31 | 4.7 | 2.0 |

Table 5-15: The root mean square errors on the determined elemental compositions for 500 randomly generated compositions of Yb, Tm, Hf and W. The randomly generated XRF spectra, created from our measured data, were fitted with DHS data and the Campbell recommended data.

| | Fit error % (DHS values) | Fit error % (Campbell values) | Fit error % (Exp. Values) |
|---|---|---|---|
| Yb | 26 | 8.3 | 3.8 |
| Tm | 6.7 | 3.4 | 5.5 |
| Hf | 6.1 | 5.3 | 2.0 |
| W | 52 | 29 | 8.0 |

Fits conducted using the DHS values poorly agree with the measured data, as is reflected in the large errors shown in Table 5-14 and Table 5-15, up to 31% for gold in the three element suite and up to 52% for tungsten in the four element suite.

The L-subshell X-ray emission intensity ratios calculated using the Campbell recommended values are closer to the measured values than those calculated with the

DHS data. So it is not unexpected that the modelled experimental data fitted with the Campbell recommended values show smaller errors than the DHS error values. Fits carried out using the 'correct' experimentally determined values for the total X-ray emission from each subshell show significantly better agreement. The agreement is not perfect, as all fits are performed using the individual line intensities within each shell from the DHS data, rather than the experimentally measured values used to generate the simulated spectra.

### 5.8.3 Error Propagation

There are two main factors that affect the error on a sample in relation to fitting with poor line intensities. The first is the number of elements in the sample with overlapping lines, and the severity of the overlap. Depending on the severity of the overlap, lines can be indistinguishable to the fitting script. The second factor is the concentration of the different elements present. If one element has a particularly low concentration and has lines overlapping with an element of high concentration, even small errors in the description of the basis function of the high concentration element will lead to large errors in the determined concentration of the lower concentration element.

A modelled experimental spectrum was created with equal concentrations of W, Au and Ta; so that when this spectrum is fitted, large variations in concentration do not affect the determination of the elemental composition. In this case, the main factor increasing the error from fitting with incorrect DHS L-shell X-ray emission values is the overlapping peaks between the elements.

Figure 5-19 shows a modelled 'experimental' spectrum with a composition of 33% W, 33% Au and 33% Ta, the fitted DHS basis functions for each element and the sum of those fitted DHS basis functions of the total fit. The elemental composition determined from the fitted DHS basis functions is 30% W, 36% Au and 34% Ta, which is close to the modelled composition. The main difference in composition was between tungsten and gold which would be due to the overlap of the gold Lα and tungsten Lβ lines. When the concentrations of the elements are allowed to vary, the results in Table 5-14 show that

errors on the tungsten and especially the gold measurements become significantly large.

Figure 5-19 is similar to Figure 5-20, but the shows the four element case modelled spectrum with a composition of 25% W, 25% Yb, 25% Tm and 25% Hf, as well as the fitted DHS basis functions for each element and the sum of those fitted DHS basis functions to give the total fit. In the more complicated four element case, the elemental composition determined from the fitted DHS basis functions is further from the modelled composition: 27% W, 20% Yb, 36% Tm and 17% Hf. From Figure 5-20, it can be seen that tungsten and ytterbium have the most overlapping peaks; however it is thulium and hafnium that deviate most from the modelled composition. Table 5-15 shows the largest root mean square errors for tungsten and ytterbium, which is most likely due to their overlapping lines.

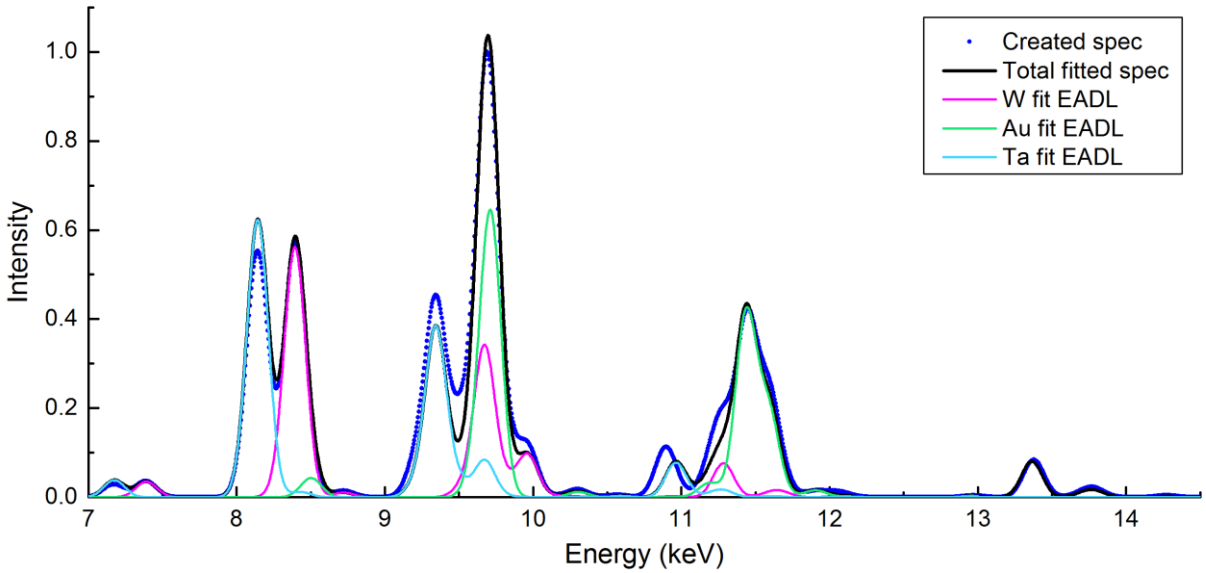


Figure 5-19: The modelled 'experimental' spectrum with a composition of 33% W, 33% Au and 33% Ta, shown with blue data points. The individual element contributions, fitted with the DHS values, are shown as solid coloured lines. The total fit is shown as a black solid line.

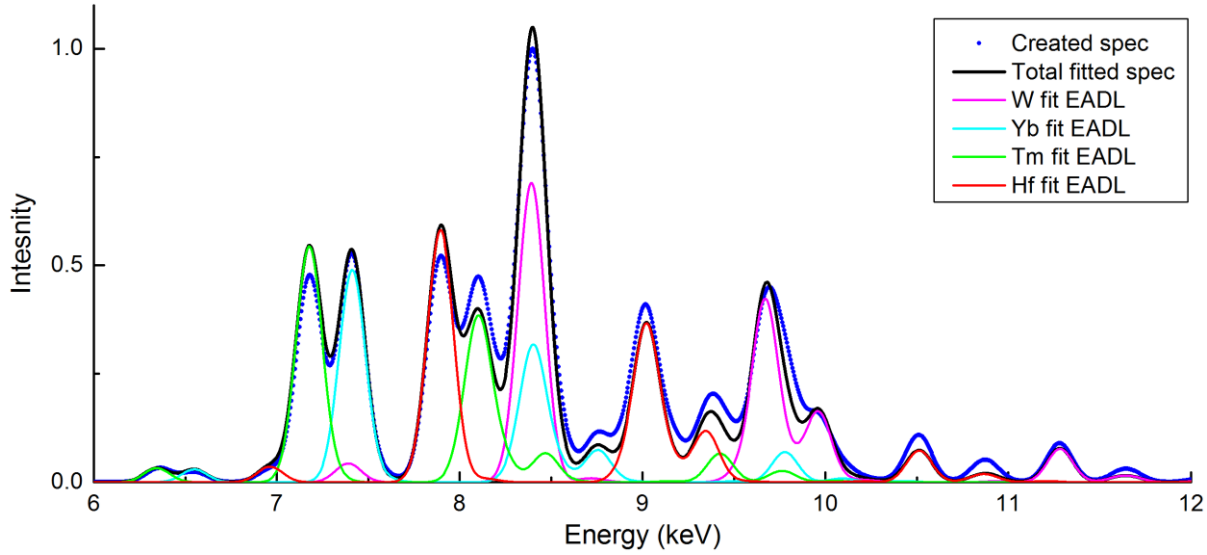


Figure 5-20: The modelled 'experimental' spectrum with a composition of 25% W, 25% Yb, 25% Tm and 25% Hf, shown with blue data points. The individual element contributions, fitted with the DHS values, are shown as solid coloured lines. The total fit is shown as a black solid line.

### 5.8.4 Impact of Relative Total L-shell Emission Intensity vs Individual Line Intensities

Fits carried out using the 'correct' experimentally determined values for the total X-ray emission from each subshell and the DHS individual line intensities are shown in the fourth column of Table 5-14 and Table 5-15. This third set of basis functions was included to show the error introduced by fitting with the incorrect individual line intensities from within each L-subshell. As the modelled experimental basis functions are created with the experimentally measured total L-subshell X-ray emission intensity ratios, and the same values are used in the third set of basis functions, the only factor contributing to the errors are the DHS individual line intensities from within each shell. These fits show significantly lower root mean square errors than the fits carried out with the DHS and Campbell values. The lower errors suggest that only a small component of the errors from the DHS and Campbell basis functions fits arise from the use of the incorrect individual line intensities from within each L-subshell. These results indicate that the ratios of total X-ray emission between different L-subshells have a stronger influence on the errors arising in fitting of complex X-ray spectra.

**PART 3: THE PARTICLE SIZE EFFECT**

X-ray fluorescence is a technique that is commonly used in the field to perform real-time, in-situ analysis of unprepared materials. For heterogeneous materials such as crushed ore or soil, the intensity of the characteristic fluorescent radiation from different mineral phases is affected by the particle size of the sample being measured. The relationship between fluorescence intensity and particle size is known as the 'particle size effect', and it can lead to substantial errors in XRF analysis if ignored.

The particle size effect is well documented in the literature, with theoretical models predicting the relationship between the intensity of characteristic fluorescent radiation and particle size in powdered samples dating back to the 1960s. Despite this, the particle size effect is usually ignored when using XRF analysis to measure particulate samples, as there is currently no documented solution to correct fluorescence intensity measurements for this effect. The quality of existing experimental data and the limitations of simple theoretical models have both prevented the development of a viable particle size effect correction method.

The particle size effect is difficult to measure, and particle size measurements available in literature all have large uncertainties. It is challenging to prepare samples with different particle sizes of powdered materials and to guarantee that the fluorescent particles are evenly dispersed throughout the overall matrix. There are also limited methods for separating powders into different particle size fractions. The most common method, sieving, introduces large uncertainties in the particle size distribution of the resulting material.

The lack of good quality experimental data in the literature has also limited the verification of the available theoretical models. These models often make significant simplifying assumptions that can lead to large inaccuracies. Further details of some of the existing theoretical models are given in section 3.2.

The particle size effect is a function of the exiting X-ray radiation energy, and it was first suggested in the 1960s that measurements using multiple exciting radiation energies could be used to correct for the particle size effect [90]. However, with a lack of good quality experimental data and with limited theoretical models to use to

develop this correction, the idea of correcting for the particle size effect in practical XRF applications has stagnated.

The following chapters report measurements of the particle size effect for certain elements, and develop a particle size correction method that can be used in practical XRF measurements of particulate samples. This work includes improved experimental measurements, the use of Monte Carlo simulations to predict the particle size effects, and the testing of a novel correction method.

# 6 Experimental Method for Measuring the Particle Size Effect

## 6.1 Sample Preparation

Particle size effect measurements require materials in powdered form with a large range of particle sizes. Elements in the Z range of 20 to 35 were considered, as excitation of K-shell lines from these elements can be conveniently achieved using an available molybdenum-target X-ray tube. Further it was necessary that the selected elements would be safe to work with and available in convenient powdered form, which ruled out many elements such as arsenic and bromine. The final requirement was that it should be possible to buy powdered forms of these elements with different particle sizes to conduct the tests. Of the elements considered, only iron, copper, nickel and manganese powders (the latter two in oxide form) met the criteria. The details of each powder are presented in Table 6-1.

Table 6-1: List of powders and their details used in this chapter.

| Powder | Source | Product number | Purity (%) | Particle size range, mesh | Particle size range, µm |
|---|---|---|---|---|---|
| Iron | Sigma-Aldrich | 209309-500G | 97 | -325 | <44 |
| Nickel (II) Oxide, green | Sigma-Aldrich | 399523-100G | 99 | -325 | <44 |
| Manganese (IV) Oxide | Sigma-Aldrich | 243442-100G | >99 | 60-230 | 63-250 |
| Manganese(IV) Oxide | Alfa Aesar | 42250 | 99.9 | -325 | <44 |
| Copper | Sigma-Aldrich | 207780-500G | 99 | -200 | <74 |
| Copper | M&B | | 99 | | |

### 6.1.1 Powder Sizing

The selected powders contained particles with a large size range, necessitating separation into different size fractions. The powders were sized using two different methods depending on the desired particle size. The iron and nickel oxide powders

with particle sizes below 44 µm could only be sized using a cyclosizing method, described below. The powders with unspecified particle size and those with diameters above approximately 40 µm were first sized using sieves.

#### 6.1.1.1 Sieving

Sieving was conducted using six different 12-inch (300 mm) diameter stainless steel sieves arranged in a sieve stack. The clear apertures of the sieves were 45, 53, 63, 75, 90 and 106 µm, arranged with the 106 µm sieve on top, and with each sieve in the stack reducing in aperture size. A pan sits at the bottom of the sieve stack to collect the particles below 45 µm.

Sieving is known for being an inaccurate technique, as it is a statistical operation it is difficult to obtain identical results even when sieving identical samples using the same procedure. For the best sieving results, the load being sieved at a time should be minimised so that every particle can have unhindered access to the sieve surface.

When sieving, there is a general rule that the most powder that should be sieved at a time is a layer at most 2 particles thick across the sieve, assuming that the size of the particles are only slightly smaller than the aperture size of the sieve [116]. For smaller aperture sieves, the amount of powder that satisfies this condition will be less than the amount of powder that can be sieved by a larger aperture sieve. Consequently, when sieving powders of unknown particle size it is best to only sieve a small amount of powder at once, or too much powder could reach the smaller aperture sieves. For this reason, a maximum of 30 grams of powder was added at a time to the six-sieve stack.

The M&B copper powder was the only powder that had a range of particle sizes above 40 µm to make it suitable for the sieving technique. The longer a sample is sieved for the more likely it is for a particle to fall through the aperture, so30 grams of the powder was sieved at a time in a sieve shaker for 15 minutes. The powder in each sieve was collected and labelled.

To determine the accuracy of the sieving method, a sample of powder for each size fraction sieved was analysed to determine particle size using laser diffraction.

#### 6.1.1.2 Cyclosizing

The particles that passed through the 40 µm sieve were cyclosized using a Warman cyclosizer, illustrated in Figure 6-1.

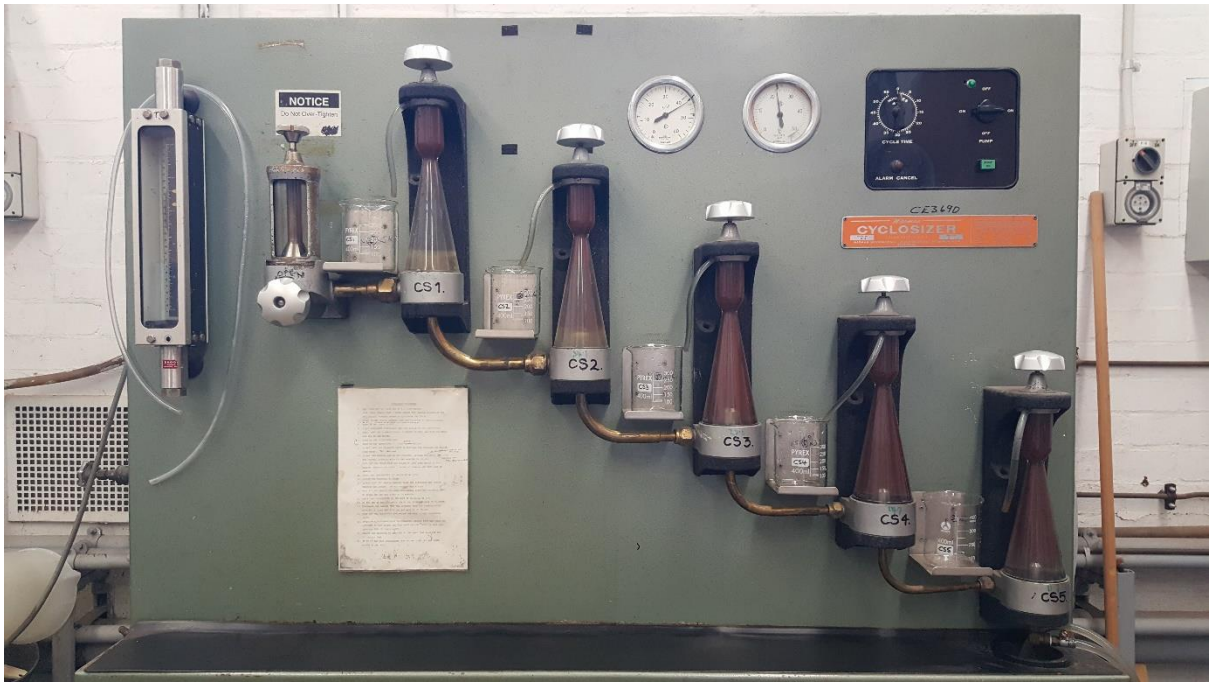


Figure 6-1: The cyclosizer used to sort the smaller-sized particles into 5 different size fractions.

The procedure for cyclosizing is as follows. The sample is transferred from a beaker to the cyclosizer sample container and a wash bottle is used to ensure that all the sample material is transferred. The sample container is then filled with clean water until the level of water sits above a tapered valve on the sample container. The valve is screwed closed so that the sample and water is sealed within the sample container and all air is eliminated. The sample container is locked in place on the cyclosizer. A schematic diagram of the cyclosizer reproduced from the cyclosizer manual [117] is shown in Figure 6-2, with the main control valve and apex values labelled in blue.

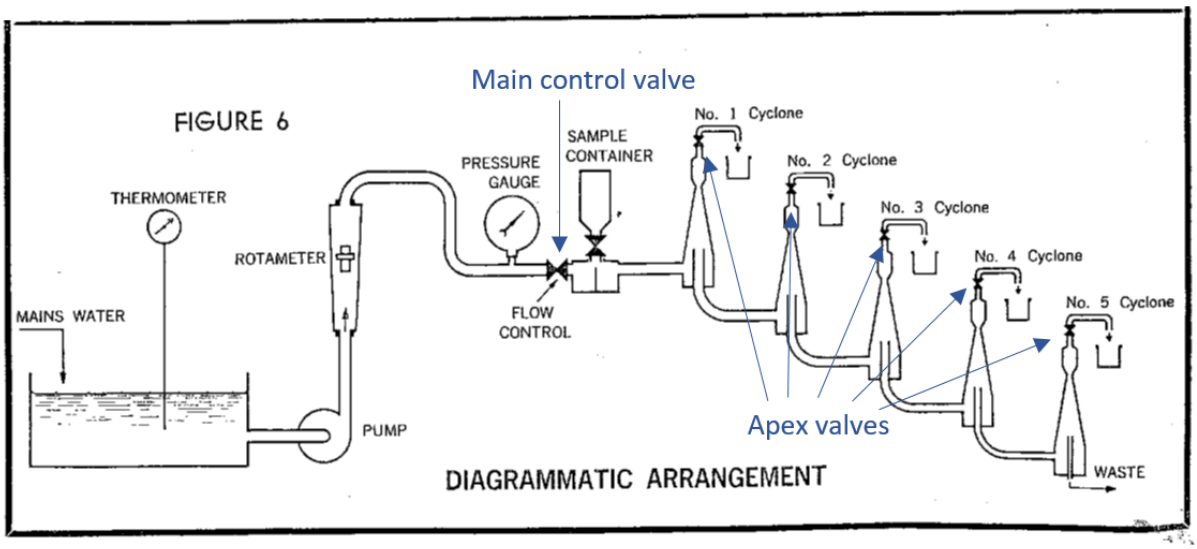


Figure 6-2: a schematic diagram of the cyclosizer reproduced from the manual [117], with the labels of the main control valve and apex valves, shown in blue, added in.

The cyclosizer was turned on and the water supply switched on with a flow rate of 12.5 L/min. The main control valve was opened slowly to allow any air bubbles to be expelled from the cyclosizer pipework. Starting from the No. 1 cyclone, air bubbles are bled by opening the apex valves one at a time. With the control valve completely open, the sample container valve is opened very slowly, to allow the sample to flow into the cyclones.

Once the sample has been completely discharged from the sample container, the flow rate is dropped to 11.6 L/min and the sample is cyclosized for 20 minutes while the particles accumulate in the different cyclones. The temperature is constantly monitored and adjusted to remain at 23˚C.

After the 20 minutes have passed, the flow rate is increased back to 12.5 L/min. A plastic tube is attached to each cyclone and feed in to a beaker. Starting with the number 5 cyclone, the apex valve is opened and the solids are discharged into a beaker. The cyclone number 5 apex valve is then closed before moving on to cyclone number 4 and upwards.

The beakers are allowed to stand until the particles have settled and the excess water is then decanted off. Figure 6-3 shows the different fractions of the copper and iron

powder settling, with the smaller particle size fractions taking notably longer to settle than the larger size particle fractions.

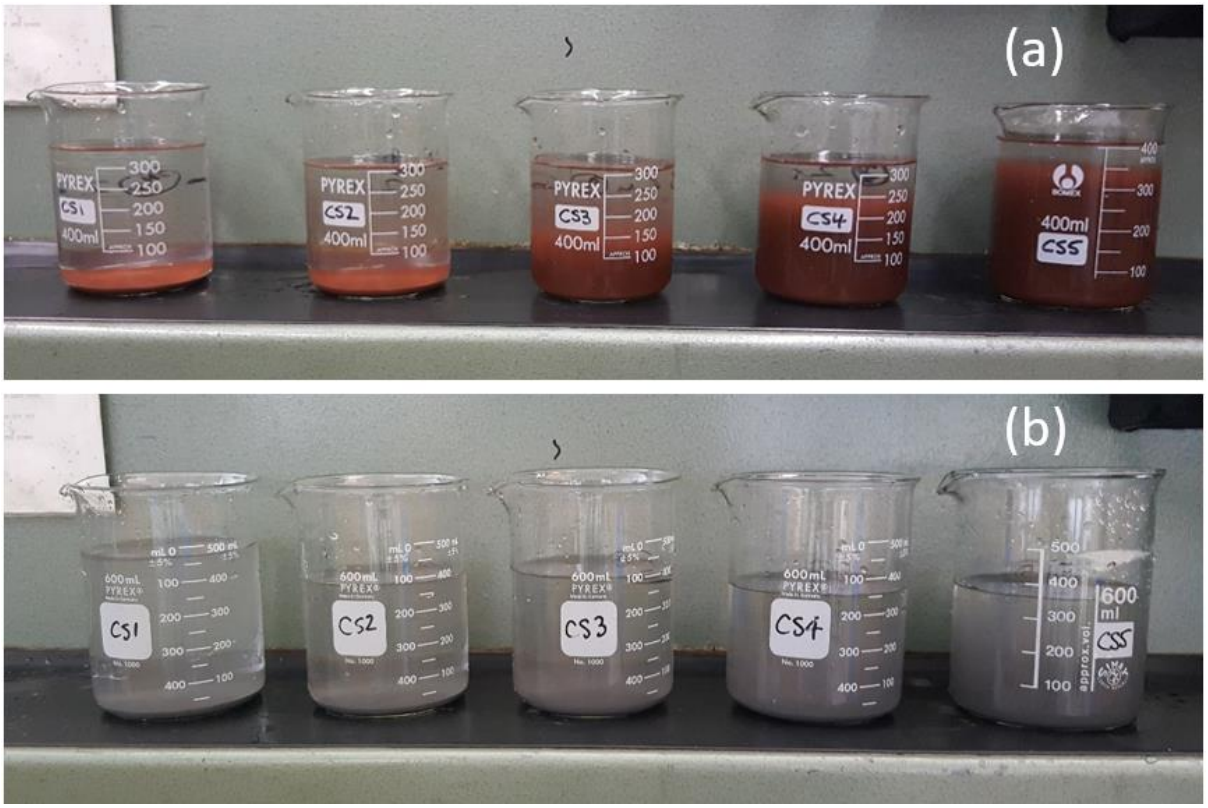


Figure 6-3: The 5 different powder fractions for iron and copper settling after being released from each cyclone. The smallest particle size fraction CS5 settles significantly slower than the larger particle size fractions.

As iron corrodes in the presence of water and air, the iron samples were sealed in the sample container as quickly as possible with excess water to minimise the contact of the water to air. After the iron samples were cyclosized, they were decanted as quickly as possible and then washed with ethanol to prevent corrosion. After the samples were decanted they were put in the drying oven overnight to remove the excess water or ethanol. Using this method, no obvious signs of corrosion were found and the cyclosized iron particles were used for particle size measurements.

When running the cyclosizer the flow rate, water temperature and time parameters of the run are kept consistent between runs. The only factor that can change between runs is the specific gravity of the material being sized. To determine the effective particle separation size of each cyclone, the cyclosizer manual [117] contains a figure

that plots specific gravity against a correction factor. Using the correction factor the effective particle separation of each of the 5 cyclones was determined for iron and copper, given in Table 6-2.

Table 6-2: The effective particle size separation lower cut off of each cyclone in the cyclosizer.

| Cyclone | Iron | Copper |
|---|---|---|
| CS1 | 21.2 | 20 |
| CS2 | 15.9 | 15 |
| CS3 | 11.1 | 11 |
| CS4 | 7.2 | 7.3 |
| CS5 | 5.3 | 5.5 |

#### 6.1.1.3 Laser Diffraction

Particle sizes were determined experimentally using the CSIRO laser diffraction particle analysis service in Waterford, WA.

The five sieved size fractions of copper powder were analysed for their particle size distribution using a Malvern 300 laser diffraction unit. Ten grams of each sample were sonicated for 20 minutes and mixed in water.

For each sample, a detailed analysis report was provided that describes the volume fraction of the powder corresponding to specific particle size intervals. Figure 6-4 plots discrete and cumulative size fractions for the sample of powder determined by sieving to be in the size range 45 µm < d < 53 µm.

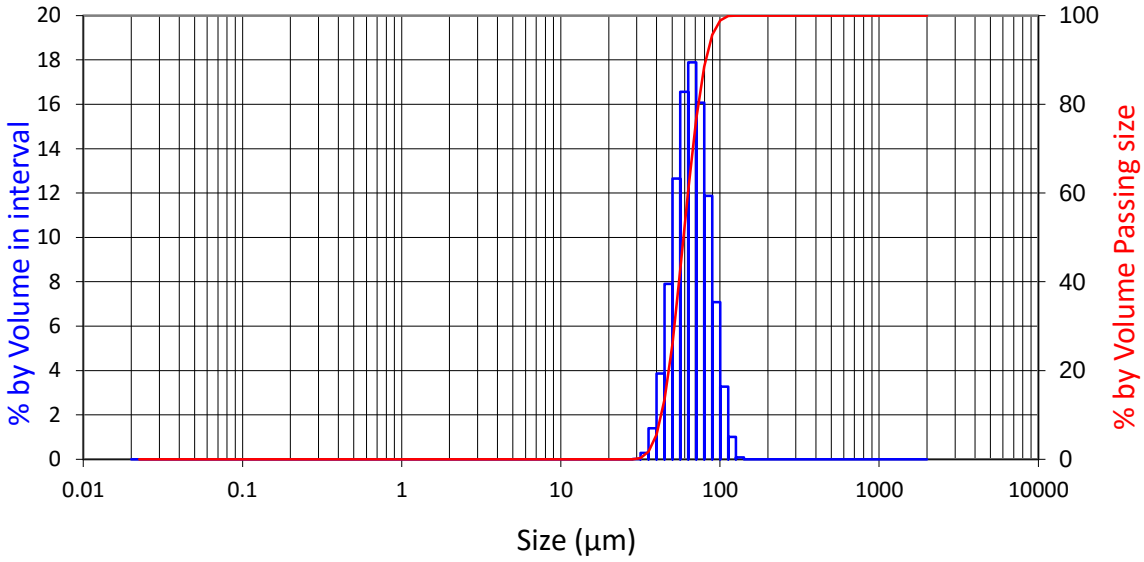


Figure 6-4: Discrete (blue) and cumulative (red) volume fraction size distribution for material retained in a 45 µm sieve but passing a 53 µm sieve.

A summary of the particle size distributions of the 5 sieved fractions is given in Table 6-3, which compares the sieve equivalent diameter range of the particles to the volume equivalent sphere diameter calculated for the range of particle sizes in each fraction measured using laser diffraction. The laser diffraction report on each sample gives the median particle size, d(0.5), and the volume weighted and surface area weighted mean diameters for each sieved copper fraction, D[4,3] and D[3,2]. The volume weighted mean is sensitive to large particles in the sample and the surface area weighted mean is sensitive to small particles in the sample. For each case, the median particle size sits in between the volume and surface weighted mean values, and there is little variation between the 3 different values.

The particle size range measured by laser diffraction is in each case significantly larger than the particle size range determined by the apertures of the sieves. This is due to differences in the particle sizing between the sieving and laser diffraction methods.

Table 6-3: A comparison of the sieve diameter range and the volume equivalent sphere diameter range as determined using laser diffraction analysis. The particle size range returned from the laser diffraction reports is expressed as d(0.1), d(0.5) and d(0.9) which are respectively the particle diameters larger than 10%, 50% and 90% of the particles by volume. D[4,3] and D[3,2] are the volume weighted and surface area weighted mean diameters respectively.

| Sieve Diameter Range (µm) | Volume equivalent sphere diameter (µm) | | | | |
|---|---|---|---|---|---|
| | d(0.1) | d(0.5) | d(0.9) | D[4,3] | D[3,2] |
| 45 - 53 | 42.9 | 59.1 | 81.1 | 60.8 | 57.3 |
| 53 - 63 | 49.1 | 65.7 | 88.5 | 67.5 | 64.2 |
| 63 - 75 | 60.7 | 83.5 | 114.9 | 86.0 | 81.0 |
| 75 - 90 | 75.0 | 98.4 | 130.0 | 100.9 | 96.5 |
| 90 - 106 | 88.4 | 116.8 | 155.3 | 119.8 | 114.4 |

The sieving method sizes particles by their equivalent sieve diameter, which is the size of a square aperture on a sieve that a particle can fall through. If the particles being sized are spherical, the equivalent sieve diameter will be equal to the particles' diameter and the particles are likely to be sieved accurately. A non-spherical particle however can have an equivalent sieve diameter of its lowest dimension, for example a particle with dimensions of 40 by 40 by 70 µm can fit through a 45 µm aperture, but will have a greater volume than a sphere that can fit through the same sized aperture. Figure 6-5 shows the appearance of the copper particles being sieved, showing that the particles are randomly shaped.

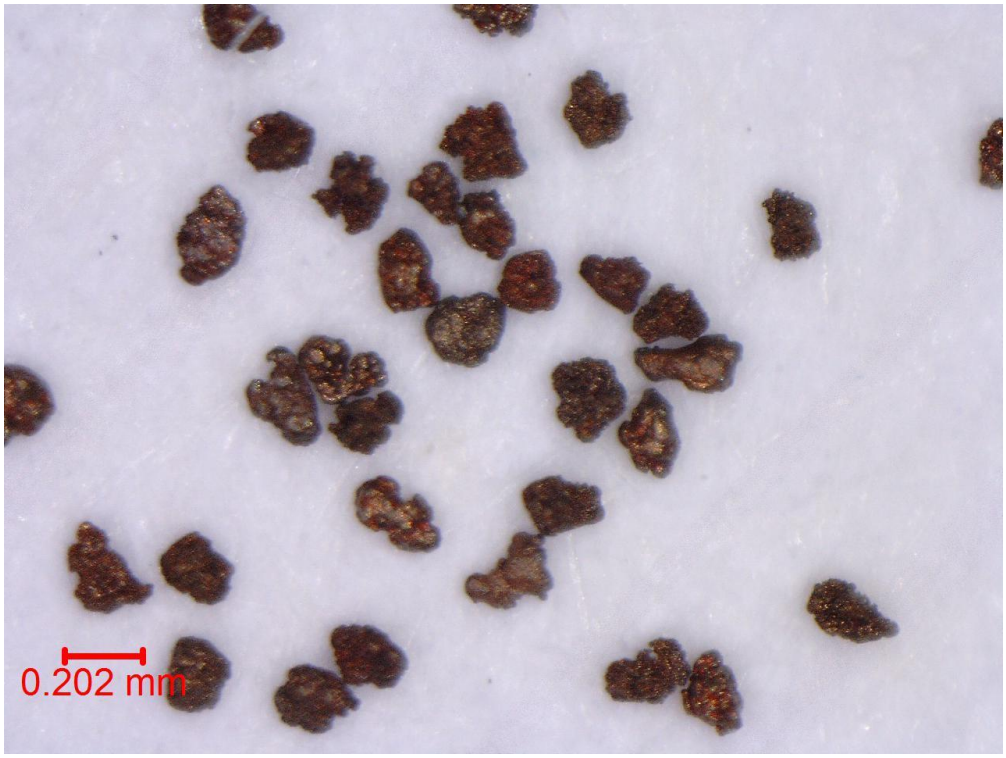


Figure 6-5: Copper particles from the sieved 90-106 um fraction.

The laser diffraction measured particle size is reported as a volume equivalent sphere diameter. Laser diffraction techniques uses theoretical models for light scattering to calculate the volume of a particle and report the equivalent sphere diameter for that volume. This is a more accurate measurement of the particle diameter than the equivalent sieve diameter.

The cyclosizing technique sizes particles based on their Stokes diameter, which is the diameter of a sphere that has the same settling rate as the particles being sized under conditions of Stoke's law. The Stokes diameter is also a volume equivalent diameter, so it can be compared directly to the diameter of the particles measured by laser diffraction. The cyclosized fractions of copper and iron powder were not tested by laser diffraction due to the costs involved and because the cyclosizing technique is recognised as a more accurate sizing method than sieving that should not introduce large errors into the sizing method.

### 6.1.2 Particle Dispersion

To precisely measure the particle size effect in X-ray fluorescence, it is essential that the particles being measured are evenly dispersed through the sample and that the

overall concentration is accurately known. If the particles are poorly dispersed, then the effective concentration in the volume of the sample being measured may vary, leading to a change in the fluorescence intensity. In this section, different ways of consistently dispersing particles of different sizes throughout various matrix materials are investigated.

#### 6.1.2.1 Small Scale Slurry Tank

Large scale slurry tanks are designed with a stirrer set-up so that the slurry is constantly moving to prevent particles from settling on the bottom of the tank, whilst producing the least amount of air entrainment. In these large slurry tanks, an X-ray window can be placed away from the stirrer region so that a constant laminar flow of slurry passes the window for XRF analysis.

It would be useful to carry out the particle size tests in one of CSIRO's existing slurry tank XRF analysers, but these proved to be too large. It is expensive and time consuming to obtain sized fractions of powdered samples. A typical slurry analyser has a minimum tank size of around 20 litres. Assuming a solids loading of at least 20%, then 4 kg of solid material would be needed to fill a 20 litre tank. Even in cases where the solids loading only requires a few weight percent of the element of interest, a few percent of 4 kg is still not viable for this study.

Using the particle sizing methods described above, at most a few grams of each particle size fraction could be obtained. Considering the cost of the raw materials and the time-consuming sizing methods, it would be unreasonable to obtain such a large amount of sized material.

Taking inspiration from the full-scale slurry tank design, a small-scale slurry tank was designed to hold stirred slurries. The tank was designed to emulate an industrial slurry tank, including having the stirrer sit on one side to push the material downwards into a U-shaped section that the material would flow smoothly around. The U-shaped design means that the tank has no corners for slurry to get caught in. The tank design is shown in Figure 6-6.

A small propeller with a diameter of 2.5 cm was attached to a 20 cm long shaft which was in turn attached to a 4.8 V motor, held above the tank with a retort stand and clamp. The shaft entered the tank through the top of the lid.

The motor speed could be varied by adjusting the source voltage. The slurry tank was made of clear plastic so that the activity of the slurry inside could be monitored. A simple slurry consisting of 20% un-sized copper powder and 80% water was used to test the slurry tank. The speed was varied until the slowest possible speed was found that resulted in no particles collecting on the bottom of the tank. A low speed is ideal to minimise air entrainment that leads to bubbles in the slurry which can affect the XRF results.

Unfortunately, it was not possible to identify a speed sufficient to suspend the copper particles with leading to excessing air entrainment. Consequently, there was no reasonable way to measure XRF spectra from the slurry and obtain consistent results, so this approach was abandoned.

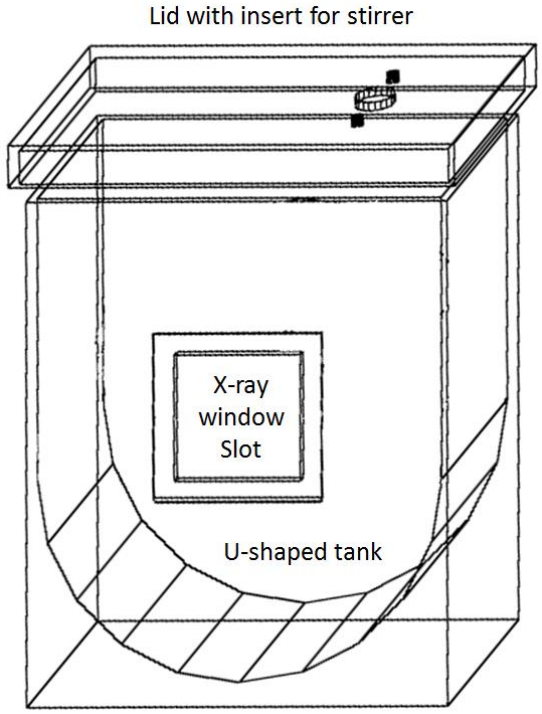


Figure 6-6: The design of the miniature slurry tank with a U-shaped bottom, slot for an X-ray window, and slot for a stirrer to enter through the tank lid and stir the slurry.

#### 6.1.2.2 Small Scale Tumbling Slurry Tank

The next iteration of the slurry tank was designed to minimise turbulence by using a tumbling slurry tank. Multiple iterations of tumbling slurry tank were developed and tested. For example, it was found that adding baffles to the slurry tank walls did not improve the mixing of the slurry. The final tumbling slurry tank was made from a simple cylindrical sample jar that could easily be attached to a 24 V motor. The sample jar had the end removed and replaced with a Mylar polyester thin film so that even low-energy X-rays form the sample could be readily measured.

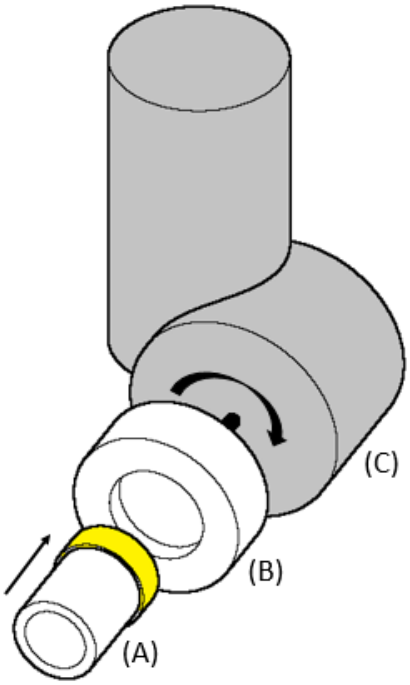


Figure 6-7: The tumbling slurry tank set-up: (a) the rotating sample jar with an open end (b) The sample jar is inserted to a plastic holder that locks the sample in place. (c) The 24 V motor used to rotate the sample jar and holder.

If the sample jar is rotated too fast, the particles will move outwards due to centrifugal force. However if the sample is rotated too slowly the particles will settle under gravity. The motor was run at a voltage of 15 V and a current of 0.7 A to keep the particles dispersed, which gave an approximate speed of 60 rev/min. While the particles seemed to be dispersed well in the water at first, over time they would visibly settle at the bottom of the sample container.

Liquids with higher viscosity keep particles suspended for longer than liquids with lower viscosity due to the increased drag force. This can be quantified by Stokes Law [118], which can arranged to give the terminal (or settling) velocity, V (m/s), of a spherical particle falling in a fluid.

$$V = \frac{2}{9}\frac{(\rho_p - \rho_f)}{\mu} g R^2 \qquad 6.1$$

where $\rho_p$ is the density of the particle (kg/m$^3$), $\rho_f$ is the density of the fluid (kg/m$^3$), $\mu$ is the dynamic viscosity of the fluid (kg/ms), g is the gravitational acceleration (m/s$^2$) and R is the radius of the spherical particle.

Two liquids with higher viscosities than water ($\mu$ = 0.001 kg/ms) were selected for further experiments; peanut oil and glucose syrup. The viscosities of peanut oil and glucose syrup are approximately 0.055 kg/ms [119] and 10 kg/ms [120], respectively. The copper powder has a range of particles from about 1 µm to 100 µm, the terminal velocity of some different sized copper particles moving through different fluids are given in Table 6-4.

Table 6-4: A comparison of the velocity different sized particles will settle in various liquids.

| | Water | Peanut Oil | Glucose Syrup |
|---|---|---|---|
| Particle Size (µm) | V(cm/s) | V(cm/s) | V(cm/s) |
| 1 | 4.30E-04 | 7.82E-06 | 4.30E-08 |
| 7 | 0.021 | 3.83E-04 | 2.11E-06 |
| 50 | 1.08 | 0.020 | 1.08E-04 |
| 100 | 3.56 | 0.065 | 3.56E-04 |

The samples were prepared in a Chemplex 1085 sample cup with one open end and a trim-less sleeve to seal the sample cup with a 6 µm thick Mylar thin film. The sample cups have a diameter of 4 cm. For the 7 µm copper particles to fall from the top of the sample cup to the bottom will take more than 3 minutes for water, more than 2 hours for peanut oil and more than 21 days for glucose syrup.

The peanut oil was poured into the sample cup and weighed, and copper powder was added to make a 1% copper mixture with the oil. The copper content was kept low as there was a limited amount of sized copper powder to work with, and because a lower particle content minimises particle interactions in the sample such as agglomeration. The sample cup was sealed shut with the thin film and shaken before being inserted into the rotating sample holder. The shaking satisfactorily dispersed the particles throughout the peanut oil medium.

For glucose syrup, even at the largest particle size, the particles are moving extremely slowly and would be expected to take more than 3 hours to travel the 4 cm diameter of the container. If the particles can be well dispersed in a glucose syrup matrix and measured relatively quickly, there may be no need to rotate the sample at all. The copper particles were added to the glucose syrup in the sample cup and stirred. The thin film seal was then quickly applied and the sample put in the motorised sample holder. Unfortunately, stirring created a new problem by introducing bubbles into the mixture. Bubbles can change XRF measurements depending on their concentration and size (private communication with J. O'Dwyer). To remove the bubbles from the sample, the sample was degassed using a vacuum pump and glass chamber. While it was useful to remove the larger bubbles, unfortunately the vacuum pump was not strong enough to create a vacuum that could completely degas the glucose syrup samples.

To slightly lower the viscosity of the glucose syrup to improve the degassing of air bubbles, a mixture of 90% glucose syrup and 10% water was subsequently used for all glucose syrup samples. This mixture would still need the copper particles to be stirred through and still need to be degassed, but there were significantly less bubbles in the sample after the degassing.

Two samples were made up to have 1% copper content using the CS2 copper fraction, one sample had a peanut oil matrix and the other sample had a matrix of 90% glucose syrup mixed with 10% water. Each sample was inserted into the tumbling slurry tank set-up immediately after being made up and sealed in the sample jar with a thin film. The samples were rotated at a speed of 60 rpm and measured with the molybdenum

X-ray tube at 40 kV, 0.6 mA with a 0.1 g/cm$^2$ Zirconium filter. An Amptek silicon drift detector was used with optimised settings to give a count rate of 500 c/s with a dead time of approximately 5% maximum count rate with no dead time and each measurement was performed for 120 seconds. The full width half maximum of the copper peak was measured to be approximately 150 eV. Further details of the experimental set up are given in section 6.4.

The two samples were kept in the tumbling slurry tank set-up and measured at different time intervals to determine if the particles were drifting over time. The resulting XRF response over 40 minutes for each sample is presented in Figure 6-8. The peanut oil sample shows considerable drift in fluorescent intensity, with the intensity of the copper K-line varying from 188+/-1.3 to 222+/-1.5 c/s over 40 minutes. The region of the sample being excited by the X-ray tube is approximately 1 cm$^2$ in area and sits in the middle of the sample. The results suggest that the particles are slowly drifting towards the centre of the sample, increasing the number of particles in the region being measured. This is the opposite of what is expected, with the particles expected to move outwards towards the sample jar walls due to centrifugal force.

The same results occurs for the glucose sample, however this time the drift in the count rate over 40 minutes is lower than the peanut oil case, going from 141+/-1.1 c/s to 153+/-1.2 c/s. In both cases, the error on each data point is the sum in quadrature of the statistical error, determined as square root of the number of counts measured, and the systematic error introduced from the fitting process. The drift in the measurements over time for each sample is not within the error of the measurement, so in both cases the drift is significant.

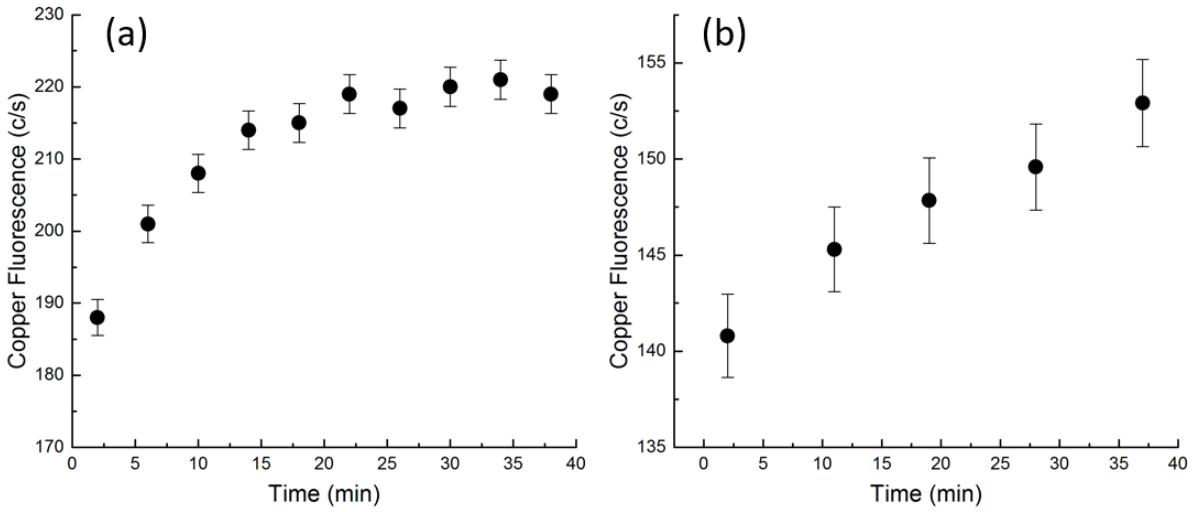


Figure 6-8: The XRF response versus time for a 1% copper sample suspended in (a) peanut oil and (b) a mixture of 90% glucose syrup and 10% water. Each sample is being rotated at a speed of 60 rpm to help keep the particles suspended.

#### 6.1.2.3 Synthetic Rock Samples

As reliable measurements of slurries proved to be difficult to obtain, solid samples were considered instead. Different methods of preparing solid samples were considered. One option considered was to mix the particles through a liquid that would quickly set, such as plaster. However, this approach risks having the particles settle as the liquid sets, resulting in an uneven particle distribution.

Another option considered was working with either loose or pressed powder samples. Both options have a significant disadvantage, in that it is difficult to evenly mix powders; any variations in particle size will result in the smaller particles falling to the bottom of the mixture. An added disadvantage of pressed powder samples is that the copper and iron particles can distort when pressed.

Particles are easier to disperse in liquid samples compared to solid samples, but it is difficult to keep them suspended in a liquid sample. A sample in between a solid and liquid would be the ideal sample matrix.

Various pastes were considered as the suspending matrix material. In the end, a recipe based on children's play-dough was chosen, as it provided a convenient consistency and a known composition. Dough was prepared from 20% salt (NaCl), water ($H_2O$) and

flour (effective formula of $C_4H_8O_2$). The density of the dough was measured to be 1.259 g/cm$^3$.

The dough was weighed and a predetermined amount of copper or iron powder was slowly kneaded through the dough to create a sample. The dough was kneaded extensively so that the copper particles appeared to be evenly dispersed.

To test that the copper particles really were evenly suspended in the dough mixture, 3 samples using material from the same particle size fraction (Cu CS1) were prepared, each with a concentration of 3% copper. Each sample was thoroughly kneaded and then rolled out to on clean non-stick surface to have a thickness of at least 1 cm. The flat surface of the sample was pressed gently up against a thin film in an enclosed sample cup and inserted into the tumbling slurry tank set-up.

All three samples were measured with exactly the same experimental set-up used to measure the peanut oil and glucose syrup samples, described in section 6.1.2.2. The error on each measurement is calculated as the sum in quadrature of the statistical error, determined as square root of the number of counts measured, and the systematic error introduced from the fitting process.

The copper counts from each sample were found to consistent within measurement errors as shown in Table 6-5. This test was done to ensure that the samples were properly mixed, and that the method resulted in samples that were consistent and repeatable.

Table 6-5: the copper fluorescence response from 3 different dough samples all made to have a concentration of 3% copper CS1 particles.

| Sample | c/s |
|---|---|
| Cu CS1 3% (a) | 179 ± 1.6 |
| Cu CS1 3% (b) | 175 ± 1.6 |
| Cu CS1 3% (c) | 178 ± 1.6 |

One drawback of working with dough was that the samples would grow mould within an hour or two of being made. A large batch of dough could be made at a time, wrapped in plastic wrap, and stored in a refrigerator with no mould growing. However, samples that had the copper particles kneaded through them were highly susceptible to growing mould.

Modelling clay was considered as a similar option as it worked just as well as dough but did not grow mould. However it is difficult to know the exact composition of modelling clay, which complicates comparisons with theory.

Dough samples were made to contain 3% copper powder by weight for each copper powder size fraction available and 5% iron powder by weight for each iron powder size fraction available.

### 6.1.3 Samples with Zero Particle Size

While measuring the particle size effect in a sample, it would be ideal to be able to measure a material having the same composition but no particle size effects. Working with dough, it would not be possible to create samples with the exact same copper content and sample composition. Changes to the sample composition can be accounted for with Monte Carlo simulations. The experimental set-up can be modelled and a correction factor can be determined by modelling a dough sample with no particle size effects and a different sample composition with no particle size effects. The ratio of these two results can be used to correct the experimental measurement of the sample with a different composition to predict the results of a dough sample with no particle size effect.

Glass fusion samples were created to contain the same copper and iron concentrations as the particle size samples. High purity copper oxide and iron oxide powders were mixed with a flux to give a concentration of 5% iron and 1% copper in one sample and 1% iron and 3% copper in the other sample. The flux material used was lithium tetra-borate, $Li_2B_4O_7$. The exact weights of the raw materials in each sample are given in Table 6-6 and

Table 6-7**.**

Table 6-6: The measured weights of the raw materials used to create the glass fusion sample with 5% iron and 1% copper.

| Raw material | Measured weight (g) |
|---|---|
| Flux | 5.0031 |
| SiO2 | 0.1001 |
| CuO | 0.06929 |
| Fe2O3 | 0.3954 |

Table 6-7: The measured weights of the raw materials used to create the glass fusion sample with 1% iron and 3% copper.

| Raw material | Measured weight (g) |
|---|---|
| Flux | 5.0136 |
| SiO2 | 0.1014 |
| CuO | 0.1959 |
| Fe2O3 | 0.07488 |

The raw materials were heated in a platinum crucible between 900°C and 1000°C, and then cast and into a mould with a flat bottom. The glass samples have a diameter of 3 cm and are approximately 3 mm thick.

## 6.2 Monte Carlo Simulations

Monte Carlo simulations of particle size effects were performed using the EGSnrc [112], [121] code. A specially developed EGS user code provides two options for modelling inhomogeneous materials comprising a background matrix containing particles of a different material.

The first method uses a built-in particulate function that adds randomly positioned spheres of a different material in the path of particles passing through the sample [122]. The size, composition and number density of the spheres can be defined by the user.

The second method uses a noise function to randomly assign points within a region to one of two materials. A Perlin noise function [123] is used which has a limited spatial frequency bandwidth, resulting in irregularly shaped particles throughout a defined region. The material, particle concentration and average scale of the particles are defined by the user. There are also two options for surface roughness: smooth and fractal, the latter summing several noise distributions with increasing frequency and decreasing amplitude to produce particles with rough surfaces. Further details of this implementation are given in [123]. Figure 6-9 shows an example of smooth and fractal Perlin function simulated particles.

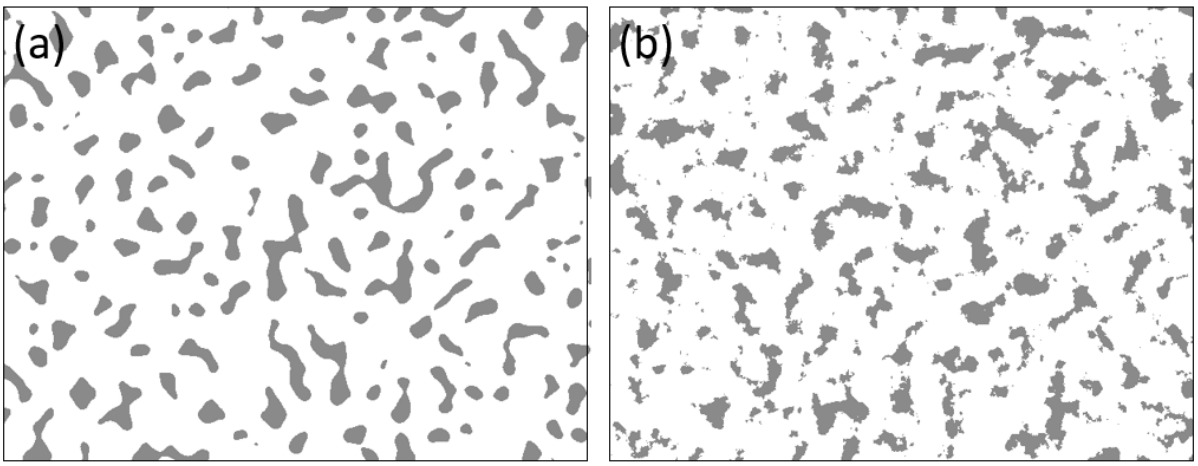


Figure 6-9: Randomly distributed Perlin function particles calculated with (a) the smooth and (b) the fractal noise functions.

The simulation modelled the experimental set-up including the positioning of the X-ray tube, detector, collimators and sample. However other aspects of the experimental set-up were optimised using Monte Carlo simulations, as will be described in the next section. The final experimental set-up is described in section 6.4, and the final Monte Carlo simulations used for comparison with the experimental measurements are based off the final experimental set-up.

## 6.3 Exciting Energy

XRF measurements taken using two different exciting radiation energies can be used to correct for the particle size effect if the exciting radiation energies are chosen well. Selecting two exciting radiation energies so that one gives a large particle size effect and the other gives a relatively smaller particle size effect gives the best correction results [95].

The particle size effect is a function of the exiting radiation energy. The greatest particle size effect occurs when the exciting radiation is just higher than the k-edge of the fluorescent element being measured. The particle size effect decreases with higher exciting energies, until an optimum energy is reached where further increases in the exiting radiation energy do not continue to decrease the particle size effect [87] . Above this optimum exciting energy, the absorption coefficient of the primary radiation in the sample is negligible in comparison with the absorption coefficient of the characteristic fluorescent radiation in the sample.

To determine the optimum exciting energy, the ratio of the mass attenuation coefficients calculated at the fluorescence and incident exciting energies is plotted as a function of the exciting radiation energy in Figure 6-10. The mass attenuation coefficient ratios are plotted for four different elements, Mn, Fe, Cu and Zn, calculated with a concentration of 3% in a dough matrix. The simulations were carried out with the dough matrix so that the copper and iron simulations would be directly comparable to the experimental measurements.

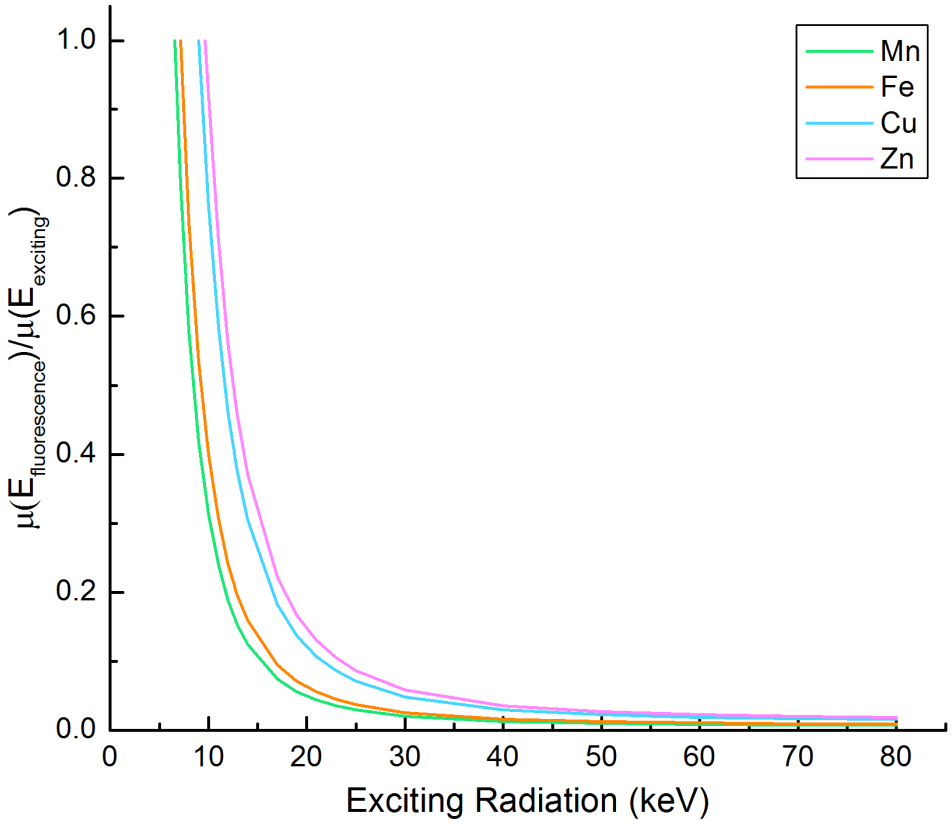


Figure 6-10: The ratio of the fluorescence mass attenuation coefficient to the exciting radiation mass attenuation coefficient for various elements, predicted for samples containing 3% of each element in a dough matrix.

For each element shown in Figure 6-10, the fluorescence mass attenuation coefficient becomes negligible compared to the exciting radiation mass attenuation coefficient when the curve plateaus along the y axis. Figure 6-11 shows the same trend as Figure 6-10, but for different copper concentrations and for different matrix materials. Figure 6-11 shows that the ratio of the fluorescence radiation mass attenuation coefficient to the exciting radiation mass attenuation coefficient is mostly independent from the sample concentration and matrix. This suggests that the particle matrix plays a more significant role in selecting the best exciting radiations, rather than the bulk matrix.

This means that the sample composition does not need to be known exactly to select the optimum exciting radiation energy, as it will remain a very similar value with changing concentrations and matrix materials.

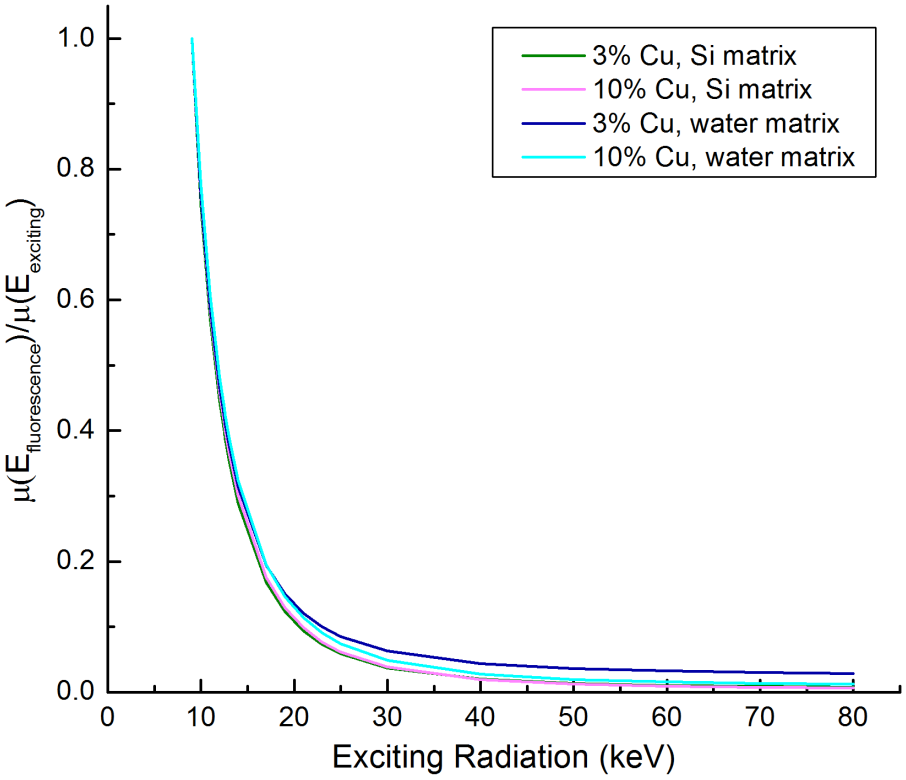


Figure 6-11: The ratio of the fluorescence mass attenuation coefficient to the exciting radiation mass attenuation coefficient for various samples with varying copper concentrations and matrixes.

The particle size effect is predicted using Monte Carlo simulations for the experimental samples, 3% copper and 5% iron in dough, with varying exciting radiation, shown in Figure 6-12 and Figure 6-13 respectively. The change in particle size effect above 25 keV is relatively insignificant compared to the changes between 7.14 keV and 25 keV for both samples. The data shown in the following figures 6-12 to 6-14 has been simulated from samples using the particulate model, described in detail in section 6.2. The particulate model randomly distributes spheres of a specified particle size and material throughout a defined matrix material. As the diameter of the spheres is held constant in the simulation, there is no uncertainty on the particle size.

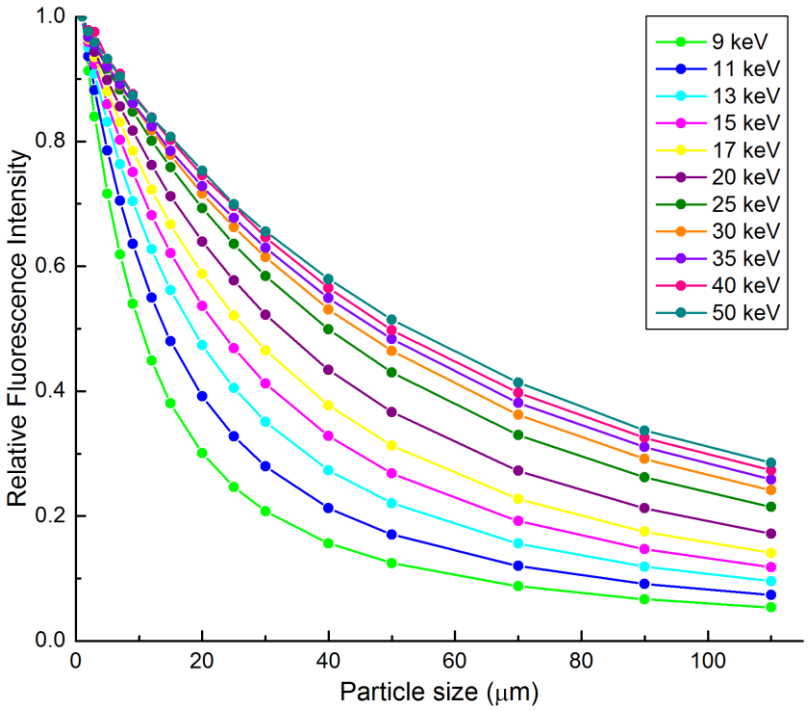


Figure 6-12: Monte Carlo simulations of the particle size effect, shown as fluorescence intensity vs particle size, for a 3% copper sample in a dough, simulated with various exciting radiation energies.

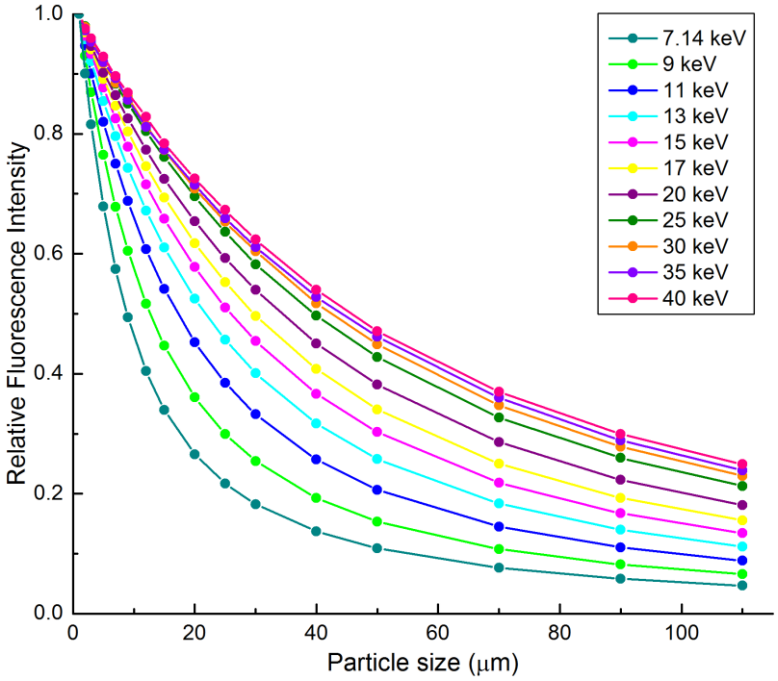


Figure 6-13: Monte Carlo simulations of the particle size effect, shown as fluorescence intensity vs particle size, for a 5% iron sample in a dough, simulated with various exciting radiation energies.

Another point to consider when selecting the ideal exciting radiation energies E1 and E2 is that as the exciting radiation energy increases significantly, the fluorescence response decreases. While a higher energy exciting radiation will give a smaller particle size effect, it can be at the cost of the overall response of the fluorescent element of interest. It is important to ensure that the source strength between E1 and E2 is chosen so that fluorescence response can be measured with good statistical precision at both energies.

The experimental set-up only has one detector, and it is ideal to run the detector with the same settings between the two different exciting radiation measurements. Large changes in the source strength can result in either detector saturation and/or high dead-times for the brighter fluorescence signal, or low count rates and poor statistical prevision for the weaker signal. To avoid the complexity of changing the detector settings between the two measurements, it is preferable to balance the source strength with the total count rate measured in the detector.

The fluorescence from a 3% copper in dough sample was simulated at different exciting energies to show how the fluorescence response changes with exciting radiation for different particle size samples. The intensity of the copper fluorescence with different exciting radiations energies simulated with identical source strengths is measured relative to the intensity produced using the lowest exciting radiation energy, which in the copper case is 9 keV. The change in fluorescence intensity between 9 and 50 keV is shown in Figure 6-14 for simulated samples containing 1 μm, 20 μm, 40 μm and 70 μm copper particles. The shape of the curves shown in Figure 6-14 area result of the interplay of the decreasing photoelectric cross-sections making it less likely to excite an atom and cause fluorescence with increasing energy and the decreasing particle size effect with increasing energy.

The fluorescence response strength varies significantly with both the particle size and incident source energy. In a practical experiment, the filter thickness and X-ray tube settings both affect the strength of the source, so it is possible to optimise these parameters to obtain source strengths at high and low energies that give similar fluorescence count rates. For example, if a copper sample is being excited by 9 keV and

30 keV exciting radiation, and the particles are known to be approximately 20 µm, then it would be ideal to have the source strength of the 30 keV exciting radiation be approximately double the source strength of the 9 keV exciting radiation. In practise, this can be achievable by optimising the operating voltages, currents and filter thicknesses used to create the two source energies, as described in the next section.

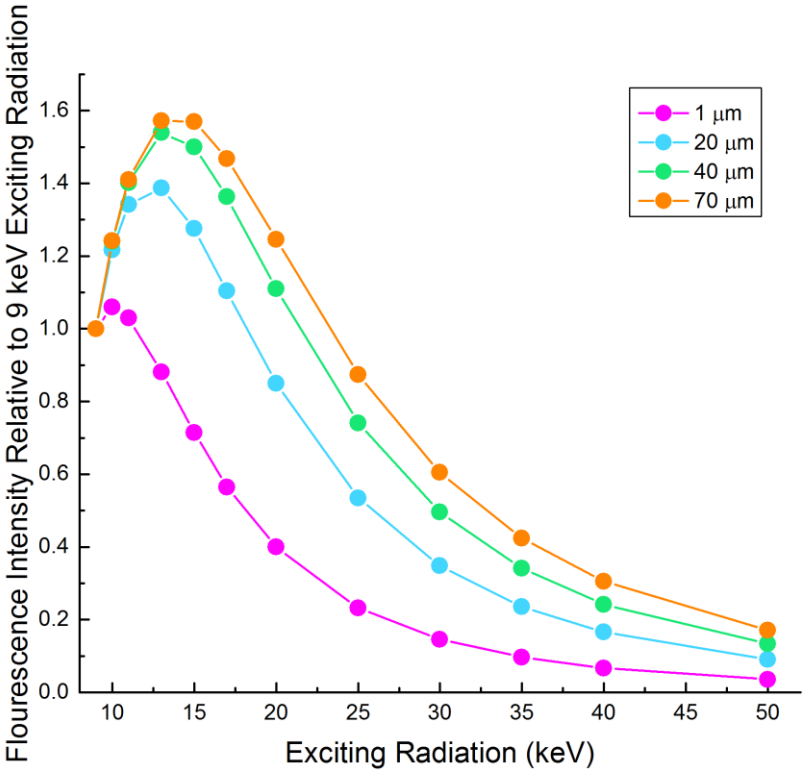


Figure 6-14: The change in fluorescence intensity resulting from Monte Carlo simulations using exciting radiation energies varying from 9 to 30 keV, all simulated with equal source strength. The change in fluorescence is shown for 3% copper in dough samples, simulated with 4 different particle sizes.

### 6.3.1 Selecting the Experimental Exciting Radiation Spectra

The ideal lower exciting radiation energy should be just above the K-edge of the element of interest, 7.1 keV for iron and 9.0 keV for copper. To simplify the experiments, only one low-energy exciting radiation setting will be used; to be able to excite both iron and copper X-rays, that energy is selected to be close to but above the copper K-edge.

X-ray tubes generate a broad radiation spectrum that depends on the tube high-voltage, the tube target and thickness and composition of any filtration. It is possible

to use the characteristic X-ray lines emitted from the tube target as a bright, quasi-monoenergetic source of X-rays. A filter can be used to absorb the Bremsstrahlung in the emitted radiation spectrum so that just the characteristic lines are used as the exciting radiation. The filter and X-ray tube settings can also be used to minimise the intensity of certain characteristic lines so that only a single characteristic line is used as the exciting radiation spectrum.

It is also possible to use filter materials and change the tube voltage so that the characteristic lines are not used in the exciting radiation spectrum. Filters can be selected so that above the K-edge of the filter material, X-rays are intensely absorbed. For example, silver has a K-edge of 25 keV and will absorb majority of X-rays occurring in a region after 25 keV, resulting in a spectrum that has a broad peak that rises up to 25 keV and then sharply drops off.

The Ebel model [109], [110], [114], [111] was used to investigate how different filters and X-ray tube voltage would affect the exciting radiation spectrum from an Oxford instruments molybdenum target X-ray tube. To obtain an energy just above 9 keV, using a molybdenum target X-ray tube, filter materials with K-edges above 9 keV were considered. When using the K-edge filter principal to create exciting broad radiation peak, it is important to keep in mind that depending on the filter thickness, these peaks can be quite wide on the low-energy side. Elements with K-edges too close to 9 keV will result in a radiation peak that overlaps with the copper peaks, and a significant proportion of the exciting radiation will be below the copper K-edge and unable to induce copper K-shell transitions. The K-edge energies of the elements just above copper in the periodic table, and therefore the likely ideal filter materials, are given in Table 6-8.

Table 6-8: The K-edge of elements above copper in the periodic table.

| Element | K-edge (keV) |
|---|---|
| Zinc | 9.6 |
| Gallium | 10.4 |
| Germanium | 11.1 |
| Arsenic | 11.9 |

| | |
|---|---|
| Selenium | 12.7 |
| Bromine | 13.5 |

The K-edge of zinc is very close to the copper K-edge, and the low energy side of the incident radiation peak will overlap with the copper lines. The other elements in Table 6-8 have K-edges at energies only a little higher than the copper K-edge, so that they will still cause a large particle size effect, but will enable the use of radiation spectra that overlap less with the copper peaks. Unfortunately, none of these elements are physically suitable to be used as X-ray filter materials. For example, gallium melts just above room temperature and cannot be handled in foil form without melting. Germanium is not available in thin enough films. X-ray filters need to be thin and consistent in thickness, and it is very difficult to present consistent thin layers of powder in front of an X-ray tube. Arsenic is difficult to obtain and work with due to its toxicity and bromine is a liquid which again is difficult to present as an even filter in front of an X-ray tube. For these reasons zinc was used as the filter material, despite the fact that the incident energy spectrum produced leads to overlap with the copper fluorescence peak.

The Ebel model was used to predict different exciting radiation spectra using different zinc filter thicknesses and different X-ray tube voltage settings. The filter thickness needs to balanced, as having a greater thickness results in a narrower range of exciting radiation energy, but also results in a less intense source strength. Figure 6-15 shows the Ebel model prediction using a 0.065 g/cm$^2$ Zinc filter, with a tube voltage of 20 kV. The energy positions of the copper Kα and Kβ peaks are marked to show the overlap with the exciting radiation spectrum.

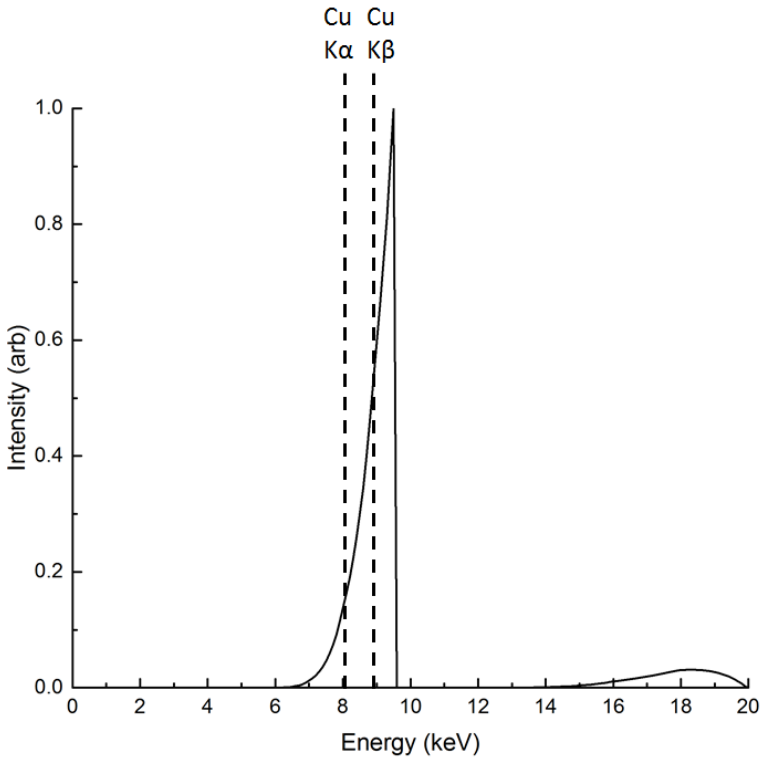


Figure 6-15: The filtered X-ray tube spectrum predicted by the Ebel model for a molybdenum target X-ray tube with a zinc filter (0.1 g/cm$^2$) operated at a tube voltage of 20 kV. The energy positions of the copper Kα and Kβ peaks are shown over the spectrum to show the overlap.

Figure 6-10, Figure 6-12 and Figure 6-13 predicts the point where increasing the exciting energy no longer significantly lowers the particle size effect to occur around 30 keV for the copper samples and around 20 keV for the iron samples. As above, only one 'high-energy' exiting radiation is used for both the copper and iron samples for simplicity. Silver has a K-edge of 25.5 keV and can be readily obtained as a thin foil, making it an ideal choice to create a broad peak in between 20 and 30 keV. The Ebel model was used to determine the best-case exciting radiation spectrum using different silver filter thicknesses and tube voltage settings. Figure 6-16 shows the predicted spectrum using a 0.4 g/cm$^2$ silver filter, and a tube voltage of 40 kV.

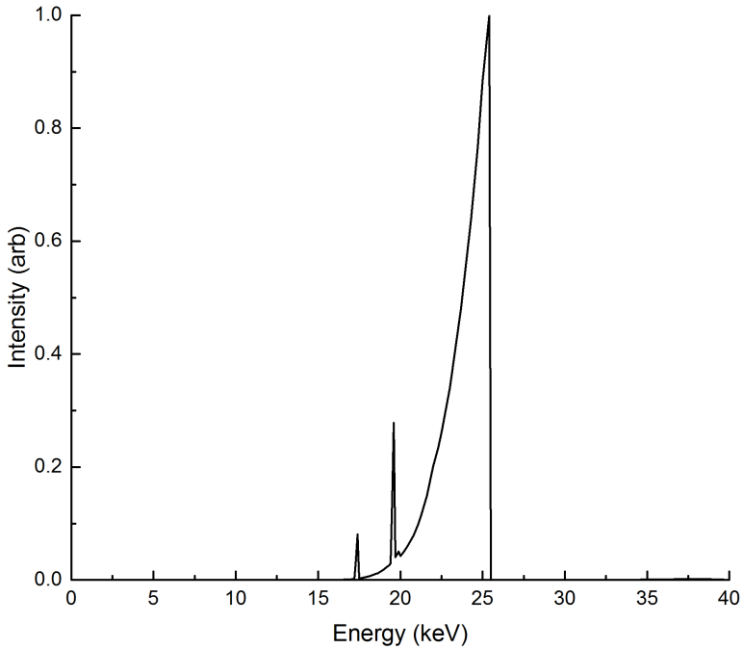


Figure 6-16: The filtered X-ray tube spectrum predicted by the Ebel model for a molybdenum target X-ray tube with a silver filter (0.4 g/cm$^2$) operated at a tube voltage of 40 kV.

The broad peak created using the silver filter covers an energy range of approximately 5 keV, a significant range considering that theoretical calculations of the particle size effect usually assume mono-energetic exciting radiations. The silver filter also transmits the molybdenum characteristic lines, making the spectrum even more complex. A greater filter thickness will filter out these lines and reduce the peak width, but at the cost of rapidly reducing intensity.

Another option to the silver filter is to use the molybdenum Kα characteristic line at 17.4 keV. A zirconium filter can be used to give a sharp, almost mono-energetic peak at 17.4 keV. Figure 6-17 shows the Ebel model predicted spectrum using a 0.1 g/cm$^2$ zirconium filter, with a tube voltage of 40 kV. The molybdenum peak at 17.4 keV is close enough to the ideal exciting radiation energy for exciting iron particles to give a minimal particle size effect but is not ideal for copper particles. However the sharp mono-energetic peak will provide useful results that can be easily compared with theoretical calculations, and as shown in Figure 6-12, will still give a substantial difference in the copper particle size effect compared to the zinc filtered exciting radiation.

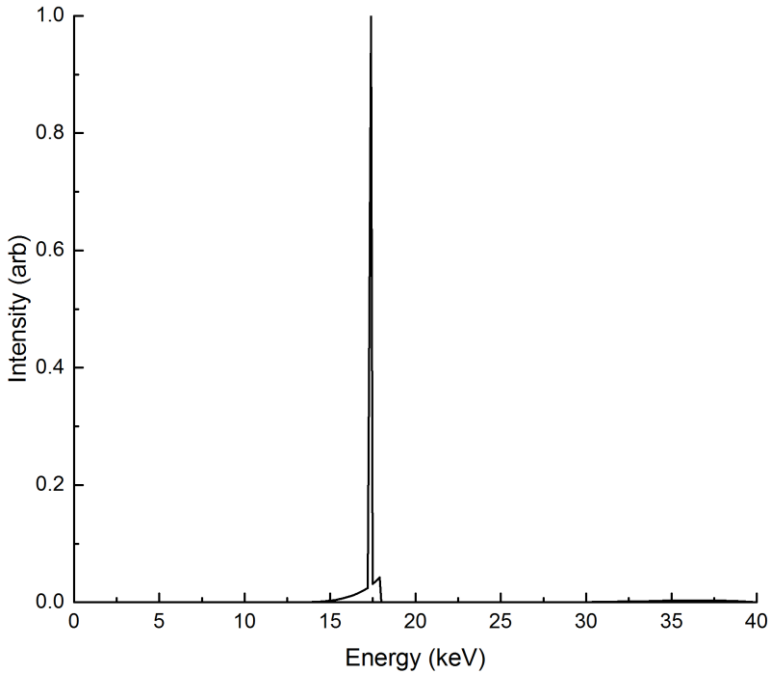


Figure 6-17: The filtered X-ray tube spectrum predicted by the Ebel model for a molybdenum target X-ray tube with a zirconium filter (0.305 g/cm$^2$) operated at a tube voltage of 40 kV.

The 0.07 g/cm$^2$ zinc filter was used for the low energy exciting radiation spectrum with tube settings of 20 keV and 0.6 mA. The 0.1 g/cm$^2$ zirconium spectrum was used for the high energy exciting radiation spectrum with tube settings of 40 keV and 0.6 mA.

## 6.4 Experimental Set Up

The experiments were conducted using a custom-designed in-house XRF system designed for measuring low concentrations of trace elements in industrial slurries. The set up consisted of a slurry tank with a polyether ether ketone (PEEK) window allow transmission of X-rays into and out of the slurry from components mounted inside a shielded steel cabinet. The mounting block is fixed inside the steel cabinet holding the X-ray tube and detector in place with respect to the PEEK window to measure slurry inside the tank. Both the X-ray tube and the detector are located at an angle of 30˚ with respect to the normal of the PEEK window. Figure 6-18 shows the design of the XRF block. The electronics that control the detector and the X-ray tube are inside the steel cabinet, and connect to an external power supply. Figure 6-18 also shows the set-up of the detector and X-ray tube against the slurry tank.

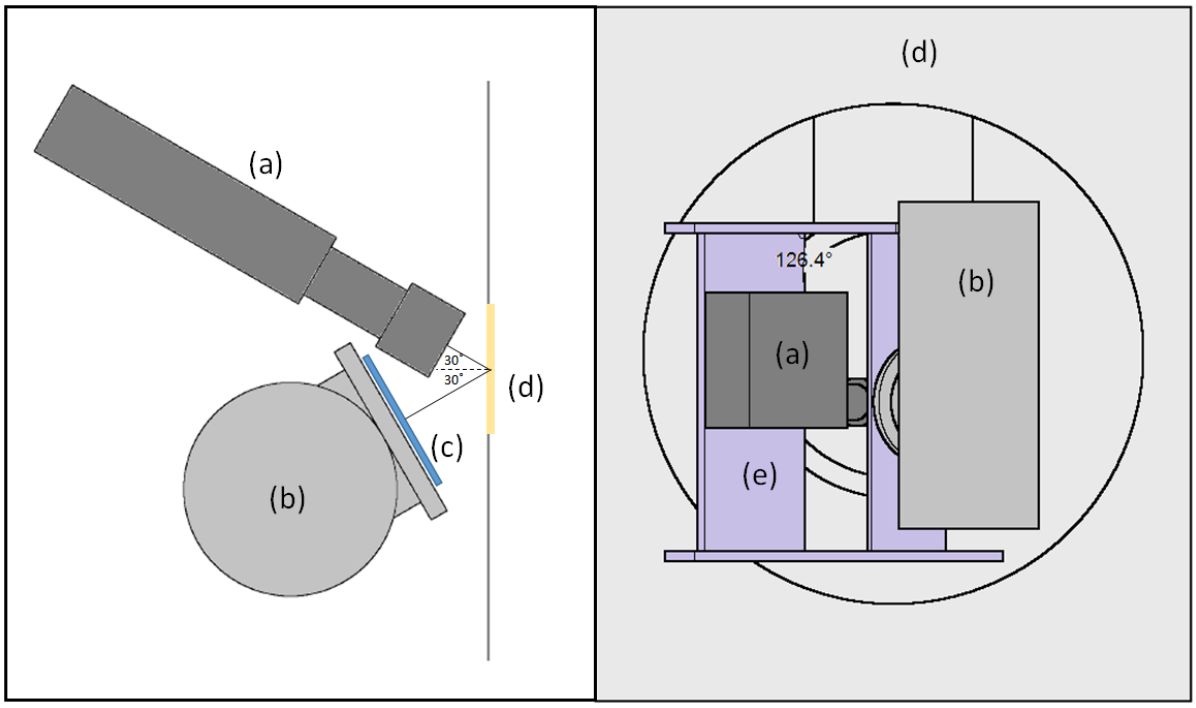


Figure 6-18: The placement of (a) the detector, (b) the X-ray tube, (c) the X-ray tube filter and (d) the slurry tank wall and X-ray the detector and (e), the XRF block. The left panel shows the view from above the set-up, with the XRF block not shown to simplify the view of the set-up. The right panel shows the view looking directly at the XRF block screwed into positon.

The tumbling tank set-up, shown in Figure 6-7, was small enough to insert inside the industrial slurry tank, lined up with the PEEK window. As the slurry was already contained in a sample container with a thin-film window, the PEEK window was not necessary and was removed. With the tumbling mini tank set up, the system could be operated as normal to measure the mini-slurry samples and the rotating dough samples described in section 6.1.

Access to the X-ray tube to change between the two filter materials positioned in front of the X-ray window is impossible once the XRF block is mounted in the steel cabinet. A filter switch was designed with a long handle that could be operated to place either filter directly in front of the source window without having to unscrew the X-ray tube from the measuring block. The filter switch was designed using the CAD software and fabricated in plastic using 3D printing. Figure 6-19 shows the filter switch design and placement.

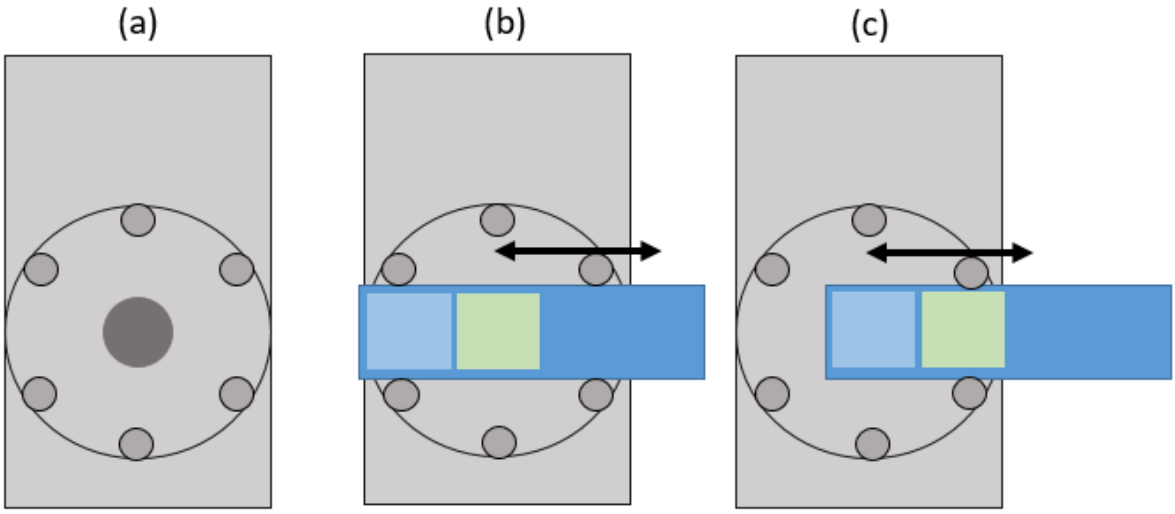


Figure 6-19: (a) shows the front of an X-ray tube with no filter applied to the X-ray window, (b) and (c) show how the filter switch can be adjusted to interpose either the Zr (light blue square) or the Zn filter (light green square) into the X-ray beam.

An Amptek X-123 FAST SDD X-Ray spectrometer with a 17 $mm^2$ silicon drift detector was used to measure the fluorescent and scattered X-ray spectrum. The Amptek DCP software, available from the Amptek website, was used to control the detector settings and measure the XRF spectra. The settings were designed to minimise dead-time whilst preserving good resolution. Each measurement was taken for 120 seconds, and repeated at least 6 times, alternating between the two different exciting radiations using the filter switch. The total count rate varied between 350 and 650 c/s for the experiments depending on the particle size and element being measured. Because of the low count rates the dead time was negligible for the experiments. The FWHM of the iron Kα at 6.4 keV peak was measured to be 135 eV.

## 6.5 Particle Size Results

As discussed above, the most reliable results were obtained using the dough matrix samples. These contained either 3% copper powder or 5% iron powder dispersed in dough, where the dough consisted of 40% flour ($C_4H_8O_2$), 40% water ($H_2O$) and 20% table salt (NaCl). A sample was made for each particle size fraction and measured separately with the high and low exciting radiation energies.

### 6.5.1 Spectra Fitting Details

At least 6 spectra were taken for each sample using alternating high and low energy settings. This approach was allowed to check for any variation from run to run, for example due to the positioning of the filter, or longer term measurement drift. The different spectra were energy calibrated and summed to give two high intensity spectra per sample, one for each exciting radiation spectrum. These high intensity spectra for each sample were carefully fitted using the fitting scripts described in Chapter 4.

Figure 6-20 and Figure 6-21 show the fitted spectrum from a 3% copper in dough sample made with CS5 copper particles. A 1×1 mm square iron foil was placed directly in front of the sample to introduce fluorescence iron peaks into the spectra, which were used to monitor the stability of the beam intensity. Figure 6-20 and Figure 6-21 shows the spectra obtained using the zinc and zirconium filtered exciting radiation respectively.

The spectra measured using the zinc filtered exciting radiation were challenging to fit due to the overlap of the Compton and Rayleigh scattered exciting radiation with the copper and iron fluorescence peaks. An empirical background function was developed, comprising the sum of a number of exponentially rising terms cutting off close to or at the K-edge energy of zinc (9.66 keV), each convoluted with a Gaussian smearing matrix as described in section 4.1, plus a third-degree polynomial.

The spectra measured using the zirconium filtered exciting radiation had very low background in comparison. These spectra were easily fit using only a third-degree polynomial background function.

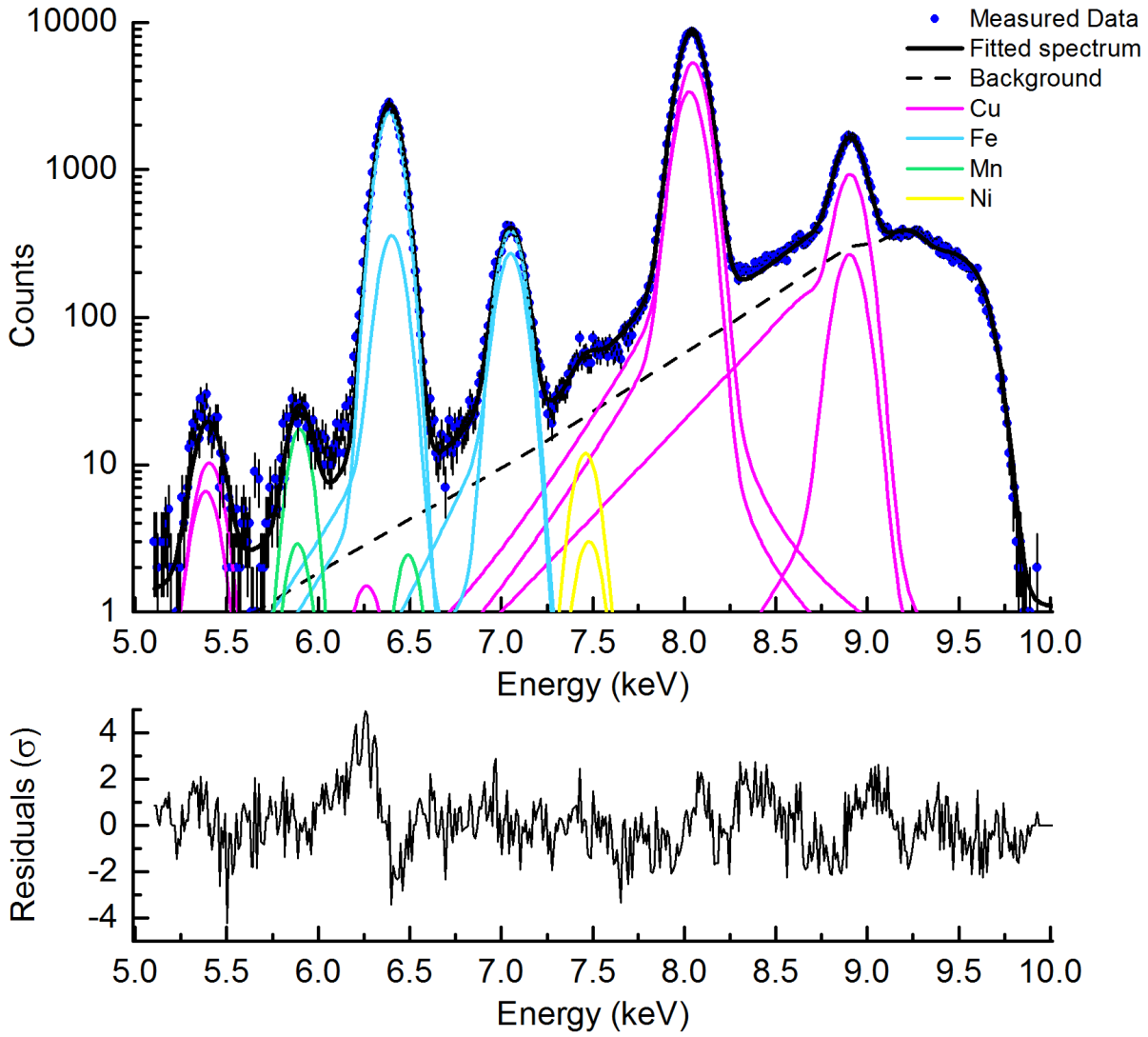


Figure 6-20: the fitted spectrum of a sample excited with the zinc filtered exciting radiation. The sample contains 3% copper. A small iron foil introduced additional peaks used for calibration and stability monitoring.

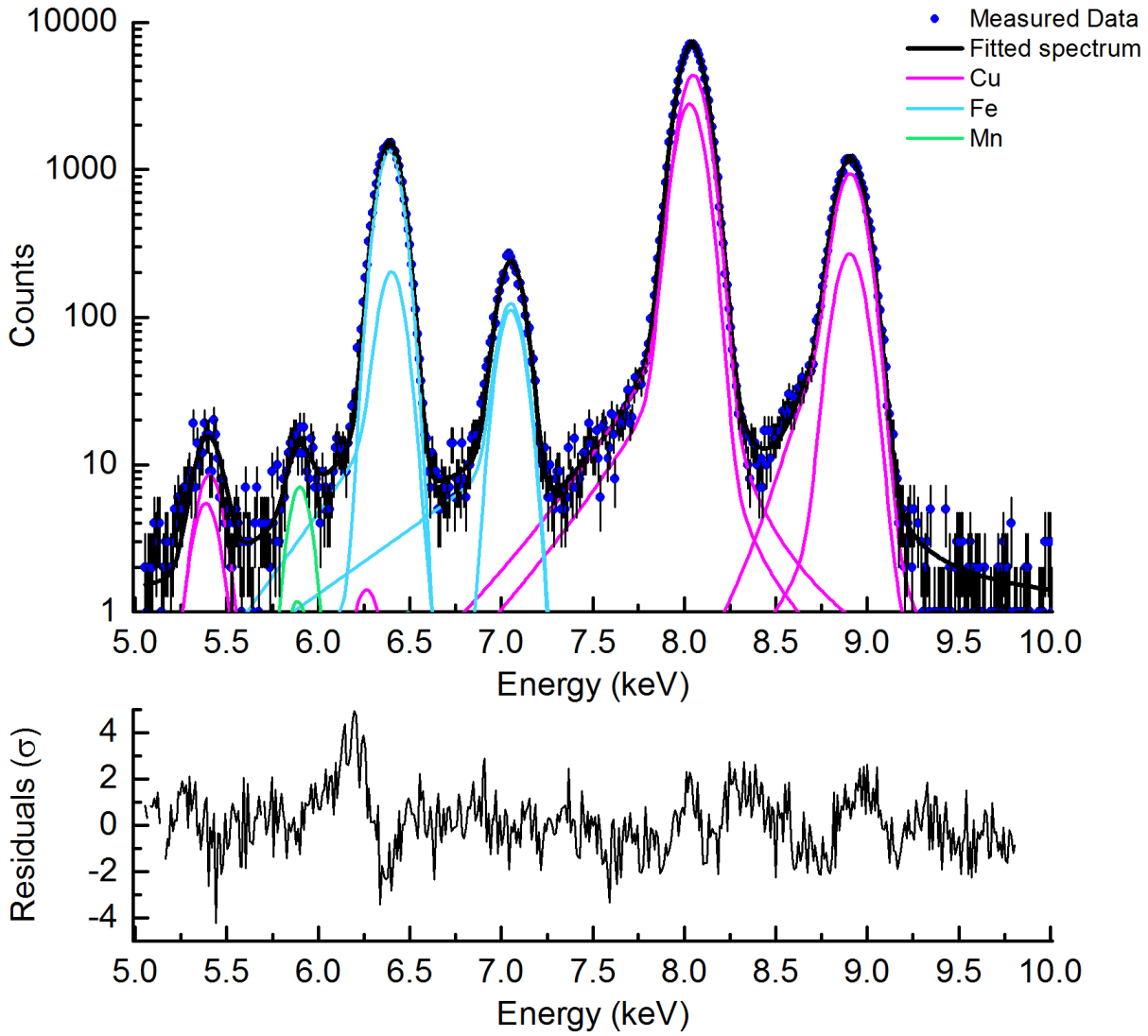


Figure 6-21: fitted spectrum of a sample excited with the zirconium filtered exciting radiation. The sample contains 3% copper plus a small iron foil. The background is fitted with a third-degree polynomial function; however the background counts are of too low intensity to appear on the selected scale.

### 6.5.2 Particle Size Measurements

The fluorescent count rate (counts per second) for each different particle size was determined directly from the fitted peak area divided by the total live time.

The counting error was calculated as the square root of the total counts, divided by the total live time; this is justified by the very low background under the fluorescent peaks. The error on the fitting process for each measurement was calculated using the process detailed in section 4.3. The fitting and counting errors were summed in quadrature to obtain the total measurement error.

The fluorescent response results versus particle size are plotted for the copper and iron powders in Figure 6-22 and Figure 6-23.

The particle size ranges for each powder fraction are shown using horizontal error bars. For the cyclosized fractions, the midpoint of the size distribution is set equal to the midpoint of the upper and low size cut offs, and the errors correspond to the total size range. For the sieved fractions, the laser diffraction data are used, with the particle size set equal to the median particle diameter d(0.5) and the errors bars equal to +/- one standard deviation as calculated from the reported particle size distribution.

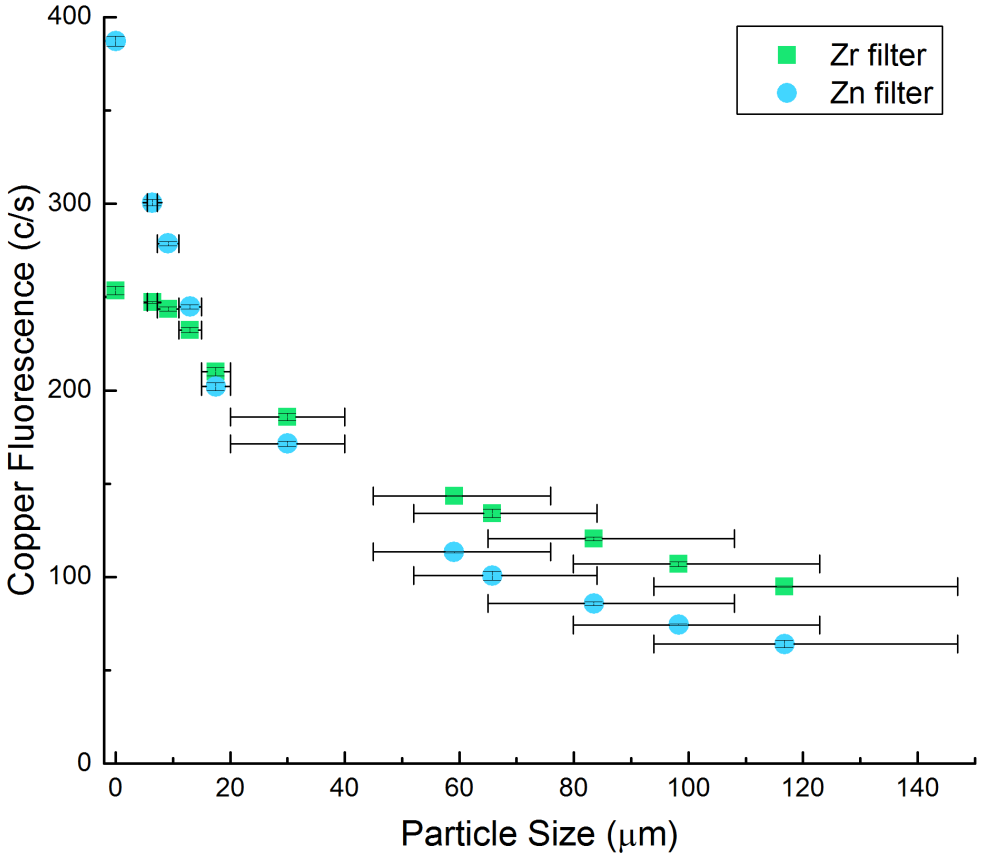


Figure 6-22: The change in copper fluorescence intensity with varying particle size, measured for samples with a 3% copper concentration in dough, prepared with different sized copper particles.

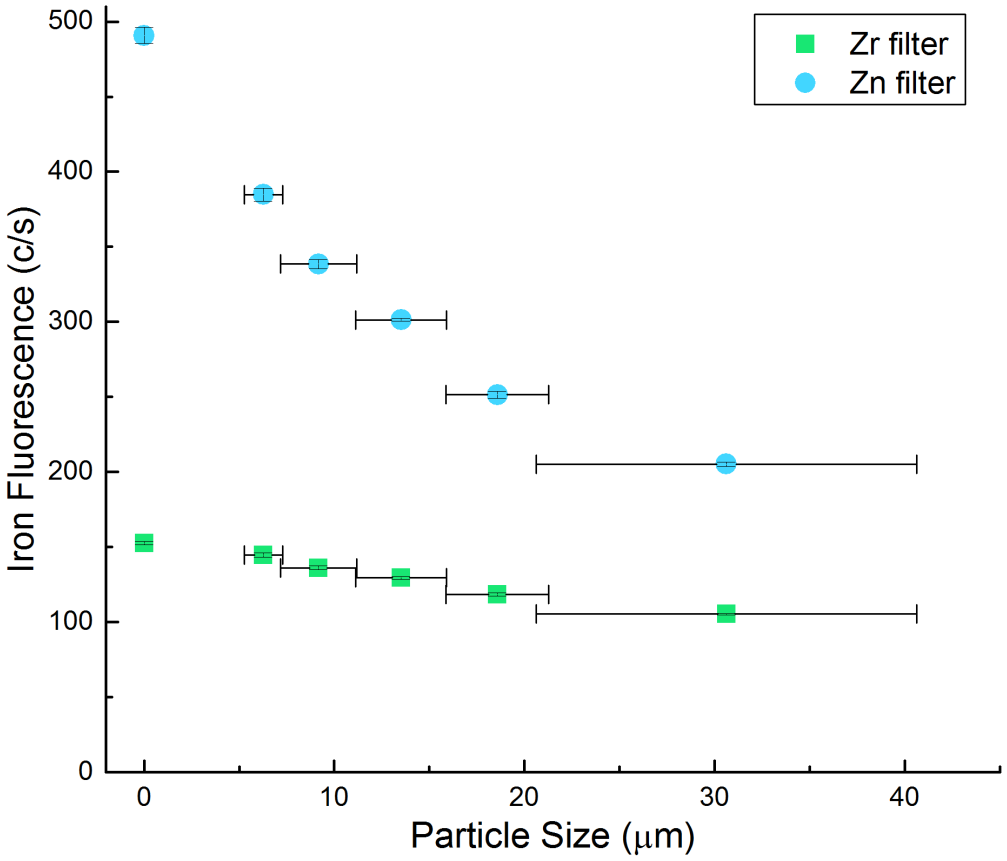


Figure 6-23: the change in iron fluorescence intensity with varying particle size, measured for samples with a 5% iron concentration in dough, prepared with different sized iron particles.

# 7 Developing a Particle Size Effect Correction Method

X-ray Fluorescence (XRF) is a portable technique that is often used to measure unprepared samples that have not undergone any sample preparation. In the mining industry, portable XRF is used for both exploration and monitoring during ore-processing. In exploration, portable XRF is used for measuring the elemental composition along rough bore cores where there are many surface, particle size and matrix effects. In processing plants, ore is often crushed and processed in slurry form, which can demonstrate significant particle size effects.

Developing a method that can be applied to measuring particulate samples and that corrects for the particle size effect would be extremely advantageous for measuring mineral slurries. Currently mineral processing plant XRF analysers need to be calibrated for mineral slurries of a given particle size. Over time, the average particle size of a slurry can vary due to changes in the ore or grinding processes, and as the particle size changes the calibration will become invalid. If the fluorescence response can be adjusted for the change in particle size of a slurry, it could significantly improve the accuracy of determining the elemental composition of the ore slurries.

This chapter describes the development of a simple XRF particle size correction method that could be potentially used to correct for particle size effects in mineral slurries.

## 7.1 Comparison between Experiment, Analytical and Monte Carlo Simulation Results

The first stage in developing a reliable correction method involves being able to accurately predict the particle size effect. While there are theoretical models for predicting the particle size effect, they often do not agree well with measured data due to simplifications necessary to make the analytical calculations tractable. Monte Carlo simulations allow a more comprehensive replication of particulate samples and other experimental set-up details, including a more accurate description of the source.

In this chapter, the experimental results presented in chapter 6 are compared with Monte Carlo simulation results, designed to replicate the experimental set-up, X-ray tube settings and filter details. Two simulation approaches - based on particulate and

Perlin noise function modelling, were used to simulate the particulate samples. Comparisons between the Monte Carlo and experimental results are shown in Figure 7-1 and Figure 7-2.

The results are also compared with the theoretically calculated particle size trend using formulae described in Lubecki et al.'s 1982 study [87]. Lubecki et al.'s model assumes that the exciting radiation is mono-energetic and that only first order fluorescence interactions occur.

Lubecki et al.'s model described in section 3.2.2 and calculated using equation 3.2:

$$I = \frac{I_0 \cdot p \cdot k_1}{\mu} \cdot \frac{1 - e^{-\mu \cdot p_z \cdot d}}{1 - \exp[-\left(\mu + \frac{1-w}{w} \cdot \mu^M\right) p \cdot p_z \cdot d]} \tag{3.2}$$

where $I_0$ is the intensity of the primary exciting radiation at the grain surface, w is the weight concentration of the fluorescent element in the sample, $d$ is the average linear dimension of a grain where $d$ is equal to two thirds of the diameter of a spherical grain, $\mu$ is the sum of the mass absorption coefficients of the fluorescent element for the primary and the fluorescent radiation, $\mu^M$ is the sum of the mass absorption coefficients of the non-fluorescent, matrix material for the primary and the fluorescent radiation, $p_z$ is the density of the fluorescent grains, $k_1$ is a constant that depends on some atomic parameters, and $p$ is a constant that depends on the density of the sample as described below. The parameter $k_1$ and the constant p are described by equations 3.3 and 3.4, given in section 3.2.2.

Lubecki et al.'s theoretical equation is designed to calculate the fluorescence intensity of a particular element contained in a particulate sample. A large number of parameters are needed, which is problematic if they are not all known. For example, in the case of the current experimental measurements the packing degree η is unknown. Rather than make assumptions about the values of uncertain parameters, a different approach was followed.

Equation 3.1 can be evaluated for a particle size so small it can be considered to be negligible (much less than the X-ray attenuation length of either incident or fluorescent radiation); below a certain particle size the fluorescence response should remain constant and be equal to the fluorescence response from a sample with no

particle size effects. The fluorescent intensity in this case is denoted $I_0$. The particle size effect is then calculated as the ratio $I/I_0$, which leads to a large number of parameters, such as the packing degree, cancelling out.

To compare the experimental and simulated results to theoretically predicted particle size trends, the counts per second of each measurement are normalised to the counts per second for the samples with no particle size effect, shown in Figure 7-3 and Figure 7-4.

It is immediately apparent from figures 7.1 through 7.4 that significant discrepancies exist, both between the results obtained using the different modelling approaches, and between the theoretical results and experimental observations. In particular, the experimentally observed particle size effect is significantly less pronounced than expected from either the Monte Carlo or Lubecki et al. models; equivalently, the effective particle size in the experimental samples is smaller than that assumed in the models. In the next sections, possible reasons for these discrepancies are explored.

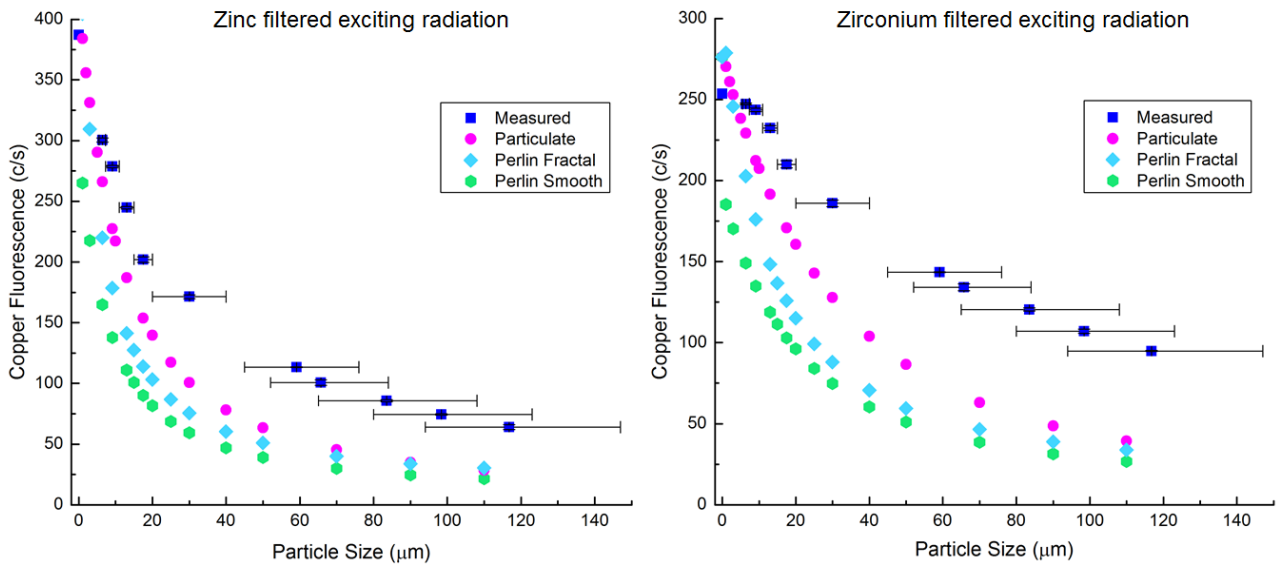


Figure 7-1: The measured particle size effect for samples containing 3% copper in dough compared with Monte Carlo simulations of the experimental set-up using the particulate and Perlin noise function modelling approaches.

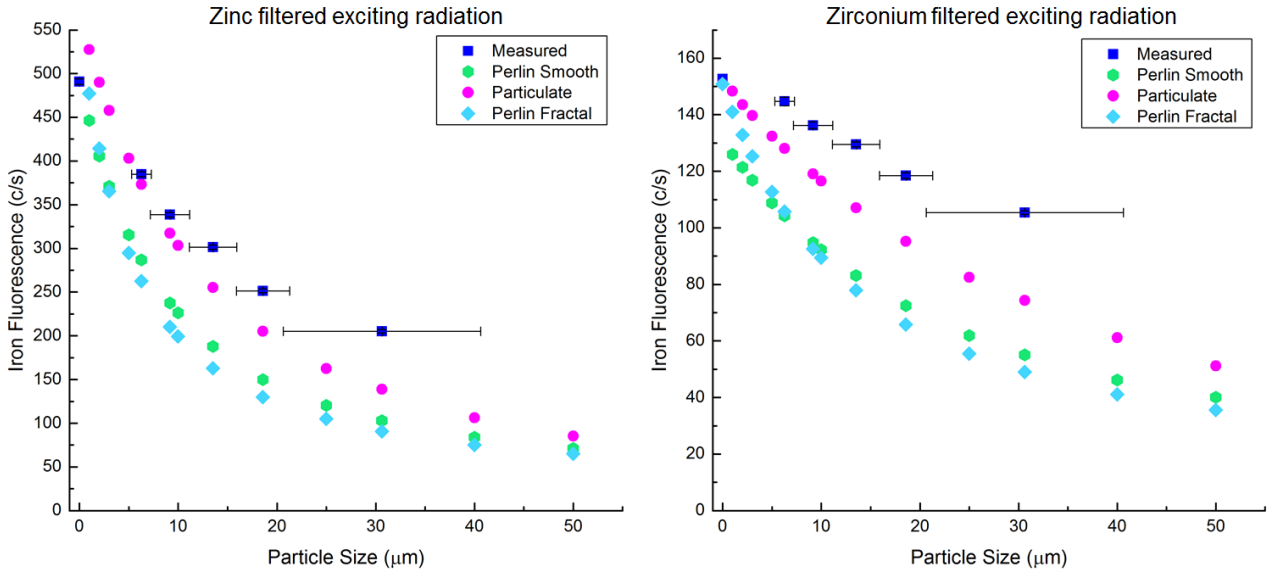


Figure 7-2: The measured particle size effect for samples containing 5% iron in dough compared with Monte Carlo simulations of the experimental set-up using the particulate and Perlin noise function modelling approaches.

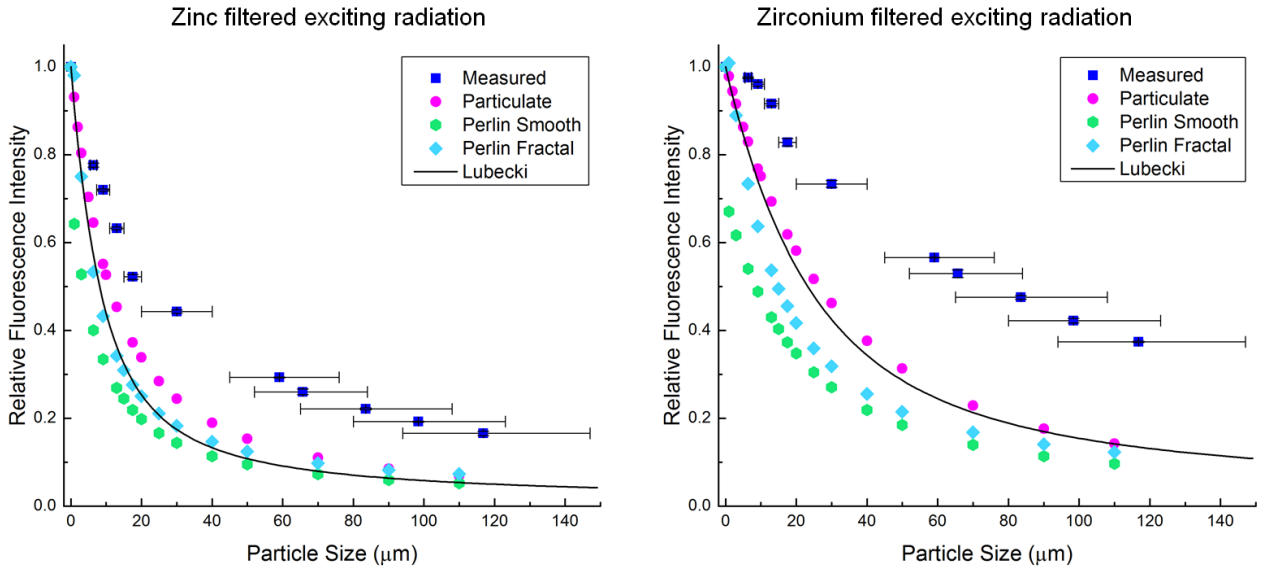


Figure 7-3: The measured relative particle size effect for samples containing 3% copper in dough compared with Monte Carlo simulations of the relative particle size effect using the particulate and perlin functions, as well as a theoretical prediction of the particle size effect using Lubecki et al.'s formula [87].

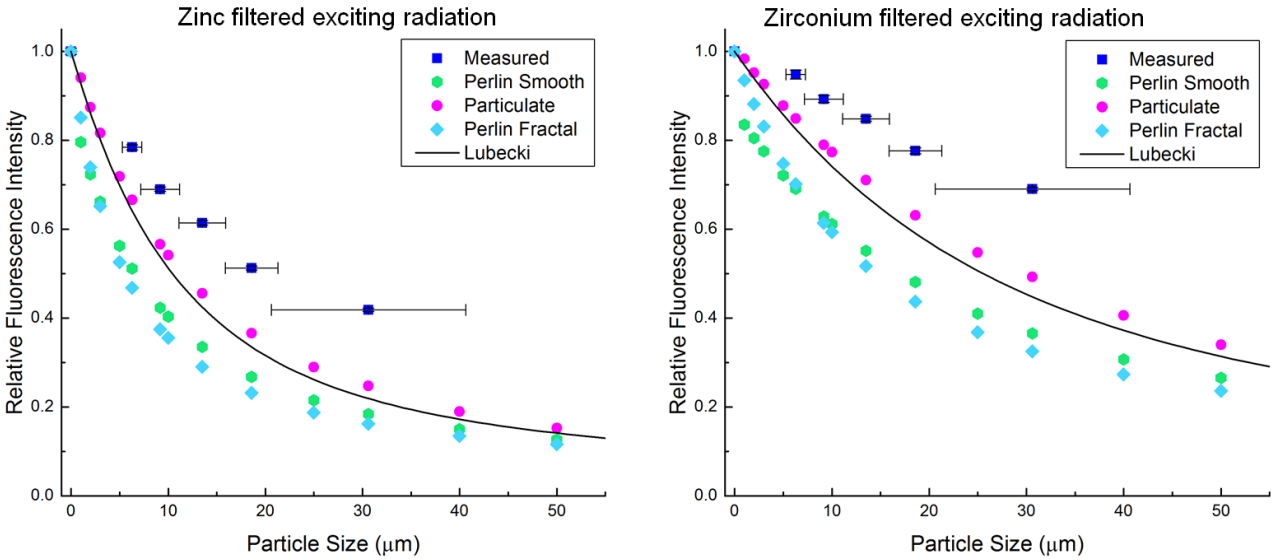


Figure 7-4: The measured relative particle size effect for samples containing 5% iron in dough compared with Monte Carlo simulations of the relative particle size effect using the particulate and perlin functions, as well as a theoretical prediction of the particle size effect using Lubecki et al.'s formula [87].

## 7.2 Discussion of Discrepancies between Experiment, Analytical and Monte Carlo Simulation Particle Size Results

### 7.2.1 The Perlin Noise Function Results

The particulate model results agree better with the experimental data than the Perlin noise function approach. This result was unexpected, as it was anticipated that the fractal Perlin noise method would better emulate the shape of the real particles compared to the spheres used in the particulate approach.

Particle modelling using the smooth Perlin noise function showed significantly lower fluorescence count rates than the fractal Perlin noise function for the copper case; however, in the iron case, the smooth Perlin noise function returned a higher count rate than the fractal case for particles above 10 μm. In both copper and iron cases however, both Perlin approaches return count rates significantly less than those obtained using the particulate approach, resulting in a more significant particle size effect.

A closer look was taken at size distribution of the particles generated by the fractal and smooth Perlin noise functions for the copper case. Figure 7-5 show an enlarged 1 $cm^2$ simulated section of the dough sample with 3% copper particles dispersed throughout the sample. In both cases, particles with a wide range of sizes are present, and this is particularly pronounced in the fractal model case.

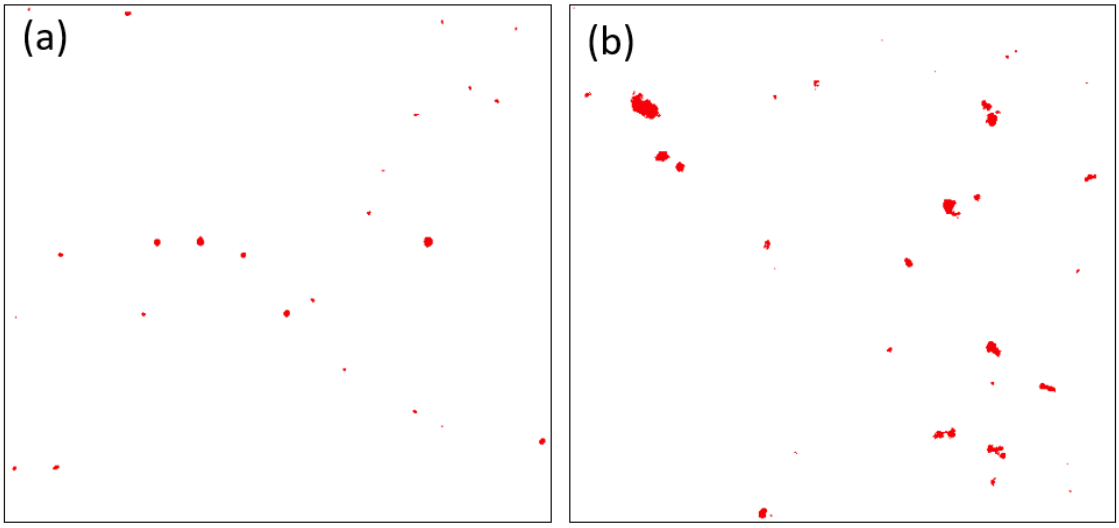


Figure 7-5: The distribution of copper particles from a 1 $cm^2$ region on the surface of a dough sample containing 3% copper particles generated using (a) the smooth Perlin noise function and (b) the fractal Perlin noise function

The simulated particle size distribution is estimated using a stochastic method, with randomly positioned and orientated 'rays' traced through the particulate material to sample the chord length distribution inside particles. The median chord length is equal to two thirds of the equivalent sphere diameter. Xpert allows the user to plot the distribution of chord lengths (expressed as the equivalent sphere diameter) of the Perlin particles. Figure 7-6 and Figure 7-7 shows the equivalent diameter distribution for both the fractal and smooth cases, both with a scale parameter chosen to give an average equivalent sphere diameter of 100 µm for the 3% copper particles in dough.

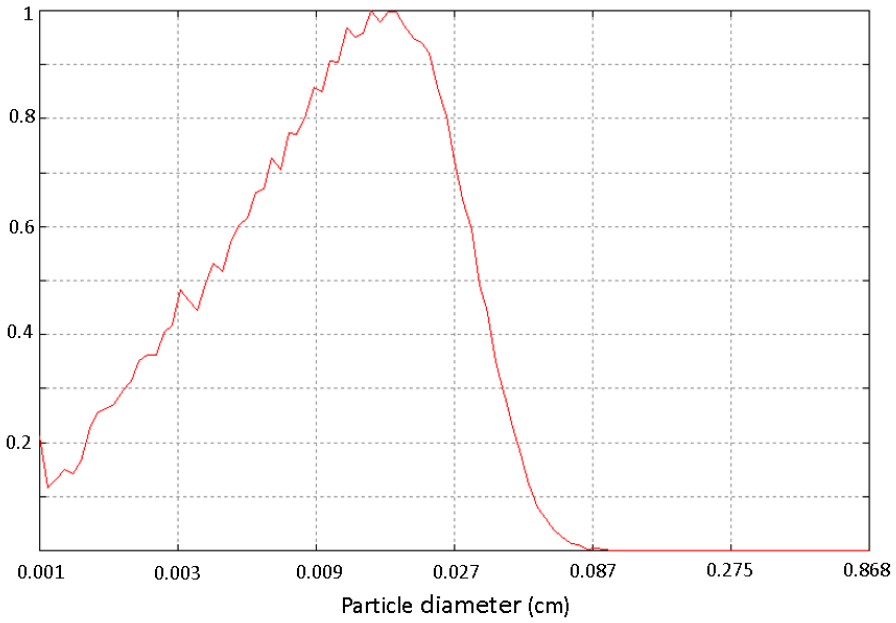


Figure 7-6: The particle equivalent sphere diameter distribution of copper particles calculated using the fractal Perlin noise function with a scale parameter set to give an average equivalent sphere diameter of 100 µm. Note the logarithmic scale on the X-axis.

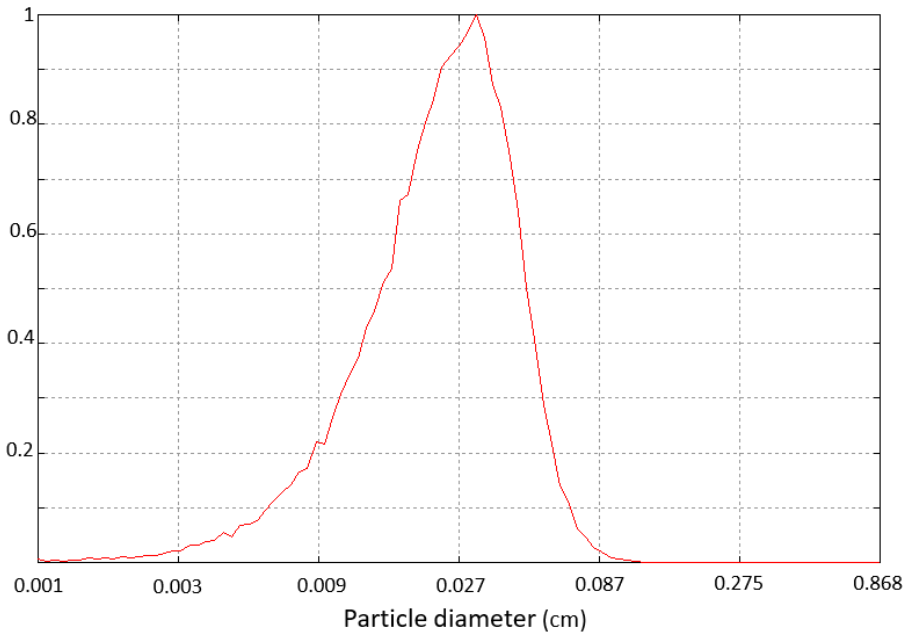


Figure 7-7: The particle equivalent sphere diameter distribution of copper particles calculated using the smooth Perlin noise function with a scale parameter set to give an average equivalent sphere diameter of 100 µm. Note the logarithmic scale on the X-axis.

Despite both samples having the same average equivalent sphere diameters, the distributions of equivalent diameters are significantly different. The fractal Perlin noise function gives a particle size distribution varying from approximately 10-400 µm, whereas the smooth Perlin noise function has a narrower particle size distribution ranging from approximately 50 to 500 µm. The fractal Perlin function includes a larger proportion of smaller particles, which will contribute to higher fluorescence intensities than for the smooth Perlin noise function with the same equivalent sphere diameter.

The particle size distributions were further examined using simulated images of particles on the surface of each sample, such as the two images in Figure 7-5. Three separate images of 1 $cm^2$ regions of a sample containing 3 % copper particles in dough were generated. Matlab scripts were written to count the number of particles and estimate their areas, measured in pixels. These 2-dimensional results provide qualitative information about the 3-dimensional structure of the solid modelled particles.

For the overall 3 $cm^2$ region examined, a total of 135 particles were detected for the fractal Perlin case. The area of each particle was measured in pixels. The particles are separated into fractions depending on their area, as shown in Table 7-1. The total area of the particles in each area fraction are summed and shown in the fourth column of Table 7-1 expressed as the percentage of the total area. Whilst the majority of the particles have an average diameter less than 100 µm, these particles account for less than 15% of the total area. In contrast, less than 10% of particles have an average diameter greater than 200 µm, but they account for more than 40% of the total area in the region examined. Extending to 3 dimensions, the largest particles will account for an even greater share of the overall particle volume.

With the majority of the copper volume being accounted for by large particles, the overall surface area of copper particles in the sample will be significantly lower than a sample created using the particulate function. For example, based on the approximate diameters of the particles examined, the total copper volume in the surface layer is approximately $2.08 \times 10^8$ $\mu m^3$ while the total surface area of copper in the sample is approximately $5.88 \times 10^6$ $\mu m^2$. For the same copper volume, using the particulate

function to insert spheres with 100 µm diameters, the surface area would be 1.25 × $10^7$ µm$^2$. The particulate function gives more surface area per unit copper volume which leads to more fluorescence and a lower particle size effect.

The equivalent diameter distribution for the smooth Perlin noise function, shown in Figure 7-7, shows that an even greater percentage of particles have diameters larger than 100 µm, and there is a commensurate decrease in the number of very small particles. The significant fraction of large particles in the smooth Perlin noise function simulations will cause a significant reduction in the copper fluorescence from the sample compared to the fractal case, as seen in Figure 7-1.

In the iron sample case, the fractal Perlin noise simulation shows a larger particle size effect than the smooth case; however in both fractal and smooth cases, the equivalent sphere diameter range is so large that an increased particle size effect is observed compared to the particulate model.

The wide particle size range obtained with the Perlin function provides a poor comparison with the narrow particle size ranges measured experimentally. The largest particle size range measured was approximately 50 µm, which is significantly smaller than the particle size range obtained using either Perlin function. The Perlin function does not give the user any control over the particle size range or distribution, other than specifying the equivalent sphere average particle size. This limitation precludes an accurate quantitative comparison with the experimental measurements.

Table 7-1: Particles are generated using a fractal Perlin function to create a 3% copper sample, where the median particle diameter is 100 μm. The number of particles and their area are examined and sorted into fractions depending on how many pixels are in each particle, reported as the 'Area'. The equivalent sphere diameter for each area fraction is given for comparison. The percentage of each area fraction to the total area is reported.

| Area (pixels) | Average Diameter (um) | No. of Particles | % total area |
|---|---|---|---|
| 0-10 | 20-70 | 71 | 5.2 |
| 10 to 20 | 70-90 | 14 | 5.0 |
| 20-30 | 90-120 | 12 | 7.5 |
| 30-40 | 120-135 | 7 | 6.0 |
| 40-50 | 135-150 | 4 | 4.8 |
| 50-60 | 150-165 | 8 | 11.1 |
| 60-70 | 165-180 | 3 | 4.6 |
| 70-80 | 180-195 | 3 | 5.8 |
| 80-90 | 195-205 | 2 | 4.2 |
| 90-100 | 205-215 | 1 | 2.4 |
| 100+ | 215+ | 10 | 43.5 |

### 7.2.2 The Particulate Model Results

In contrast to the Perlin model, the particulate model allows for precise control of particle diameter. However, particles are constrained to be spherical in shape.

In practice, the experimental shapes of the metal particles used were far from spherical. Figure 7-8 shows photographs of the copper particles from the three sieved size-fractions taken using a 200x zoom USB microscope. Unfortunately the microscope did not have enough magnification to see the smaller cyclosized particles clearly, and no other microscopes with a greater zoom were available.

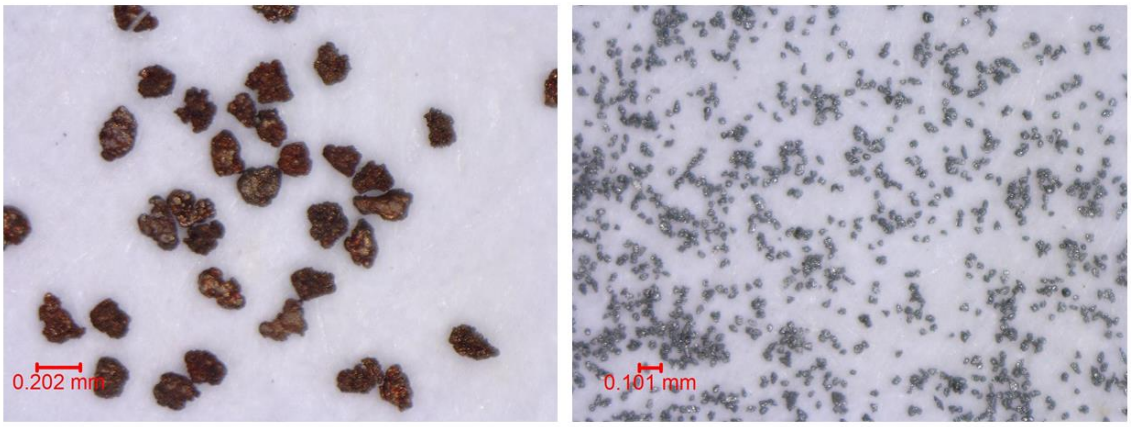


Figure 7-8: The left panel shows copper particles from the sieved 90-106 um fraction and the right panel shows the cyclosized iron powders in the 20-40 µm fraction.

The particles in Figure 7-8 are irregular with a rough surface finish. Some of the particles are more oblong than spherical and others appear to be broken, shard-like shapes. These particles are expected to give a larger fluorescence response than particles modelled as spheres with the same equivalent diameter, due to their larger surface area. This would account qualitatively for the differences between the measured particle size effect and the Monte Carlo simulated particle size effect using the particulate function.

Both of the Monte Carlo particle modelling methods used in this study so far have shortcomings.

The Perlin noise function approach, whilst producing particle shapes that more closely resemble those seem experimentally, provides only limited control over the particle size, with size distributions covering several orders of magnitude. The experimental particle size distributions are much narrow, with size ranges typically just 1-13% of the size ranges obtained using the Perlin noise function. As a result, particle size effects modelling using the Perlin noise function method agree poorly with the experimental data. For this study using narrow particle size fractions, only the particulate function can be used to model the particle size effect with reasonable accuracy, but differences in particle shape need to be accounted for as discussed later.

### 7.2.3 Effect of Uncertainty in Filter Thickness

The Monte Carlo modelling assumes that the thicknesses of the filters used to shape the energy spectrum of the incident X-ray beam are well-known. Any uncertainty in the thickness could translate to uncertainty in the incident beam energy, and hence perhaps the particle size effect magnitude.

The zinc filter in particular, was only available as thin foil that had to be folded over multiple times to give the desired thickness. This could introduce inconsistencies into the thickness of the foil.

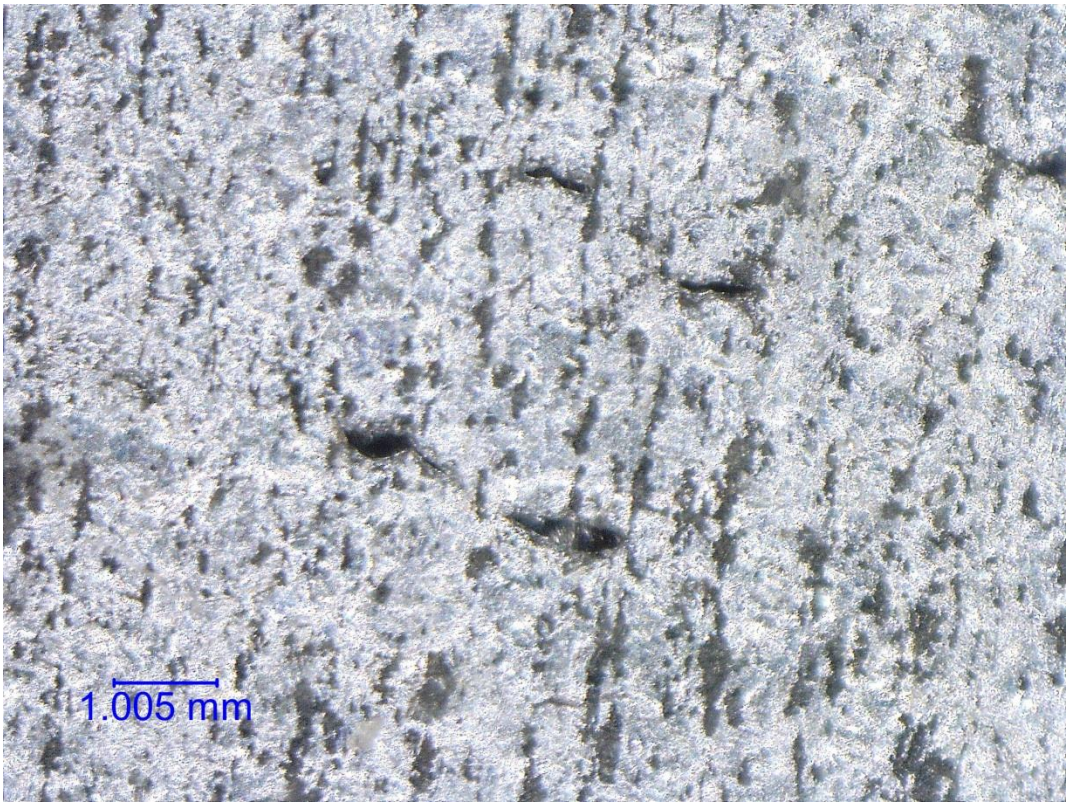


Figure 7-9: Close up image of the zinc foil used showing tears and holes in the foil.

Figure 7-9 shows a close up image of the zinc filter that reveals some tears. This confirms that the zinc filter has localised inconsistencies in thickness. The true thickness of the small region of the foil that is filtering the exciting radiation may then be different from the average. To check for potential impact on the particle size effect modelling, the Monte Carlo simulations of the 3% copper sample were repeated with

the zinc filter thickness varied by 10%. The Monte Carlo simulations with varying zinc filter thickness are compared to the experimental data in Figure 7-10.

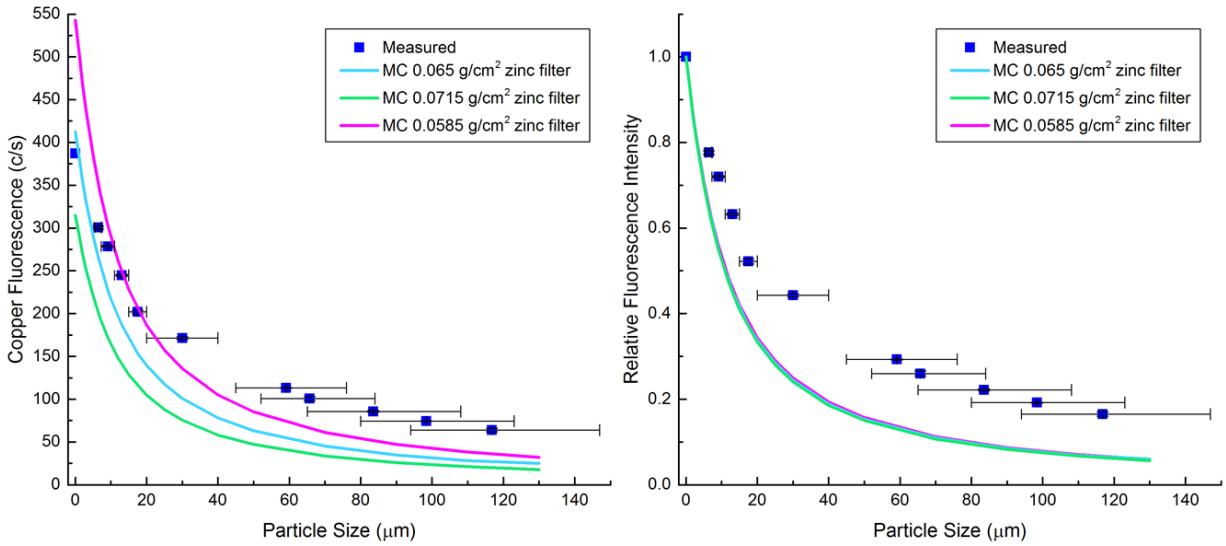


Figure 7-10: The measured particle size effect for samples containing 3% copper in dough compared with Monte Carlo simulations of the relative particle size effect using the particulate function with varying zinc filter thickness. 0.065 g/cm$^2$ is the measured thickness of the zinc filter used in the experimental measurements, and 0.0715 and 0.0585 g/cm$^2$ are the measured thickness plus or minus 10%, respectively. The left panel shows the absolute c/s measurements, and the right panel shows the normalised relative values.

Variances in the thickness of the zinc filter significantly affect the copper count rate; however the shape of the decrease in fluorescence intensity with increasing particle size does not change with varying zinc filter thickness. Inconsistencies in the zinc filter will cause large changes in the copper count rates measured and using poor quality filter materials will adversely affect the direct comparison with Monte Carlo simulations. However as shown in the right panel of Figure 7-10, once if the values are normalised, it cancels out the large differences in intensity. Future measurements can be normalised to a measurement of a sample with no particle size effects to cancel out inaccuracies in the simulated experimental set-up.

### 7.2.4 Analytical Results

Using Lubecki's formula to predict the particle size trend is limited only to situations where the data can be normalised, so that the unknown parameters in Equation 3.1 can cancel out, as discussed in section 7.1. However, once the data is normalised there is good agreement between the Monte Carlo particulate model and the calculated values. This is not unexpected as both models assume the particles are spherical. As shown in Figure 7-8 the particles used for the experimental measurements are not spherical but completely irregular in the size. Lubecki's model is limited at predicting the particle size effect of irregular shaped particles using spherical particle, due to the larger surface area of the irregular shaped particles. This is suspected to be the main reason for the large differences between the measured results and the calculated results.

Lubecki's model also assumes that the exciting radiation is mono-energetic and does not include secondary or tertiary fluorescence. These limitations contribute to the small differences between the particulate model simulated data and the calculated data.

## 7.3 Dual Energy Correction

For most real-world X-ray fluorescence applications measuring particulate materials, both the sample composition and the particle size will be unknown. To enable the composition to be determined without particle size information, the sample is measured using two different exciting radiation energies. To transform the two different fluorescent responses of the sample into a useful particle size correction, it is important to have a reasonably accurate method to Monte Carlo simulate the particle size effect of a sample with a similar composition to the sample being measured. This section will explore using Monte Carlo simulations to develop a simple particle size correction to improve the accuracy of using XRF to measure particulate samples.

### 7.3.1 Particle Size Effect Correction using Multiple Exciting Radiation Energies

The proposed correction method involves using the measured ratio I1(s)/I2(s) to determine the size of the particle size effect I1(s)/I1(0). Here I1 and I2 are the

intensities of the fluorescence from the element of interest, excited using low-energy and high-energy sources respectively. The notation (s) denotes measurement of the target sample and includes particles size effects; (0) denotes measurements of a hypothetical sample with no particle size effect. The ratio I1/I1(0) is a measure of the particle size effect, and is equivalent to the relative fluorescence intensity shown in Figure 7-3 and Figure 7-4.

While I1(s)/I1(0) can be measured experimentally using the methods described above, it is unrealistic to perform these experimental measurements for every possible sample that could be analysed. Instead, the proposed particle size correction method relies on predicting I1(s)/I1(0) from the corresponding measured I1(s)/I2(s) value. The relationship between the two quantities is determined for a range of particle sizes and/or sample compositions using Monte Carlo simulation. The Monte Carlo results can then be used to determine a mapping that allows the measured I1(s)/I2(s) values to be mapped to the corresponding I1(s)/I1(0) value, thereby allowing the particle size effect to be estimated and corrected.

For the proposed particle size correction method to work, it is essential that the relationship between I1(s)/I1(0) and I1(s)/I2(s) can be predicted with reasonably accuracy using Monte Carlo simulation. The experimentally measured I1 and I2 values for the 3% copper in dough and 5% iron in dough samples are used to plot I1/I2 against I1/I(0); these data are compared to values determined using the Monte Carlo simulation using the particulate method and also the values predicted using the Lubecki theoretical model. The particle size correction results for copper and iron are shown in Figure 7-11 and Figure 7-12.

The x-axis error bars on each measured data point are the sum-in-quadrature of the errors for each of the I1 and I2 values used. The y-axis error bars on each measured data point are the sum-in-quadrature combination of the errors on the I1(0) and I1 measurements. In both cases, the individual I1(0), I1 and I2 errors are the relative errors on the counts per second values.

Despite being a significant source of error, the errors due to the particle size ranges involved with each measurement cannot be directly shown on these correction figures.

Both the x and y axis values on the correction figures are associated with fluorescence intensity measurements, and there is no way to measure the error on the fluorescence intensity due to the particle size range. For example, the CS3 copper particles have a range of 11 – 15 µm, with a midpoint of 13 µm. The fluorescence intensity of these particles is measured, and assumed to be representative of a 13 µm sample. There is no way to measure the fluorescence intensity at 11 and 15 µm to determine the error on the fluorescence intensity due to the particle size range, and so the error cannot be shown in the correction figures. This becomes particularly problematic for the larger particle size fractions, especially the CS1 size fraction of both copper and iron powder and the sieved particle size fractions of copper powder. The CS1 cyclosized powder fractions have large particle size ranges due to the difference in the sieve sizing cut-off of 40 µm, and the cyclosized powder's first cut being approximately 20 µm for both iron and copper powder. The sieved particle size fractions of copper powder have large particle size ranges due to the inaccuracy of the sieving method, as discussed in section 6.1.1.

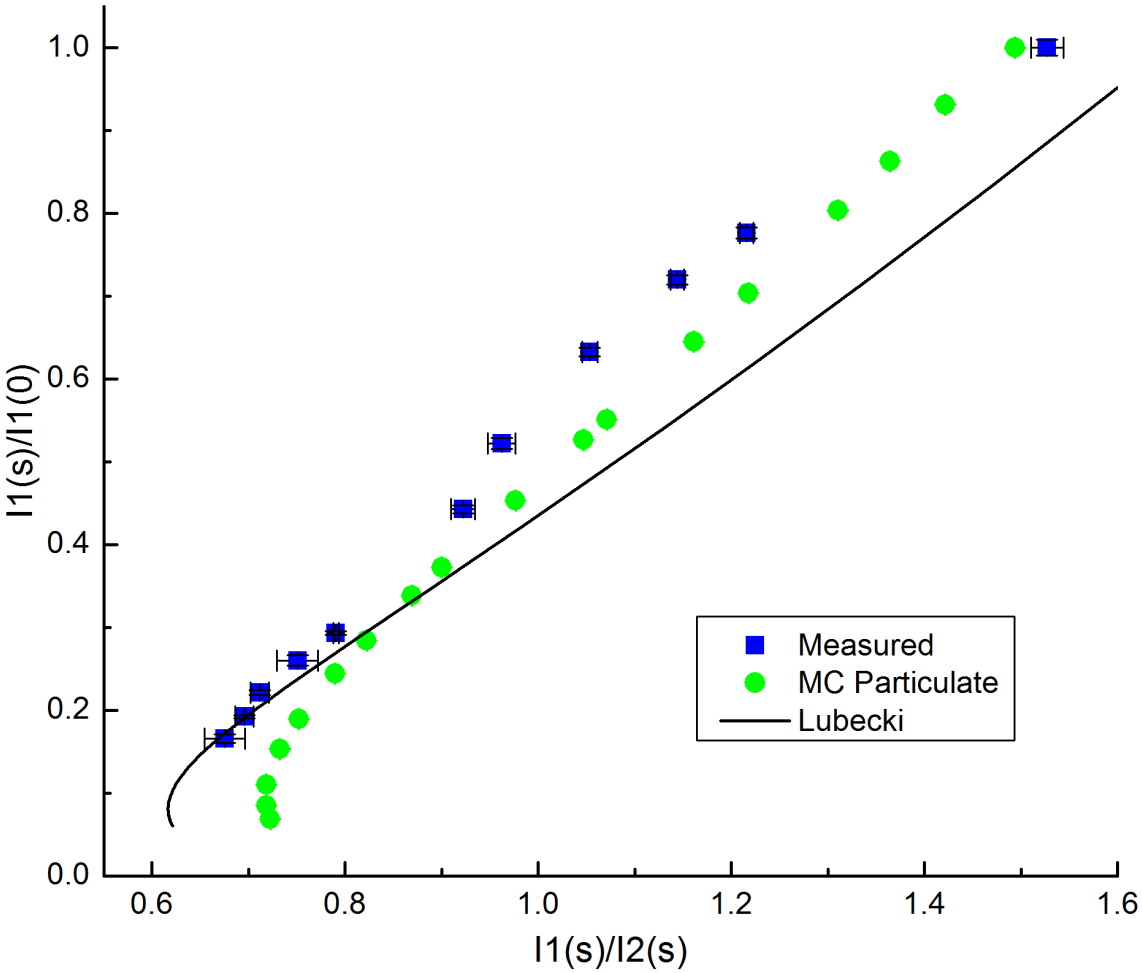


Figure 7-11: I1/I2 vs I1/I1(0) for a measured 3% copper in dough sample compared to Monte Carlo simulated data using the particulate function, MC Particulate, and the corrected equivalent smooth sphere diameter values, MC Particulate ESD, and theoretically predicted data using Lubecki et al.'s theoretical model.

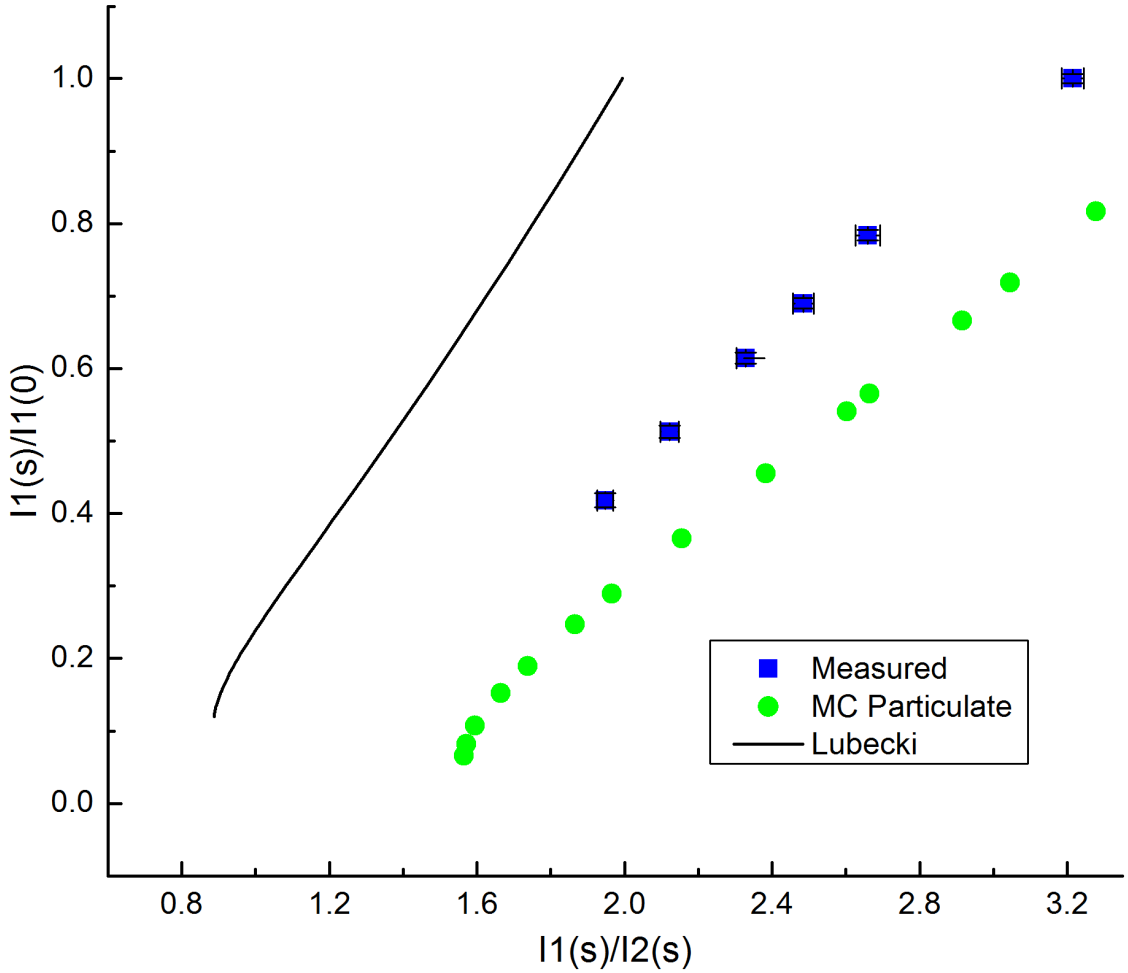


Figure 7-12: I1/I2 vs I1/I1(0) for a measured 5% iron in dough sample compared to Monte Carlo simulated data using the particulate function, MC Particulate, and the corrected equivalent smooth sphere diameter values, MC Particulate ESD, and theoretically predicted data using Lubecki et al.'s theoretical model.

The copper powder Monte Carlo simulated data using the particulate function agrees better with the measured data than the Lubecki model for majority of the measured data points shown in Figure 7-11. As the particle size becomes larger, characterised by a smaller I1/I1(0) value, the Lubecki model agrees better with the measured data.

The iron powder Monte Carlo simulated data using the particulate function agrees best with the measured data as shown in Figure 7-12. The Lubecki theoretically calculated values of I1/I2 vs I1/I1(0) agree poorly with the measured data.

At the low intensity I1(s)/I1(0) copper measured data points, for a given I1(s)/I2(s) value, the Monte Carlo simulated I1(s)/I1(0) values can vary by up to 0.1 compared to the measured I1(S)/I1(0) values, and for low values of I1(s)/I1(0) a 0.1 difference can lead to a relative error of up to 35%. The differences in the I1(s)/I1(0) vs I1(s)/I2(s)trends between the Monte Carlo simulated values and the experimental values will introduce errors when using the I1(s)/I1(0) values to correct for the particle size effect, especially for the low intensity I1/I1(0) values, which correspond to large particle sizes.

The poor correction values given from low I1(s)/I2(s) values can be avoided by only allowing the correction for a given range of I1(s)/I2(s) values. In the copper powder example given above, the correction values span over a particle size range up to 120 um, with the poor correction values resulting from the larger particle sizes. The range of I1(s)/I1(0) values is extremely large, and for majority of these values the correction will improve the copper counts measurement significantly, compared to the case with no correction and an unknown particle size sample being measured.

## 7.4 Future work: Improvements to the Quantitative Comparison of Simulation and Experimental Results

In this chapter so far, a simple method has been described for correcting for the particle size effect that involves measuring a sample with two different exciting radiation energies and using a correction function determined via Monte Carlo simulation to reduce particle size effects. The method has only been applied so far in its simplest form, and there is room for significant improvement, particularly with the (dis)agreement between measured and simulated data. Potential improvements are

discussed in the following sections and will be the subject of additional study, outside the scope of this thesis.

Considering that the simulation is performed from first principles and includes modelling of the X-ray tube output, sample geometry, and detection efficiency, the agreement with the experimental data is generally very good. However, model-data discrepancies of order 20% in individual simulations are observed, and whilst this variance might be acceptable in some applications, for the current correction method involving the absolute count measurements of I1(s) and I2(s), the uncertainties lead to a significant disagreement between the measured and simulated I1(s)/I11(0) and I1(s)/I2(s) values.

The factors that contribute to the discrepancies between simulated and experimental measurements can be split into two groups. The first group contains the factors associated the unrealistic modelling of the sample due to the use of the particulate function. As discussed in section 7.2, there is currently no method available to simulate realistically shaped particles with fine control of particle size. Instead the particulate function is being used to model the particles as spheres. Spheres minimise the surface area of the particle, which in turn increases the particle size effect. With a more realistic particle size shape as shown in Figure 7-8, the surface area will be greater and as a result the particle size effect will be less.

The second group of factors contributing to the inconsistencies between the Monte Carlo simulations and experimental data are associated with performing the simulations from first principles. The simulations include modelling of the X-ray tube output, sample geometry, and detection efficiency. Uncertainties in measurements such as the filter thickness, the distance between the X-ray tube, sample and detector or the sample geometry can cause errors in the absolute count rate measurement. In section 7.2.3 issues with inconsistencies in the thickness of the zinc filter are discussed. A small error in the measurement of the thickness of the zinc or zirconium filters will result in large differences in the intensity of the source simulated using the Ebel model.

The following sections discuss possible methods for minimising the uncertainties in the Monte Carlo simulations.

### 7.4.1 Standards Method

A simple standards method is considered to eliminate some of the uncertainties in the Monte Carlo simulations. Standards are often used to calibrate X-ray Fluorescence (XRF) systems, where a sample of known concentration is measured and the corresponding XRF response is compared to the concentration of each element. In the particle size correction case, measurements of known standards could be used to cancel out many of the unknowns in the Monte Carlo simulation.

One factor that cannot be easily modelled is the thickness inconsistencies in the zinc foil that compromise the zinc filter. Even small uncertainties in the filter thickness can result in significant uncertainties in the fluorescent count rate predicted by the Monte Carlo simulations. Figure 7-10 shows that varying the measured zinc filter by ± 10% can vary the absolute count rate by up to 30%, however these discrepancies cancel out completely when the data is normalised to the measurement of a sample with no particle size effects.

To use the standards method to correct for the inconsistencies in the experimental set-up, first a known sample with no particle size effects would be measured. A sample with no particle size effects and a known composition should be used to create the simplest case for the modelling the sample with a Monte Carlo simulation. The known sample should have as similar a composition to the samples being measured as possible, to make the correction as simple as possible.

When the unknown particulate sample is measured, the count rate can be normalised to the count rate of the known sample. The Monte Carlo simulations for the range of particulate materials being modelled could then be normalised to the simulation results for the known sample, for example by adjusting the simulated source strength. The comparison between the simulated normalised data and the measured normalised data should improve due to the normalisation with the known standard. Any count rate discrepancies due to uncertainties in the factors modelled using a first principles Monte Carlo simulation method, as well as any uncontrollable errors in the

experimental set-up, should cancel out, especially if the samples have similar compositions.

Future work will involve measuring a range of standards with both exciting radiation energies and comparing the normalised experimental and simulated data. While this method will not compensate for the poor comparison of data due to the poor modelling of the particulate materials themselves, it should improve the agreement of the intensity of the count rate data, especially for the zero particle size measurement I1(0).

### 7.4.2 Particle Shape Effects

The major drawback of the particulate modelling approach is the assumed spherical particle shape, which leads to an overestimate of the particle size effect in the model. To overcome this problem, and to allow the particulate approach to be used to model the fluorescence response from non-spherical particles, the concept of "equivalent smooth sphere diameter" (ESSD) is introduced. The ESSD of a material with non-spherical and/or non-monosized particles is defined to be the diameter of spherical particles that give the same measured drop in fluorescence as the real measured particles. For example, in Figure 7-1, the measured particles with a mean particle size of 28 μm gives an intensity drop ratio I/I(0) of 0.79; the equivalent particulate function simulated spherical particle diameter that gives the same intensity value drop of 0.79 is 8 μm.

As an example of this method, the ESSD for each measured iron particle size fraction was determined and the relationship between the measured particle mean diameters and their ESSDs are plotted in Figure 7-13.

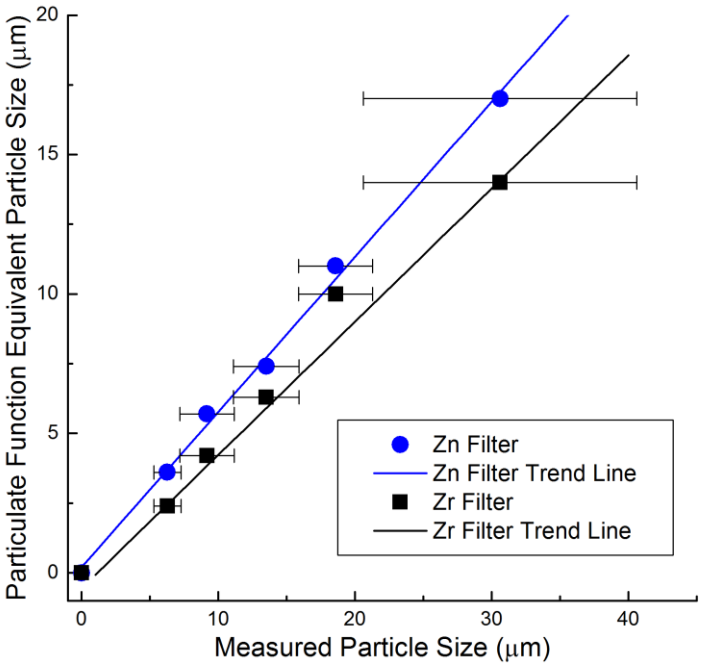


Figure 7-13: The relationship between the measured particle size and the equivalent smooth sphere diameter, defined as the particle size modelled using the particulate function that gives the same drop in intensity measured experimentally. The equivalent smooth sphere diameter is plotted for iron powder measurements, measured with both the zinc and zirconium filtered exciting radiation. For each case a trend line is also included to show the linearity of the relationship between the measured particle size and the particulate function calculated equivalent smooth sphere diameter.

A simple coefficient can be used to correct the experimentally measured particle size to an ESSD diameter that can then be substituted into the Monto Carlo particulate function simulation to give a much more accurate response. The coefficient is determined by the linear trend line that best fits the data points and the origin of the plot. In the iron case the coefficients for both the zinc and zirconium filtered exciting radiation trend lines are given in Table 7-2.

Table 7-2: The coefficients a and b are listed for the four different ESSD correction trend lines shown in Figure 7-13, as well as the $R^2$ values to indicate the goodness of the fit of the trend line to the data.

| Element | Exciting radiation Filter | ESSD coefficient | $R^2$ |
|---|---|---|---|
| Fe | Zr | 0.474 | 0.985 |
| Fe | Zn | 0.566 | 0.996 |

The Monte Carlo simulations using the particulate modelling approach are repeated using the equivalent smooth sphere diameter values for the particle diameters; calculated using the linear ESSD correction function using the ESSD coefficients given in Table 7-2. The new particulate simulated results are compared to the measured iron results in Figure 7-14.

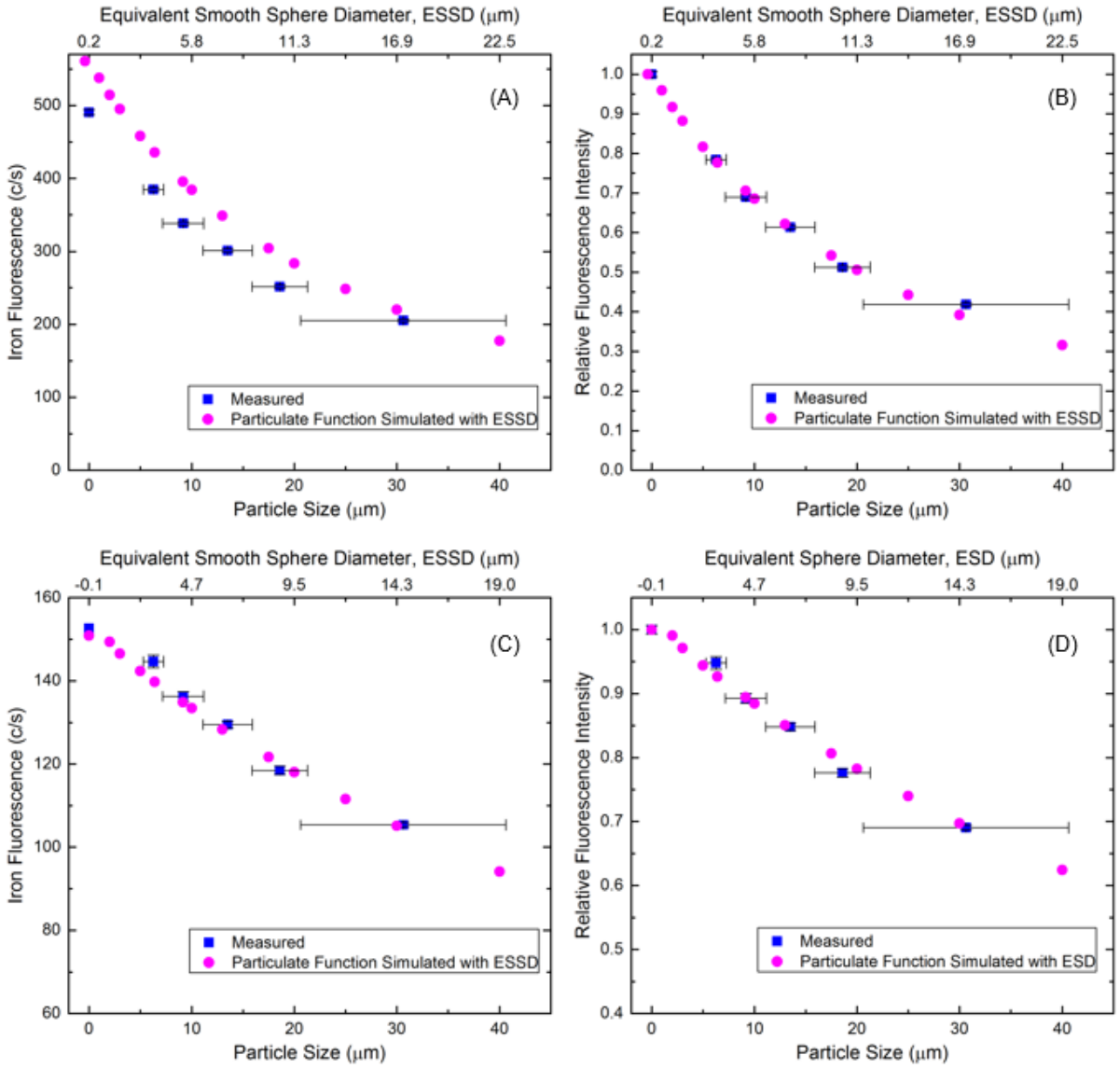


Figure 7-14: The measured particle size effect for samples containing 5% iron in dough compared with Monte Carlo simulations of the particle size effect using the particulate function and the equivalent smooth sphere diameter particle size. The top two panels, (A) and (B), show the zinc filtered exciting radiation case and the bottom two panels, (C) and (D), show the zirconium filtered exciting radiation case. (A) and (C) show the fluorescence response in counts/second while (B) and (D) show the fluorescence response normalised to the sample with no particle size effects.

In each case there is a disagreement between the simulated and the measured absolute count rates; the disagreement is significant for the zinc filtered exciting radiation case, but minimal for the zirconium filtered exciting radiation case. Each dataset is normalised to the case with zero particle size to show that the shape of the Monte Carlo simulated particle size effect data with particle diameter now agrees well with the measured data. This suggests that the ESSD is a reasonable correction to make to simulate the particle size effect from non-spherical particles using a simple spherical model.

The determination of the ESSD correction coefficients is an empirical calibration used to improve the accuracy of the Monte Carlo simulation method for predicting particle size effects. Depending on the type of material being analysed, particle shapes and surface roughness, the correction coefficient will vary. For each material being measured, the ESSD correction would also have to be determined. Measurements of a wider range of materials will give useful insight into how the ESSD correction coefficients will change between materials.

Correcting for the particle shape is not enough alone. The correction method involves using the raw counts I1(s) and I2(s) to correct for the particle size effect. If the absolute count measurements simulated do not agree well with the measured values, then the measured ratio I1(s)/I2(s) will not align to the true I1(s)/I1(0) value, as predicted by the Monte Carlo simulations.

The previous section discussed methods that could be used to correct for the absolute intensity of the count rates being simulated by normalising the measured count rate to the count rate of a prior measured known standard. Future work will involve combining both corrections to help mitigate the limitations of using the Monte Carlo simulations to predict the I1(s)/I2(s) and I1(s)/I1(0) values used in the particle size correction method.

### 7.5 Future Work: Particle Size Correction of Unknown Materials

Using Monte Carlo simulations to predict the particle size effects of a material currently relies on knowing the composition of that material. For samples with

unknown concentrations, a figure can be constructed with a range of possible concentrations.

Fortunately, for the application of analysing minerals process slurries, it is likely that the composition of the slurry matrix material will not vary greatly within a given stream in a particular plant. For the sake of the particle size correction, the matrix elemental content can be approximated and the element of interest content can be varied to create multiple correction lines for the correction figure.

Figure 7-15 shows the predicted particle size correction trends for 3 different slurries, consisting of silica and water and varying copper content from 1-5%. Figure 7-15 can be used to determine an approximate range for the particle size correction from a silica matrix slurry with an unknown copper concentration. For example, if an unknown sample is measured using the proposed method, and returns the copper fluorescence values I1(s) = 480 c/s and I2(s) = 460 c/s, then I1/I2 = 1.04. Figure 7-15 shows an example of reading the figure to determine the I1/I1(0) value from the I1/I2 value. As shown on Figure 7-15, the corresponding range of I1/I1(0) = 0.52-0.64. An average correction value of 0.58 can be used and the original value of I1 is now equal to I1/(I1/I1(0)) = 480/0.58 = 828 c/s.

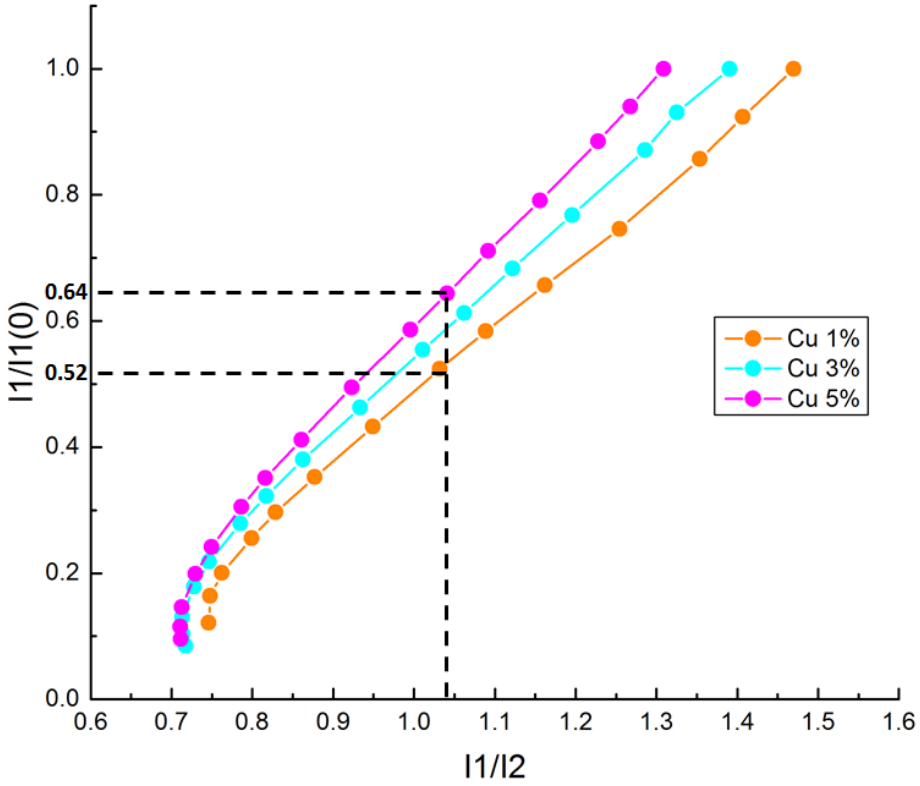


Figure 7-15: I1(s)/I2(s) vs I1(s)/I1(0) for Monte Carlo particulate function simulated silica and copper slurries containing 1%, 3% and 5% copper concentrations. An example measurement of I1(s)/I2(s) of 1.04 and the corresponding I1(s)/I1(0) range over the different concentration curves is shown.

The particle size correction can be more accurate if an iterative approach is used. The particle size effect is also a function of the overall sample composition, and the correction will be included in a fundamental parameters approach for determining the sample composition. An iterative approach would involve measuring the intensities of the relevant elements, correcting for the particle size with the assumed 'average' composition from the particle size correction figure. This first guess of the composition can be used in the fundamental parameters method to determine a more accurate sample composition. Then the more accurate sample composition can be used to make a better particle size correction and improve the composition again, with the possibility to iterate again if needed.

Figure 7-15 shows the concept for using the particle size correction method described in section 7.3 for materials with a partially unknown composition. This method relies

on the Monte Carlo simulations being able to emulate the true data accurately. However as shown in Figure 7-1 and Figure 7-2, an error is already being introduced to the particle size correction from inconsistencies in the Monte Carlo simulated counts/second measurements. The combination of errors to do with unknown compositions and poor comparisons with Monte Carlo simulated data can make the correction poor.

With the standard method and equivalent sphere shape diameter (ESSD) corrections in place, hopefully the Monte Carlo simulated data and the experimentally measured data will agree well. This will prevent further error is introduced by using the Monte Carlo simulated correction figure.

## 7.6 Conclusion

The particle size effect can be an extremely large effect. For example, a change in particle size of just 20 microns results in an approximate 50% drop in fluorescence count rates for both the 3% copper and 5% iron in dough samples measured in this section. If uncorrected, this would be interpreted as a 50% reduction in the concentrations of these elements in standard XRF analysis.

Section 7.3 introduces a method that can correct for particle size effects in XRF measurements. The accuracy of the correction is currently limited by the accuracy of the Monte Carlo simulations used in creating the correction curves. The particle size correction relationship plotted using the Monte Carlo particulate function simulations has being compared to experimentally measured data and was found to agree reasonably well for copper, but less well for iron. However, given the magnitude of the particle size effect, even an approximate correction can be useful for applications where sample preparation and homogenisation is not possible.

Section 7.4 discusses two methods that could potentially be used to improve the agreement between the Monte Carlo simulation and the experimentally measured data. Both of these methods require a significant amount of experimental data to prove their viability. Future work will involve measuring more known particulate samples and comparing their fluorescence intensities to known standards with no particle size effects.

There are multiple applications where XRF is used to measure particulate samples that would benefit from a particle size correction method; these particularly include measurements of environmental and mineral samples. While XRF is commonly used to measure environmental samples such as soil and sand, these samples can have a large variability in their composition and particle size which makes correcting for the particle size effect challenging. The most viable mineral application would be measuring slurries within minerals processing plants, where changes in the overall slurry composition tend to be small. Processing plants aim to continuously grind ore to a consistently fine particle size; however changes in the average particle size can occur over time and lead to drifts in XRF measurements. Further work is needed to investigate whether the particle size correction method can be applied to mineral slurries. For example, to investigate whether the correction method can be used with XRF measurements of copper ore slurries, experimental data for the particle size effect in common copper minerals such as chalcopyrite and chalcocite would be useful. Further experimental measurements involving slurries with large particle size ranges but varying average particle sizes is also needed. Eventually the method could be tested on real slurry examples to determine whether it can reduce XRF measurement errors induced by changes in the average particle size of the slurry.

# PART 4: CONCLUSIONS AND RECOMMENDATIONS

## 8 Conclusion

This thesis describes two different approaches for improving the accuracy of X-ray fluorescence analysis, in particular for portable and in-situ applications.

The first approach involved measuring the L-shell X-ray emission spectra for 8 different heavy elements. Accurate knowledge of these intensities is highly relevant for improving theoretical descriptions of atomic X-ray emission, as well as for performing quantitative X-ray fluorescence analysis. Individual line intensity ratios relative to the brightest line from within each subshell, and the total L-subshell intensity ratios L1/L3 and L2/L3, are reported for the 8 different elements.

The second approach involved careful measurements of the particle size effect for copper and iron powders suspended in a weakly absorbing matrix. A method for correcting for particle size effects by taking two measurements of each sample with different exciting radiation energies was developed based on these measurements.

### 8.1 L-shell Emission Intensity Measurements and their Impact on X-ray Fluorescence

L-shell X-ray spectra from 8 different elements were collected using a custom-designed spectrometer and analysed using fitting software developed by the author that allowed the intensities and energy position of the different lines to be determined with high accuracy and precision. The fitting process is particularly complex due to the large number of lines present and the high degree of overlap. The intensities of each of these lines were reported as ratios to the brightest line from within each subshell to simplify the comparison with theoretically predicted values. For each element, this study was able to measure the intensities of up to fifteen individual L-shell line intensity ratios, which represented a significant improvement over previous work. The line intensity ratios are compared with Schofield's DF [10] and DHS [11] theoretical values as well as the values presented in Elam's database [75] and significant disagreement was found, both in intensity and overall trend with Z.

In the case of the L-shell X-ray emission, the majority of the total intensity stems from the first 10 brightest lines, which together account for more than 90% of the total intensity. The measured line intensities across the 3 L-subshells could be summed to give the total fluorescent intensity for each L-subshell. In the cases where a low intensity line could not be measured, its theoretical value was used to include that line in the total L-subshell intensity calculation. Theoretical values were only used for low intensity lines that would have minimal contribution to the total L-subshell intensity, and a large error was included for the theoretical component. The total L-subshell intensities are reported as the ratios L1/L3 and L2/L3 for comparison with theoretically predicted values, and they are compared with DHS predicted values [45],[12] and also values calculated using data recommended by Campbell [44], [52]. Significant disagreement is found between the measured values and the theoretically predicted data; in both cases the measured values are significantly higher in intensity than the calculated values.

These line intensity ratios are widely used in X-ray spectroscopy, and underpin much quantitative X-ray fluorescence analysis work performed using the fundamental parameters method. Mineral samples often contain multiple elements with many overlapping lines at varying intensities throughout a spectrum. Samples being measured for precious elements such as gold and platinum are particularly difficult to fit as these elements are usually present in the ppm range and overlap with many elements present at higher concentrations. Using incorrect theoretical values to fit complex experimental XRF spectra is shown to introduce large errors in the determination of the elemental composition.

Two journal articles have been published detailing the work on L-shell emission intensity measurements and their impact on X-ray fluorescence, summarising the information presented in Chapter 5 and Chapter 6. These papers are included in the references as reference [108] and reference [124].

## 8.2 Measurement and Modelling of Particle Size Effects

Particle size effects are very important in the X-ray fluorescence analysis of coarse and unprepared samples, but are normally ignored in practice due to the lack of an agreed correction framework and absence of high-quality experimental data for comparison. A cyclosizing technique was used to prepare particle samples with size fractions below 40 µm more accurately than any of the studies found in a comprehensive literature review. Particle samples above 40 µm were prepared using conventional sieving, but their particle distributions were measured using laser diffraction techniques to ensure accurate particle sizing. A method for suspending copper and iron powders in a weakly absorbing matrix was developed to enable accurate measurements to be made simulating particle size effects in mineral slurries.

Experimental measurements showed that the particle size effect can lead to a drop in fluorescence intensity of up to 80% compared to samples with the same matrix composition but no particle size effects. The measured particle size effects for iron and copper powder were compared with Lubecki et al.'s mathematical model [87] and Monte Carlo simulations. Lubecki et al.'s mathematical model makes significant simplifying assumptions. These include that the particles are spherical and of a single diameter, and that monoenergetic exciting radiation is used. Monte Carlo methods allow a more realistic simulation to be performed, including detailed X-ray physics, an accurate geometry model, and a polychromatic X-ray source. The measured results are compared to Monte Carlo simulations using spherical particles and randomly generated, roughly shaped particles as well Lubecki et al.'s model. The best agreement with experimental measurements was found using the simulated spherical particles with modified diameters.

To explore the possibility of developing a correction for particle size effects, measurements of copper and iron powders were made using two different exciting radiation energies. The two exciting radiation energies were selected so that one is located just above the K-edge of the element being measured, E1, and the other is significantly higher in energy so that the particle size effect is reduced, E2. For the optimal measurement of the copper particle size effect, E1 and E2 are selected to be 9.6 keV and 17.4 keV, respectively. A filter switch mechanism was developed to allow

rapid switching of filter material and X-ray tube settings, so that the two exciting radiation energies can be generated using a single molybdenum target X-ray tube.

A particle size effect correction method was developed that relates the dual-energy fluorescent intensity ratio I1(s)/I2(s) to the total particle size effect I1(s)/I1(0), where I1(s) and I2(s) are the measured fluorescent count rates using exciting radiation energies E1 and E2. The quantity I1(0) is the fluorescence intensity for a hypothetical sample of the same composition with no particle size effect, measured with exciting radiation energy I1; I1(s)/I1(0) is then a direct measurement of the particle size effect. Measurement of I1(s) and I2(s) then allows the unknown ratio I1(s)/I1(0) to be estimated. The correction method involves first predicting the relevant intensity values using Monte Carlo simulations and constructing a correction figure plotting I1(s)/I2(s) against I1(s)/I1(0) for a range of concentrations of the element of interest in a matrix similar to the slurry being measured.

The copper and iron powder measurements taken at energies E1 an E2 are plotted and compared to the Monte Carlo simulated values. The agreement between experimental measurements and Monte Carlo simulated measurements is good for copper, but less accurate for iron with differences of up to 30%. However given the magnitude of the particle size effect, even an approximate correction can be useful for applications where sample preparation and homogenisation is not possible, and there is the potential to substantially improve analysis accuracy for such materials.

### 8.3 Recommendations for Future Work

For the L-shell spectra measurements, future work would involve expanding the range of elements measured to produce a comprehensive database of relative and absolute fluorescent yields. This would be particularly useful for comparing the trends of line and subshell intensity ratios with atomic number, Z.

There are also theoretical models in the literature [125]–[128] that predict that the intensity of some L-shell X-ray lines should depend on angle of emission relative to the incident X-ray direction, something that is ignored in X-ray fluorescence analysis. Limited experimental studies undertaken so far agree with the literature, but have not used high quality spectral fitting methods to accurately determine the individual L-shell

X-ray lines that are showing the angular dependence. Future work will involve performing angular-dependent L-shell spectra measurements and using the high-accuracy fitting methods developed in this thesis to determine any changes in intensity of L-shell lines with angle.

Recommendations for future work to further develop the particle size correction method introduced in this thesis are discussed in detail in section7.4. This work will first focus on improving the agreement between the Monte Carlo simulations and experimentally measured particle size effect data. New methods will be explored to simulate stochastic media with a better control over the particle size distribution, allowing the impact of particle size and shape to be explored together.

Significantly more experimental data is needed for a more comprehensive comparison with Monte Carlo simulation data. New elements and minerals should be measured to determine particle size effects at various concentrations, and these should be compared to standards with no particle size effects.

The aim of the particle size correction method is to improve the XRF analysis of slurries. Slurries are significantly more complicated that the binary systems measured in this thesis, as they can have large particle size distributions, different size distributions for different mineral phases, and complex matrix effects caused by the presence of multiple mineral. Future work should involve experimental measurements of slurries with different particle size distributions. Comparisons with Monte Carlo simulations including large particle size distributions will be needed to determine whether the correction method can accurately be applied to slurries.

**REFERENCES**


[1] A. Einstein, “Über einen die Erzeugung und Verwandlung des Lichtes betreffenden heuristischen Gesichtspunkt,” *Ann. Phys.*, vol. 322, no. 6, pp. 132–148, Jan. 1905.

[2] R. Grieken and A. Markowicz, *Handbook of X-ray spectometry*, Second. Boca Raton: CRC PRess, 2001.

[3] B. Beckhoff, B. Kanngießer, N. Langhoff, R. Wedell, and H. Wolff, Eds., *Handbook of Practical X-Ray Fluorescence Analysis*. Berlin, Heidelberg: Springer Berlin Heidelberg, 2006.

[4] C. Da *et al.*, “Online X-ray Fluorescence (XRF) Analysis of Heavy Metals in Pulverized Coal on a Conveyor Belt,” *Appl. Spectrosc. Vol. 70, Issue 2, pp. 272-278*, vol. 70, no. 2, pp. 272–278, Feb. 2016.

[5] B. Hołyńska, M. Lankosz, J. Ostachowicz, and K. Wolski, “On-stream XRF measuring system for ore slurry analysis and particle-size control,” *Int. J. Appl. Radiat. Isot.*, vol. 36, no. 5, pp. 369–373, May 1985.

[6] F. Nakhaei, A. Sam, M. Mosavi, and A. Nakhaei, “Prediction of XRF analyzers error for elements on-line assaying using Kalman Filter,” *Int. J. Min. Sci. Technol.*, vol. 22, no. 4, pp. 595–601, Jul. 2012.

[7] R. Sitko and B. Zawisz, “Quantification in X-Ray Fluorescence Spectrometry,” in *X-Ray Spectroscopy*, InTech, 2012.

[8] R. M. Rousseau, “Fundamental algorithm between concentration and intensity in XRF analysis 1—theory,” *X-Ray Spectrom.*, vol. 13, no. 3, pp. 115–120, Mar. 1984.

[9] R. Tanaka and Y. Orihashi, *XRF analysis of major and trace elements for silicate rocks using low dilution ratio fused glass*, vol. 2. Division of Earth and Planetary Sciences (Earth and Planetary Materials Science) Graduate School of Science Hokkaido University, 1997.

[10] J. H. Scofield, “Hartree-Fock values of L x-ray emission rates,” *Phys. Rev. A*, vol.

10, no. 5, pp. 1507–1510, Nov. 1974.

[11] J. H. Scofield, “Relativistic hartree-slater values for K and L X-ray emission rates,” *At. Data Nucl. Data Tables*, vol. 14, no. 2, pp. 121–137, Aug. 1974.

[12] J. H. Scofield, “Theoretical photoionization cross sections from 1 to 1500 keV.,” U.S. Atomic Energy Commission, Jan. 1973.

[13] Ö. Şimşek, “Photon-Induced L 3 Subshell x-ray Intensity Ratios for Re, Au, Tl and Pb,” *Phys. Scr.*, vol. 67, no. 4, pp. 301–305, Jan. 2003.

[14] A.-M. Vlaicu *et al.*, “Investigation of the 74W L emission spectra and satellites,” *Phys. Rev. A*, vol. 58, no. 5, pp. 3544–3551, Nov. 1998.

[15] T. Papp, J. L. Campbell, and S. Raman, “Experimental test of Dirac-Fock versus Dirac-Hartree-Slater L X-ray intensity ratios,” *J. Phys. B At. Mol. Opt. Phys.*, vol. 26, no. 22, pp. 4007–4017, Nov. 1993.

[16] B. Dziunikowski, *Energy dispersive x-ray fluorescence analysis*. Elsevier, 1989.

[17] A. Markowicz, “Evaluation of a correction method for the particle-size effect in x-ray fluorescence analysis of ‘Thin’ and monolayer samples,” *X-Ray Spectrom.*, vol. 12, no. 4, pp. 134–137, Oct. 1983.

[18] P. Berry, T. Furuta, and J. Rhodes, “Particle-size effects in radioisotope x-ray spectrometry,” *Adv. X-Ray Anal.*, vol. 12, no. 1, pp. 612–632, 1969.

[19] S. T. Perkins, D. E. Cullen, M. H. Chen, J. H. Hubbell, J. Rathkopf, and J. Scofield, “Tables and graphs of atomic subshell and relaxation data derived from the LLNL Evaluated Atomic Data Library (EADL), Z=1-100,” *UCRL-50400*, vol. 30, 1991.

[20] D. E. Cullen, J. H. Hubbell, and L. Kissel, “EPDL97: the Evaluated Photon Data Library, ’97 Version,” *UCRL--50400 Vol 6 Rev 5*, 1997.

[21] B. Beckhoff, T. Jach, M. Lepy, and M. Mantler, “International initiative on X-ray fundamental parameters Roadmap document on atomic Fundamental Parameters for X-ray methodologies,” 2012. [Online]. Available: http://www.nucleide.org/IIFP/IIFP_Roadmap_V1.pdf. [Accessed: 10-Oct-2017].

[22] A. Zangwill, “Hartree and Thomas: the forefathers of density functional theory,” *Archive for History of Exact Sciences*, vol. 67. Springer, pp. 331–348, 2013.

[23] P. A. M. Dirac, “The Quantum Theory of the Electron,” *Proc. R. Soc. A Math. Phys. Eng. Sci.*, vol. 117, no. 778, pp. 610–624, Feb. 1928.

[24] P. A. M. Dirac, “Note on Exchange Phenomena in the Thomas Atom,” *Math. Proc. Cambridge Philos. Soc.*, vol. 26, no. 3, p. 376, Jul. 1930.

[25] V. Fock, “Nherungsmethode zur Losung des quantenmechanischen Mehrkorperproblems,” *Zeitschrift fur Phys.*, vol. 61, no. 1–2, pp. 126–148, Jan. 1930.

[26] J. Slater, “A Simplification of the Hartree-Fock Method,” *Phys. Rev.*, vol. 81, no. 3, pp. 385–390, Feb. 1951.

[27] W. Kohn, A. D. Becke, and R. G. Parr, “Density Functional Theory of Electronic Structure,” *J. Phys. Chem.*, vol. 100, no. 31, pp. 12974–12980, 1996.

[28] P. Hohenberg and W. Kohn, “Inhomogeneous Electron Gas,” *Phys. Rev.*, vol. 136, no. 3B, pp. B864–B871, Nov. 1964.

[29] W. Kohn and L. J. Sham, “Self-Consistent Equations Including Exchange and Correlation Effects,” *Phys. Rev.*, vol. 140, no. 4A, pp. A1133–A1138, Nov. 1965.

[30] A. K. Rajagopal and J. Callaway, “Inhomogeneous Electron Gas,” *Phys. Rev. B*, vol. 7, no. 5, pp. 1912–1919, Mar. 1973.

[31] A. K. Rajagopal, “Inhomogeneous relativistic electron gas,” *J. Phys. C Solid State Phys.*, vol. 11, no. 24, pp. L943–L948, Dec. 1978.

[32] A. H. MacDonald and S. H. Vosko, “A relativistic density functional formalism,” *J. Phys. C Solid State Phys.*, vol. 12, no. 15, pp. 2977–2990, Aug. 1979.

[33] J. P. Desclaux, “A multiconfiguration relativistic DIRAC-FOCK program,” *Comput. Phys. Commun.*, vol. 9, no. 1, pp. 31–45, Jan. 1975.

[34] M. Reiher and A. Wolf, *Relativistic quantum chemistry : the fundamental theory of molecular science*, 2nd ed. Weinheim: Wiley-VCH, 2015.

[35] I. P. Grant, B. J. McKenzie, P. H. Norrington, D. F. Mayers, and N. C. Pyper, “An atomic multiconfigurational Dirac-Fock package,” *Comput. Phys. Commun.*, vol. 21, no. 2, pp. 207–231, Dec. 1980.

[36] K. G. Dyall, I. P. Grant, C. T. Johnson, F. A. Parpia, and E. P. Plummer, “GRASP: A general-purpose relativistic atomic structure program,” *Comput. Phys. Commun.*, vol. 55, no. 3, pp. 425–456, Oct. 1989.

[37] C. Froese Fischer, “Average-energy-of-configuration Hartree-Fock results for the atoms helium to radon charlotte froese fischer,” *At. Data Nucl. Data Tables*, vol. 4, pp. 301–399, Mar. 1972.

[38] C. Froese Fischer, “A multi-configuration Hartree-Fock program with improved stability,” *Comput. Phys. Commun.*, vol. 4, no. 1, pp. 107–116, Oct. 1972.

[39] C. Froese Fischer, *The Hartree-Fock Method for Atoms : A Numerical Approach*. Wiley, 1977.

[40] Deutsch, Hölzer, Härtwig, Wolf, Fritsch, and Förster, “K alpha and K beta x-ray emission spectra of copper.,” *Phys. Rev. A, At. Mol. Opt. Phys.*, vol. 51, no. 1, pp. 283–296, Jan. 1995.

[41] C. T. Chantler, A. C. L. Hayward, and I. P. Grant, “Theoretical Determination of Characteristic X-Ray Lines and the Copper K α Spectrum,” *Phys. Rev. Lett.*, vol. 103, no. 12, p. 123002, Sep. 2009.

[42] C. T. Chantler, J. A. Lowe, and I. P. Grant, “Anomalous satellite intensity discrepancy in copper x-ray lines,” *Phys. Rev. A*, vol. 85, no. 3, p. 32513, Mar. 2012.

[43] T. L. Pham, T. V. Nguyen, J. A. Lowe, I. P. Grant, and C. T. Chantler, “Characterization of the copper *K β* x-ray emission profile: an *ab initio* multi-configuration Dirac–Hartree–Fock approach with Bayesian constraints,” *J. Phys. B At. Mol. Opt. Phys.*, vol. 49, no. 3, p. 35601, Feb. 2016.

[44] J. L. Campbell, “Fluorescence yields and Coster–Kronig probabilities for the atomic L subshells,” *At. Data Nucl. Data Tables*, vol. 85, no. 2, pp. 291–315, Nov.

2003.

[45] M. H. Chen, B. Crasemann, and H. Mark, “Widths and fluorescence yields of atomic L-shell vacancy states,” *Phys. Rev. A*, vol. 24, no. 1, pp. 177–182, Jul. 1981.

[46] S. Puri, D. Mehta, B. Chand, N. Singh, and P. N. Trehan, “L shell fluorescence yields and coster—kronig transition probabilities for the elements with 25 < Z < 96,” *X-Ray Spectrom.*, vol. 22, no. 5, pp. 358–361, Sep. 1993.

[47] J. H. Scofield, “‘Radiative transitions,’ in Atomic Inner-Shell Processes,” pp. 265–292, 1975.

[48] M. H. Chen, B. Crasemann, and H. Mark, “Radiationless Transitions to Atomic M 1,2,3 Shells: Results of Relativistic Theory,” *Phys. Rev. A*, vol. 27, 1983.

[49] J. H. Hubbell, *Bibliography and current status of K, L and higher shell fluorescence yields for computations of photon energy absorption coefficients*, NISTIR 89-. National Bureau of Standards, 1989.

[50] J. L. Campbell, “X-Ray Energies : Transition Probabilities, Fluorescence and Coster-Kronig Probabilities,” *Int. Initiat. X-ray Fundam. Parameters*, vol. 24, no. 1, pp. 17–30, 2010.

[51] J. L. Campbell and T. Papp, “Widths of the Atomic K–N7 Levels,” *At. Data Nucl. Data Tables*, vol. 77, no. 1, pp. 1–56, Jan. 2001.

[52] J. L. Campbell, “Fluorescence yields and Coster–Kronig probabilities for the atomic L subshells. Part II: The L1 subshell revisited,” *At. Data Nucl. Data Tables*, vol. 95, no. 1, pp. 115–124, 2009.

[53] M. O. Krause and J. H. Oliver, “Natural widths of atomic K and L levels, Kα X-ray lines and several KLL Auger lines,” *J. Phys. Chem. Ref. Data*, vol. 8, no. 2, p. 329, Jan. 1979.

[54] M. J. Berger *et al.*, “XCOM: Photon Cross Section Database (version 1.5),” *Natl. Inst. Stand. Technol.*

[55] C. T. Chantler *et al.*, “X-Ray Form Factor, Attenuation and Scattering Tables (version 2.1),” *[Online] Available: http://physics.nist.gov/ffast [2017, October 1].* National Institute of Standards and Technology, Gaithersburg, MD., 2005. Originally published as Chantler, C.T., J. Phys. Chem. Ref. Data **29**(4), 597-1048 (2000); and Chantler, C.T., J. Phys. Chem. Ref. Data **24**, 71-643 (1995).

[56] C. T. Chantler, “Theoretical Form Factor, Attenuation, and Scattering Tabulation for Z=1–92 from E=1–10 eV to E=0.4–1.0 MeV,” *J. Phys. Chem. Ref. Data*, vol. 24, no. 1, p. 71, 1995.

[57] C. T. Chantler, “Detailed tabulation of atomic form factors, photoelectric absorption and scattering cross section, and mass attenuation coefficients in the vicinity of absorption edges in the soft X-ray (Z = 30-36, Z = 60-89, E = 0.1-10 keV)--addressing convergence issue,” *J. Phys. Chem. Ref. Data*, vol. 29, no. 4, pp. 597–1048, Jul. 2000.

[58] D. T. Cromer and D. Liberman, “Internal report LA-4403 UC-34,” 1970.

[59] D. T. Cromer and D. Liberman, “Anomalous dispersion calculations near to and on the long-wavelength side of an absorption edge,” *Acta Cryst.*, vol. A37, no. 2, pp. 267–268, 1981.

[60] D. T. Cromer and D. Liberman, “Relativistic calculation of anomalous scattering factors for X rays,” *J. Chem. Phys.*, vol. 53, no. 5, pp. 1891–1898, 1970.

[61] D. T. Cromer and J. B. Mann, “X-ray scattering factors computed from numerical Hartree-Fock wave functions,” *Acta Cryst.*, vol. A24, no. 2, pp. 321–324, 1968.

[62] C. M. Heirwegh, “Studies of Light Element X-Ray Fundamental Parameters Used in PIXE Analysis,” University of Guelph, 2014.

[63] J. H. Hubbell and I. Overbo, “Relativistic atomic form factors and photon coherent scattering cross sections,” *J. Phys. Chem. Ref. Data*, vol. 8, no. 1, pp. 69–106, Jan. 1979.

[64] J. H. Hubbell, W. J. Veigele, E. A. Briggs, R. T. Brown, D. T. Cromer, and R. J. Howerton, “Atomic form factors, incoherent scattering functions, and photon

scattering cross sections," *J. Phys. Chem. Ref. Data*, vol. 4, no. 3, pp. 471–538, Jul. 1975.

[65] J. H. Hubbell, "Review and history of photon cross section calculations.," *Phys. Med. Biol.*, vol. 51, no. 13, pp. R245-62, Jul. 2006.

[66] J. H. Hubbell, "Review of photon interaction cross section data in the medical and biological context," *Phys. Med. Biol.*, vol. 44, no. 1, pp. R1–R22, Jan. 1999.

[67] W. Jitschin, U. Werner, G. Materlik, and G. D. Doolen, "Electron correlations in the L -shell photoionization of heavy elements," *Phys. Rev. A*, vol. 35, no. 12, pp. 5038–5045, Jun. 1987.

[68] J. Bearden, "X-Ray Wavelengths," *Rev. Mod. Phys.*, vol. 39, no. 1, pp. 78–124, Jan. 1967.

[69] R. Deslattes, E. Kessler, P. Indelicato, L. de Billy, E. Lindroth, and J. Anton, "X-ray transition energies: new approach to a comprehensive evaluation," *Rev. Mod. Phys.*, vol. 75, no. 1, pp. 35–99, Jan. 2003.

[70] U. W. Arndt *et al.*, "X-rays," in *International Tables for Crystallography Volume C: Mathematical, physical and chemical tables*, 3rd ed., E. Prince, Ed. Dordrecht, Boston, London: International Union of Crystallography by Kluwer Academic Publishers, 2004, pp. 191–258.

[71] G. Roach, J. Tickner, and Y. Van Haarlem, "Discrepancies in atomic shell and fluorescent X-ray energies in the Evaluated Photon Data Library EPDL97," *X-Ray Spectrom.*, vol. 41, no. 5, pp. 279–283, Sep. 2012.

[72] J. W. Fowler *et al.*, "A Reassessment of Absolute Energies of the X-ray L Lines of Lanthanide Metals," Feb. 2017.

[73] J. L. Campbell and J.-X. Wang, "Interpolated Dirac-Fock values of L-subshell x-ray emission rates including overlap and exchange effects," *At. Data Nucl. Data Tables*, vol. 43, no. 2, pp. 281–291, Nov. 1989.

[74] S. I. Salem, S. L. Panossian, and R. A. Krause, "Experimental K and L relative x-ray emission ratess," *At. Data Nucl. Data Tables*, vol. 14, no. 2, pp. 91–109, Aug.

1974.

[75] W. T. Elam, B. D. Ravel, and J. R. Sieber, “A new atomic database for X-ray spectroscopic calculations,” *Radiat. Phys. Chem.*, vol. 63, no. 2, pp. 121–128, Feb. 2002.

[76] M. C. Martins, M. I. Marques, F. Parente, and J. G. Ferreira, “Some K X-ray relative transition probabilities for Z=47, 49, 52, 55 and 56,” *J. Phys. B At. Mol. Opt. Phys.*, vol. 22, no. 20, pp. 3167–3174, Oct. 1989.

[77] J. L. Campbell, “Non-monotonic behaviour of the Kβ 2 ’/Kβ 1 â€™ x-ray intensity ratio in the atomic number region 40⩽ Z ⩽50,” *J. Phys. B At. Mol. Opt. Phys.*, vol. 34, no. 17, pp. 3543–3553, Sep. 2001.

[78] C. Ximeng, L. Zhaoyuan, C. Xiaohong, M. Shuxun, and Z. Hualin, “K x-ray relative transition probabilities for 39⩽ Z ⩽68,” *J. Phys. B At. Mol. Opt. Phys.*, vol. 34, no. 17, pp. 3563–3568, Sep. 2001.

[79] C. V. Raghavaiah *et al.*, “Lα/Lβ; and Lα/Lγ x-ray intensity ratios for elements in the range Z = 55-80,” *X-Ray Spectrom.*, vol. 19, no. 1, pp. 23–26, Feb. 1990.

[80] D. V Rao, G. E. Gigante, and R. Cesareo, “L-shell x-ray intensity ratios for Au and Pb at excitation energies 36.82, 43.95, 48.60, 50.20 and 53.50 keV,” *Phys. Scr.*, vol. 47, no. 6, pp. 765–768, Jun. 1993.

[81] M. K. Alqadi, Y. Alsenjlawi, and F. Y. Alzoubi, “Measurement of L X-Ray relative intensities for selected heavy elements,” *Radiat. Phys. Chem.*, vol. 87, pp. 31–34, 2013.

[82] P. Yalcin, S. Porikli, Y. Kurucu, and S. Y., “Measurement of relative L X-ray intensity ratio following radioactive decay and photoionization,” *Phys. Lett. B*, vol. 663, no. 3, pp. 186–190, May 2008.

[83] A. Küçükönde, B. G. Durdu, Ö. Sögüt, and E. Büyükkasap, “L X-ray production cross sections, average L shell fluorescence yield and intensity ratios in heavy elements,” *J. Radioanal. Nucl. Chem.*, vol. 260, no. 1, pp. 89–97, 2004.

[84] M. Ertuğrul, “The vacancy transfer probability dependence on relative L X-ray

intensities in the atomic range 57 ≤ Z ≤ 92 at 59.5 keV," *Nucl. Instruments Methods Phys. Res. Sect. B Beam Interact. with Mater. Atoms*, vol. 111, no. 3–4, pp. 229–233, May 1996.

[85] A. Kumar, Y. Chauhan, and S. Puri, "Incident photon energy and Z dependence of L X-ray relative intensities," *At. Data Nucl. Data Tables*, vol. 96, no. 6, pp. 567–585, Nov. 2010.

[86] A. Vlaicu, T. Tochio, T. Ishizuka, D. Ohsawa, Y. Ito, and T. Mukoyama, "Detailed L Emission Spectra and Satellites of 74 W," *ICR Annu. Rep.*, vol. 4, 1997.

[87] A. Lubecki, B. Hołyńska, and M. Wasilewska, "Grain size effect in non-dispersive X-ray fluorescence analysis," *Spectrochim. Acta Part B At. Spectrosc.*, vol. 23, no. 7, pp. 465–479, Jun. 1968.

[88] F. Claisse, "Overcoming the particle size effect in the internal standard method of X-ray fluorescence analysis," *Spectrochim. Acta Part B At. Spectrosc.*, vol. 25, no. 5, pp. 209–218, May 1970.

[89] C. T. Chantler *et al.*, "Stereochemical analysis of ferrocene and the uncertainty of fluorescence XAFS data," *J. Synchrotron Radiat.*, vol. 19, no. 2, pp. 145–158, Mar. 2012.

[90] F. Claisse and C. Samson, *Heterogeneity Effects in X-Ray Analysis*. Springer, 1962.

[91] C. B. Hunter and J. R. Rhodes, "Particle size effects in X-Ray emission analysis: Formulae for continuous size distributions," *X-Ray Spectrom.*, vol. 1, no. 3, pp. 107–111, Jul. 1972.

[92] B. Hołyńska and A. Markowicz, "Experimental evaluation of the Rhodes-Hunter model for the particle size effect in X-ray fluorescence analysis of 'thin' samples," *X-Ray Spectrom.*, vol. 10, no. 2, pp. 61–63, Apr. 1981.

[93] B. Hołyńska and A. Markowicz, "Correction method for the particle-size effect in the x-ray fluorescence analysis of 'Thin' and monolayer samples," *X-Ray Spectrom.*, vol. 11, no. 3, pp. 117–120, Jul. 1982.

[94] A. L. Finkelshtein and N. Brjansky, "Estimating particle size effects in X-ray

fluorescence spectrometry," *Nucl. Instruments Methods Phys. Res. Sect. B Beam Interact. with Mater. Atoms*, vol. 267, no. 14, pp. 2437–2439, Jul. 2009.

[95] B. Hołyńska, "Non-dispersive X-ray fluorescence method using two X-ray sources for the determination of grain size and concentration of the major element in simulated ore slurries," *Spectrochim. Acta Part B At. Spectrosc.*, vol. 27, no. 7, pp. 287–294, Jul. 1972.

[96] M. Lankosz, "A new approach to the particle-size effect correction in the x-ray fluorescence analysis of multimetallic ore slurries," *X-Ray Spectrom.*, vol. 17, no. 4, pp. 161–165, Aug. 1988.

[97] Y. Maruyama, K. Ogawa, T. Okada, and M. Kato, "Laboratory experiments of particle size effect in X-ray fluorescence and implications to remote X-ray spectrometry of lunar regolith surface," *Earth, Planets Sp.*, vol. 60, no. 4, pp. 293–297, Apr. 2008.

[98] P. Van Dyck, A. Markowicz, and R. Van Grieken, "Influence of sample thickness, excitation energy and geometry on particle size effects in XRF," *X-Ray Spectrom.*, vol. 14, no. 4, pp. 183–187, Oct. 1985.

[99] N. Ritchie, D. Davis, and M. Sailey, "DTSA-II." NIST, Gaithersburg, 2017.

[100] P. Kregsamer, "QXAS X-ray Analysis Software." IAEA Laboratories Seibersdorf, Seibersdorf, 1995.

[101] "MATLAB R2013a." The MathWorks, Inc., Natick, Massachusetts, United States, 2013.

[102] M. L. Hildner, A. J. Antolak, and G. S. Bench, "Improved fitting of PIXE spectra: the Voigt profile and Si(Li) detector modeling," *Nucl. Instruments Methods Phys. Res. Sect. A Accel. Spectrometers, Detect. Assoc. Equip.*, vol. 373, no. 1, pp. 124–130, Apr. 1996.

[103] J. L. Campbell and J.-X. Wang, "Lorentzian contributions to x-ray lineshapes in Si(Li) spectroscopy," *X-Ray Spectrom.*, vol. 21, no. 5, pp. 223–227, Sep. 1992.

[104] G. W. Phillips and K. W. Marlow, "Automatic analysis of gamma-ray spectra from

germanium detectors," *Nucl. Instruments Methods*, vol. 137, no. 3, pp. 525–536, Sep. 1976.

[105] J. L. Campbell, "Si(Li) detector lineshapes for PIXE analysis and improvement of the PIXE database," *Nucl. Instruments Methods Phys. Res. Sect. B Beam Interact. with Mater. Atoms*, vol. 22, no. 1–3, pp. 13–20, Mar. 1987.

[106] F. James and M. Roos, "Minuit - a system for function minimization and analysis of the parameter errors and correlations," *Comput. Phys. Commun.*, vol. 10, no. 6, pp. 343–367, Dec. 1975.

[107] G. Allodi, "FMINUIT - a binding to Minuit for Matlab, Octave and Scilab." .

[108] B. Ganly, Y. Van Haarlem, and J. Tickner, "Measurement of relative line intensities for L-shell X-rays from selected elements between Z = 68 (Er) and Z = 79 (Au)," *X-Ray Spectrom.*, vol. 45, no. 4, pp. 233–243, Jul. 2016.

[109] H. Ebel, M. F. Ebel, J. Wernisch, C. Poehn, and H. Wiederschwinger, "Quantification of continuous and characteristic tube spectra for fundamental parameter analysis," *X-Ray Spectrom.*, vol. 18, no. 3, pp. 89–100, Jun. 1989.

[110] H. Ebel, "L1, L1,2, L, L1,2,3,4,5,6 and L1,2,3 spectra of x-ray tubes," *X-Ray Spectrom.*, vol. 32, no. 1, pp. 46–51, Jan. 2003.

[111] H. Ebel, "X-ray tube spectra," *X-Ray Spectrom.*, vol. 28, no. 4, pp. 255–266, Jul. 1999.

[112] I. Kawrakow and D. W. O. Rogers, "The EGSnrc Code System:Monte Carlo Simulation of Electron and Photon Transport," *NRCC Rep. PIRS-701*, 2003.

[113] I. Kawrakow, "Accurate condensed history Monte Carlo simulation of electron transport. I. EGS nrc, the new EGS4 version," *Med. Phys.*, vol. 27, no. 3, pp. 485–498, Mar. 2000.

[114] H. Ebel, "Fundamental Parameter Programs: Algorithms for the Description of K, L and M Spectra of X-ray Tubes," 2006.

[115] N. K. Del Grande, "Measured 1 to 40 keV Photoabsorption Cross Sections for: Fe,

Ni, Sn, Ta, Pt, Au, Pb, U," 1986, vol. 691, p. 2.

[116] F. A. Shergold, "The effect of sieve loading on the results of sieve analysis of natural sands," *J. Soc. Chem. Ind.*, vol. 65, no. 9, pp. 245–249, Sep. 1946.

[117] *Cycloszier Instruction Manual*, 3rd ed. Sydney: WARMAN INTERNATIONAL LTD, 1997.

[118] K. J. Hsü, "Grains Settle," in *Physics of Sedimentology*, Berlin, Heidelberg: Springer Berlin Heidelberg, 2004, pp. 25–46.

[119] L. M. Diamante and T. Lan, "Absolute Viscosities of Vegetable Oils at Different Temperatures and Shear Rate Range of 64.5 to 4835 s-1," *J. Food Process.*, vol. 2014, pp. 1–6, 2014.

[120] P. Hull, *Glucose Syrups: Technology and Applications*. Wiley, 2010.

[121] I. Kawrakow, E. Mainegra-Hing, D. W. O. Rogers, F. Tessier, and B. R. B. Walters, "The EGSnrc Code System: Monte Carlo Simulation of Electron and Photon Transport," 2010.

[122] J. Tickner, "Particle Transport in Inhomogeneous Media," in *Advanced Monte Carlo for Radiation Physics, Particle Transport Simulation and Applications*, Berlin, Heidelberg: Springer Berlin Heidelberg, 2001, pp. 111–116.

[123] J. Tickner and James, "Simulating nuclear particle transport in stochastic media using Perlin noise functions," *Nucl. Instruments Methods Phys. Res. Sect. B Beam Interact. with Mater. Atoms*, vol. 213, pp. 124–128, Jan. 2004.

[124] B. Ganly, Y. Van Haarlem, and J. Tickner, "Relative total L-subshell X-ray emission intensities and their impact on the fitting of complex X-ray fluorescence spectra," *X-Ray Spectrom.*, 2017.

[125] M. L. Garg, J. Singh, H. R. Verma, N. Singh, P. C. Mangal, and P. N. Trehan, "Relative intensity measurements of L-shell X-rays for Ta, Au, Pb and Bi in the energy range 17-60 keV," *J. Phys. B At. Mol. Phys.*, vol. 17, no. 4, pp. 577–584, Feb. 1984.

[126] K. S. Kahlon, K. Shatendra, K. L. Allawadhi, and B. S. Sood, “Experimental investigation of angular dependence of photon induced L-shell X-ray emission intensity,” *Pramana*, vol. 35, no. 1, pp. 105–114, Jul. 1990.

[127] J. K. Sharma and K. L. Allawadhi, “Angular distribution of Lbeta x-rays from decay of $L_3$ subshell vacancies in uranium and thorium following photoionization,” *J. Phys. B At. Mol. Opt. Phys.*, vol. 32, no. 10, pp. 2343–2349, May 1999.

[128] A. Tartari, C. Baraldi, E. Casnati, A. Da Re, J. E. Fernandez, and S. Taioli, “On the angular dependence of L x-ray production cross sections following photoionization at an energy of 59.54 keV,” *J. Phys. B At. Mol. Opt. Phys.*, vol. 36, no. 5, pp. 843–851, Mar. 2003.

[129] J. H. Hubbell *et al.*, “A Review, Bibliography, and Tabulation of *K* , *L* , and Higher Atomic Shell X-Ray Fluorescence Yields,” *J. Phys. Chem. Ref. Data*, vol. 23, no. 2, pp. 339–364, Mar. 1994.

[130] J. H. Hubbell *et al.*, “Erratum: ‘A Review, Bibliography, and Tabulation of *K* , *L* , and Higher Atomic Shell X-Ray Fluorescence Yields’ [J. Phys. Chem. Ref. Data **23** , 339 (1994)],” *J. Phys. Chem. Ref. Data*, vol. 33, no. 2, pp. 621–621, Jun. 2004.